ISSN 0042-8469
e-ISSN 2217-4753
УДК 623 + 355/359

Вол. 73, бр. 2
2025

НАУЧНИ ЧАСОПИС МИНИСТАРСТВА ОДБРАНЕ И ВОЈСКЕ СРБИЈЕ

ВОЈНОТЕХНИЧКИ ГЛАСНИК

2 2025 ВОЈНОТЕХНИЧКИ ГЛАСНИК

ВТГ.МО.УПР.СРБ

www.vtg.mod.gov.rs

ISSN 0042-8469
e-ISSN 2217-4753
УДК 623 + 355/359

Том 73, № 2
2025

ВТГ

НАУЧНЫЙ ЖУРНАЛ МИНИСТЕРСТВА ОБОРОНЫ
И ВООРУЖЕННЫХ СИЛ РЕСПУБЛИКИ СЕРБИЯ

ВОЕННО-ТЕХНИЧЕСКИЙ ВЕСТНИК

ВОЕННО-ТЕХНИЧЕСКИЙ ВЕСТНИК

2 2025

ВТГ.МО.УПР.СРБ

www.vtg.mod.gov.rs

ISSN 0042-8469
e-ISSN 2217-4753
UDC 623 + 355/359

Vol. 73, Issue 2
2025

MTC

SCIENTIFIC JOURNAL OF THE MINISTRY OF DEFENCE AND THE SERBIAN ARMED FORCES

MILITARY TECHNICAL COURIER

MILITARY TECHNICAL COURIER
2 2025

ВТГ.МО.УПР.СРБ

www.vtg.mod.gov.rs

ISSN 0042-8469
e-ISSN 2217-4753
UDC 623 + 355/359

НАУЧНИ ЧАСОПИС МИНИСТАРСТВА ОДБРАНЕ И ВОЈСКЕ СРБИЈЕ

ВОЈНОТЕХНИЧКИ ГЛАСНИК

ВОЛУМЕН 73•БРОЈ 2• АПРИЛ – ЈУН 2025.

NAUČNI ČASOPIS MINISTARSTVA ODBRANE I VOJSKE SRBIJE

VOJNOTEHNIČKI GLASNIK

VOLUMEN 73•BROJ 2•APRIL – JUN 2025.

втг.мо.упр.срб
www.vtg.mod.gov.rs
COBISS.SR-ID 4423938
DOI: 10.5937/VojnotehnickiGlasnik

ISSN 0042-8469
e-ISSN 2217-4753
UDC 623 + 355/359

НАУЧНЫЙ ЖУРНАЛ МИНИСТЕРСТВА ОБОРОНЫ И ВООРУЖЁННЫХ СИЛ РЕСПУБЛИКИ СЕРБИЯ

ВОЕННО-ТЕХНИЧЕСКИЙ ВЕСТНИК

ТОМ 73•НОМЕР ВЫПУСКА 2•АПРЕЛЬ – ИЮНЬ 2025.

SCIENTIFIC JOURNAL OF THE MINISTRY OF DEFENCE AND SERBIAN ARMED FORCES

MILITARY TECHNICAL COURIER

VOLUME 73•ISSUE 2•APRIL – JUNE 2025

ВТГ.МО.УПР.СРБ
www.vtg.mod.gov.rs
COBISS.SR-ID 4423938
DOI: 10.5937/VojnotehnickiGlasnik

ВЛАСНИЦИ:
Министарство одбране и Војска Србије

ИЗДАВАЧ:
Универзитет одбране у Београду, Војна академија

СОБСТВЕННИКИ: Министерство обороны и Вооружённые силы Республики Сербия
ИЗДАТЕЛЬСТВО: Университет обороны в г. Белград, Военная академия

OWNERS:
Ministry of Defence and Serbian Armed Forces
PUBLISHER:
University of Defence in Belgrade, Military Academy

С А Д Р Ж А Ј

С О Д Е Р Ж А Н И Е

C O N T E N T S

Sombor index of thorny graphs

Ivan Gutman

University of Kragujevac, Faculty of Science,
Kragujevac, Republic of Serbia,
e-mail: gutman@kg.ac.rs,
ORCID iD: https://orcid.org/0000-0001-9681-1550

https://doi.org/10.5937/vojtehg73-56402

FIELD: mathematics (mathematics subject classification: primary 05C07, secondary 05C09)
ARTICLE TYPE: original scientific paper

Abstract:

Introduction/purpose: The thorny graph of a graph G is obtained by attaching pendent vertices to the vertices of G. A mathematical study of the Sombor index of thorny graphs is undertaken.

Methods: Combinatorial graph theory is applied.

Results: A general expression for the Sombor index of thorny graphs is obtained, as well as lower and upper bounds. Several special cases of this general expression are pointed out.

Conclusion: The paper contributes to the theory of the Sombor index.

Keywords: degree (of vertex), Sombor index, thorny graph.

Introduction

In this paper, G will denote a simple graph with $n > 1$ vertices and m edges. Its vertices are labeled by $v_1, v_2, \ldots, v_n$. The degree (= number of first neighbors) of a vertex v_i will be denoted by $d(v_i)$. A vertex of degree one is said to be pendent. An edge whose one end vertex is of degree one is also said to be pendent.

For additional details of graph theory, see (Harary, 1969; Bondy & Murty, 1976).

In the last few years, a vertex-degree-based graph invariant, named the Sombor index, has attracted much attention in mathematics, see e.g. (Li et al., 2024; Rather et al., 2024; Wang et al., 2024) and found numerous applications, both in chemistry, see e.g. (Hayat et al., 2024; Rauf & Ahmad,

2024), network theory, see e.g. (Hamid et al., 2022; Imran et al., 2024), and in other areas, see e.g., (Alqahtani et al., 2024; Anwar et al., 2024; Jamil et al., 2025).

The Sombor index of the graph G is defined as (Gutman, 2021a)

$$SO = SO(G) = \sum_{e_{ij}} \sqrt{d(v_i)^2 + d(v_j)^2}$$

where e_{ij} denotes the edge connecting the vertices v_i and v_j, and the summation goes over all edges of G. The basic mathematical properties of the Sombor index can be found in the review (Liu et al., 2022).

Let $p_1, p_2, \ldots, p_n$ be non-negative integers. Then the *thorny graph* of the graph G, denoted by G^*, is obtained by attaching p_i pendent vertices to the vertex v_i, for all $i = 1, 2, \ldots, n$. Thus, the number of vertices and edges of G^* is

$$n^* = n + \sum_{i=1}^{n} p_i \qquad \text{and} \qquad m^* = m + \sum_{i=1}^{n} p_i$$

respectively.

If $p_1 = p_2 = \cdots = p_n$, then G^* is said to be a thorn-regular graph.

Thorny graphs have been extensively studied, see for example (Bonchev & Klein, 2002; De, 2012; Lakshmi & Parvathi, 2023; Marinescu-Ghemeci, 2010; Walikar et al., 2006). The Sombor index of thorny graphs was considered only in (Krishnan & Narayan, 2023) and (Lakshmi & Parvathi, 2023), but only for special cases when G is a complete graph, star, wheel, path, and similar, and only when G^* is thorn-regular. In the present paper, we examine the general case, namely when G is an arbitrary (simple, not necessarily connected) graph, and $p_1, p_2, \ldots, p_n$ are arbitrary non-negative integers.

Main results

In this section we state some general properties of thorny graphs. In order to avoid trivialities, it is assumed that such graphs possess at least one edge, i.e., more than one vertex.

THEOREM 1. *Let G be a simple graph on $n > 1$ vertices, and $p_1, p_2, \ldots, p_n$ be non-negative integers. Let G^* be the thorny graph of G. Then the Sombor*

index of G^* satisfies the relation

$$SO(G^*) = \sum_{e_{ij}} \sqrt{[d(v_i) + p_i]^2 + [d(v_i) + p_j]^2} + \sum_{i=1}^{n} p_i \sqrt{[d(v_i) + p_i]^2 + 1}\,. \tag{1}$$

Proof. For $i = 1, 2, \ldots, n$, the degree of the vertex v_i of the thorny graph G^* is equal to $d(v_i) + p_i$. This implies the first term on the right-hand side of (1), in which the summation goes over all edges of the graph G. In addition to these edges, in G^* there are p_i pendent edges attached to the vertex v_i, for each $i = 1, 2, \ldots, n$. Their contributions to the Sombor index of G^* are collected in the second term on the right-hand side of (1). □

The first Zagreb index

$$M_1 = M_1(G) = \sum_{e_{ij}} \big[d(v_i) + d(v_j)\big] = \sum_{i=1}^{n} d(v_i)^2$$

is one of the oldest and best studied vertex-degree-based topological indices (Gutman & Trinajstić, 1972; Nikolić et al., 2003; Gutman & Das, 2004).

Using the inequalities

$$\frac{1}{\sqrt{2}}(a + b) \le \sqrt{a^2 + b^2} < a + b$$

the following well-known estimates for the Sombor index are straightforwardly obtained (Milovanović et al., 2021; Gutman, 2021b, 2024):

$$\frac{1}{\sqrt{2}}\, M_1(G) \le SO(G) < M_1(G)\,. \tag{2}$$

The equality on the left-hand side holds if and only if G is a regular graph.

By the same argument, we now have

$$\begin{aligned} \sum_{e_{ij}} \sqrt{[d(v_i) + p_i]^2 + [d(v_i) + p_j]^2} &< \sum_{e_{ij}} \big[d(v_i) + p_i + d(v_i) + p_j\big] \\ &= \sum_{e_{ij}} \big[d(v_i) + d(v_i)\big] + \sum_{e_{ij}} \big[p_i + p_j\big] \end{aligned}$$

$$= \quad M_1(G) + \sum_{i=1}^{n} p_i\, d(v_i) \tag{3}$$

where we applied the identity (Došlić et al., 2011)

$$\sum_{e_{ij}} \left[f(v_i) + f(v_j) \right] = \sum_{i=1}^{n} d(v_i)\, f(v_i)$$

valid for any vertex-dependent function f.

The lower bound, analogous to (3) is

$$\sum_{e_{ij}} \sqrt{[d(v_i)+p_i]^2 + [d(v_i)+p_j]^2} > \frac{1}{\sqrt{2}} \left[M_1(G) + \sum_{i=1}^{n} p_i\, d(v_i) \right]. \tag{4}$$

The equality in (4) cannot occur since no graph G^* is regular.

For the other term in (1) we have

$$\begin{aligned} \sum_{i=1}^{n} p_i \sqrt{[d(v_i)+p_i]^2 + 1} \quad &< \quad \sum_{i=1}^{n} p_i \left[d(v_i) + p_i + 1 \right] \\ &= \quad \sum_{i=1}^{n} p_i\, d(v_i) + \sum_{i=1}^{n} p_i(p_i+1)\,. \end{aligned} \tag{5}$$

and

$$\sum_{i=1}^{n} p_i \sqrt{[d(v_i)+p_i]^2 + 1} \geq \frac{1}{\sqrt{2}} \left[\sum_{i=1}^{n} p_i\, d(v_i) + \sum_{i=1}^{n} p_i(p_i+1) \right]. \tag{6}$$

The equality in (6) would occur for thorn-regular graphs of a regular graph.

Combining the estimates (3)–(6) we arrive at:

THEOREM 2. *Let G be a simple graph on $n > 1$ vertices, and $p_1, p_2, \ldots, p_n$ be non-negative integers. Let G^* be the thorny graph of G. Then the Sombor index of G^* is bounded as*

$$\begin{aligned} &\frac{1}{\sqrt{2}} \left[M_1(G) + 2 \sum_{i=1}^{n} p_i\, d(v_i) + \sum_{i=1}^{n} p_i(p_i+1) \right] < SO(G^*) < \\ &M_1(G) + 2 \sum_{i=1}^{n} p_i\, d(v_i) + \sum_{i=1}^{n} p_i(p_i+1)\,. \end{aligned} \tag{7}$$

The bounds (7) should be compared with inequalities (2). In fact, (2) is the special case of (7) when $p_1 = p_2 = \cdots = p_n = 0$.

Corollaries

In this section, we list a few interesting special cases of Theorem 1.

COROLLARY 1. *Let G be a regular graph on n vertices, of the degree r. Then the Sombor index of a thorn-regular graph of G is*

$$SO(G^*) = \frac{\sqrt{2}\,nr}{2}(r+p) + np\,\sqrt{(r+p)^2+1}$$

Proof. Setting $d(v_i) = r$ and $p_i = p$ for all $i = 1, 2, \ldots, n$, the left-hand term in (1) becomes $\sqrt{2}m(r+p)$. For regular graphs, $2m = nr$. □

COROLLARY 2. *If $p_i = \lambda\, d(v_i)$ holds for all $i = 1, 2, \ldots, n$, then*

$$SO(G^*) = (\lambda+1)\,SO(G) + \lambda(\lambda+1)\sum_{i=1}^{n} d(v_i)\,\sqrt{d(v_i)^2 + \frac{1}{(\lambda+1)^2}}\,.$$

If λ is sufficiently large, then

$$SO(G^*) \approx (\lambda+1)\,SO(G) + \lambda(\lambda+1)\,M_1(G)\,.$$

COROLLARY 3. *If $p_i + d(v_i) = D$ holds for all $i = 1, 2, \ldots, n$, then*

$$SO(G^*) = \sqrt{2}\,Dm + \sqrt{D^2+1}\,(n^* - n)$$

where n and m are the numbers of the vertices and edges of G, whereas n^* is the number of the vertices of G^*.

It is worth noting that the thorny graphs considered in Corollary 3 are of chemical interest. Namely, for $D = 3$, if G is the molecular graph of an unsaturated conjugated molecule, then G^* is its plerogram (= hydrogen filled molecular graph) (Gutman & Vidovic, 1998; Gutman et al., 1998). If $D = 4$, then G^* is the plerogram of the molecular graph of a saturated hydrocarbon.

References

Alqahtani, M., Kaviyarasu, M. & Rajeshwari, M. 2024. Site Selection for Thermal Power Plant Based on Sombor Index in Neutrosophic Graph. *European Journal of Pure and Applied Mathematics*, 17(4), pp. 2586–2620. Available at: https://doi.org/10.29020/nybg.ejpam.v17i4.5461.

Anwar, S., Azeem, M., Jamil, M.K., Almohsen, B. & Shang, Y. 2024. Single-valued neutrosophic fuzzy Sombor numbers and their applications in trade flows between different countries via sea route. *The Journal of Supercomputing*, 80(14), pp. 19976–20019. Available at: https://doi.org/10.1007/s11227-024-06169-8.

Bonchev, D. & Klein, D.J. 2002. On the Wiener Number of Thorn Trees, Stars, Rings, and Rods. *Croatica Chemica Acta*, 75(2), pp. 613–620 [online]. Available at: https://hrcak.srce.hr/127540 [Accessed: 25 January 2025].

Bondy, J.A. & Murty, U.S.R. 1976. *Graph theory with applications*. The Macmillan Press Ltd. ISBN: 0-444-19451-70.

De, N. 2012. On Eccentric Connectivity Index and Polynomial of Thorn Graph. *Applied Mathematics*, 3(8), art.ID:21477. Available at: https://doi.org/10.4236/am.2012.38139.

Došlić, T., Réti, T. & Vukičević, D. 2011. On the vertex degree indices of connected graphs. *Chemical Physics Letters*, 512(4-6), pp. 283–286. Available at: https://doi.org/10.1016/j.cplett.2011.07.040.

Gutman, I. 2021a. Geometric Approach to Degree–Based Topological Indices: Sombor Indices. *MATCH Communications in Mathematical and in Computer Chemistry*, 86(1), pp. 11–16 [online]. Available at: https://match.pmf.kg.ac.rs/electronic_versions/Match86/n1/match86n1_11-16.pdf [Accessed: 25 January 2025].

Gutman, I. 2021b. Some basic properties of Sombor indices. *Open Journal of Discrete Applied Mathematics (ODAM)*, 4(1), pp. 1–3. Available at: https://www.doi.org/10.30538/psrp-odam2021.0047.

Gutman, I. 2024. Improved Estimates of Sombor Index. *Iranian Journal of Mathematical Chemistry*, 15(1), pp. 1–5. Available at: https://www.doi.org/10.22052/ijmc.2023.253825.1782.

Gutman, I. & Das, K.C. 2004. The first Zagreb index 30 years after. *MATCH Communications in Mathematical and in Computer Chemistry*, 50(1), pp. 83–92 [online]. Available at: https://match.pmf.kg.ac.rs/electronic_versions/Match50/match50_83-92.pdf [Accessed: 25 January 2025].

Gutman, I., Popović, L. et al. 1998. Graph representation of organic molecules Cayley's plerograms vs. his kenograms. *Journal of the Chemical Society, Faraday Transactions*, 94(7), pp. 857–860. Available at: https://www.doi.org/10.1039/A708076J.

Gutman, I. & Trinajstić, N. 1972. Graph theory and molecular orbitals. Total φ-electron energy of alternant hydrocarbons. *Chemical Physics Letters*, 17(4), pp. 535–538. Available at: https://doi.org/10.1016/0009-2614(72)85099-1.

Gutman, I. & Vidovic, D. 1998. Relations between Wiener-type topological indices of plerograms and kenograms. *Journal of the Serbian Chemical Society*, 63(9), pp. 695–702 [online]. Available at: https://www.shd.org.rs/JSCS/Start.html [Accessed: 25 January 2025].

Hamid, K., Waseem Iqbal, M., Abbas, Q., Arif, M., Brezulianu, A. & Geman, O. 2022. Discovering irregularities from computer networks by topological mapping. *Applied Sciences*, 12(8), art.number:12051. Available at: https://doi.org/10.3390/app122312051.

Harary, F. 1969. *Graph Theory (on Demand Printing Of 02787), 1st Edition*. Boca Raton: CRC Press. Available at: https://doi.org/10.1201/9780429493768.

Hayat, S., Arshad, M. & Khan, A. 2024. Graphs with given connectivity and their minimum Sombor index having applications to QSPR studies of monocarboxylic acids. *Heliyon*, 10(1), e23392. Available at: https://doi.org/10.1016/j.heliyon.2023.e23392.

Imran, M., Azeem, M., Jamil, M.K. & Deveci, M. 2024. Some operations on intuitionistic fuzzy graphs via novel versions of the sombor index for internet routing. *Granular Computing*, 9(2), art.number:53. Available at: https://doi.org/10.1007/s41066-024-00467-5.

Jamil, M.K., Anwer, S., Azeem, M. & Gutman, I. 2025. Intuitionistic fuzzy Sombor indices: A novel approach for improving the performance of vaccination centers. *Communications in Combinatorics and Optimization*, 10(3), pp. 563–593. Available at: https://doi.org/10.22049/cco.2023.28767.1709.

Krishnan, V.L. & Narayan, P. 2023. Analysis of Sombor and Harmonic Indices of Thorn Cog-Graphs. *Mathematical Modelling of Engineering Problems*, 10(5), pp. 1777–1784. Available at: https://doi.org/10.18280/mmep.100529.

Lakshmi, K.V. & Parvathi, N. 2023. An Analysis of Thorn Graph on Topological Indices. *IAENG International Journal of Applied Mathematics*, 53(3), pp. 313–322 [online]. Available at: https://www.iaeng.org/IJAM/issues_v53/issue_3/IJAM_53_3_38.pdf [Accessed: 25 January 2025].

Li, Y., Deng, H. & Tang, Z. 2024. Sombor index of maximal outerplanar graphs. *Discrete Applied Mathematics*, 356, pp. 96–103. Available at: https://doi.org/10.1016/j.dam.2024.05.019.

Liu, H., Gutman, I., You, L. & Huang, Y. 2022. Sombor index: review of extremal results and bounds. *Journal of Mathematical Chemistry*, 60(5), pp. 771–798. Available at: https://doi.org/10.1007/s10910-022-01333-y.

Marinescu-Ghemeci, R. 2010. Radio number for some thorn graphs. *Discussiones Mathematicae Graph Theory*, 30(2), pp. 201–222. Available at: https://doi.org/10.7151/dmgt.1487.

Milovanović, I., Milovanović, E. & Matejić, M. 2021. On some mathematical properties of Sombor indices. *Bulletin of the International Mathematical Virtual Institute*, 11(2), pp. 341–353 [online]. Available at: http://www.imvibl.org/buletin/bulletin_imvi_11_2_2021/bulletin_imvi_10_2_2020_341_353.pdf [Accessed: 25 January 2025].

Nikolić, S., Kovačević, G., Miličević, A. & Trinajstić, N. 2003. The Zagreb indices 30 years after. *Croatica Chemica Acta*, 76(2), pp. 113–124 [online]. Available at: https://hrcak.srce.hr/103086 [Accessed: 25 January 2025].

Rather, B.A., Imran, M. & Pirzada, S. 2024. Sombor index and eigenvalues of comaximal graphs of commutative rings. *Journal of Algebra and its Applications*, 23(06), art.number:2450115. Available at: https://doi.org/10.1142/S02194988245011599.

Rauf, A. & Ahmad, S. 2024. On sombor indices of tetraphenylethylene, terpyridine rosettes and QSPR analysis on fluorescence properties of several aromatic hetero-cyclic species. *International Journal of Quantum Chemistry*, 124(1), e27261. Available at: https://doi.org/10.1002/qua.27261.

Walikar, H.B., Ramane, H.S., Sindagi, L., Shirakol, S.S. & Gutman, I. 2006. Hosoya polynomial of thorn trees, rods, rings, and stars. *Kragujevac Journal of Science*, 28, pp. 47–56 [online]. Available at: https://www.pmf.kg.ac.rs/KJS/en/volumes/kjs28/kjs28walikarramane47.pdf [Accessed: 25 January 2025].

Wang, Z., Gao, F., Zhao, D. & Liu, H. 2024. Sharp upper bound on the Sombor index of bipartite graphs with a given diameter. *Journal of Applied Mathematics and Computing*, 70(1), pp. 27–46. Available at: https://doi.org/10.1007/s12190-023-01955-8.

Índice de Sombor de gráficos espinosos

Ivan Gutman

Universidad de Kragujevac, Facultad de Ciencias, Kragujevac, República de Serbia

CAMPO: matemáticas (clasificación de materias de matemáticas: primaria 05c07, secundaria 05c09)

TIPO DE ARTÍCULO: artículo científico original

Resumen:

Introducción/objetivo: El gráfico espinoso de un gráfico G se obtiene uniendo vértices colgantes a los vértices de G. Se realiza un estudio matemático del índice de Sombor de gráficos espinosos.

Métodos: Se aplica la teoría de gráficos combinatorios.

Resultados: Se obtiene una expresión general para el índice de Sombor de gráficos espinosos, así como sus límites inferior y superior. Se señalan varios casos especiales de esta expresión general.

Conclusión: El artículo contribuye a la teoría del índice de Sombor.

Palabras claves: grado (de vértice), índice de Sombor, gráfico espinoso.

Сомборский индекс тернистого графа

Иван Гутман

Крагуевацкий университет, естественно-математический факультет, г. Крагуевац, Республика Сербия

РУБРИКА ГРНТИ: 27.29.19 Краевые задачи и задачи на собственные значения для обыкновенных дифференциальных уравнений и систем уравнений

ВИД СТАТЬИ: оригинальная научная статья

Резюме:

Введение/цель: Тернистый граф графа G получается путем присоединения висячей вершины к вершинам G. В данной статье представлено математическое исследование Сомборского индекса тернистых графов.

Методы: В исследовании применены комбинаторика и теория графов.

Результаты: В результате исследования получена новая общая формула для Сомборского индекса тернистых графов, а также нижняя и верхняя грани. Указано на несколько частных случаев относительно результатов.

Выводы: Данная статья вносит вклад в теорию Сомборского индекса.

Ключевые слова: степень (вершины), Сомборский индекс, тернистый граф.

Сомборски индекс трновитог графа

Иван Гутман

Универзитет у Крагујевцу, Природно-математички факултет, Крагујевац, Република Србија

ОБЛАСТ: математика
КАТЕГОРИЈА (ТИП) ЧЛАНКА: оригинални научни рад

Сажетак:

Увод/циљ: Трновити граф графа G добија се додавањем висећих чворова на чворове графа G. Проучаване су математичке осовине Сомборског индекса трновитих графова.

Методе: Примењивани су поступци комбинаторне теорије графова.

Резултати: Нађена је нова општа формула за Сомборски индекс трновитих графова, као и доње и горње границе. Истакнуто је неколико специјалних случајева ових резултата.

Закључак: Рад доприноси теорији Сомборског индекса.

Кључне речи: степен чвора, Сомборски индекс, трновити граф.

Paper received on: 30.01.2025.
Manuscript corrections submitted on: 28.03.2025.
Paper accepted for publishing on: 29.03.2025.

Paired-Chatterjea type contractions: Novel fixed point results and continuity properties in metric spaces

Deep Chand[a], *Yumnam* Rohen[b], *Sanasam Surenda* Singh[c], *Nicola* Fabiano[d]

[a] National Institute of Technology Manipur, Department of Mathematics, Langol, Imphal, Manipur, Republic of India,
e-mail: deepak07872@gmail.com,
ORCID iD: https://orcid.org/0000-0002-9274-620X

[b] National Institute of Technology Manipur, Department of Mathematics, Langol, Imphal, Manipur, Republic of India +
Manipur University, Department of Mathematics, Canchipur, Imphal, Manipur, Republic of India,
e-mail: ymnehor2008@yahoo.com,
ORCID iD: https://orcid.org/0000-0002-1859-4332

[c] National Institute of Technology Manipur, Department of Mathematics, Langol, Imphal, Manipur, Republic of India,
e-mail: ssuren.mu@gmail.com,
ORCID iD: https://orcid.org/0000-0002-3004-4499

[d] University of Belgrade, "Vinča" Institute of Nuclear Sciences - National Institute of the Republic of Serbia, Belgrade, Republic of Serbia,
e-mail: nicola.fabiano@gmail.com, **corresponding author**,
ORCID iD: https://orcid.org/0000-0003-1645-2071

https://doi.org/10.5937/vojtehg73-54620

FIELD: mathematics
ARTICLE TYPE: original scientific paper

Abstract:

Introduction/purpose: The paper deals with Paired-Chatterjea type contraction mappings as an extension of traditional Chatterjea type contractions that operates on three points rather than two, in the framework of standard metric spaces.

Methods: The concept of Chatterjea type contraction mappings is employed in a metric space on three points rather than two using the idea of paired contraction mappings.

Results: A series of corresponding properties has been discussed. Furthermore, it is established that Paired-Chatterjea type mappings form

ACKNOWLEDGMENT: The first author is thankful to the University Grant Commission (UGC), India, for the financial support to this work under the Senior Research Fellowship (SRF)[Award Id: 1174/(CSIR-NETJUNE2019)].

a distinct class from traditional Chatterjea type mappings and obtain at least one fixed point in the absence periodic points of prime period 2 within complete metric spaces. It is also demonstrated that how additional criteria to these mappings, such as continuity and asymptotic regularity, broaden the scope of fixed point results. Extending beyond Chatterjea's foundational contributions, two additional fixed point results applicable to Paired-Chatterjea type mappings in metric spaces are established, even in scenarios where completeness is not required.

Conclusions: Paired-Chatterjea type mappings are generally discontinuous; they exhibit continuity at fixed points similar to Kannan and Chatterjea type mappings. In the absence of a periodic point of prime period 2, these mappings have a fixed point within the complete metric space.

Keywords: metric space, fixed point, Chatterjea type mappings, Paired contraction, Paired-Chatterjea type mapping.

Introduction

The study of fixed point theory (*FPT*), a captivating area in mathematics, delves into the existence and properties of fixed points (*FPs*). In mathematics, a *FP* of a function is an element that stays the same when the function is executed on it. Formally, if $\Im$ is a function, then ζ is a *FP* if $\Im(\zeta) = \zeta$.

Numerous findings regarding *FPs* and their diverse applications in various mathematical and scientific domains have been documented. To yield fresh and intriguing results, two principal approaches can be pursued. Firstly, by modifying the characteristics of the operators involved, achieved through the imposition or relaxation of specific constraints (Kannan, 1968; Chatterjea, 1972; Chand & Rohen, 2024; Petrov, 2023; Bisht & Petrov, 2024). Secondly, by altering the framework, or the abstract space structure itself, which includes variations like metric spaces, symmetric or non-symmetric spaces, b-metric spaces, S-metric spaces, and G-metric spaces (Chand & Rohen, 2023; Chand et al., 2024; Bimol et al., 2024).

The Kannan's *FP* theorem is a notable result in *FPT*, specifically within metric spaces. It ensures the existence of a *FP* for mappings, even when these mappings are discontinuous. It was introduced by R. Kannan in 1968 (Kannan, 1968) and provides conditions under which a mapping possesses a unique *FP*.

THEOREM 1. *Let* $(\mho, \partial)$ *be a complete metric space, and suppose that* $\Im : \mho \to \mho$ *is a self-map for which we obtain a constant* $0 \leq \lambda < \frac{1}{2}$ *satisfying:*

$$\partial(\Im\zeta, \Im\varepsilon) \leq \lambda(\partial(\zeta, \Im\zeta) + \partial(\varepsilon, \Im\varepsilon)) \text{ for all } \zeta, \varepsilon \in \mho. \tag{1}$$

Then $\Im$ *has a unique FP.*

Another noteworthy outcome in *FPT* is the Chatterjea *FP* theorem; it also provides a *FP* for mappings that are discontinuous too. It was introduced by S.K. Chatterjea in 1972 (Chatterjea, 1972) and provides conditions under which a mapping has a unique *FP*.

THEOREM 2. *Let* $(\mho, \partial)$ *be a complete metric space, and suppose that* $\Im : \mho \to \mho$ *is a self-map for which we obtain a constant* $0 \leq \eta < \frac{1}{2}$

$$\partial(\Im\zeta, \Im\varepsilon) \leq \eta(\partial(\zeta, \Im\varepsilon) + \partial(\varepsilon, \Im\zeta)) \text{ for all } \zeta, \varepsilon \in \mho. \tag{2}$$

Then there is a unique FP for $\Im$.

DEFINITION 1. *A self-map* $\Im : \mho \to \mho$ *is termed as a Chatterjea type map if a constant can be found* $0 \leq \eta < \frac{1}{2}$ *such that*

$$\partial(\Im\zeta, \Im\varepsilon) \leq \eta(\partial(\zeta, \Im\varepsilon) + \partial(\varepsilon, \Im\zeta)), \tag{3}$$

satisfied for all $\zeta, \varepsilon \in \mho$.

Like Kannan's fixed-point theorem (Theorem 1), the mapping $\Im$ is guaranteed to be continuous at the *FP* (Rhoades, 1988) by condition (3). Moreover, the uniqueness of the *FP* is the only thing that unites Chatterjea mappings, Kannan mappings, and the Banach Contraction Principle; otherwise, they are independent of one another.

Within the field of *FPT*, there are different types of generalizations of the Chatterjea theorem that can be distinguished from one another. The contractive property of the mapping is loosened in the first instance as illustrated, for example, in references (Chandok & Postolache, 2013; Debnath et al., 2021; Kadelburg & Radenovic, 2016; Subrahmanyam, 2018; Bisht & Petrov, 2024). The second instance involves relaxing the topology, as examined, for instance, in reference (Agarwal et al., 2018). And the third instance concerns theorems developed for multivalued mappings of the Chatterjea type, which are covered in works such as (Choudhury et al.,

2019; Tassaddiq et al., 2022). Lastly, the fourth instance provides a thorough investigation of several generalization paths in this field by examining notable extensions in a more flexible or comprehensive framework of the metric space (Harjani et al., 2011; Karahan & Isik, 2019; Kohsaka & Suzuki, 2017; Malčeski et al., 2016; Berinde & Păcurar, 2021).

In 2024, D. Chand and Y. Rohen (Chand & Rohen, 2024) presented a novel class of mappings, referred to as a three-point version of the Banach contraction, and termed them Paired-Contraction: the mapping is known as Paired-contraction mapping, defined as follows.

DEFINITION 2. *If* $(\mho, \partial)$ *is a metric space with* $|\mho| \geq 3$. *The self-mapping* $\Im : \mho \to \mho$ *is referred to as a Paired contraction mapping if there is a constant* $\lambda \in [0, 1)$ *so that the inequality*

$$\partial(\Im\zeta, \Im\varepsilon) + \partial(\Im\varepsilon, \Im\xi) \leq \lambda(\partial(\zeta, \varepsilon) + \partial(\varepsilon, \xi)), \tag{4}$$

holds for all pairwise distinct $\zeta, \varepsilon, \xi \in \mho$.

Geometric refinement in metric *FPT* is obtained through the use of different combinations of unique distances, which are important. For 6 points $\zeta, \varepsilon, \xi, \Im\zeta, \Im\varepsilon, \Im\xi$ specified in Definition 2, there are ${}^6C_2$ pairs that, when taken two at a time, yield 15 unique distances. One of these combinations, specifically $\partial(\Im\zeta, \Im\varepsilon) + \partial(\Im\varepsilon, \Im\xi)$, appears in the left part of (4). However, the expression in the right part combines two distances, that is, $\partial(\zeta, \varepsilon) + \partial(\varepsilon, \xi)$ for the pairwise distinct points ζ, ε and ξ. This motivates the development of various classes of three-point version mappings, similar to the well-established two-point counterparts.

Inspired by the insights from (Chand & Rohen, 2024), we introduce a Paired-Chatterjea type mapping on three point analogue by using four distances among the points $\zeta, \varepsilon, \xi, \Im\zeta, \Im\varepsilon, \Im\xi$, represented as $\partial(\zeta, \Im\varepsilon) + \partial(\varepsilon, \Im\zeta) + \partial(\varepsilon, \Im\xi) + \partial(\xi, \Im\zeta)$ for the pairwise distinct points ζ, ε, ξ respectively.

These mappings led to the establishment of a fixed-point theorem. While the proof draws inspiration from Banach's classical theorem, the key distinction lies in these mappings - instead of using two points to define it, three points are used. Moreover, we need an assumption for these mappings in order to prevent periodic points with prime period 2. Notably, normal contraction mappings are a significant subset of these mappings.

In the second Section, Paired-Chatterjea Type Mappings, we study the relationship between Paired-Chatterjea type mappings, Chatterjea type mappings, Kannan type mappings and Paired-Contraction mappings. In addition, we introduce Example 1, a Paired-Chatterjea type mapping that deviates from a Chatterjea type mapping.

In the third Section, Fixed Point Results of the Paired-Chatterjea Type Mappings, the primary outcome of this article, Theorem 3, which gives a fixed-point theorem for Paired-Chatterjea type mappings, is proved. Notably, this result states that for Paired-Chatterjea type mappings there exists at least one *FP* and there exist at most two *FPs*. In addition, we also establish that Paired-Chatterjea type mappings exhibit continuity at their *FPs*. We also included two examples (2) and (3) to support our findings.

In the fourth Section, Results on Paired Chatterjea-Style Mappings within Incomplete Metric Spaces, based on Kannan's work (Kannan, 1969), we offer two new *FP* results for Paired-Chatterjea type mappings. In the first theorem (Theorem 4), we eliminate the necessity of the metric space $\mho$ being complete. In the second theorem (Theorem 5), we need the mapping $\Im$ to be continuous in space, and condition (5) to only hold on a dense subset M of the space $\mho$. The concept of continuity and discontinuity at the fixed point is further elaborated in the recent papers (Savaliya et al., 2024; Jachymski, 1994; Pant et al., 2021).

Paired-Chatterjea type mappings

In this section, we will introduce the Paired-Chatterjea type contraction and discuss Paired-Chatterjea type mappings and also establish the connections between Paired-Chatterjea type mappings, Paired-Contractions mappings, Kannan-type mappings and Chatterjea-type mappings.

DEFINITION 3. *If $(\mho, \partial)$ is a metric space with $|\mho| \geq 3$. A mapping $\Im : \mho \to \mho$ is known as a Paired-Chatterjea type mapping on $\mho$ if the following inequality:*

$$\partial(\Im\zeta, \Im\varepsilon) + \partial(\Im\varepsilon, \Im\xi) \leq \lambda(\partial(\zeta, \Im\varepsilon) + \partial(\varepsilon, \Im\zeta) + \partial(\xi, \Im\varepsilon) + \partial(\varepsilon, \Im\xi)), \quad (5)$$

holds for the constant $\lambda \in [0, \frac{1}{2})$ and pairwise distinct points $\zeta, \varepsilon, \xi \in \mho$.

REMARK 1. It is essential that $\zeta, \varepsilon, \xi \in \mho$ be pairwise distinct. Without this condition, the definition would reduce to that of a standard definition of Chatterjea-type mapping of a two point version.

PROPOSITION 1. *Chatterjea type mappings are Paired-Chatterjea type mappings.*

Proof. In a metric space $(\mho, \partial)$ with $|\mho| \geq 3$, let $\Im : \mho \to \mho$ represent a Chatterjea type mapping. Take three $\zeta, \varepsilon, \xi \in \mho$ pairwise distinct points. Examine inequality (2) for the pairs (ζ, ε), (ε, ξ), we get inequalities, we obtain:

$$\partial(\Im\zeta, \Im\varepsilon) \leq \eta(\partial(\zeta, \Im\varepsilon) + \partial(\varepsilon, \Im\zeta)), \tag{6}$$

and

$$\partial(\Im\varepsilon, \Im\xi) \leq \eta(\partial(\varepsilon, \Im\xi) + \partial(\xi, \Im\varepsilon)), \tag{7}$$

Adding inequalities (6) and (7), we have

$$\partial(\Im\zeta, \Im\varepsilon) + \partial(\Im\varepsilon, \Im\xi) \leq \eta(\partial(\zeta, \Im\varepsilon) + \partial(\varepsilon, \Im\zeta) + \partial(\varepsilon, \Im\xi) + \partial(\xi, \Im\varepsilon)). \tag{8}$$

This supports the desired claim. □

PROPOSITION 2. *Kannan type mappings are Paired-Chatterjea type mappings for the contracting coefficient* $\delta \in [0, \frac{1}{4})$.

Proof. Let $(\mho, \partial)$ be a metric space with $|\mho| \geq 3$. Consider three pairwise distinct points $\zeta, \varepsilon, \xi \in \mho$, examine inequality (3) for the pairs (ζ, ε), (ε, ξ)„ we get

$$\partial(\Im\zeta, \Im\varepsilon) \leq \delta(\partial(\zeta, \Im\zeta) + \partial(\varepsilon, \Im\varepsilon)), \tag{9}$$

and

$$\partial(\Im\varepsilon, \Im\xi) \leq \delta(\partial(\varepsilon, \Im\varepsilon) + \partial(\xi, \Im\xi)). \tag{10}$$

Adding these inequalities, we have

$$\partial(\Im\zeta, \Im\varepsilon) + \partial(\Im\varepsilon, \Im\xi) \leq \delta(\partial(\zeta, \Im\zeta) + \partial(\varepsilon, \Im\varepsilon) + \partial(\varepsilon, \Im\varepsilon) + \partial(\xi, \Im\xi)),$$

(Using triangle inequality)

$$\leq \delta \left\{ \begin{matrix} \partial(\zeta, \Im\varepsilon) + \partial(\Im\zeta, \Im\varepsilon) + \partial(\varepsilon, \Im\zeta) + \partial(\Im\zeta, \Im\varepsilon) \\ +\partial(\varepsilon, \Im\xi) + \partial(\Im\varepsilon, \Im\xi) + \partial(\xi, \Im\varepsilon) + \partial(\Im\varepsilon, \Im\xi) \end{matrix} \right\},$$

$$\implies (1 - 2\delta)(\partial(\Im\zeta, \Im\varepsilon) + \partial(\Im\varepsilon, \Im\xi)) \leq \delta(\partial(\zeta, \Im\varepsilon) +$$

$$\partial(\varepsilon, \Im\zeta) + \partial(\varepsilon, \Im\xi) + \partial(\xi, \Im\varepsilon))$$

$$\implies \partial(\Im\zeta, \Im\varepsilon) + \partial(\Im\varepsilon, \Im\xi) \leq$$

$$\frac{\delta}{1 - 2\delta}(\partial(\zeta, \Im\varepsilon) + \partial(\varepsilon, \Im\zeta) + \partial(\varepsilon, \Im\xi) + \partial(\xi, \Im\varepsilon)).$$

Since $0 \leq \delta < \frac{1}{4}$, we get $0 \leq \lambda = \frac{\delta}{1-2\delta} < \frac{1}{2}$. Thus, $\Im$ is a Paired-Chatterjea type mapping. □

PROPOSITION 3. *In a metric space $(\mho, \partial)$, where $|\mho| \geq 3$, a Paired contraction(PC) mapping $\Im : \mho \to \mho$ with contracting coefficient $\alpha \in [0, \frac{1}{3})$ represents a Paired-Chatterjea Type mapping.*

Proof. Consider three pairwise distinct points $\zeta, \varepsilon, \xi \in \mho$. Since $\Im$ is a Paired contraction mapping, then we have

$$\partial(\Im\zeta, \Im\varepsilon) + \partial(\Im\varepsilon, \Im\xi) \leq \alpha(\partial(\zeta, \varepsilon) + \partial(\varepsilon, \xi)).$$

Utilizing triangle inequality many times to the above inequality, we get

$$\partial(\Im\zeta, \Im\varepsilon) + \partial(\Im\varepsilon, \Im\xi) \leq \alpha \left\{ \begin{array}{l} \partial(\zeta, \Im\varepsilon) + \partial(\varepsilon, \Im\zeta) + \partial(\Im\zeta, \Im\varepsilon) \\ +\partial(\varepsilon, \Im\xi) + \partial(\xi, \Im\varepsilon) + \partial(\Im\varepsilon, \Im\xi) \end{array} \right\},$$

$$(1-\alpha)(\partial(\Im\zeta, \Im\varepsilon) + \partial(\Im\varepsilon, \Im\xi)) \leq$$

$$\alpha(\partial(\zeta, \Im\varepsilon) + \partial(\varepsilon, \Im\zeta) + \partial(\varepsilon, \Im\xi) + \partial(\xi, \Im\varepsilon)),$$

$$(\partial(\Im\zeta, \Im\varepsilon) + \partial(\Im\varepsilon, \Im\xi)) \leq$$

$$\frac{\alpha}{1-\alpha}(\partial(\zeta, \Im\varepsilon) + \partial(\varepsilon, \Im\zeta) + \partial(\varepsilon, \Im\xi) + \partial(\xi, \Im\varepsilon)).$$

As $0 \leq \alpha < \frac{1}{3}$, we have $0 \leq \lambda = \frac{\alpha}{1-\alpha} < \frac{1}{2}$. Consequently, $\Im$ is a mapping of the Paired-Chatterjea type. □

PROPOSITION 4. *In a metric space $(\mho, \partial)$, where $|\mho| \geq 3$, and let $\Im : \mho \to \mho$ be a Paired-Chatterjea type mapping. We obtain the following inequality for any $\varepsilon \in \mho$ if ζ is an accumulation point of $\mho$ and $\Im$ is a continuous mapping at ζ:*

$$\partial(\Im\zeta, \Im\varepsilon) \leq \lambda(\partial(\zeta, \Im\varepsilon) + \partial(\varepsilon, \Im\zeta)). \tag{11}$$

Proof. Suppose ζ is an accumulation point in $\mho$, and let $\varepsilon \in \mho$ be another element. If $\varepsilon = \zeta$, then there is nothing to prove. Let $\varepsilon \neq \zeta$. Given that ζ is an accumulation point, we can assert the existence of a sequence (ξ_n) where $\xi_n \neq \zeta$, $\xi_n \neq \varepsilon$, and all ξ_n are distinct for every n. Hence, by (5) we conclude that

$$\partial(\Im\zeta, \Im\varepsilon) + \partial(\Im\varepsilon, \Im\xi_n) \leq \lambda(\partial(\zeta, \Im\varepsilon) + \partial(\varepsilon, \Im\zeta) + \partial(\xi_n, \Im\varepsilon) + \partial(\varepsilon, \Im\xi_n)),$$

satisfied for each $n \in N$. Given that at ζ, $\Im$ is continuous and $\xi_n \to \zeta$ as $n \to +\infty$, therefore, $\Im\xi_n \to \Im\zeta$. We get

$$\begin{aligned}\partial(\Im\zeta, \Im\varepsilon) + \partial(\Im\varepsilon, \Im\zeta) &\leq \lambda(\partial(\zeta, \Im\varepsilon) + \partial(\varepsilon, \Im\zeta) + \partial(\zeta, \Im\varepsilon) + \partial(\varepsilon, \Im\zeta)),\\ \implies 2\partial(\Im\zeta, \Im\varepsilon) &\leq \lambda(2\partial(\zeta, \Im\varepsilon) + 2\partial(\varepsilon, \Im\zeta)),\\ \implies \partial(\Im\zeta, \Im\varepsilon) &\leq \lambda(\partial(\zeta, \Im\varepsilon) + \partial(\varepsilon, \Im\zeta)),\end{aligned}$$

which is the desired inequality. □

COROLLARY 1. *In a metric space $(\mho, \partial)$ where, $|\mho| \geq 3$, and let $\Im : \mho \to \mho$ be a continuous Paired-Chatterjea mapping, then $\Im$ is a Chatterjea type mapping if all points in $\mho$ are accumulation points.*

Proof. As per proposition (2), the following inequalities are established:

$$\partial(\Im\zeta, \Im\varepsilon) \leq \lambda(\partial(\zeta, \Im\varepsilon) + \partial(\varepsilon, \Im\zeta)), \text{ for all } \varepsilon \in \mho, \tag{12}$$

$$\partial(\Im\varepsilon, \Im\zeta) \leq \lambda(\partial(\varepsilon, \Im\zeta) + \partial(\zeta, \Im\varepsilon)), \text{ for all } \zeta \in \mho. \tag{13}$$

Adding equations (12) and (13), we get

$$\partial(\Im\zeta, \Im\varepsilon) \leq \lambda(\partial(\zeta, \Im\varepsilon) + \partial(\varepsilon, \Im\zeta)) \text{ for all } \zeta, \varepsilon \in \mho. \tag{14}$$

Since $\lambda \in [0, \frac{1}{2})$, thereby concluding the proof. □

EXAMPLE 1. Let $\mho = \{\zeta, \varepsilon, \xi\}$ and the metric ∂ defined on this set by $\partial(\zeta, \zeta) = \partial(\varepsilon, \varepsilon) = \partial(\xi, \xi) = 0$, $\partial(\zeta, \xi) = \partial(\varepsilon, \xi) = 2$, $\partial(\zeta, \varepsilon) = 1$. Let a mapping $\Im : \mho \to \mho$ be such that $\Im\zeta = \zeta$, $\Im\varepsilon = \varepsilon$ and $\Im\xi = \varepsilon$.

Now, we have

$$\partial(\Im\zeta, \Im\varepsilon) = \partial(\zeta, \varepsilon) = 1, \text{ and } \partial(\zeta, \Im\varepsilon) + \partial(\varepsilon, \Im\zeta) = \partial(\zeta, \varepsilon) + \partial(\varepsilon, \zeta) = 2.$$

It is evident that for every $\eta \in [0, 1)$, inequality (2) does not hold. Therefore, $\Im$ is not a Chatterjea type mapping.

But, we get that inequality (5) holds for $\lambda = \frac{2}{5}$ and for all $\zeta, \varepsilon, \xi \in \mho$, implies that $\Im$ is a Paired-Chatterjea type mapping.

Fixed point results of Paired-Chatterjea type mappings

A point $\zeta \in \mho$ is termed a periodic point of period n if applying the mapping $\Im$ repeatedly n times returns ζ to its original position, i.e., $\Im^n(\zeta) = \zeta$,

where $\mho$ is a metric space and ζ is a self-map on it. The smallest positive integer n that satisfies this condition is known as the prime period of ζ. If $\Im(\Im(\zeta)) = \zeta$ and $\Im\zeta \neq \zeta$, then ζ has prime period 2.

We will now demonstrate the main result of this paper, which is stated and proven as follows:

THEOREM 3. *Let $(\mho, \partial)$ be a complete metric space, where $|\mho| \geq 3$, and consider the mapping $\Im : \mho \to \mho$ that is a Paired-Chatterjea contraction mapping and has no periodic elements of prime period 2. Under these conditions, there exists at least one FP of $\Im$, and the number of FPs can be at most two.*

Proof. Consider an arbitrary point $\zeta \in \mho$, and set the sequence $\{\zeta_n\}$ as $\zeta_0 = \zeta$, $\zeta_1 = \Im\zeta_0$ and $\zeta_n = \Im\zeta_{n-1} = \Im^n\zeta_0$. If for some n, ζ_n is a *FP* then there is nothing to prove. Assuming that ζ_n is not a *FP* for any $n = 0, 1, 2, ...$, we can deduce that $\zeta_{n-1} \neq \zeta_n \neq \zeta_{n+1}$. Since, $\Im$ had no periodic point with prime period 2 implies $\zeta_{n+1} \neq \zeta_{n-1}$. Therefore, ζ_{n-1}, ζ_n and ζ_{n+1} are pairwise distinct. Placing $\zeta = \zeta_{n-1}$, $\varepsilon = \zeta_n$ and $\xi = \zeta_{n+1}$ in (5), then we get

$$\begin{gathered}\partial(\Im\zeta_{n-1}, \Im\zeta_n) + \partial(\Im\zeta_n, \Im\zeta_{n+1}) \leq \\ \lambda\left\{\partial(\zeta_{n-1}, \Im\zeta_n) + \partial(\zeta_n, \Im\zeta_{n-1}) + \partial(\zeta_n, \Im\zeta_{n+1}) + \partial(\zeta_{n+1}, \Im\zeta_n)\right\}, \\ \partial(\zeta_n, \zeta_{n+1}) + \partial(\zeta_{n+1}, \zeta_{n+2}) \leq \\ \lambda\left\{\partial(\zeta_{n-1}, \zeta_{n+1}) + \partial(\zeta_n, \zeta_n) + \partial(\zeta_n, \zeta_{n+2}) + \partial(\zeta_{n+1}, \zeta_{n+1})\right\}. \qquad (15)\end{gathered}$$

Utilizing the triangle inequality in (15), we have

$$\begin{gathered}\partial(\zeta_n, \zeta_{n+1}) + \partial(\zeta_{n+1}, \zeta_{n+2}) \leq \\ \lambda\left\{\partial(\zeta_{n-1}, \zeta_n) + \partial(\zeta_n, \zeta_{n+1}) + \partial(\zeta_n, \zeta_{n+1}) + \partial(\zeta_{n+1}, \zeta_{n+2})\right\}, \\ (1-\lambda)(\partial(\zeta_n, \zeta_{n+2}) + \partial(\zeta_{n+1}, \zeta_{n+2})) \leq \lambda\left\{\partial(\zeta_{n-1}, \zeta_n) + \partial(\zeta_n, \zeta_{n+1})\right\}, \\ \partial(\zeta_n, \zeta_{n+2}) + \partial(\zeta_{n+1}, \zeta_{n+2}) \leq \frac{\lambda}{1-\lambda}\left\{\partial(\zeta_{n-1}, \zeta_n) + \partial(\zeta_n, \zeta_{n+1})\right\}, \\ \partial(\zeta_n, \zeta_{n+2}) + \partial(\zeta_{n+1}, \zeta_{n+2}) \leq \alpha\left\{\partial(\zeta_{n-1}, \zeta_n) + \partial(\zeta_n, \zeta_{n+1})\right\}. \qquad (16)\end{gathered}$$

Where $\alpha = \frac{\lambda}{1-\lambda}$. Since $0 \leq \lambda < \frac{1}{2}$, therefore $0 \leq \alpha = \frac{\lambda}{1-\lambda} < 1$. From inequality (16), we get

$$\partial(\zeta_n, \zeta_{n+2}) + \partial(\zeta_{n+1}, \zeta_{n+2}) \leq \alpha\left\{\partial(\zeta_{n-1}, \zeta_n) + \partial(\zeta_n, \zeta_{n+1})\right\}$$

$$\begin{aligned}
&\leq \alpha^2 \{\partial(\zeta_{n-2}, \zeta_{n-1}) + \partial(\zeta_{n-1}, \zeta_n)\} \\
&. \\
&. \\
&. \\
&\leq \alpha^n \{\partial(\zeta_0, \zeta_1) + \partial(\zeta_1, \zeta_2)\}.
\end{aligned}$$

If we consider $K_0 = \partial(\zeta_0, \zeta_1) + \partial(\zeta_1, \zeta_2$, $K_1 = \partial(\zeta_1, \zeta_2) + \partial(\zeta_2, \zeta_3)$,...$K_n = \partial(\zeta_n, \zeta_{n+1}) + \partial(\zeta_{n+1}, \zeta_{n+2}$, then it follows that

$$K_n \leq \alpha K_{n-1} \leq \alpha^2 K_{n-2} \leq \ldots \leq \alpha^n K_n. \tag{17}$$

Suppose there is the smallest number $j \geq 3$ such that $\zeta_j = \zeta_i$ for some i where $0 \leq i \leq j-2$. In the present situation, it appears that $\zeta_{j+1} = \zeta_{i+1}$ and $\zeta_{j+2} = \zeta_{i+2}$. Therefore

$$\begin{aligned}
K_i &= \partial(\zeta_i, \zeta_{i+1}) + \partial(\zeta_{i+1}, \zeta_{i+2}) \\
&= \partial(\zeta_j, \zeta_{j+1}) + \partial(\zeta_{j+1}, \zeta_{j+2}) \\
&= K_i.
\end{aligned}$$

This results in a conflict with equation (17). Therefore, such values of i and j cannot exist.

Now, let us show that $\{\zeta_n\}$ is a Cauchy sequence. Based on the previous arguments, it is evident that:

$$\partial(\zeta_n, \zeta_{n+1}) \leq K_n \leq \alpha^n K_0. \tag{18}$$

Taking into consideration equation (18), for $(m-n) \in \mathbb{N}$, assuming $m > n$ for the sake of simplicity and utilizing repeatedly triangle inequality, we find that

$$\begin{aligned}
\partial(\zeta_n, \zeta_m) &\leq \partial(\zeta_n, \zeta_{n+1}) + \partial(\zeta_{n+1}, \zeta_{n+2}) + \ldots + \partial(\zeta_{m-1}, \zeta_m) \\
&\leq \alpha^n K_0 + \alpha^{n-1} K_0 + \ldots + \alpha^{m-1} K_0 \\
&= \alpha^n (1 + \alpha + \alpha^2 + \ldots + \alpha^{m-1}) K_0 \\
&= \alpha^n \left(\frac{1 - \alpha^m}{1 - \alpha} \right) K_0.
\end{aligned}$$

Under the assumption that $\alpha \in [0, 1)$, we can observe that $\partial(\zeta_n, \zeta_m) < \alpha^n \frac{1}{1-\alpha} K_0$. Consequently, as we let $m, n \to \infty$, we find that $\partial(\zeta_n, \zeta_m) \to 0$.

This proves that sequence $\{\zeta_n\}$ is a Cauchy. This sequence has a limit $\zeta^* \in \mho$ according to the completeness of $(\mho, \partial)$.

Note that any consecutive three elements of $\{\zeta_n\}$ are distinct from each other. If $\zeta^* \neq \zeta_k$ for any $k \in \{1, 2, 3, \ldots\}$, then inequality (5) is satisfied for any three elements ζ^*, ζ_{n-1} and ζ_n. Assume that $\zeta_k = \zeta^*$ for the smallest possible $k \in \{1, 2, 3, \ldots\}$. If $m > k$ exists such that $\zeta_m = \zeta^*$, then the sequence, beginning from k, is cyclic and cannot be a Cauchy. Therefore, for $n - 1 > k$, the points ζ^*, ζ_{n-1}, and ζ_n are distinct from each other.

Now, we demonstrate that the limit point ζ^* is a *FP* of $\Im$ that is $\Im\zeta^* = \zeta^*$. If there exists a $k \in \{1, 2, 3, \ldots\}$ such that $\zeta_k = \zeta^*$, then assuming $n-1 > k$, and applying the triangle inequality with inequality (5) follows that:

$$\begin{aligned}
\partial(\zeta^*, \Im\zeta^*) &\leq \partial(\zeta^*, \zeta_n) + \partial(\zeta_n, \Im\zeta^*) \\
&\leq \partial(\zeta^*, \zeta_n) + \partial(\Im\zeta_{n-1}, \Im\zeta^*) \\
&\leq \partial(\zeta^*, \zeta_n) + \partial(\Im\zeta_{n-1}, \Im\zeta^*) + \partial(\Im\zeta^*, \Im\zeta_n) \\
&\leq \partial(\zeta^*, \zeta_n) + \lambda(\partial(\zeta_{n-1}, \Im\zeta^*) + \partial(\zeta^*, \Im\zeta_{n-1}) + \partial(\zeta_n, \Im\zeta^*) + \partial(\zeta^*, \Im\zeta_n)) \\
&\leq \partial(\zeta^*, \zeta_n) + \lambda(\partial(\zeta_{n-1}, \Im\zeta^*) + \partial(\zeta^*, \zeta_n) + \partial(\zeta_n, \Im\zeta^*) + \partial(\zeta^*, \zeta_{n+1})).
\end{aligned}$$

Considering the continuity of the metric ∂ and letting $n \to \infty$, we obtain

$$\partial(\zeta^*, \Im\zeta^*) \leq 2\lambda\partial(\zeta^*, \Im\zeta^*). \tag{19}$$

Since $0 \leq \lambda < \frac{1}{2}$, we have $0 \leq \lambda < 1$ which implies from inequality (19) that $\partial(\zeta^*, \Im\zeta^*) = 0$ that is $\Im\zeta^* = \zeta^*$.

Assume there are three distinct *FPs* ζ, ε and ξ implies that $\Im\zeta = \zeta$, $\Im\varepsilon = \varepsilon$ and $\Im\xi = \xi$. Consequently, it follows from equation (5) that:

$$\partial(\zeta, \varepsilon) + \partial(\varepsilon, \xi) \leq 2\lambda(\partial(\zeta, \varepsilon) + \partial(\varepsilon, \xi)),$$

which is a contradiction for any $\lambda \in [0, \frac{1}{2})$. It concludes the theorem's proof. □

REMARK 2. If under the supposition of Theorem 3, ζ^* is a *FP* of the mapping $\Im$ which is the limit of a Picard sequence defined as $\zeta_n = \Im\zeta_{n-1}$ for all $n \in \{1, 2, 3, \ldots\}$, where $\zeta_0 \in \mho$. Then ζ^* is a unique *FP*.

On the contrary, suppose that $\Im$ has another *FP* ζ^{**} such that $\zeta^{**} \neq \zeta^*$. Then, we have $\zeta_n \neq \zeta^{**}$ for all $n \in \{1, 2, 3, \ldots\}$. Hence, ζ^*, ζ^{**} and ζ_n are

distinct from each other for all $n = 1, 2, 3, \ldots$. Think about the ratio:

$$\Gamma_n = \frac{\partial(\Im\zeta^*, \Im\zeta^{**}) + \partial(\Im\zeta^{**}, \Im\zeta_n)}{\partial(\zeta^*, \Im\zeta^{**}) + \partial(\zeta^{**}, \Im\zeta^*) + \partial(\zeta^{**}, \Im\zeta_n) + \partial(\zeta_n, \Im\zeta^{**})}$$
$$= \frac{\partial(\zeta^*, \zeta^{**}) + \partial(\zeta^{**}, \zeta_{n+1})}{\partial(\zeta^*, \zeta^{**}) + \partial(\zeta^{**}, \zeta^*) + \partial(\zeta^{**}, \zeta_{n+1}) + \partial(\zeta_n, \zeta^{**})}.$$

Taking into consideration that $\partial(\zeta^*, \zeta_{n+1}) \to 0$, $\partial(\zeta^{**}, \zeta_{n+1}) \to \partial(\zeta^{**}, \zeta^*)$ and $\partial(\zeta_n, \zeta^*) \to 0$, we get $\Gamma_n \to \frac{1}{2}$ as $n \to \infty$, this is against condition (5).

In general, Chatterjea-type mappings are continuous at their *FPs* under reasonable conditions. This follows from the contraction property and the fact that for a sequence converging to the *FP*, the images of the sequence under the mapping also converge to the *FP*. The continuity at the *FP* guarantees that the *FP* is stable under small perturbations of initial conditions, which is a crucial property in iterative schemes used in practical applications.

In the next proposition we will prove that Paired-Chatterjea type mappings are also continuous at their *FPs*.

PROPOSITION 5. *Paired-Chatterjea type mappings are continuous at their FPs.*

Proof. Consider a metric space $(\mho, \partial)$, where $|\mho| \geq 3$. Let $\Im : \mho \to \mho$ be a Paired-Chatterjea type mapping and ζ^* be a *FP* of $\Im$. If $\{\zeta_n\}$ is a sequence such that $\zeta_n \to \zeta^*$. To show continuity at ζ^* of $\Im$, we need to show that $\Im\zeta_n \to \Im\zeta^*$. We consider the following cases to complete the proof.

Case 1: $\zeta_n \neq \zeta_{n+1}$ and $\zeta_n \neq \zeta^*$ for all n;
Utilizing inequality (5), we get

$$\partial(\Im\zeta_n, \Im\zeta^*) + \partial(\Im\zeta^*, \Im\zeta_{n+1}) \leq$$
$$\lambda(\partial(\zeta^*, \Im\zeta_n) + \partial(\zeta_n, \Im\zeta^*) + \partial(\zeta^*, \Im\zeta_{n+1}) + \partial(\zeta_{n+1}, \Im\zeta^*)).$$

By utilizing triangle inequality and *FP* property, we get

$$\partial(\Im\zeta_n, \Im\zeta^*) + \partial(\Im\zeta^*, \Im\zeta_{n+1}) \leq$$
$$\lambda(\partial(\Im\zeta^*, \Im\zeta_n) + \partial(\zeta_n, \zeta^*) + \partial(\Im\zeta^*, \Im\zeta_{n+1}) + \partial(\zeta_{n+1}, \zeta^*)).$$

Therefore, we have

$$(1-\lambda)(\partial(\Im\zeta_n, \Im\zeta^*) + \partial(\Im\zeta^*, \Im\zeta_{n+1})) \leq \lambda(\partial(\zeta_n, \zeta^*) + \partial(\zeta_{n+1}, \zeta^*)).$$

Which implies that

$$\partial(\Im\zeta_n, \Im\zeta^*) + \partial(\Im\zeta^*, \Im\zeta_{n+1}) \leq \frac{\lambda}{1-\lambda}(\partial(\zeta_n, \zeta^*) + \partial(\zeta_{n+1}, \zeta^*)).$$

Since $\partial(\zeta_n, \zeta^*) \to 0$ and $\partial(\zeta_{n+1}, \zeta^*) \to 0$, we have

$$\partial(\Im\zeta_n, \Im\zeta^*) + \partial(\Im\zeta^*, \Im\zeta_{n+1}) \to 0,$$

and, hence, $\partial(\Im\zeta_n, \Im\zeta^*) \to 0$ implies that $\Im\zeta_n \to \Im\zeta^*$.

Case 2: $\zeta_n \neq \zeta^*$ for all n, but $\zeta_n = \zeta_{n+1}$ is possible.

Consider the subsequence $\{\zeta_{n_k}\}$ obtained by removing corresponding repeating terms of $\{\zeta_n\}$ so that $\zeta_{n_k} \neq \zeta_{n_{k+1}}$ for all k. Clearly $\zeta_{n_k} \to \zeta^*$, as it was just proved that $\Im\zeta_{n_k} \to \Im\zeta^* = \zeta^*$. The difference between $\Im\zeta_{n_k}$ and $\Im\zeta_n$ is that $\Im\zeta_n$ can be achieved by adding the corresponding repeating terms to $\Im\zeta_{n_k}$. It implies that $\Im\zeta_n \to \Im\zeta^*$.

Case 3: If $\zeta_n = \zeta^*$ for all $n > N$, where N is a fixed natural number, then it is evident that $\Im\zeta_n \to \Im\zeta^*$.

Case 4: Let $\{\zeta_n\}$ be an arbitrary sequence such that $\zeta_n \to \zeta^*$, but in a manner different from the previously discussed cases:

Let us consider (ζ_{n_k}) achieved by removing ζ^*(if exist) from the sequence (ζ_n). Hence, $\zeta_{n_k} \to \zeta^*$. It was just demonstrated that $\Im\zeta_{n_k} \to \Im\zeta^*$ for such a sequence. Again, we observe that $\Im\zeta_n$ can be derived from $\Im\zeta_{n_k}$ by adding the term ζ^* at certain positions. Hence, it is clear that $\Im\zeta_n = \Im\zeta^*$. □

EXAMPLE 2. Let us consider $\mho = \{a, b, c, d, e, f\}$ as shown in Figure 1. And let the metric d on $\mho$ be defined by

$\mathsf{d}(a,b) = \mathsf{d}(a,c) = \mathsf{d}(b,c) = \mathsf{d}(b,d) = \mathsf{d}(c,e) = \mathsf{d}(d,e) = \mathsf{d}(d,f) = \mathsf{d}(e,f) = 1,$

and

$\mathsf{d}(a,d) = \mathsf{d}(a,e) = \mathsf{d}(b,e) = \mathsf{d}(c,d) = \mathsf{d}(b,f) = \mathsf{d}(c,f) = 2$ and $\mathsf{d}(a,f) = 3.$

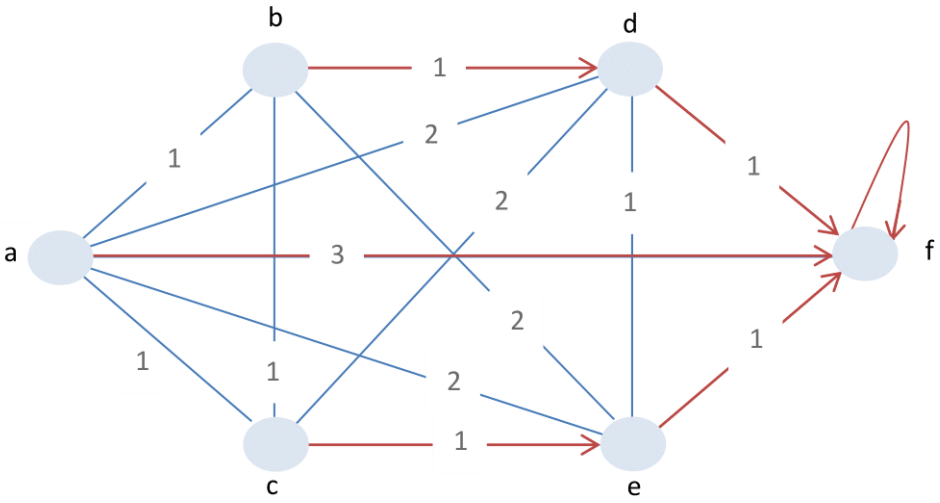

Figure 1 – A Paired-Chatterjea type mapping

Let $\Im : \mho \to \mho$ be such that $\Im a = \Im d = \Im e = \Im f = f$, $\Im b = d$ and $\Im c = e$.(Note: We denote left-side by $L(\zeta, \varepsilon, \xi)$ and right-side by $R(\zeta, \varepsilon, \xi)$ of inequality (5)) We have

$$L(a,d,e) = L(a,e,d) = L(d,a,e) = L(a,d,f) = L(a,f,d) = L(d,a,f)$$
$$= L(a,e,f) = L(a,f,e) = L(e,a,f) = L(d,e,f) = L(d,f,e) = L(e,d,f) = 0,$$

$$L(a,d,b) = L(b,a,d) = L(a,e,b) = L(b,a,e) = L(a,f,b) = L(b,a,f)$$
$$= L(a,d,c) = L(c,a,d) = L(a,e,c) = L(c,a,e) = L(a,f,c) = L(c,a,f)$$
$$= L(d,b,e) = L(b,e,d) = L(b,d,f) = L(b,f,d) = L(b,e,f) = L(b,f,e)$$
$$= L(c,d,e) = L(c,e,d) = L(c,d,f) = L(c,f,d) = L(c,e,f) = L(c,f,e) = 1,$$

$$L(a,b,c) = L(a,c,b) = L(b,a,c) = L(a,b,d) = L(a,b,e) = L(a,b,f)$$

$$= L(a,c,d) = L(a,c,e) = L(a,c,f) = L(b,c,d) = L(b,d,c) = L(c,b,d)$$
$$= L(b,c,e) = L(b,e,c) = L(c,b,e) = L(b,c,f) = L(b,f,c) = L(c,b,f)$$
$$= L(d,b,e) = L(d,b,f) = L(e,b,f) = L(d,c,e) = L(d,c,f) = L(e,c,f) = 2.$$

And

$$R(a,b,c) = R(a,c,b) = R(b,a,c) = R(b,a,d) = R(b,a,e)$$
$$= R(c,a,d) = R(c,a,e) = R(d,a,e) = 8,$$

$$R(a,b,e) = R(a,e,b) = R(a,b,f) = R(f,a,b) = R(a,c,d)$$
$$= R(a,d,c) = R(a,c,f) = R(c,a,f) = R(d,a,f) = R(b,c,d) = R(b,c,e)$$
$$= R(b,c,f) = R(c,b,f) = R(e,a,f) = 7,$$

$$R(a,b,d) = R(a,d,b) = R(a,f,b) = R(a,e,c) = R(a,f,c) = R(a,d,e)$$
$$= R(a,e,d) = R(c,b,d) = R(b,c,e) = R(b,f,c) = R(e,b,f) = R(d,c,f) = 6,$$

$$R(b,d,c) = R(b,e,c) = R(b,e,d) = R(d,b,e) = R(d,b,f)$$
$$= R(d,c,e) = R(e,c,f) = 5,$$

$$R(a,f,d) = R(a,e,f) = R(a,f,e) = R(b,d,e) = R(b,f,d) = R(b,e,f)$$
$$= R(b,f,e) = R(c,d,e) = R(d,e,c) = R(c,d,f) = R(c,f,d) = R(c,f,e) = 4,$$

$$R(b,d,f) = R(c,e,f) = R(d,e,f) = R(e,d,f) = 3, \text{and} d(d,f,e) = 2.$$

We note that

$$L(\zeta,\varepsilon,\xi) \leq \frac{2}{5}R(\zeta,\varepsilon,\xi),$$

for all pairwise distinct points $\zeta,\varepsilon,\xi \in \mho$. Therefore, $\Im$ is a Paired-Chatterjea type mapping.

Since

$$\mathsf{d}(\Im b, \Im d) = \mathsf{d}(b,d) = 1,$$

and

$$\mathsf{d}(b,\Im d) + \mathsf{d}(d,\Im b) = \mathsf{d}(b,f) + \mathsf{d}(d,d) = 2,$$

it does not satisfy (3) for any $0 \leq \eta < \frac{1}{2}$, so $\Im$ is not a Chatterjea type mapping.

Also

$$\mathsf{d}(\Im a, \Im b) + \mathsf{d}(\Im b, \Im c) = \mathsf{d}(f, d) + \mathsf{d}(d, e) = 2,$$

and

$$\mathsf{d}(a, b) + \mathsf{d}(b, c) = 2,$$

it does not satisfy (4) for any $0 \leq \lambda < 1$, so $\Im$ is not a Paired contraction mapping.

We observe that $\Im$ possesses a unique *FP*.

EXAMPLE 3. Let $\mho = R$, $\partial(\zeta, \varepsilon) = |\zeta - \varepsilon|$ and $\Im : \mho \to \mho$ defined as

$$\Im\zeta = \begin{cases} 0, & if\ \zeta < \frac{5}{2}, \\ \\ 1, & if\ \zeta \geq \frac{5}{2}. \end{cases}$$

To prove a Paired-Chatterjea type mapping, we will discuss all possible cases. When ζ, ε, ξ are pairwise distinct and $\zeta < \frac{5}{2}, \varepsilon < \frac{5}{2}, \xi < \frac{5}{2}$ or $\zeta \geq \frac{5}{2}, \varepsilon \geq \frac{5}{2}, \xi \geq \frac{5}{2}$, then inequality (5) satisfy trivially as $L(\zeta, \varepsilon, \xi) = 0$. The other possible cases are as follows:

Case 1: $\zeta, \varepsilon \geq \frac{5}{2}, \xi < \frac{5}{2}$,

$$L(\zeta, \varepsilon, \xi) = \partial(1, 1) + \partial(1, 0) = 1,$$

$$R(\zeta, \varepsilon, \xi) = \partial(\zeta, 1) + \partial(\varepsilon, 1) + \partial(\varepsilon, 0) + \partial(\xi, 1) = |\zeta - 1| + |\varepsilon - 1| + |\varepsilon| + |\xi - 1| = \zeta + 2\varepsilon - 2 + |\xi - 1| \geq \frac{11}{2}.$$

Case 2: $\zeta, \xi \geq \frac{5}{2}, \varepsilon < \frac{5}{2}$,

$$L(\zeta, \varepsilon, \xi) = \partial(1, 0) + \partial(0, 1) = 2,$$

$$R(\zeta, \varepsilon, \xi) = |\zeta| + |\varepsilon - 1| + |\varepsilon - 1| + |\xi| = \zeta + \xi + 2|\varepsilon - 1| \geq 5.$$

Case 3: $\varepsilon, \xi \geq \frac{5}{2}, \zeta < \frac{5}{2}$,

$$L(\zeta, \varepsilon, \xi) = \partial(0, 1) + \partial(1, 1) = 1,$$

$$R(\zeta, \varepsilon, \xi) = |\zeta - 1| + |\varepsilon| + |\varepsilon - 1| + |\xi - 1| = |\zeta - 1| + 2\varepsilon + \xi - 2 \geq \frac{11}{2}.$$

Case 4: $\zeta \geq \frac{5}{2}, \varepsilon, \xi < \frac{5}{2}$,

$$L(\zeta, \varepsilon, \xi) = \partial(1,0) + \partial(0,0) = 1,$$

$$R(\zeta, \varepsilon, \xi) = |\zeta| + |\varepsilon - 1| + |\varepsilon| + |\xi| = \zeta + |\varepsilon| + |\varepsilon - 1| + |\xi| \geq \frac{7}{2}.$$

Case 5: $\varepsilon \geq \frac{5}{2}, \zeta, \xi < \frac{5}{2}$,

$$L(\zeta, \varepsilon, \xi) = \partial(0,1) + \partial(1,0) = 2,$$

$$R(\zeta, \varepsilon, \xi) = |\zeta - 1| + |\varepsilon| + |\varepsilon| + |\xi - 1| = |\zeta - 1| + 2\varepsilon| + |\xi - 1| \geq 5.$$

Case 6: $\xi \geq \frac{5}{2}, \zeta, \varepsilon < \frac{5}{2}$,

$$L(\zeta, \varepsilon, \xi) = \partial(0,0) + \partial(0,1) = 1,$$

$$R(\zeta, \varepsilon, \xi) = |\zeta| + |\varepsilon| + |\varepsilon - 1| + |\xi| = |\zeta| + |\varepsilon| + |\varepsilon - 1| + \xi \geq \frac{7}{2}.$$

It can be seen, in all cases, that

$$L(\zeta, \varepsilon, \xi) \leq \frac{2}{5} R(\zeta, \varepsilon, \xi).$$

Hence, $\Im$ is a Paired-Chatterjea type mapping. We observe that $\Im$ possesses a unique *FP*.

Now, for $\zeta = 1.9, \varepsilon = 2, \xi = 2.1$, we have

$$\partial(\Im\zeta, \Im\varepsilon) + \partial(\Im\varepsilon, \Im\xi) = \partial(0,1) + \partial(1,1) = 1,$$

and

$$\partial(\zeta, \varepsilon) + \partial(\varepsilon, \xi) = \partial(1.9, 2) + \partial(2, 2.1) = 0.1 + 0.1 = 0.2,$$

so, we get that $\Im$ is not a Paired contraction mapping.

Also, for $\zeta = 2, \varepsilon = 3$,

$$\partial(\Im\zeta, \Im\varepsilon) = \partial(0, \frac{5}{2}) = \frac{5}{2},$$

and

$$\partial(\zeta, \Im\zeta) + \partial(\varepsilon, \Im\varepsilon) = \partial(2,0) + \partial(3, \frac{5}{2}) = \frac{5}{2},$$

hence, $\Im$ is not Kannan type mapping.

Moreover,

$$\partial(\zeta, \Im\varepsilon) + \partial(\varepsilon, \Im\zeta) = \partial(2, \frac{5}{2}) + \partial(3,0) = \frac{7}{2},$$

also, we get that $\Im$ is not a Chatterjea type mapping.

We observe that $\Im$ is a discontinuous mapping.

Results on Paired Chatterjea-style mappings within incomplete metric spaces

In the theorem corresponding to Theorem 1 in (Kannan, 1969) we presented here, exclude the completeness requirement for the metric space and includ two assumptions, denoted as (PC_1) and (PC_2):

THEOREM 4. *Let $(\mho, \partial)$ be a complete metric space, where $|\mho| \geq 3$, and consider the mapping $\Im : \mho \to \mho$ that is a Paired-Chatterjea contraction mapping and has no periodic elements of prime period 2. If $\Im$ holds following two assumptions:*

(PC_1) $\Im$ is continuous at $\zeta^* \in \mho$.

(PC_2) There exists $\zeta_0 \in \mho$ such that the sequence $\{\zeta_n\}$, where $\zeta_n = \Im\zeta_{n-1}$ for $n = 1, 2, ...$, has a convergent subsequence $\{\zeta_{n_k}\}$ to ζ^*.

Then ζ^* is a FP of $\Im$. Moreover, $\Im$ exhibit no more than two FPs.

Proof. Given that $\Im$ is continuous at ζ^* and $\zeta_{n_k} \to \zeta^*$, it follows that $\Im\zeta_{n_k} = \zeta_{n_k+1} \to \Im\zeta^*$. Note that while ζ_{n_k+1} is a subsequence of ζ_n, it is not necessarily a subsequence of ζ_{n_k}. Let us consider, for the sake of contradiction, that $\zeta^* \neq \Im\zeta^*$. Let us examine two balls:

$$B_1 = B_1(\zeta^*, r) \text{ and } B_2 = B_2(\Im\zeta^*, r),$$

where $r < \frac{1}{3}\partial(\zeta^*, \Im\zeta^*)$. Therefore, a positive integer N exists such that, for each $i > N$, we have

$$\zeta_{n_i} \in B_1 \text{ and } \zeta_{n_i+1} \in B_2,$$

which implies that,

$$\partial(\zeta_{n_i}, \zeta_{n_i+1}) > r \text{ for } i > N. \tag{20}$$

If the mapping $\Im$ has no fixed points in the sequence $\{\zeta_n\}$, then we can apply the arguments presented in Theorem 3. For $n = 3, 4, ...$, by (17), we get

$$\partial(\zeta_n, \zeta_{n+1}) \leq \alpha^n K_0,$$

where $K_0 = \partial(\zeta_0, \zeta_1) + \partial(\zeta_1, \zeta_2)$ and $\alpha = \frac{\lambda}{1-\lambda} \in [0, 1)$. Therefore,

$$\partial(\zeta_{n_i}, \zeta_{n_i+1}) \leq \alpha^{n_i} K_0.$$

Which tends to 0 as $i \to \infty$, which leads to a contradiction to (20). Therefore, it follows that $\Im\zeta^* = \zeta^*$.

From the final paragraph of Theorem 3, it can be proven there exist at most two fixed points. □

In the next theorem corresponding to Theorem 2 in (Kannan, 1969), we consider $\Im$ as a Paired-Chatterjea type mapping defined on an everywhere dense subset of $\mho$. The mapping $\Im$ is continuous on $\mho$, although this continuity is not necessarily restricted to the point ζ^*.

THEOREM 5. *Let $(\mho, \partial)$ be a metric space with $|\mho| \geq 3$, and consider a mapping $\Im : \mho \to \mho$ that has no periodic point with prime period 2 and is a Paired-Chatterjea type mapping on $(\mathfrak{M}, \partial)$, where $\mathfrak{M}$ is an everywhere dense subset of $\mho$. If $\Im$ holds following two assumptions:*

(PC_1) $\Im$ is continuous at $\zeta^* \in \mho$.

(PC_2) There exists $\zeta_0 \in \mho$ such that the sequence $\{\zeta_n\}$, where $\zeta_n = \Im\zeta_{n-1}$ for $n = 1, 2, ...,$ has a convergent subsequence $\{\zeta_{n_k}\}$ to ζ^*.

Then ζ^* is a FP of $\Im$. Moreover, $\Im$ exhibits at most two FPs.

Proof. The proof will be based on Theorem 4, provided that $\Im$ is demonstrated to be a Paired-Chatterjea type mapping on $\mho$. Consider three pairwise distinct points ζ, ε, ξ from $\mho$. To demonstrate that $\Im$ is a Paired-Chatterjea type mapping, we will examine three distinct cases:

Case 1. $\zeta, \varepsilon \in \mathfrak{M}$ and $\xi \in \mho/\mathfrak{M}$;

Since $\mathfrak{M}$ is an everywhere dense subset of $\mho$, we can find a sequence $\{\xi_n\} \subset \mathfrak{M}$ such that $\xi_n \to \xi$, $\xi_n \neq \zeta$, $\xi_n \neq \varepsilon$ for every n, and $\xi_i \neq \xi_j$ for $i \neq j$. Consequently,

$$\begin{aligned}
\partial(\Im\zeta, \Im\varepsilon) + \partial(\Im\varepsilon, \Im\xi) &\leq \partial(\Im\zeta, \Im\varepsilon) + \partial(\Im\varepsilon, \Im\xi_n) + \partial(\Im\xi_n, \Im\xi) \\
&\text{(Using triangle inequality)} \\
&\leq \lambda(\partial(\zeta, \Im\varepsilon) + \partial(\varepsilon, \Im\zeta) + \partial(\xi_n, \Im\varepsilon) + \partial(\varepsilon, \Im\xi_n)) + \partial(\Im\xi_n, \Im\xi) \\
&\leq \lambda(\partial(\zeta, \Im\varepsilon) + \partial(\varepsilon, \Im\zeta) + \partial(\xi, \Im\varepsilon) + \partial(\xi, \xi_n) + \partial(\varepsilon, \Im\xi) + \partial(\Im\xi, \Im\xi_n)) \\
&\quad + \partial(\Im\xi_n, \Im\xi) \\
&\leq \lambda(\partial(\zeta, \Im\varepsilon) + \partial(\varepsilon, \Im\zeta) + \partial(\xi_n, \Im\varepsilon) + \partial(\varepsilon, \Im\xi)) \\
&\quad + \lambda\partial(\xi_n, \xi) + (1 + \lambda)\partial(\Im\xi_n, \Im\xi).
\end{aligned}$$

As $n \to \infty$, we have $\partial(\xi_n, \xi) \to 0$ and $\partial(\Im\xi_n, \Im\xi) \to 0$. Therefore, inequality (5) is established.

Case 2. $\zeta \in \mathfrak{M}$ and $\varepsilon, \xi \in \mho/\mathfrak{M}$;

Let $\{\varepsilon_n\}$, $\{\xi_n\}$ be sequences in $\mathfrak{M}$ such that $\varepsilon_n \to \varepsilon$ and $\xi_n \to \xi$. (Here

and in the next case, we will consider the points ζ, ε, ξ and all points of the sequences including the limit points of the sequences are pairwise distinct.) Then, by applying the triangle inequality and (5) on $\mathfrak{M}$, we obtain

$$\begin{gathered}\partial(\Im\zeta,\Im\varepsilon)+\partial(\Im\varepsilon,\Im\xi)\leq\partial(\Im\zeta,\Im\varepsilon_n)+\partial(\Im\varepsilon_n,\Im\varepsilon)+\partial(\Im\varepsilon,\Im\varepsilon_n)+\\ \partial(\Im\varepsilon_n,\Im\xi_n)+\partial(\Im\xi_n,\Im\xi)=(\partial(\Im\zeta,\Im\varepsilon_n)+\partial(\Im\varepsilon_n,\Im\xi_n))+\\ 2\partial(\Im\varepsilon_n,\Im\varepsilon)+\partial(\Im\xi_n,\Im\xi)\\ \leq\lambda(\partial(\zeta,\Im\varepsilon_n)+\partial(\varepsilon_n,\Im\zeta)+\partial(\varepsilon_n,\Im\xi_n)+\partial(\xi_n,\Im\varepsilon_n))\\ +2\partial(\Im\varepsilon_n,\Im\varepsilon)+\partial(\Im\xi_n,\Im\xi)\\ \leq\lambda(\partial(\zeta,\Im\varepsilon)+\partial(\varepsilon,\Im\zeta)+\partial(\varepsilon,\Im\xi)+\partial(\xi,\Im\zeta))+2\lambda\partial(\varepsilon_n,\varepsilon)+\lambda\partial(\xi_n,\xi)\\ +2(1+\lambda)\partial(\Im\varepsilon_n,\Im\varepsilon)+(1+\lambda)\partial(\Im\xi_n,\Im\xi).\end{gathered}$$

Once again, inequality (5) is obtained by letting $n\to\infty$ as $\partial(\varepsilon_n,\varepsilon)\to 0$, $\partial(\xi_n,\xi)\to 0$, $\partial(\Im\varepsilon_n,\Im\varepsilon)\to 0$ and $\partial(\Im\xi_n,\Im\xi)\to 0$.

Case 3. $\zeta,\varepsilon,\xi\in\mho/\mathfrak{M}$, and let $\{\zeta_n\}$, $\{\varepsilon_n\}$ and $\{\xi_n\}$ are sequences in $\mathfrak{M}$ such that $\zeta_n\to\zeta$, $\varepsilon_n\to\varepsilon$ and $\xi_n\to\xi$. Consequently,

$$\begin{gathered}\partial(\Im\zeta,\Im\varepsilon)+\partial(\Im\varepsilon,\Im\xi)\\ \leq\partial(\Im\zeta,\Im\zeta_n)+\partial(\Im\zeta_n,\Im\varepsilon_n)+\partial(\Im\varepsilon_n,\Im\varepsilon)+\partial(\Im\varepsilon,\Im\varepsilon_n)\\ +\partial(\Im\varepsilon_n,\Im\xi_n)+\partial(\Im\xi_n,\Im\xi)=(\partial(\Im\zeta_n,\Im\varepsilon_n)+\partial(\Im\varepsilon_n,\Im\xi_n))\\ +\partial(\Im\zeta,\Im\zeta_n)+2\partial(\Im\varepsilon,\Im\varepsilon_n)+\partial(\Im\xi,\Im\xi_n)\\ \leq\lambda(\partial(\zeta_n,\Im\varepsilon_n)+\partial(\varepsilon_n,\Im\zeta_n)+\partial(\varepsilon_n,\Im\xi_n)+\partial(\xi_n,\Im\varepsilon_n))\\ +\partial(\Im\zeta,\Im\zeta_n)+2\partial(\Im\varepsilon,\Im\varepsilon_n)+\partial(\Im\xi,\Im\xi_n)\\ \leq\lambda(\partial(\zeta,\Im\varepsilon)+\partial(\varepsilon,\Im\zeta)+\partial(\varepsilon,\Im\xi)+\partial(\xi,\Im\varepsilon))\\ +\lambda(\partial(\zeta_n,\zeta)+2\partial(\varepsilon_n,\varepsilon)+\partial(\xi_n,\xi))\\ +(1+\lambda)(\partial(\Im\zeta,\Im\zeta_n)+2\partial(\Im\varepsilon,\Im\varepsilon_n)+\partial(\Im\xi,\Im\xi_n)).\end{gathered}$$

Again, allowing $n\to\infty$, inequality (5) is obtained as $\partial(\zeta_n,\zeta)\to 0$, $\partial(\varepsilon_n,\varepsilon)\to 0$, $\partial(\xi_n,\xi)\to 0$, $\partial(\Im\zeta_n,\Im\zeta)\to 0$, $\partial(\Im\varepsilon_n,\Im\varepsilon)\to 0$ and $\partial(\Im\xi_n,\Im\xi)\to 0$.

Hence, $\Im$ is a Paired-Chatterjea type mapping on $\mho$. Therefore, mapping $\Im$ satisfies all assumptions of Theorem 4, which completes the proof. □

EXAMPLE 4. Let $\mho = [0,1)$ equipped with standard metric $\partial(\zeta,\varepsilon) = |\zeta - \varepsilon|$. It is an incomplete metric space. Let a self map $\Im$ be defined on $\mho$ as:

$$\Im\zeta = \begin{cases} \frac{\zeta}{4}, & if\ \zeta \in \mathbb{Q} \cap [0,1); \\ \\ \frac{\zeta}{2}, & if\ \zeta \in \mathbb{Q}^c \cap [0,1). \end{cases}$$

Here, it is clear that $\Im$ is a discontinuous map over $\mho = [0,1)$ except at $\zeta = 0$. Consequently, the Banach contraction principle is not applicable. Let us consider a nonempty subset $\mathfrak{M} = \mathbb{Q} \cap [0,1)$ of $\mho$ which is everywhere dense in $\mho$. For any three points $\zeta, \varepsilon, \xi \in \mathfrak{M}$, we have

$$\partial(\zeta, \Im\varepsilon) + \partial(\varepsilon, \Im\zeta) + \partial(\varepsilon, \Im\xi) + \partial(\xi, \Im\varepsilon) = \partial(\zeta, \frac{\varepsilon}{4}) + \partial(\varepsilon, \frac{\zeta}{4}) + \partial(\varepsilon, \frac{\xi}{4}) + \partial(\xi, \frac{\varepsilon}{4}) = |\zeta - \frac{\varepsilon}{4}| + |\varepsilon - \frac{\zeta}{4}| + |\varepsilon - \frac{\xi}{4}| + |\xi - \frac{\varepsilon}{4}| \tag{21}$$

and

$$\partial(\Im\zeta, \Im\varepsilon) + \partial(\Im\varepsilon, \Im\xi) = \partial(\frac{\zeta}{4}, \frac{\varepsilon}{4}) + \partial(\frac{\varepsilon}{4}, \frac{\xi}{4}) = |\frac{\zeta}{4} - \frac{\varepsilon}{4}| + |\frac{\varepsilon}{4} - \frac{\xi}{4}|. \tag{22}$$

Now,

$$|\frac{\zeta}{4} - \frac{\varepsilon}{4}| + |\frac{\varepsilon}{4} - \frac{\xi}{4}| = \frac{1}{4}|\zeta - \frac{\zeta}{4} + \frac{\zeta}{4} - \frac{\varepsilon}{4} + \frac{\varepsilon}{4} - \varepsilon| + \frac{1}{4}|\varepsilon - \frac{\varepsilon}{4} + \frac{\varepsilon}{4} - \frac{\xi}{4} + \frac{\xi}{4} - \xi|$$
$$\leq \frac{1}{4}\left\{|\zeta - \frac{\varepsilon}{4}| + |\frac{\zeta}{4} - \frac{\varepsilon}{4}| + |\varepsilon - \frac{\zeta}{4}|\right\} + \frac{1}{4}\left\{|\varepsilon - \frac{\xi}{4}| + |\frac{\varepsilon}{4} - \frac{\xi}{4}| + |\xi - \frac{\varepsilon}{4}|\right\}$$

$$\Longrightarrow \frac{3}{4}\left\{|\frac{\zeta}{4} - \frac{\varepsilon}{4}| + |\frac{\varepsilon}{4} - \frac{\xi}{4}|\right\} \leq \frac{1}{4}\left\{|\zeta - \frac{\varepsilon}{4}| + |\varepsilon - \frac{\zeta}{4}| + |\varepsilon - \frac{\xi}{4}| + |\xi - \frac{\varepsilon}{4}|\right\}$$

$$\Longrightarrow |\frac{\zeta}{4} - \frac{\varepsilon}{4}| + |\frac{\varepsilon}{4} - \frac{\xi}{4}| \leq \frac{1}{3}\left\{|\zeta - \frac{\varepsilon}{4}| + |\varepsilon - \frac{\zeta}{4}| + |\varepsilon - \frac{\xi}{4}| + |\xi - \frac{\varepsilon}{4}|\right\}. \tag{23}$$

Therefore, from (21), (22) and (23), we can conclude that $\Im$ is a Paired-Chatterjea type mapping with the parameter $\lambda = \frac{1}{3} \in [0, \frac{1}{2})$, on $(\mathfrak{M}, \partial)$.

Hence, it can be easily verified that the mapping $\Im$ satisfies all the assumptions of Theorem 5 with $\zeta^* = 0$, which implies that there exists a fixed point of the mapping $\Im$ on $\mho$. In this example, "0" is the only fixed point of the mapping $\Im$.

References

Agarwal, P., Jleli, M. & Samet, B. 2018. *Fixed Point Theory in Metric Spaces: Recent Advances and Applications*. Springer Singapore. Available at: https://doi.org/10.1007/978-981-13-2913-5.

Berinde, V. & Păcurar, M. 2021. Approximating fixed points of enriched Chatterjea contractions by Krasnoselskij iterative algorithm in Banach spaces. *Journal of Fixed Point Theory and Applications*, 23, art.number:66. Available at: https://doi.org/10.1007/s11784-021-00904-x.

Bimol, T., Priyobarta, N., Rohen, Y. & Singh, K.A. 2024. Fixed Points for S-Contractions of Type E on S-Metric Space. *Nonlinear Functional Analysis and Applications (NFAA)*, 29(3), pp. 635–648. Available at: https://doi.org/10.22771/nfaa.2024.29.03.02.

Bisht, R.K. & Petrov, E. 2024. A three point extension of Chatterjea's fixed point theorem with at most two fixed points. *arXiv:2403.07906v1*. Available at: https://doi.org/10.48550/arXiv.2403.07906.

Chand, D. & Rohen, Y. 2023. Fixed Points of α_s-β_s-ψ-Contractive Mappings in S-Metric Spaces. *Nonlinear Functional Analysis and Applications*, 28(2), pp. 571–587. Available at: https://doi.org/10.22771/nfaa.2023.28.02.15.

Chand, D. & Rohen, Y. 2024. Paired contractive mappings and fixed point results. *AIMS Mathematics*, 9(1), pp. 1959–1968. Available at: https://doi.org/10.3934/math.2024097.

Chand, D., Rohen, Y., Saleem, N., Aphane, M. & Razzaque, A. 2024. S-Pata-type contraction: a new approach to fixed-point theory with an application. *Journal of Inequalities and Applications*, 2024, art.number:59. Available at: https://doi.org/10.1186/s13660-024-03136-y.

Chandok, S. & Postolache, M. 2013. Fixed point theorem for weakly Chatterjea-type cyclic contractions. *Fixed Point Theory and Applications*, 2013, art.number:28. Available at: https://doi.org/10.1186/1687-1812-2013-28.

Chatterjea, S.K. 1972. Fixed-point theorems. *Comptes Rendus de l'Academie bulgare des Sciences*, 25(6), pp. 727–730.

Choudhury, B.S., Metiya, N., Kundu, S. & Khatua, D. 2019. Fixed points of multivalued mappings in metric spaces. *Surveys in Mathematics and its Applications*, 14, pp. 1–16. [online]. Available at: https://www.utgjiu.ro/math/sma/v14/a14_01.html [Accessed: 05 November 2024].

Debnath, P., Mitrović, Z.D. & Cho, S.Y. 2021. Common fixed points of Kannan, Chatterjea and Reich type pairs of self-maps in a complete metric space. *São Paulo Journal of Mathematical Sciences*, 15, pp. 383–391. Available at: https://doi.org/10.1007/s40863-020-00196-y.

Harjani, J., López, B. & Sadarangani, K. 2011. Fixed point theorems for weakly *C*-contractive mappings in ordered metric spaces. *Computers & Mathematics with Applications*, 61(4), pp. 790–796. Available at: https://doi.org/10.1016/j.camwa.2010.12.027.

Jachymski, J. 1994. An iff fixed point criterion for continuous self-mappings on a complete metric space. *Aequationes mathematicae*, 48(2-3), pp. 163–170. [online]. Available at: https://eudml.org/doc/137605 [Accessed: 05 November 2024].

Kadelburg, Z. & Radenovic, S. 2016. Fixed point theorems under Pata-type conditions in metric spaces. *Journal of the Egyptian Mathematical Society*, 24(1), pp. 77–82. Available at: https://doi.org/10.1016/j.joems.2014.09.001.

Kannan, R. 1968. Some results on fixed points. *Bulletin of the Calcutta Mathematical Society*, 60, pp. 71–76.

Kannan, R. 1969. Some Results on Fixed Points—II. *The American Mathematical Monthly*, 76(4), pp. 405–408. Available at: https://doi.org/10.1080/00029890.1969.12000228.

Karahan, I. & Isik, I. 2019. Generalizations of Banach, Kannan and Ciric fixed point theorems in bv(s) metric spaces. *University Politehnica of Bucharest Scientific Bulletin, Series A - Applied Mathematics and Physics*, 81(1), pp. 73–80. [online]. Available at: https://www.scientificbulletin.upb.ro/rev_docs_arhiva/full714_520656.pdf [Accessed: 05 November 2024].

Kohsaka, F. & Suzuki, T. 2017. Existence and approximation of fixed points of Chatterjea mappings with Bregman distances. *Linear Nonlinear Analysis*, 3(1), pp. 73–86. [online]. Available at: http://yokohamapublishers.jp/online2/oplna/vol3/p73.html [Accessed: 05 November 2024].

Malčeski, A., Ibrahimi, A. & Malčeski, R. 2016. Extending Kannan and Chatterjea theorems in 2-Banach spaces by using sequentialy convergent mappings. *Matematichki Bilten*, 40(1), pp. 29–36. Available at: https://doi.org/10.37560/matbil16100029m.

Pant, R., Rakočević, V., Gopal, D., Pant, A. & Ram, M. 2021. A general fixed point theorem. *Filomat*, 35(12), pp. 4061–4072. Available at: https://doi.org/10.2298/FIL2112061P.

Petrov, E. 2023. Fixed point theorem for mappings contracting perimeters of triangles. *Journal of Fixed Point Theory and Applications*, 25(3), art.number:74. Available at: https://doi.org/10.1007/s11784-023-01078-4.

Rhoades, B.E. 1988. Contractive definitions and continuity. In: *Brown, R.F. (Ed.) Fixed Point Theory and Its Applications, Vol. 72, MR0956495*. Providence, RI, USA: American Mathematical Society. Available at: https://doi.org/10.1090/conm/072.

Savaliya, J., Gopal, D., Moreno, J.M. & Srivastava, S.K. 2024. Solution to the Rhoades' problem under minimal metric structure. *The Journal of Analysis*, 32, pp. 1787–1799. Available at: https://doi.org/10.1007/s41478-024-00722-7.

Subrahmanyam, P. 2018. *Elementary Fixed Point Theorems*. Springer Singapore. Available at: https://doi.org/10.1007/978-981-13-3158-9.

Tassaddiq, A., Kanwal, S., Perveen, S. & Srivastava, R. 2022. Fixed points of single-valued and multi-valued mappings in sb-metric spaces. *Journal of Inequalities and Applications*, 2022, art.number:85. Available at: https://doi.org/10.1186/s13660-022-02814-z.

Contracciones de tipo Paired-Chatterjea sincronizada: nuevos resultados de punto fijo y propiedades de continuidad en espacios métricos

Deep Chand[a], *Yumnam* Rohen[ab], *Sanasam Surenda* Singh[a], *Nicola* Fabiano[c]

[a] Instituto Nacional de Tecnología de Manipur, Departamento de Matemáticas, Langol, Imphal, Manipur, República de la India

[b] Universidad de Manipur, Departamento de Matemáticas, Canchipur, Imphal, Manipur, República de la India

[c] Universidad de Belgrado, Instituto de Ciencias Nucleares "Vinča" - Instituto Nacional de la República de Serbia, Belgrado, República de Serbia, **autor de correspondencia**

CAMPO: matemáticas

TIPO DE ARTÍCULO: artículo científico original

Resumen:

Introducción/objetivo: El artículo trata sobre las aplicaciones de contracciones de tipo Paired-Chatterjea como una extensión de las contracciones de tipo Chatterjea tradicionales que operan en tres puntos en lugar de dos, en el marco de espacios métricos estándar.

Métodos: Se emplea el concepto de Mapeo de tipos de Chatterjea sincronizado en un espacio métrico en tres puntos en lugar de dos utilizando la idea de Mapeo de tipos de Chatterjea sincronizados.

Resultados: Se ha discutido una serie de propiedades correspondientes. Además, se establece que los mapeos de tipo de Chatterjea sincronizada constituyen una clase distinta al de mapeo de tipos de Chatterjea tradicionales y obtienen al menos un punto fijo en ausencia de puntos periódicos de periodo primo 2 dentro de espacios métricos completos. También se demuestra cómo criterios adicionales a estas aplicaciones, como la continuidad y la regularidad asintótica, amplían el alcance de los resultados de punto fijo. Más allá de las contribuciones fundamentales de Chatterjea, se establecen dos resultados adicionales de punto fijo aplicables a las aplicaciones de mapeo de tipos

de Chatterjea sincronizada en espacios métricos, incluso en escenarios donde no se requiere la completitud.

Conclusión: Los mapeos de tipos de Chatterjea sincronizada son generalmente discontinuas; presentan continuidad en puntos fijos, similar a las aplicaciones de tipo Kannan y Chatterjea. En ausencia de un punto periódico de periodo primo 2, estas aplicaciones tienen un punto fijo dentro del espacio métrico completo.

Palabras claves: espacio métrico, punto fijo, aplicaciones de tipo Chatterjea, contracción sincronizada, Mapeo de tipos de Chatterjea sincronizada.

Парное сжатие типа Чаттерджи: новые результаты с неподвижной точкой и свойства непрерывности в метрических пространствах

Дип Чанд[а], *Юмнам* Рохен[аб],
Санасам Суренда Синг[а], *Никола* Фабиано[в]

[а] Национальный технологический институт Манипура, математический факультет, г. Лангол, Импхал, Манипур, Республика Индия

[б] Манипурский университет, математический факультет, г. Канчипур, Импхал, Манипур, Республика Индия

[в] Белградский университет, Институт ядерных исследований «Винча» − Институт государственного значения для Республики Сербия, г. Белград, Республика Сербия, **корреспондент**

РУБРИКА ГРНТИ: 27.25.17 Метрическаятеорияфункций,
27.39.15 Линейныепространства, снабженныетопологией, порядкомидругимиструктурами

ВИД СТАТЬИ: оригинальная научная статья

Резюме:

Введение/цель: В статье рассматриваются парные отображения Чаттерджи, которые являются расширением традиционных сжимающих отображений типа Чаттерджи и оперирующие тремя точками вместо двух в рамках стандартных метрических пространств.

Методы: Сжимающие отображения типа Чаттерджи используются в метрическом пространстве в трех точках вместо двух, основываясь на идее о парных сжимающих отображениях.

Результаты: В статье также представлен ряд свойств соответствующих отображений. Установлено, что парные отображения Чаттерджи образуют особый класс по сравнению с традиционными отображениями типа Чаттерджи, которые обладают хотя бы одной неподвижной точкой при отсутствии периодических точек простого периода 2 в рамках полных метрических пространств. В ходе исследования было выявлено, что дополнительные критерии для этих отображений, такие как непрерывность и асимптотическая регулярность, расширяют диапазон результатов с фиксированной точкой. Расширяя вклад Чаттерджи, были получены два дополнительных результата с неподвижной точкой, применимые к парным отображениям Чаттерджи даже в неполных метрических пространствах.

Выводы: Парные отображения типа Чаттерджи, как правило, прерывисты. Они демонстрируют непрерывность в неподвижных точках, аналогичных отображениям типа Каннан и Чаттерджи. При отсутствии периодической точки с простым периодом 2, неподвижная точка этих отображений располагается внутри полного метрического пространства.

Ключевые слова: метрическое пространство, неподвижная точка, отображения типа Чаттерджи, парное сжатие, парные отображения Чаттерджи.

Врста упарених пресликавања типа Chatterjee: нови резултати фиксне тачке и својства континуитета у метричким просторима

Дип Чанд[а], *Јумнам* Рохен[аб], *Санасам Суренда* Синг[а], *Никола* Фабиано[в]

[а] Национални институт за технологију Манипур, Одсек за математику, Лангол, Имфал, Манипур, Република Индија

[б] Универзитет Манипура, Одсек за математику, Канчипур, Имфал, Манипур, Република Индија

[в] Универзитет у Београду, Институт за нуклеарне науке „Винча” – Национални институт Републике Србије, Београд, Република Србија, **аутор за преписку**

ОБЛАСТ: математика
КАТЕГОРИЈА (ТИП) ЧЛАНКА: оригинални научни рад

Сажетак:

Увод/циљ: У раду је разматрано увођење упарених пресликавања типа Chatterjee која представљају проширење традиционалних контрактивних пресликавања овог типа, а која делују на три тачке уместо на две, у оквиру стандардних метричких простора.

Методе: Контрактивна пресликавања типа Chatterjee користе се у метричком простору на три тачке, уместо на две применом идеје упарених контрактивних пресликавања.

Резултати: Размотрен је низ својстава предметних пресликавања. Установљено је да упарена пресликавања типа Chatterjee чине посебну класу у односу на традиционална пресликавања овог типа која поседују најмање једну фиксну тачку у одсуству периодичних тачака простог периода 2 унутар комплетних метричких простора. Такође, показано је да додатни критеријуми за ова пресликавања, као што су непрекидност и асимптотска регуларност, проширују опсег резултата фиксне тачке. Проширујући доприносе Chatterjeea, успостављена су два додатна резултата фиксне тачке применљива на упарена пресликавања типа Chatterjee у метричким просторима, чак и у ситуацијама где није потребна комплетност.

Закључак: Упарена пресликавања типа Chatterjee која су најчешће дисконтинуална, показују непрекидност у фиксним тачкама слично пресликавањима типа Kannan и Chatterjee. У одсуству периодичне тачке простог периода 2, ова пресликавања имају фиксну тачку унутар комплетног метричког простора.

Кључне речи: метрички простор, фиксна тачка, пресликавања типа Chatterjee, упарена контракција, упарена пресликавања типа Chatterjee.

Paper received on: 07.11.2024.
Manuscript corrections submitted on: 26.03.2025.
Paper accepted for publishing on: 27.03.2025.

Solving a damped spring-mass system via the MA-simulation function

Shobha Jain[a], *Stojan* N. Radenović[b], *Shishir* Jain[c]

[a] Shri Vaishnav Vidyapeeth Vishwavidyalaya,
Faculty of Mathematics, Indore, Madhya Pradesh, Republic of India,
e-mail: shobajain1@yahoo.com, **corresponding author**,
ORCID iD: https://orcid.org/0000-0002-9253-8689

[b] University of Belgrade, Faculty of Mechanical Engineering,
Belgrade, Republic of Serbia,
e-mail: radens@beotel,
ORCID iD: https://orcid.org/0000-0001-8254-6688

[c] Shri Vaishnav Vidyapeeth Vishwavidyalaya,
Faculty of Mathematics, Indore, Madhya Pradesh, Republic of India,
e-mail: jainshishir11@rediffmail.com,
ORCID iD: https://orcid.org/0009-0005-2165-7196

https://doi.org/10.5937/vojtehg73-53193

FIELD: mathematics
ARTICLE TYPE: original scientific paper

Abstract:

Introduction/purpose: In an interesting article, Perveen & Imdad (2019) introduced the notion of an MA-simulation function, and utilized it to prove the existence of a fixed point for a self mapping through α-admisibilty and the continuity of the self-map in a fuzzy metric space. The purpose of this paper is to establish a unique fixed point theorem for an MA-contractive mapping by relaxing the condition of continuity and α-admissibilty of the map in a fuzzy metric space. As an application of our result, we study the existence and uniqueness of the solution to the damped spring-mass system. The article includes an example which shows the validity of our results.

Methods: The fixed point method with an MA-simulation function was used.

Results: A unique fixed point for a self map in a fuzzy metric space is obtained.

Conclusions: A fixed point of the self map is obtained without the continuity and α-admissibility of the self map via the MA-simulation function. Also, the existence and uniqueness of the solution of a damped spring-mass system in the setting of a fuzzy metric space is obtained.

Key words: fuzzy metric space, M-Cauchy sequence, fixed points, MA-simulation function.

Introduction

In 1965, the fuzzy set theory was initiated by Zadeh (1965) introducing a method to deal with uncertainty and vagueness in everyday life.The concept of fuzzy sets was used by Kramosil & Michálek (1975) to introduce fuzzy metric spaces. Later on, it was modified by George & Veeraman (1994) in order to obtain a Hausdorff topology for this class of fuzzy metric spaces. Contractive mappings in fuzzy metric spaces were studied by various authors, see, e.g. Mihet (2008), Mihet (2010), Tirado (2012) and Wardowski (2013),Gregori & Miñana (2014), and used in establishing some fixed point theorems in a fuzzy metric space in the sense of George & Veeraman. Jain et al. (2009), established fixed point results in a fuzzy metric space by using the concept of a compatible map and a weakly compatible map. Khojasteh et al. (2015) introduced simulation functions defined as follows

A mapping $\zeta : [0, +\infty) \times [0, +\infty) \to R$ is said to be a simulation function if it satisfies the following:

(1) $\zeta(0, 0) = 0$;

(2) $\zeta(t, s) < s - t$, for all $t, s > 0$;

(3) if $\{t_n\}$ and $\{s_n\}$ are sequences in $(0, +\infty)$ such that $\lim_{n\to+\infty} t_n = \lim_{n\to+\infty} s_n > 0$, then $\limsup_{n\to+\infty} \zeta(t_n, s_n) < 0$.

After this, several authors utilized a simulation function by modifying it in various spaces and proved results on a fixed point. Recently, Perveen & Imdad (2019) introduced an MA-simulation function and proved some fixed point theorem for a self map through α-admissibility and continuity of the self map. In this paper, we establish a new fixed point theorem for a self map using a new contractive condition via the MA-simulation function. The paper is organized as follows

Following the preliminaries discussions, we introduce a new contractive condition using the MA-simulation function.Then we study a fuzzy contractive mapping due to Gregori & Miñana (2014), Mihet (2010), Tirado (2012) and Wardowski (2013). Subsequently, we establish the existence of a unique fixed point of a self mapping in an M-complete fuzzy metric space and provide an illustrative example to demonstrate our result. Lastly, we apply our results to demonstrate the existence and uniqueness of the solution for the damped spring-mass system in the setting of a fuzzy metric space.

Now, let us recall the definition of a fuzzy metric space and other results given in George & Veeraman (1994).

DEFINITION 1. *(Schweizer & Sklar, 1983) A mapping* $* : [0,1] \times [0,1] \to [0,1]$ *is called a continuous triangular norm (t-norm for short) if* $*$ *is continuous and satisfies the following conditions:*

(i) $*$ *is commutative and associative, i.e.* $a * b = b * a$ *and* $a * (b * c) = (a * b) * c$, *for all* $a, b, c \in [0,1]$;

(ii) $1 * a = a$, *for all* $a \in [0,1]$;

(iii) $a * c \leq b * d$, *for* $a \leq b, c \leq d$, *for* $a, b, c, d \in [0,1]$.

The well-known examples of the t-norm are the minimum t-norm $*_m, a *_m b = min\{a, b\}$ written as $*_m$ and the product t-norm $*, a * b = ab$.

DEFINITION 2. *(George & Veeraman, 1994) A fuzzy metric space is an ordered triple* $(X, M, *)$ *such that* X *is a (nonempty) set,* $*$ *is a continuous t-norm and M is a fuzzy set on* $X \times X \times (0, +\infty)$ *satisfying the following conditions, for all* $x, y, z \in X$ *and* $t, s > 0$;

(GV1) $M(x, y, t) > 0$;

(GV2) $M(x, y, t) = 1$ *if and only if* $x = y$;

(GV3) $M(x, y, t) = M(y, x, t)$;

(GV4) $M(x, z, t + s) \geq M(x, y, t) * M(y, z, s)$;

(GV5) $M(x, y, .) : (0, +\infty) \to (0, 1]$ *is continuous.*

Note that in view of the condition (GV2) we have $M(x, x, t) = 1$, for all $x \in X$ and $t > 0$ and $M(x, y, t) < 1$, for all $x \neq y$ and $t > 0$.
The following notion was introduced by George & Veeraman (1994).

DEFINITION 3. *(George & Veeraman, 1994) A sequence* $\{x_n\}$ *in a fuzzy metric space* $(X, M, *)$ *is said to be M-Cauchy, or simply Cauchy, if for each* $\epsilon \in (0,1)$ *and each* $t > 0$ *there exists an* $n_0 \in N$, *such that* $M(x_n, x_m, t) > 1 - \epsilon$, *for all* $n, m \geq n_0$. *Equivalently,* $\{x_n\}$ *is Cauchy if* $\lim_{m,n \to +\infty} M(x_n, x_m, t) = 1$, *for all* $t > 0$.

LEMMA 1. *(Grabiec, 1988) Let* $(X, M, *)$ *be a fuzzy metric space. Then* $M(x, y, .)$ *is non-decreasing for all* $x, y \in X$.

THEOREM 1. *(George & Veeraman, 1994) Let $(X, M, *)$ be a fuzzy metric space and τ be the topology induced by the fuzzy metric. Then for a sequence $\{x_n\}$ in $X, \{x_n\} \to x$ if and only if $M(x_n, x, t) \to 1$ as $n \to \infty$.*

DEFINITION 4. *George & Veeraman (1994) $(X, M, *)$ (or simply X) is called M-complete if every M-Cauchy sequence in X is convergent.*

LEMMA 2. *(Saha et al., 2016) If $*$ is a continuous t-norm, and $\{\alpha_n\}, \{\beta_n\}, \{\gamma_n\}$ are sequences such that $\alpha_n \to \alpha$ and $\gamma_n \to \gamma$ as $n \to +\infty$ then*

$$\overline{\lim_{k\to+\infty}}(\alpha_k * \beta_k * \gamma_k) = \alpha * \overline{\lim_{k\to+\infty}}\beta_k * \gamma,$$

and

$$\underline{\lim}_{k\to+\infty}(\alpha_k * \beta_k * \gamma_k) = \alpha * \underline{\lim}_{k\to+\infty}\beta_k * \gamma.$$

LEMMA 3. *(Saha et al., 2016) Let $\{f(k,.) : (0,+\infty) \to (0,1]; k = 0, 1, 2, ..., \}$ be a sequence of functions such that $f(k,.)$ is continuous and monotone increasing for each $k \geq 0$. Then $\overline{\lim}_{k\to+\infty} f(k,t)$ is a left continuous function in t and $\underline{\lim}_{k\to+\infty} f(k,t)$ is a right continuous function in t.*

DEFINITION 5. *(Perveen & Imdad, 2019) Let $(X, M, *)$ be a fuzzy metric space. A mapping $S : X \to X$ is said to be α-admissible if there exists a function $\alpha : X \times X \times (0,+\infty) \to [0,+\infty)$ such that for all $t > 0$*

$$z, y \in X, \alpha(z, y, t) \geq 1 \qquad \textit{implies} \qquad \alpha(Sz, Sy, t) \geq 1.$$

MA-Simulation function

In Perveen & Imdad (2019), the authors have defined the following MA-simulation function in a fuzzy metric space:
A mapping $\xi : (0,1] \times (0,1] \to \Re$ is said to be an MA-simulation function if it satisfies the following conditions:

(ξ_1) $\xi(t,s) < \frac{1}{t} - \frac{1}{s}$, for all $t, s \in (0,1)$;

(ξ_2) if $\{t_n\}, \{s_n\}$ are a sequence in $(0,1]$ such that $\lim_{n\to+\infty} t_n = \lim_{n\to+\infty} s_n = l \in (0,1)$, and $t_n < s_n$, for all $n \in N$, then $\limsup_{n\to+\infty} \xi(t_n, s_n) < 0$.

The set of all MA-simulation functions is denoted by Ξ_{MA}.

DEFINITION 6. *(Perveen & Imdad, 2019) Let $(X, M, *)$ be a fuzzy metric space and $\xi \in \Xi_{MA}$. A mapping $S : X \to X$ is said to be α-admissible*

Ξ_{MA}-contraction if there exists a function $\xi \in \Xi_{MA}$ such that for all $t > 0$, it satisfies the following:

$$z, y \in X, \alpha(z, y, t) \geq 1 \qquad \textit{implies} \qquad \xi(M(z, y, t), M(Sz, Sy, t)) \geq 0.$$

Now we define a new contractive condition employing an MA-simulation function as follows:

DEFINITION 7. *Let $(X, M, *)$ be a fuzzy metric space and $\xi \in \Xi_{MA}$. A mapping $S : X \to X$ is said to be Ξ_{MA} contractive if for some $\xi \in \Xi_{MA}$ and for all $t > 0$, it satisfies the following condition:*

$$x, y \in X, x \neq y, \xi(M(x, y, t), M(Sx, Sy, t)) \geq 0. \tag{1}$$

Gregori & Sapena (2002) defined the fuzzy contractive mappings as follows:
Let $(X, M, *)$ be a fuzzy metric space. A mapping $T : X \to X$ is called a fuzzy contractive mapping if there exists $k \in (0, 1)$ such that
$\frac{1}{M(Tx,Ty,t)} - 1 \leq k\left(\frac{1}{M(x,y,t)} - 1\right)$, for all $x, y \in X$.

REMARK 1. The fuzzy contractive mapping defined by Gregori & Sapena (2002), is Ξ_{MA}-contractive if we take $\xi \in \Xi_{MA}$ to be $\xi(t, s) = k(\frac{1}{t} - 1) - (\frac{1}{s} - 1)$, for all $s, t \in (0, 1)$, and $k \in (0, 1)$ in (1).

Tirado (2012) defined the following contraction.
Let $(X, M, *)$ be a fuzzy metric space. A mapping $T : X \to X$ is a Tirado contraction if there exists $k \in (0, 1)$ such that
$1 - M(Tx, Ty, t) \leq k(1 - M(x, y, t))$, for all $x, y \in X$.

REMARK 2. Every Tirado contraction is Ξ_{MA}-contractive if we take $\xi \in \Xi_{MA}$ to be $\xi(t, s) = k(1 - t) + (s - 1)$, for all $t, s \in (0, 1)$, in (1).

Mihet (2010) defined the class Ψ of mappings as follows:
Let $\psi : (0, 1] \to (0, 1]$ such that ψ is continuous, non-decreasing and $\psi(t) > t$, for all $t \in (0, 1)$.
Let $\psi \in \Psi$. A mapping $T : X \to X$ is called a fuzzy ψ-contractive mapping

if

$$M(x,y,t) > 0 \qquad \text{implies} \qquad M(Tx,Ty,t) \geq \psi(M(x,y,t)),$$

for all $x, y \in X$ and $t > 0$.

REMARK 3. Every fuzzy ψ-contractive mapping is Ξ_{MA}-contractive, if we take $\xi \in \Xi_{MA}$ to be $\xi(t,s) = s - \psi(t)$, for all $t, s \in (0,1)$.

Wardowski (2013) defined the following class *H* of mappings as follows: Let *H* be the family of the mappings $\eta : (0,1] \to [0,+\infty)$ satisfying the following conditions:
(H-1) η transforms $(0,1]$ onto $[0,+\infty)$;
(H-2) η is strictly decreasing.
A mapping $T : X \to X$ is called fuzzy H-contractive with respect to $\eta \in H$ if there exists $k \in (0,1)$ satisfying the following condition:

$$\eta(M(Tx,Ty,t)) \leq k\eta(M(x,y,t)),$$

for all $x, y \in X$ and $t > 0$.

REMARK 4. In view of the remark in Gregori & Miñana (2014), every fuzzy H-contractive mapping with respect to $\eta \in H$ is Ξ_{MA}-contractive with respect to the function $\xi \in \Xi_{MA}$, if we define $\xi(t,s) = k(\eta(t)) - \eta(s))$, for all $t, s \in (0,1)$ in equation (1).

The following result has been established in Perveen & Imdad (2019)
Theorem 3.1 (Perveen & Imdad, 2019) Let $(X, M, *)$ be a complete fuzzy metric space and $S : X \to X$ is an α-admissible Ξ_{MA}-contraction with respect to ξ. Assume that the following conditions are satisfied

$$z, y \in X, \alpha(z,y,t) \geq 1 \qquad \text{implies} \qquad \xi(M(z,y,t), M(Sz,Sy,t) \geq 0,$$

(a) there exists $z_0 \in X$ such that $\alpha(z_0, Sz_0, t) \geq 1$;

(b) S is triangular α-admissible;

(c) S is continuous
or
if $\{z_n\}$ is a sequence in X such that $\alpha(z_n, z_{n+1}, t) \geq 1$, for all $n \in N, t > 0$ and $\{z_n\} \to z$, for some $z \in X$, there exists a sub sequence $\{z_{n_k}\}$ of $\{z_n\}$ such that $\alpha(z_{n_k}, z, t) \geq 1$, for all $k \in N$ and $t > 0$.

Then, S has a fixed point in X.

Main results

Our first new result is the next one.

Theorem 1 Let S be a self map on a complete fuzzy metric space $(X, M, *)$. For some $\xi \in \Xi_{MA}$ the map S is Ξ_{MA} contractive. Then, S has a unique fixed point in X.

Proof. First we prove the uniqueness of the fixed point. Suppose u and v be two fixed points of S. Then $u = Su$ and $v = Sv$. We show that $u = v$. Suppose, on the contrary, that $u \neq v$, then $Su \neq Sv$. Now

$$\begin{aligned} 0 &\leq \xi(M(u,v,t), M(Su,Sv,t)), \text{(using equation (1))} \\ &= \xi(M(u,v,t), M(u,v,t)), \\ &< \frac{1}{M(u,v,t)} - \frac{1}{M(u,v,t)}, \text{(using } \xi_1 \text{)} \\ &= 0. \end{aligned}$$

which is not possible. So, $u = v$. Thus, if the map S has a fixed point, then it is unique.

Now we prove the existence of the fixed point of the self map S. For $x_0 \in X$ define the sequence $\{x_n\}$ by $Sx_n = x_{n+1}$, for $n = 0, 1, 2, ...$

Now we consider the different cases for the sequence $\{x_n\}$.

CASE I Suppose $x_n = x_{n+1}$, for some $n \in N$. Now $x_n = x_{n+1} = Sx_n$ and so we have $Sx_n = x_n$. Thus, x_n is a fixed point of the map S in this case. So we can assume the consecutive terms of the sequence $\{x_n\}$ are distinct.

Again, to see the existence of the fixed point in the other case, we first show that all the terms of the sequence $\{x_n\}$ are distinct.

CASE II Suppose $x_n = x_m$, for some $m > n$, and consecutive terms of the sequence $\{x_n\}$ are distinct. Then $Sx_n = Sx_m$, i.e. , $x_{n+1} = x_{m+1}$. Also

$$\begin{aligned} 0 &\leq \xi(M(x_n, x_{n+1}, t), M(Sx_n, Sx_{n+1}, t), \text{ (using equation (1))} \\ &= \xi(M(x_n, x_{n+1}, t), M(x_{n+1}, x_{n+2}, t)) \end{aligned}$$

$$< \frac{1}{M(x_n, x_{n+1}, t)} - \frac{1}{M(x_{n+1}, x_{n+2}, t)}, \text{ (using } \xi_1. \text{)}$$

i. e.

$$M(x_n, x_{n+1}, t) < M(x_{n+1}, x_{n+2}, t), \text{ for all t} > 0. \tag{2}$$

Repeating the above procedure m-times, we get

$$M(x_n, x_{n+1}, t) < M(x_{n+1}, x_{n+2}, t) < \cdots < M(x_m, x_{m+1}, t) = M(x_n, x_{n+1}, t),$$

which yield $M(x_n, x_{n+1}, t) < M(x_n, x_{n+1}, t)$ which is not true. So, this case does not arise and we conclude that $x_n \neq x_m$ for distinct $n, m \in N$. Thus, the elements of the sequence $\{x_n\}$ are distinct.

STEP 1 In this step, we prove that $\lim_{n\to+\infty} M(x_n, x_{n+1}, t) = 1$, for all $t > 0$. From equation (2), we have

$$M(x_n, x_{n+1}, t) < M(x_{n+1}, x_{n+2}, t), \text{ for all t} > 0.$$

Thus, $\{M(x_n, x_{n+1}, t)\}$, for each $t > 0$, is a strictly increasing sequence which is bounded above by 1. Let $\lim_{n\to+\infty} M(x_n, x_{n+1}, t) = a(t)$, for $t > 0$. We claim that $a(t) = 1$.

Suppose, if possible, on the contrary, that $a(s) < 1$, for some $s > 0$.

Taking $s_n = M(x_{n+1}, x_{n+2}, s)$ and $t_n = M(x_n, x_{n+1}, s)$ then again from equation (2), $t_n < s_n$, for all n and using the condition (ξ_2) we have

$$0 \leq \limsup_{n\to+\infty} \xi(M(x_n, x_{n+1}, s), M(x_{n+1}, x_{n+2}, s)) < 0,$$

which is not possible and we arrive at a contradiction. Hence $a(s) = 1$ i. e.

$$\lim_{n\to+\infty} M(x_n, x_{n+1}, t) = 1, \text{ for all t} > 0. \tag{3}$$

Now we prove that the sequence $\{x_n\}$ is M-Cauchy. Suppose, if possible, on the contrary, that it is not true: then there exist $\eta \in (0, 1), t_0 > 0$ and the sequences $\{p(n)\}, \{q(n)\}$ ($q(n)$) being the smallest integer corresponding to $p(n)$.

$$n < p(n) < q(n), M(x_{p(n)}, x_{q(n)}, t_0) \leq 1 - \eta, M(x_{p(n)}, x_{q(n)-1}, t_0) > 1 - \eta. \tag{4}$$

STEP 2 In this step, we show that $\lim_{n\to+\infty} M(x_{p(n)-1}, x_{q(n)-1}, t_0) = 1 - \eta$. Now for all $n \geq 1, 0 < \lambda < t_0/2$, we obtain,

$$\begin{aligned} 1 - \eta &\geq M(x_{p(n)}, x_{q(n)}, t_0), \quad \text{(using(4))} \\ &\geq M(x_{p(n)}, x_{p(n)-1}, \lambda) * M(x_{p(n)-1}, x_{q(n)-1}, t_0 - 2\lambda) * M(x_{q(n)-1}, x_{q(n)}, \lambda). \end{aligned}$$

Let

$$h_1(t) = \overline{\lim}_{n\to\infty} M(x_{p(n)-1}, x_{q(n)-1}, t), t > 0.$$

Taking the limit supremum on both sides of the above inequality and using the properties of M and $*$, and by Lemma 2, we obtain

$$\begin{aligned} 1-\eta &\geq 1 * \overline{\lim}_{n\to+\infty} M(x_{p(n)-1}, x_{q(n)-1}, t_0 - 2\lambda) * 1 \qquad \text{(using(3))} \\ &= h_1(t_0 - 2\lambda). \end{aligned} \tag{5}$$

Since M is bounded with the range in $(0, 1]$ continuous and non-decreasing in the third variable t, it follows from Lemma 3, that h_1 is continuous from the left. Therefore, for $\lambda \to 0$, we obtain

$$h_1(t_0) = \overline{\lim}_{n\to+\infty} M(x_{p(n)-1}, x_{q(n)-1}, t_0) \leq 1 - \eta. \tag{6}$$

Let

$$h_2(t) = \underline{\lim}_{n\to+\infty} M(x_{p(n)-1}, x_{q(n)-1}, t), t > 0.$$

Again, for all $n \geq 1, t_0 > 0$

$$\begin{aligned} M(x_{p(n)-1}, x_{q(n)-1}, \lambda + t_0) &\geq M(x_{p(n)-1}, x_{p(n)}, \lambda) * M(x_{p(n)}, x_{q(n)-1}, t_0) \\ &\geq M(x_{p(n)}, x_{p(n)-1}, \lambda) * (1-\eta) \quad \text{(using(4))} \end{aligned}$$

Taking the limit infimum as $n \to +\infty$ in above inequality, we obtain

$$\begin{aligned} h_2(\lambda + t_0) &= \underline{\lim}_{n\to+\infty} M(x_{p(n)-1}, x_{q(n)-1}, \lambda + t_0), \\ &\geq \underline{\lim}_{n\to+\infty} M(x_{p(n)}, x_{p(n)-1}, \lambda) * (1-\eta), \\ &= 1 * (1-\eta), \qquad \text{(using(3))} \\ &= (1-\eta) \end{aligned}$$

Since M is continuous and bounded with the range in $(0, 1]$ and non-decreasing in the third variable t, it follows from Lemma 3, that h_2 is continuous from the right. Therefore, for $\lambda \to 0$, we obtain

$$\underline{\lim}_{n\to+\infty} M(x_{p(n)-1}, x_{q(n)-1}, t_0) \geq 1 - \eta. \tag{7}$$

Combining inequalities (6) and (7), we get

$$\lim_{n\to+\infty} M(x_{p(n)-1}, x_{q(n)-1}, t_0) = 1 - \eta. \tag{8}$$

STEP 3 In this step, we show that $\lim_{n\to+\infty} M(x_{p(n)}, x_{q(n)}, t_0) = 1-\eta$. From equation (6), we have

$$\overline{\lim}_{n\to+\infty} M(x_{p(n)}, x_{q(n)}, t_0) \leq 1-\eta. \tag{9}$$

Also, for all $n \geq 1$ and $t_0 > 0$, we have

$$M(x_{p(n)}, x_{q(n)}, t_0+2\lambda) \geq M(x_{p(n)}, x_{p(n)-1}, \lambda) * M(x_{p(n)-1}, x_{q(n)-1}, t_0) * M(x_{q(n)-1}, x_{q(n)}, \lambda)$$

Taking the limit infimum as $n \to +\infty$ in the above inequality, using(8) and the properties of M and $*$ and by Lemma 3, we obtain

$$\begin{aligned} \underline{\lim}_{n\to+\infty} M(x_{p(n)}, x_{q(n)}, t_0+2\lambda) &\geq 1 * \underline{\lim}_{n\to+\infty} M(x_{p(n)-1}, x_{q(n)-1}, t_0) * 1 \\ &= 1-\eta, \end{aligned} \tag{10}$$

Since M is bounded with the range in $(0,1]$ continuous and non-decreasing in the third variable t, it follows by Lemma 3 that $\underline{\lim}_{n\to+\infty} M(x_{p(n)}, x_{q(n)}, t_0)$ is a continuous function of t from the right. Therefore, for $\lambda \to 0$, we obtain

$$\underline{\lim}_{n\to+\infty} M(x_{p(n)}, x_{q(n)}, t_0) \geq 1-\eta. \tag{11}$$

Combining inequalities (9) and (11), we get

$$\lim_{n\to+\infty} M(x_{p(n)}, x_{q(n)}, t_0) = 1-\eta. \tag{12}$$

STEP 4 In this step, we show that the sequence $\{x_n\}$ is an M-Cauchy sequence.
Taking $x = x_{p(n)-1}$ and $y = x_{q(n)-1}$ in equation (1), we have

$$\begin{aligned} 0 &\leq \xi(M(x_{p(n)-1}, x_{q(n)-1}, t), M(Sx_{p(n)-1}, Sx_{q(n)-1}, t)) \\ &= \xi(M(x_{p(n)-1}, x_{q(n)-1}, t), M(x_{p(n)}, x_{q(n)}, t)) \\ &< \frac{1}{M(x_{p(n)-1}, x_{q(n)-1}, t)} - \frac{1}{M(x_{p(n)}, x_{q(n)}, t)}, \end{aligned}$$

i.e.

$$M(x_{p(n)-1}, x_{q(n)-1}, t) < M(x_{p(n)}, x_{q(n)}, t), \text{ for all t} > 0.$$

Taking $t_n = M(x_{p(n)-1}, x_{q(n)-1}, t)$ and $s_n = M(x_{p(n)}, x_{q(n)}, t)$ then $t_n < s_n$, for all n and using equations (8) and (12), we have

$$\lim_{n\to+\infty} t_n = \lim_{n\to+\infty} s_n = 1 - \eta.$$

Using (ξ_2) we have

$$0 \leq \limsup_{n\to+\infty} \xi(M(x_{p(n)-1}, x_{q(n)-1}, t), M(x_{p(n)}, x_{q(n)}, t)) < 0.$$

which is not possible and we arrive at a contradiction. So, the sequence $\{x_n\}$ is an M-Cauchy sequence in X which is M-complete. Therefore, there exists $u \in X$ such that

$$\{x_n\} \to u. \tag{13}$$

i. e.

$$\{Sx_n\} \to u. \tag{14}$$

STEP 5 Now we show that $Su = u$. Suppose, on the contrary, that $Su \neq u$. Then there exists a positive integer n_0 such that $Su \neq x_n$, for all $n \geq n_0$ (for otherwise we get $Su = u$). Taking $x = u$ and $y = x_n$ in equation (1) we get

$$\begin{aligned} 0 &\leq \xi(M(u, x_n, t), M(Su, Sx_n, t)) \\ &< \frac{1}{M(u, x_n, t)} - \frac{1}{M(Su, Sx_n, t)} \end{aligned}$$

i. e.

$$M(u, x_n, t) < M(Su, Sx_n, t), \text{ for all t} > 0.$$

As M is continuous and for $n \to +\infty$ and using equations (13) and (14), we obtain

$$M(u, u, t) \leq M(Su, u, t), \text{ for all t} > 0.$$

So, $M(Su, u, t) \geq 1$, and we arrive at a contradiction as $Su \neq u$. Thus $Su = u$. □

We illustrate by the following example that the necessity of the α-admissibility and the continuity of the self map S is not all required for the existence of the unique fixed point of the map.

Example (of Theorem 1): Let $X = [-1, 1]$, and define a fuzzy set M on $X \times X \times (0, +\infty)$ by:

$$M(x, y, t) = \begin{cases} 1; & \text{if } x = y, \\ \min\{1 - \frac{|x|}{2}, 1 - \frac{|y|}{2}\}, & \text{if } x \neq y. \end{cases} \text{, for all x, y} \in X,\ t \in (0, +\infty).$$

Taking $\xi(t, s) = k(\frac{1}{s} - 1) - (\frac{1}{t} - 1)$, for all t, s $\in (0, 1]$ and $a * b = \min\{a, b\}$ then $(X, M, *)$ is an M-complete fuzzy metric space.
Define the mapping $\alpha : X \times X \times (0, +\infty)$ by

$$\alpha(x, y, t) = \begin{cases} 1; & \text{if } x, y \in [0, 1/2], \\ 0, & \text{otherwise.} \end{cases} \text{, for all x, y } \in X,\ t \in (0, +\infty).$$

Define the self-map S on X by

$$S(x) = \begin{cases} 0; & \text{if } -1 < x < 0, \\ 1, & \text{if } 0 \leq x \leq 1. \end{cases} \text{, for all x, y} \in X,\ t \in (0, +\infty).$$

Thus, all the conditions of primary result theorem are satisfied and $x = 1$ is the unique fixed point of the map S.
Note that the map S is neither continuous nor α-admissible as
for $x = 0$ and $y = 1/2$ we have $S(0) = 0, S(1/2) = 0$ and $\alpha(x, y, t) = \alpha(0, 1/2, t) = 1$ but $\alpha(Sx, Sy, t) = \alpha(S(0), S(1/2), t) = \alpha(1, 1, t) = 0 < 1$.

Application (to the damped spring-mass system)

In this section, by applying our theorem, we prove the existence of the unique solution for the spring mass system in an automobile suspension system. Let m be the mass of the spring and F be the external force acting on it, then the critical damped motion of this system subjected to the external force F is governed by the following initial value problem:

$$m\frac{d^2v}{dt^2} + \wp\frac{dv}{dt} - mF(r, v(r)) = 0, \tag{15}$$

$v(0) = 0, v'(0) = 0,$
where m is the mass of the spring, $\wp(> 0)$ is the damping constant and F is the external force acting on it given by $F : [0, J] \times R^+ \to R$ is continuous.

In terms of in integral equation, the above problem is

$$v(r) = \int_0^J R(r,z)F(z,v(z))dz, \quad r \in [0,J] \tag{16}$$

where the respective Green's function $R(r,z)$ with $\mu = \frac{\wp}{m}$ is given by

$$R(r,z) = \begin{cases} \frac{1-e^{\mu(r-z)}}{\mu}, & \text{if } 0 \le z \le r \le J; \\ 0, & \text{if } 0 \le r \le z \le J \end{cases} \tag{17}$$

Theorem 2 Consider equation (16) with $R(r,z)$ given by (17). Suppose

(2.11) $\beta \in (C[0,J],R)$ is a lower solution of problem equation (16), i. e.

$$\beta(r) \le \int_0^J R(r,z)F(z,v(z))dz, \tag{18}$$

(2.12) $F(z,.)$ is an increasing function on $(0,1]$ for every $z \in [0,J]$ and choose μ suitably such that
$\inf_{0\le r\le J} R(r,z) > 0$.

$$0 \le \sup_{0\le r\le J} (\delta(\mu,r))^2 < 1/2. \tag{19}$$

$$R(r,z)F(z,1) \le J^{-1},$$

where $\delta(\mu,r) = \frac{(1+r\mu-e^{r\mu})}{\mu^2}$

(2.13) For each $r \in [0,J]$ and $u,v \in X$, we have

$$|F(r,u(r)) - F(r,v(r))| < \lambda|u(r)-v(r)|, \ \ \lambda \in (0,1). \tag{20}$$

Then equation (16) has a solution in $(C[0,1],R)$ which is a unique solution for initial value problem (15).

Proof. Taking $X = (C[0,J],R)$. Then X is a complete metric space with a sup-metric

$$d(z,y) = \sup_{t\in\Omega} |z(t) - y(t)|$$

and the space $(X,M,*)$ is a complete metric space if we take $M(z,y,t) = \frac{t}{t+d(z,y)}$, for all $z,y \in X$ and $t > 0$ and taking $p * q = pq$, for all p, q $\in (0,1]$.

Define $S : X \to X$ by

$$Sv(r) = \int_0^J R(r,z)F(z,v(z))dz, \text{ for all v} \in X. \tag{21}$$

Then v is a solution of (16), if v is a fixed point of S.
For $u, v \in X$ we have

$$\begin{aligned}
|Su(r) - Sv(r)| &= |\int_0^J R(r,z)F(z,u(z))dz - \int_0^J R(r,z)F(z,v(z))dz| \\
&\leq \int_0^J R(r,z)|F(z,u(z)) - F(z,v(z))|dz \\
&\leq \int_0^J R(r,z) \sup_{0\leq r\leq J} |F(z,u(z)) - F(z,v(z))|dz \\
&= \sup_{0\leq r\leq J} |F(z,u(z)) - F(z,v(z))| \int_0^J R(r,z)dz \\
&\leq \lambda \sup_{0\leq r\leq J} |u(z) - v(z)| \int_0^J R(r,z)dz \\
&\leq \lambda \sup_{0\leq r\leq J} |u(z) - v(z)| \frac{1 + r\mu - e^{ru}}{\mu^2}
\end{aligned}$$

i. e.

$$|Su(r) - Sv(r)| \leq \lambda \sup_{0\leq r\leq J} |u(z) - v(z)| \frac{1 + r\mu - e^{ru}}{\mu^2}.$$

Taking the supremum, we get

$$\sup_{0\leq r\leq J} |Su(r) - Sv(r)| \leq \lambda \sup_{0\leq r\leq J} |u(z) - v(z)| \sup_{0\leq r\leq J} (\delta(\mu,r))^2.$$

$$\begin{aligned}
d(Su, Sv) &\leq \lambda \sup_{0\leq r\leq J} (\delta(\mu,r))^2 d(u,v) \\
&\leq \frac{\lambda}{2} d(u,v).
\end{aligned}$$

Also

$$\begin{aligned}
\frac{1}{M(Su, Sv, t)} - 1 &= \frac{d(Su, Sv)}{t} \\
&\leq \frac{\lambda d(u,v)}{2t}
\end{aligned}$$

Jain, Shobha. et al., Solving a damped spring-mass system via the MA-simulation functionn, pp.450–468

$$= \frac{\lambda}{2}\left(\frac{1}{M(u,v,t)} - 1\right), \quad \text{for all u, } v \in X, t > 0.$$

Taking $\xi(t,s) = \frac{\lambda}{2}(\frac{1}{s} - 1) - (\frac{1}{t} - 1)$, for all t, s $\in (0,1]$. All the conditions of the primary result theorem are met. As a result S has a unique fixed point in X.

□

References

George, A. & Veeraman, P. 1994. On some results in fuzzy metric spaces. *Fuzzy Sets and Systems*, 64(3), pp.395-399. Available at: https://doi.org/10.1016/0165-0114(94)90162-7.

Grabiec, M. 1988. Fixed points in fuzzy meric spaces. *Fuzzy Sets and Systems*, 27(3), pp.385-389. Available at: https://doi.org/10.1016/0165-0114(88)90064-4.

Gregori, V. & Miñana, J.-J. 2014. Some remarks on fuzzy contractive mappings. *Fuzzy Sets and Systems*, 251, pp.101-103. Available at: https://doi.org/10.1016/j.fss.2014.01.002.

Gregori, V. & Sapena, A. 2002. On fixed-point theorems in fuzzy metric spaces. *Fuzzy Sets and Systems*, 125(2), pp.245-252. Available at: https://doi.org/10.1016/S0165-0114(00)00088-9.

Jain, S., Jain, S & Jain, L.B. 2009. Compatible mappings of type (β) and weak compatibility in fuzzy metric spaces. *Mathematica Bohemica*, 134(2), pp.151-164. Available at: https://doi.org/10.21136/MB.2009.140650.

Khojasteh, F., Shukla, S. & Radenović, S. 2015. A new approach to the study of fixed point theory for simulation functions. *Filomat*, 29(6), pp.1189-1194. Available at: https://doi.org/10.2298/FIL1506189K.

Kramosil, I. & Michálek, J. 1975. Fuzzy metrics and statistical metric spaces. *Kybernetica*, 11(5), pp.336-344 [online]. Available at: http://dml.cz/dmlcz/125556 [Accessed: 02 September 2024].

Mihet, D. 2008. Fuzzy ψ-contractive mappings in non-Archimedean fuzzy metric spaces. *Fuzzy Sets and Systems*, 159(6), pp.739-744. Available at: https://doi.org/10.1016/j.fss.2007.07.006.

Mihet, D. 2010. A class of contractions in fuzzy metric spaces. *Fuzzy Sets and Systems*, 161(8), pp.1131-1137. Available at: https://doi.org/10.1016/j.fss.2009.09.018.

Perveen, A. & Imdad, M. 2019. Proving new fixed point results in fuzzy metric spaces employing simulation function. *Journal of Intelligent and Fuzzy Systems*, 36(6), pp.6493-6501. Available at: https://doi.org/10.3233/JIFS-182873.

Saha, P., Choudhury, B.S. & Das, P. 2016. Weak Coupled Coincidence Point Results Having a Partially Ordering in Fuzzy Metric Spaces. *Fuzzy Information and Engineering*, 8(2), pp.199-216. Available at: https://doi.org/10.1016/j.fiae.2016.06.005.

Schweizer, B. & Sklar, A. 1983. *Probabilistic Metric Spaces*. Mineola, New York: Dover Publications. Inc. ISBN: 0-486-44515-3.

Tirado, P. 2012. Contraction mappings in fuzzy quasi-metric spaces and [0, 1]-fuzzy posets. *Fixed Point Theory*, 13(1), pp.273-283 pp.273-283 [online]. Available at: https://www.math.ubbcluj.ro/~nodeacj/vol_13(2012)__no1.php [Accessed: 02 September 2024].

Wardowski, D. 2013. Fuzzy contractive mappings and fixed points in fuzzy metric spaces. *Fuzzy Sets and Systems*, 222, pp.108-114. Available at: https://doi.org/10.1016/j.fss.2013.01.012.

Zadeh, L.A. 1965. Fuzzy Sets. *Information and Control*, 8(3), pp.338-353. Available at: https://doi.org/10.1016/S0019-9958(65)90241-X.

Resolución de un sistema resorte-masa amortiguado mediante la función de simulación MA

Shobha Jain[a], **autor de correspondencia**, *Stojan* N. Radenović[b], *Shishir* Jain[a]

[a] Shri Vaishnav Vidyapeeth Vishwavidyalaya,
Facultad de Matemáticas,
Indore, Madhya Pradesh, República de la India

[b] Universidad de Belgrado, Facultad de Ingeniería Mecánica,
Belgrado, República de Serbia

CAMPO: matemáticas
TIPO DE ARTÍCULO: artículo científico original

Resumen:

Introducción/objetivo: En un interesante artículo, Perveen & Imdad (2019) introdujeron la noción de una función de simulación MA y la utilizaron para demostrar la existencia de un punto fijo para una auto papeo mediante α-admisibilidad y la continuidad del auto mapeo en un espacio métrico difuso. El propósito de este trabajo es establecer un teorema de punto fijo único para una aplicación MA-contractiva mediante la relajación de la condición de continuidad y α-admisibilidad del mapa en un espacio métrico difuso. Como aplicación de nuestro resultado, estudiamos la existencia y unicidad de la solución para el sistema resorte-masa amortiguado. El artículo incluye un ejemplo que muestra la validez de nuestros resultados.

Métodos: Se utilizó el método de punto fijo con una función de simulación MA

Resultados: Se obtuvo un único punto fijo para una auto mapa en un espacio métrico difuso.

Conclusión: Se obtiene un punto fijo de los auto mapas sin la continuidad ni la α-admisibilidad del auto mapa mediante la función de simulación MA. Además, se obtiene la existencia y unicidad de la solución de un sistema resorte-masa amortiguado en el contexto de un espacio métrico difuso.

Palabras claves: espacio métrico difuso, secuencia M-Cauchy, puntos fijos, función de simulación MA.

Решение проблемы демпфирования системы масса-пружина с помощью тематического моделирования

Шоба Джайн[а], **корреспондент**, *Стоян* Н. Раденовичс[б], *Шишир* Джайн[а]

[а] Шри Вайшнав Видьяпитх Вишвавидьялайя,
Математический факультет,
Индаур, Мадхья-Прадеш, Республика Индия

[б] Белградский университет, машиностроительный факультет,
г. Белград, Республика Сербия

РУБРИКА ГРНТИ: 27.25.17 Метрическая теория функций,
27.39.15 Линейные пространства,
снабженные топологией,
порядком и другими структурами

ВИД СТАТЬИ: оригинальная научная статья

Резюме:

Введение/цель: В своей интереснейшей статье Perveen & Imdad (2019) ввели понятие функции математического моделирования, используя его для доказательства существования неподвижной точки при самоотображении через α-допустимость и непрерывность отображения в нечетком метрическом пространстве. Цель данной статьи − представить уникальную теорему о неподвижной точке для математического отображения, ослабив условие непрерывности и α-допустимости самоотображения в нечетком метрическом пространстве. В целях подтверждения результатов исследования были изучены существование и уникальность решения проблемы демпфи-

рования системы масса-пружина. В статье приведен пример, который доказывает достоверность результатов исследования.

Методы: В статье использован метод нподвижной точки с функцией МА-моделирования.

Результаты: Получена уникальная неподвижная точка для самоотображения в нечетком метрическом пространстве.

Выводы: Неподвижная точка самоотображения получена без учета непрерывности и α-допустимости самоотображения с помощью функции МА-моделирования. Помимо того, подвержено существование и уникальность решения проблемы демпфирования системы масса-пружина в условиях нечеткого метрического пространства.

Ключевые слова: нечеткое метрическое пространство, последовательность Коши, неподвижные точки, МА-имитационное моделирование.

Решавање пригушеног система опруга-маса помоћу МА симулационе функције

Шоба Џајн[а], **аутор за преписку**, *Стојан* Н. Раденовић[б], *Шишир* Џајн[а]

[а] Универзитет Шри Вешнав Видјапит, Математички факултет, Индор, Мадја Прадеш, Република Индија

[б] Универзитет у Београду, Машински факултет, Београд, Република Србија

ОБЛАСТ: математика
КАТЕГОРИЈА (ТИП) ЧЛАНКА: оригинални научни рад

Сажетак:

Увод/циљ: У свом занимљивом раду Perveen & Imdad (2019) увели су појам МА симулационе функције користећи га за доказивање постојања фиксне тачке за самопресликавање кроз α-прихватљивост и континуитет самопресликавања у расплинутим метричким просторима. Циљ овог рада јесте да установи теорему јединствене фиксне тачке за МА контрактивно пресликавање релаксацијом услова континуитета и α-прихватљивости мапе у расплинутом метричком простору. Ради примене добијених резултата, испитано је постојање и јединственост решења пригуше-

ног система опруга-маса. Наводи се и пример који показује валидност резултата.

Методе: Коришћена је метода фиксне тачке са MA симулационом функцијом.

Резултати: Добијена је јединствена фиксна тачка за самопресликавање у расплинутом метричком простору.

Закључак: Фиксна тачка самопресликавања добијена је без континуитета и α-прихватљивости самопресликавања путем MA симулационе функције. Утврђено је, такође, постојање и јединственост решења пригушеног система опруга-маса при постављању расплинутог метричког система.

Кључне речи: расплинути метрички простор, M-Кошијев низ, фиксне тачке, MA симулациона функција.

Paper received on: 04.09.2024.
Manuscript corrections submitted on: 26.03.2025.
Paper accepted for publishing on: 27.03.2025.

Research into the effect of ammunition belt stiffness on the operation of automatic firing systems using experimental methods

Bien V. Vo[a], *Phon* D. Nguyen[b],
Phu M. Nguyen[c], *Long* X. Vu[d]

[a] Le Quy Don Technical University, Faculty of Special Equipment, Hanoi, Socialist Republic of Vietnam,
e-mail: vovanbien@lqdtu.edu.vn,
ORCID iD: https://orcid.org/0000-0002-1364-2884

[b] Le Quy Don Technical University, Faculty of Special Equipment, Hanoi, Socialist Republic of Vietnam,
e-mail: phonnduy@gmail.com, **corresponding author**,
ORCID iD: https://orcid.org/0000-0002-1329-3653

[c] Le Quy Don Technical University, Faculty of Special Equipment, Hanoi, Socialist Republic of Vietnam,
e-mail: nguyenminhphu9793@gmail.com,
ORCID iD: https://orcid.org/0009-0000-8599-1445

[d] Tran Dai Nghia University, Ho Chi Minh City, Socialist Republic of Vietnam,
e-mail: vuxuanlong@gmail.com,
ORCID iD: https://orcid.org/0009-0005-3633-7902

https://doi.org/10.5937/vojtehg73-54574

FIELD: mathematics, mechanical engineering
ARTICLE TYPE: original scientific paper

Abstract:

Introduction/purpose: This article focuses on determining the dynamic characteristics of the automatic firing system through experimental methods. Additionally, the study mentions the impact of ammunition belt stiffness.

Methods: The research findings include the displacements of the basic part (bolt carrier) and the ammunition belt of automatic weapons during firing series. To measure and determine these parameters, a high-speed camera model FASTCAM SA1.1, specifically the 675K-C1 variant, was utilized. The elastic force between the belt links was determined using deformation stamps equipped with force-measuring sensors. To validate the reliability of the method, experiments were conducted on the PKMS machine gun.

Results: The results obtained show that, when using a tape with a stiffness of 42 [N/mm], the kinematic characteristics of the basic link such as recoil velocity and recoil time change significantly compared to using a tape which has a stiffness of 98 [N/mm]. In particular, the maximum recoil velocity of the base gun can be reduced by ~8% when firing a series of 6 bullets.

These results can be applied in calculations and designs to optimize the structure of the ammunition belt and the automatic firing system. Furthermore, these findings can aid in calculating the firing rate of the gun, thus facilitating the operation of automatic weapons.

Conclusion: The testing procedure developed in this study serves as a crucial theoretical foundation for evaluating and determining the dynamic characteristics of other automatic weapon systems.

Keywords: automatic firing system, ammunition belt, 7.62 mm PKMS machine gun.

Introduction

In the final years of the 20th century, numerous armies worldwide were engaged in large-scale conflicts, utilizing infantry weapons and various other arms with great intensity. The emphasis was on improving these weapons to minimize weight, ensure reliable operation, reduce recoil force impacting the gunner, enhance shooting stability, and enable quick maneuvering on the battlefield. To address these challenges, multiple solutions were implemented, with a specific focus on studying the dynamics and stability of automatic guns. A crucial aspect of weapon design involved researching the interplay between different structures to achieve optimal solutions. This knowledge can be applied to the process of exploiting and designing weapons and equipment, particularly compact firepower mounted on racks or mobile vehicles.

The effectiveness of a soldier in combat relies heavily on the reliable performance of guns and artillery. This includes factors like shooting accuracy, stability, and the ability to function effectively in harsh conditions (Fiser & Popelinsky, 2007; Van Hung et al, 2024; Wang & Jiang, 2008). One of the causes that can impact these factors is the movement of the ammunition belt during firing. The bullets must be positioned accurately and quickly, with low energy consumption for reloading, while also avoiding vibrations and strong collisions with the gun. If these requirements are not met, the ammunition belt can disrupt the mechanisms of the automatic firing system, leading to wear and intense vibrations, resulting in inconsistent and unstable shots. Additionally, the working period and firing cycle of the automatic firing system can be affected. This can lead to issues like bullet choking or jamming, causing damage to the ammunition belt or automatic firing system, ultimately rendering the shot unable to be fired.

The movement of the ammunition feeding mechanism relies on the movement of the automatic firing system (Dingguo, 1996; Balla et al, 2015). Bullets in the ammunition belt move in different planes and at

varying speeds. The movement of a subsequent shot in a series of shots is influenced by both the operation of the ammunition belt pull mechanism operation and the initial speed of the ammunition belt, as well as the forces acting on it in space. To facilitate the study of ammunition belt dynamics, previous studies have made use of several assumptions to simplify calculations (Balla et al, 2011; Balla & Mach, 2007). Figure 1 illustrates some typical computational models of ribbon dynamics.

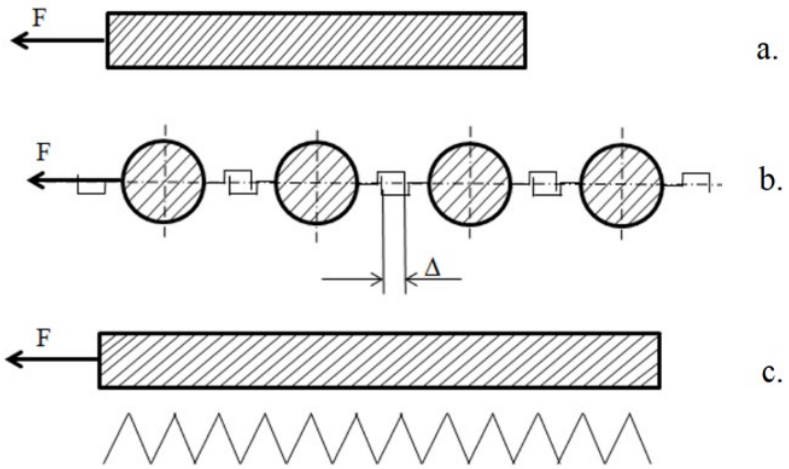

Figure 1 – Models for calculating ammunition belt movement

In the models presented in Figure 1, the ammunition belt is treated as a rigid bar affected by a pulling force, as seen in Figure 1a. In contrast, Figure 1b takes into account the bullets in the ammunition belt being connected by rigid joints and experiencing a horizontal pulling force. Finally, Figure 1c considers the ammunition belt as an elastic bar that is affected by a horizontal pulling force (Doan et al, 2023; Vo et al, 2021; Vitek, 2019). However, both theoretical calculations and testing have shown that these models are overly simplistic, resulting in significant errors and not accurately representing the movement of the ammunition belt in real-life scenarios.

Furthermore, the theory of multi-body mechanics has been utilized in various studies to examine the dynamics of ammunition belts. One notable example is the research conducted by Dingguo Zhang (Dung et al, 2023; Tien et al, 2022). In this study, the theory of many-body system dynamics was employed to construct a mathematical model for the dynamics of

aircraft gun ammunition belts. Additionally, Matlab software was utilized for numerical simulation. The study also mentions a dynamic model for the ammunition belt of the Gatling machine gun (Goldberg & Goldberg, 2019; Macko et al, 2021). This model describes the continuous reloading process and identifies specific factors that affect it. Another study (Bien et al, 2021a, 2021b) analyzed the mechanical properties of a vertical ammunition belt system using a spiral guide. To simulate the impact and contact between two points in the ammunition belt, a virtual spring was utilized. It is worth noting that the impact of belts is rarely addressed in recent studies on the dynamics of automatic firing systems, as seen in (Balla et al, 2010; Hung et al, 2024; Tien et al, 2021).

In general, previous studies on ammunition belt dynamics have been relatively simplistic and do not accurately reflect real-life ammunition belt movement. The interaction between the automatic firing system and the ammunition belt as well as the influence of various ammunition belt parameters on the loading process have not been thoroughly studied. Additionally, the impact of ammunition belt stiffness on the operation of automatic guns using gas extraction has not been addressed. The dynamic parameters of both the ammunition belt and the automatic firing system are affected by numerous random input factors, making it impossible for mathematical models to fully capture the complexity of the system. To improve the accuracy of studying ammunition belt dynamics, this study utilized experimental methods. These experiments not only provide valuable data on ammunition belt dynamics, but also play a crucial role in the calculation, design, manufacturing, and improvement of weapon models. The results of these tests allow for a comparison between theoretical calculations and actual data, providing a measure of the accuracy of the theoretical model.

Problem formulation

Theoretical basis

Many physical and mathematical models have been established to determine the dynamic parameters of automatic firing systems worldwide. Among them, the model presented in the document is relatively complete and clear (Macko et al, 2021).

In this article, the physical model of the automatic firing system is presented as shown in Figure 2 and Figure 3.

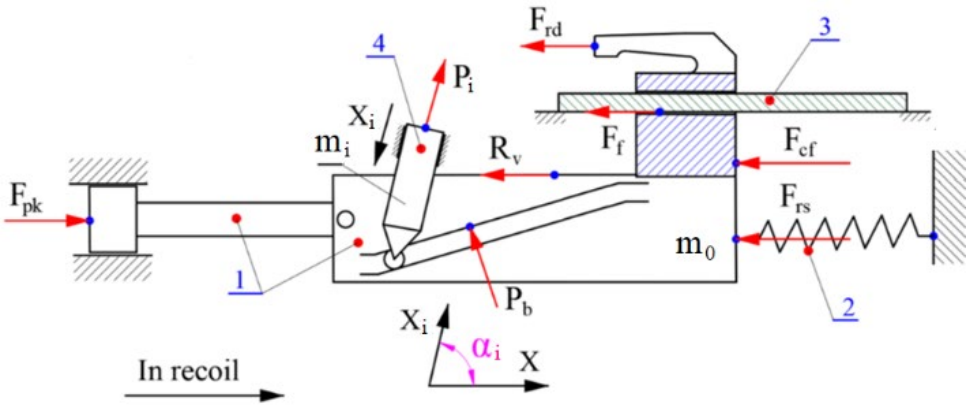

Figure 2 – Forces acting on the bolt carrier when reversing

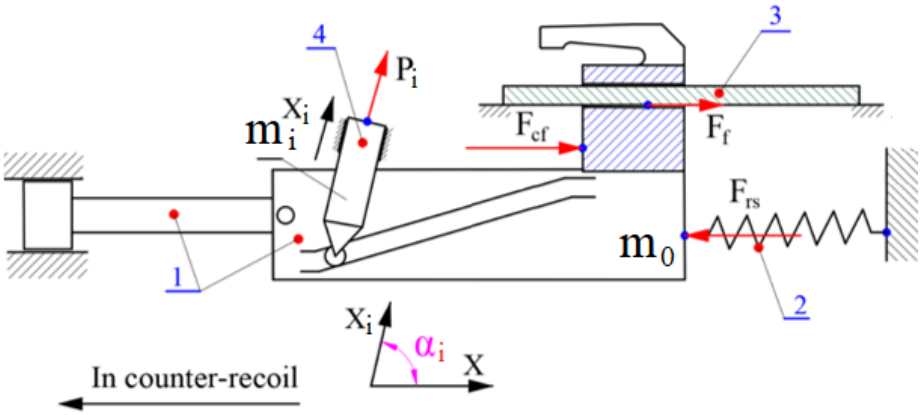

Figure 3 – Forces acting on the bolt carrier when pushed up

Symbols in Figure 2 and Figure 3: 1. the bolt carrier and the piston; 2. the return spring; 3. the guide rail on the weapon casing; 4. the *i*-th working mechanism; F_{pk} – the force of the combustion gas pressure acting on the piston; P_i – generalized force effects on the *i*-th working mechanism; x – displacement of the bolt carrier relative to the gun body; x_i – displacement of the *i*-th working mechanism relative to the gun body; F_{rs} – the force of the return spring; F_{cf} – collision force between the bolt carrier and the gun body; F_{rd} – the force to remove a cartridge from the cartridge belt; R_v – cartridge case extraction force; P_b – resistance of the cartridge belt; F_f – friction force between the bolt carrier and the gun body.

The link diagram between the bolt carrier and the feed lever is shown in Figure 4.

Vo, B.V. et al, Research into the effect of ammunition belt stiffness on the operation of automatic firing systems using experimental methods, pp.469-495

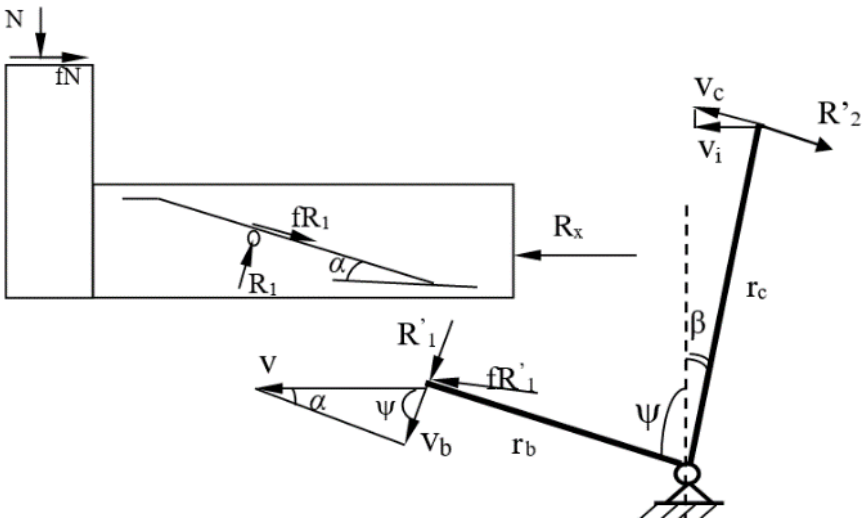

Figure 4 – Link diagram between the bolt carrier and the feed lever

The second type Lagrange equation is used to establish the mathematical model for this model.

$$\frac{d}{dt}\left(\frac{\partial T}{\partial \dot{q}_j}\right)-\frac{\partial T}{\partial q_j}+\frac{\partial \Pi}{\partial q_j}=Q_j \quad (j=1,2,...). \tag{1}$$

where: T – total kinetic energy of the whole system; Π – potential energy of the system; q_j – independent generalized coordinate; Q_j – generalized force; and j - number of degrees of freedom.

Set up an experimental model

Purpose, objects, and testing conditions

- Testing purpose

The following parameters are determined by experimental methods: elastic force, displacement law, and velocity of the ammunition belt link in the ammunition belt when firing series with belts of different stiffnesses. In addition, the law of displacement and velocity of the breech of the automatic firing system is also determined when firing in series with belts of different stiffnesseses. These parameters are the scientific basis for evaluating the impact of ammunition belt stiffnesses on the working process of the automatic firing system.

- Test subject

+ PKMS machine gun (Figure 5) and K53 ammunition at level 1, still packaged in a zinc box at a storage temperature of 20^0C;

Figure 5 – The PKMS Kalashnikov 7.62 mm machine gun

+ Two belt samples with different stiffnesses were used for testing (Figure 6). A prototype belt made in Russia and a belt made in Vietnam were softened to reduce stiffness. The stiffness of these tapes was determined experimentally by the Testometric M500-100AT tensile and compression testing system. This system is controlled by a computer, and WinTest™ Analysis software running on the Windows™ operating system was used. Some basic parameters of the Testometric M500-100AT tensile and compression testing machine system are shown in Table 1. The stiffness of the straps is determined based on the graph obtained in combination with Hooke's overturning test. After 5 measurements, the average stiffness of the belts is determined in Table 2.

Figure 6 – Belts used for the testing

Table 1 – Basic parameters of the Testometric M500-100AT tensile and compression testing system

	Machine capacity: 100kN
	Speed range: 0.001 to 500mm/min in steps of 0.001mm/min
	Crosshead travel (excluding grips): 1059mm
	Throat: 420mm

Table 2 – Belt stiffness for two different samples

Belt model	Made in Russia	Made in Vietnam
Medium stiffness [N/mm]	98	42

- Test conditions

+ The test was conducted at the Weapons Testing Center - Le Quy Don Technical University;

+ Ambient temperature 20^0C, humidity 50%, no wind;

+ Gun prices are considered fixed, not affected by external factors.

The simulation belt link is made to measure the elastic force

To determine the elastic force of the belts, the principle of deformation stamp force measurement was utilized (Wang & Jiang, 2008). The simulated belt link was made from a material similar to that of the ammunition belt of the PKMS machine gun, with manufacturing dimensions shown in Figure 7.

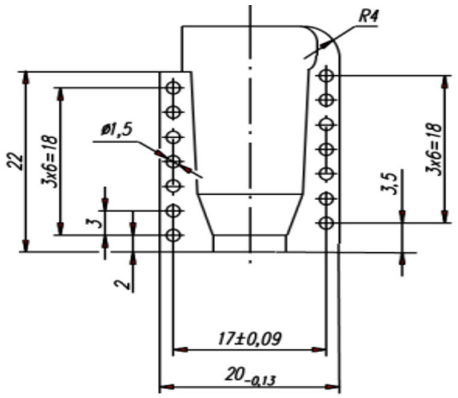

Figure 7 – Dimensions for manufacturing the simulated belt links

A sensor is attached to the simulated belt link and it is then installed into the ammunition belt to measure the elastic force between the belt links during a series of 7.62mm PKMS machine gun firings, as depicted in Figure 8.

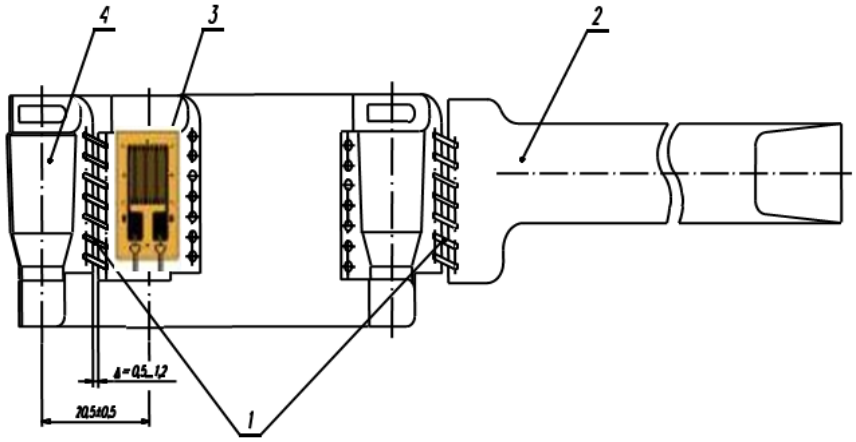

Figure 8 – Ammunition belt with the sensor attached:
1 - springs connecting the belt links; 2 - ammunition belt puller;
3 - simulated belt link with sensor stickers; 4 - belt link

The simulated belt link is installed on the belt, which is then calibrated to determine the conversion factor.

Figure 9 – Force measurement system calibration equipment

Vo, B.V. et al, Research into the effect of ammunition belt stiffness on the operation of automatic firing systems using experimental methods, pp.469-495

Measuring devices

- FASTCAM SA1.1 high-speed camera 675K - C1

The FASTCAM SA1.1 high-speed camera system is utilized for measuring the belt movement and the displacement of the basic part. This system consists of a Fastcam SA1.1 high-speed camera with the basic parameters listed in Table 3, a computer for installing PFV software and storing information, a lighting system, and a connection cable. The PFV software allows for control of the high-speed camera from a computer, while TEMA software is used for processing the records and collecting necessary data (Fiser, 2007; Bien et al, 2021a, 2021b).

Figure 10 – SA1.1 High-speed camera system

Table 3 – Some basic parameters of the high-speed camera SA1.1

Parameters	Values
Maximum write speed	675000 fps at 64x16 pixels
Data memory	8GB is equivalent to 5457 64x16 pixels photos or 5400 1024x1024 pixels photos
Sensor	12bit DAC

- DEWETRON 4000 dynamic signal analyzer

The sensor for measuring the elastic force of the belts is connected to the DEWE-4000 multi-function measuring system (Figure 11). DEWE-4000 is a multi-function measuring system that synchronizes mechanical, thermal, deformation, pressure, and force parameters.

Figure 11 – DEWE-4000 multifunction measuring system

Figure 12 – Modul DAQN – BRIDGE

To connect the belt elastic force measuring sensor to the DEWE-4000 multi-function measuring system, the DAQN - BRIDGE channel module available in the machine (Figure 12) is used. The main technical characteristics of these modules are as follows:

- They can be used synchronously with resistive stamp measuring sensors with a spherical structure, with sensor sensitivities of 0.1, 0.2, 0.5, 1.0, 2.0, and 5.0 mV/V.
- Selecting the working mode corresponding to the above sensitivities of the sensor and filter modes can be done manually or by software.
- The sensor's stable DC power supply is provided by Modules 2.5, 5, 10 and 15 volts.
- The measuring range of the spherical resistors is from 120 Ω to 10 k Ω.
- Output impedance is lower than 10 Ω.
- The signal is received from the measuring sensor through the 9-pin jack.

To ensure the safety of people and the measuring equipment, the distance from the measuring sensor to the location of the measuring equipment must be greater than 50 m. Therefore, a specialized shielded cable to prevent interference on the transmission line is used to transmit measurement signals from the sensor to the center.

The signal from the measurement sensor (about a few tens of mV) is transmitted from the sensor to the DAQN - BRIDGE module, where the measurement signal is amplified to a few volts and sent to the PCI-DAS1620/16 ADC CARD for processing and display. This signal is stored on Dasy Lab 11.0 software.

Test diagram

- Diagram determining the elastic force between the belt links

To determine the elastic force between the belt links, a test model is built as shown in Figure 13. The actual implementation image is presented in Figure 14.

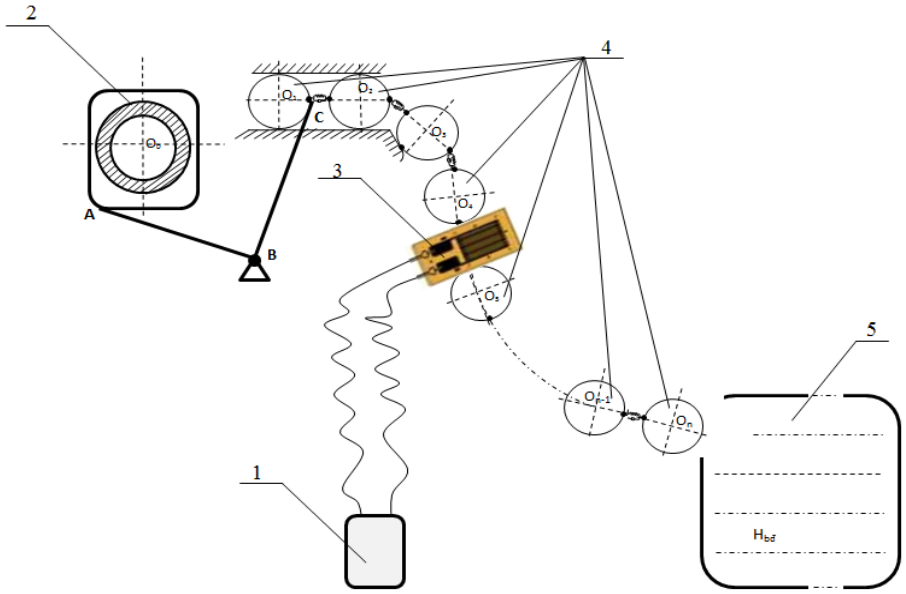

Figure 13 – Diagram of the testing system for measuring the elastic forces between the belt links:
1 - DEWETRON 4000 dynamic signal analyzer; 2 - PKMS machine gun;
3 - the simulated belt link is installed in the ammunition belt; 4 - bullets on the belt;
5 - ammunition belt box

Figure 14 – Simulated belt link installed on a machine gun ammunition belt

The operating principle is as follows: after replacing the simulated belt link with a real one, the belt puller will draw the belt inward to feed ammunition during firing. A sensor attached to the simulated belt link will record its deformation when stretched. The DEWETRON 4000 dynamic signal analysis system will then convert the tensor strain into force which is exported to the elastic force data file between the belt links.

- Diagram to determine the displacement of the ammunition belt

The test model to determine the displacement and velocity of the belt link is set up as a diagram in Figure 15.

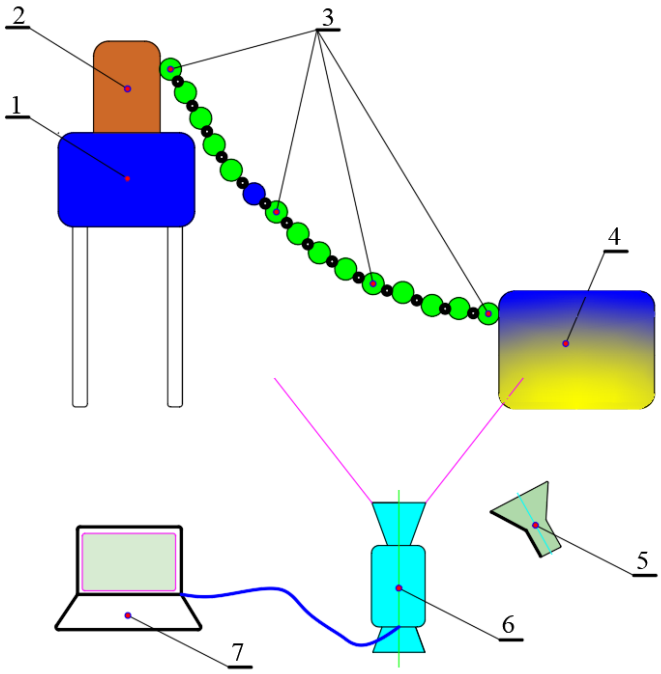

Figure 15 – Schematic diagram of the experimental model:
1 - specialized gun rack; 2 - PKMS machine gun;3 - ammunition;
4 - ammunition belt box; 5 – lighting system;
6 - FASTCAM SA1.1 high speed camera 675K - C1; 7 – computer

In this test, the high-speed camera FASTCAM SA1.1 model 675K - C1 was arranged in an appropriate position to record the movement of the bullet belt when firing multiple shots and then export the data file, displacement, and velocity of each bullet in the ammunition belt, see Figure 16.

Vo, B.V. et al, Research into the effect of ammunition belt stiffness on the operation of automatic firing systems using experimental methods, pp.469-495

Figure 16 – Experimental setup in the tunnel

- Displacement and velocity test diagram of the bolt carrier

The test model was set up to measure the displacement of the base part of the PKMS machine gun automatic firing system when firing in series, as shown in Figure 17.

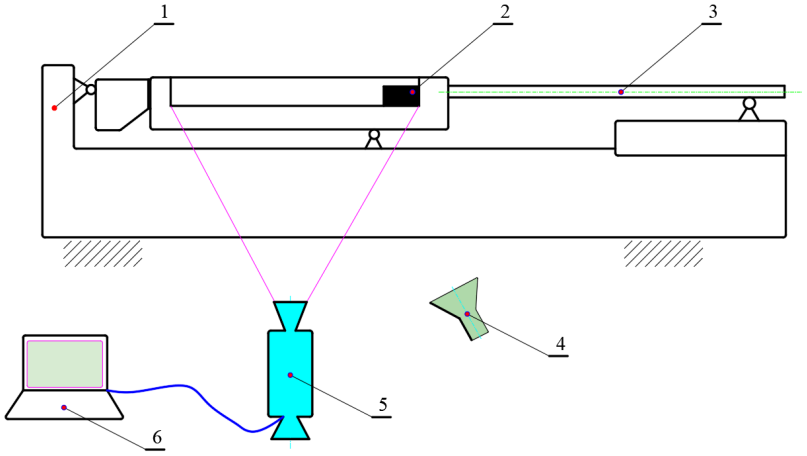

Figure 17 – Displacement measurement test diagram of the bolt carrier: 1 - specialized gun rack; 2 - bolt carrier; 3 - gun barrel; 4 - lighting system; 5 - FASTCAM SA1.1 high-speed camera 675K - C1; 6 – computer

To facilitate the process of observing the movement of the bolt carrier, the bolt box cover part is cut. The high-speed camera FASTCAM SA1.1 model 675K - C1 is used to record the bolt carrier movement when firing

in series. The recorded data is exported into graphs and images of the bolt carrier movement.

Figure 18, Figure 19, and Figure 20 show the images obtained by the high-speed camera FASTCAM SA1.1 model 675K - C1. The maximum recording speed was 675000 fps at 64x16 pixels of the base part at different positions during burst firing.

Figure 18 – Bolt carrier of the PKMS machine gun in the firing position

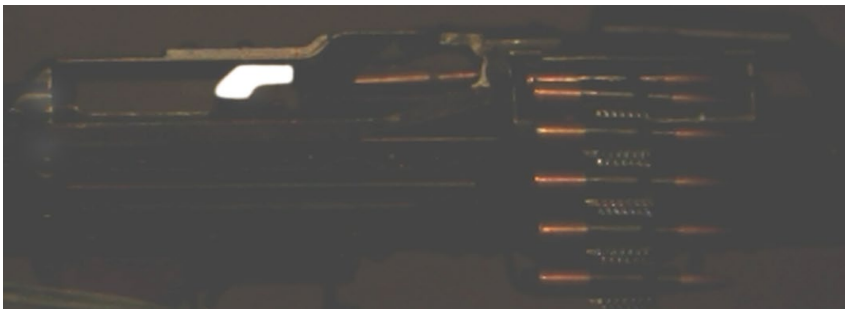

Figure 19 – Bolt carrier of the PKMS machine gun when backing up and withdrawing the cartridge case

Figure 20 – Bolt carrier of the machine gun when in the bottom position

Vo, B.V. et al, Research into the effect of ammunition belt stiffness on the operation of automatic firing systems using experimental methods, pp.469-495

Results and discussion

Problem solution

Elastic force between the belt links

During automatic fire, the platform pulls the ammunition belt in as the bolt carrier moves backward. This process ensures that the ammunition belt is always pulled, preventing any gaps from appearing between the belt links. The pulling force of the belt causes the connection between the first and second links to elastically deform, allowing them to move together during the first shot. This process is then repeated for the subsequent links in the belt. Experiments have shown that the elastic force between the belt links is at its highest during the first shot and varies depending on the stiffness of the bullet belt. Graphs depicting the elastic force between the belt links for a series of 6 bullets, each corresponding to a bullet belt of different stiffness, can be seen in Figure 21 and Figure 22. The maximum elastic force values for the belt links are listed in Table 4.

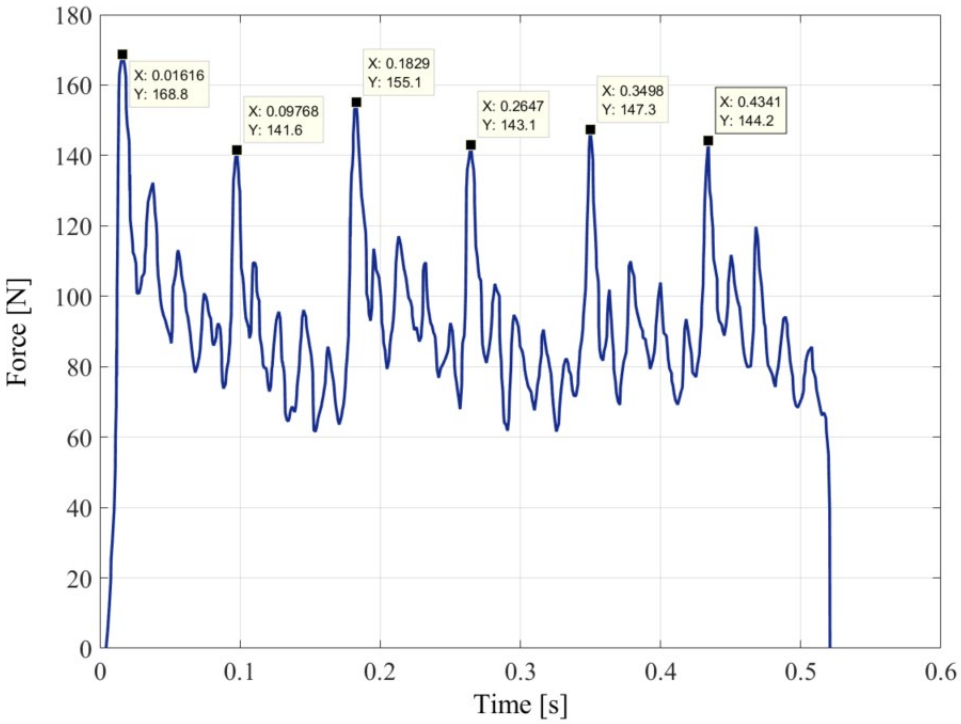

Figure 21 – Elastic force between the belt links during a series of firing with the belts of a stiffness of K=42 [N/mm]

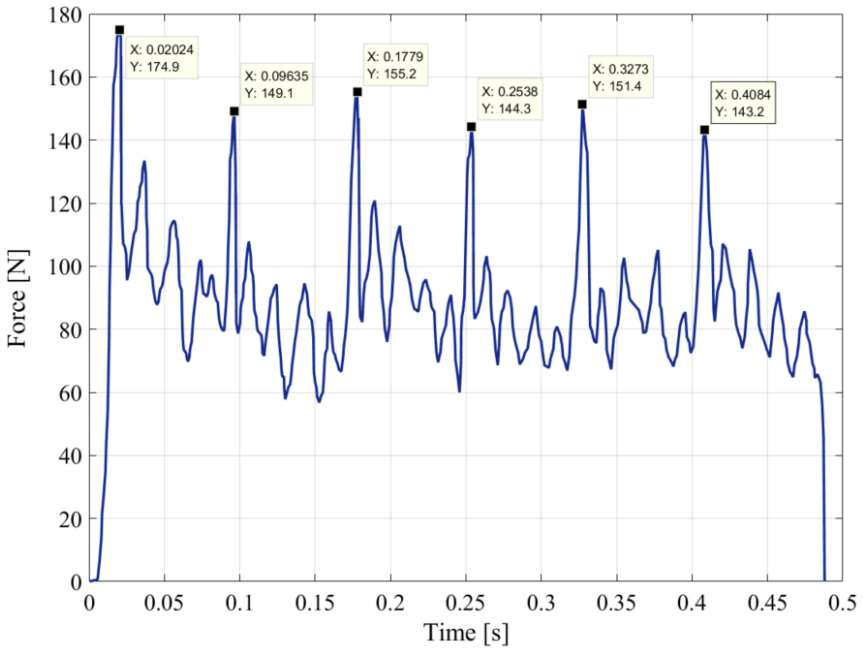

Figure 22 – Elastic force between the belt links during a series of firing with the belts of a stiffness of K=98 [N/mm]

Table 4 – Maximum elastic force at the belt link when firing a series of 6 shots

Order of firing	Maximum elastic force [N] with K=98 [N/mm]	Maximum elastic force [N] with K=42 [N/mm]
1	174.9	168.8
2	149.1	141.6
3	155.2	155.1
4	144.3	143.1
5	151.4	147.3
6	143.2	144.2

Displacement and velocity of each belt link during burst firing

The ammunition belt was observed with a high-speed camera FASTCAM SA1.1 model 675K - C1. The maximum recording speed was 675000 fps at 64x16 pixels. The movement of the ammunition belt is observed when firing in series with Russian test belts with a stiffness of K=98 [N/mm] and Vietnamese belts with a stiffness of K = 42 [N/mm], see Figure 23.

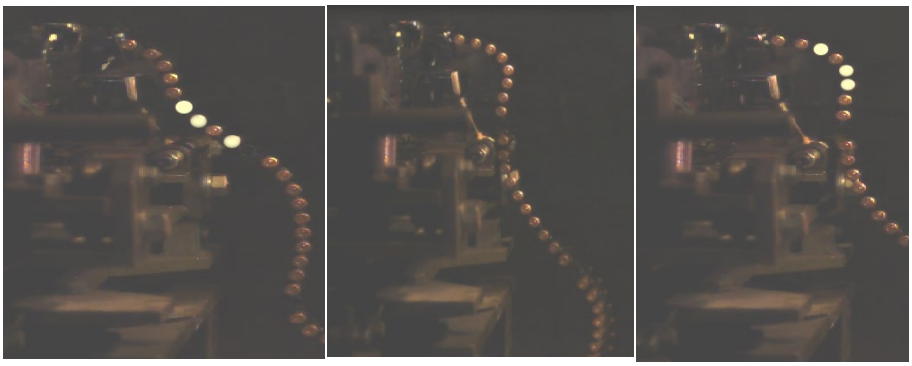

Figure 23 – Image of the bullet belt movement during burst firing

The displacement trajectory and displacement velocity of the belt link during a series of firing corresponding to the stiffness K=42 [N/mm] and K=98 [N/mm] are shown in Figure 24 and Figure 25.

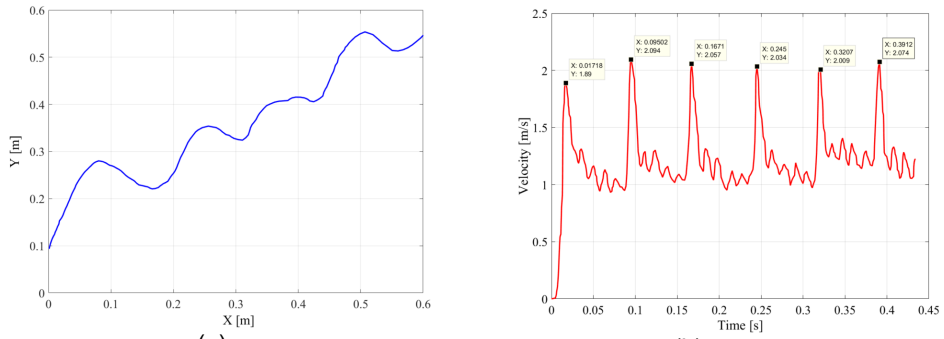

(a) (b)

Figure 24 – Displacement trajectory and displacement velocity of the belt link when firing in series with a belt with stiffness of K= 42 [N/mm]:
a) displacement trajectory; b) displacement velocity

The maximum speed of the belt link corresponding to different belt stiffness is shown in Table 5 and Table 6.

Table 5 – Maximum speed of the belt link with a belt stiffness of K=42 [N/mm]

Order of firing	1	2	3	4	5	6
Maximum speed [m/s]	1.89	2.094	2.057	2.034	2.009	2.074

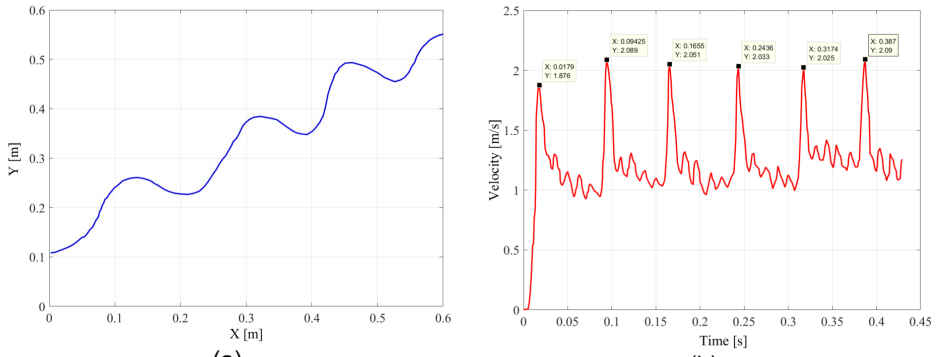

(a) (b)

Figure 25 – Displacement trajectory and displacement velocity of belt link during a series of firing with the Russian prototype belt with a stiffness of K= 98 [N/mm]: a) displacement trajectory; b) displacement velocity

Table 6 – The maximum speed of the belt link with a belt stiffness of K=98 [N/mm]

Order of firing	1	2	3	4	5	6
Maximum speed [m/s]	1.876	2.089	2.051	2.033	2.025	2.09

Displacement and displacement velocity of the bolt carrier

The displacement and displacement velocity of the bolt carrier can be determined based on the images obtained from the Fastcam SA1.1 high-speed camera. TEMA software was used to process images as well as to collect necessary data. The displacement and velocity of the base link with different belt stiffnesses are shown in Figures 26 - 29. The motion parameters of the base link when firing in series with different belt stiffnesses are presented in Table 7 and Table 8.

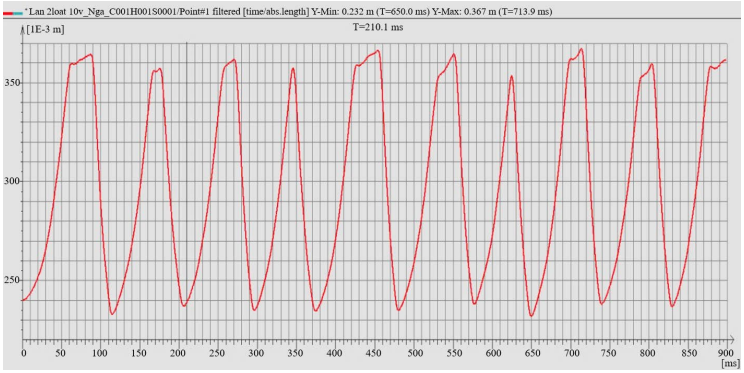

Figure 26 – Displacement of the bolt carrier corresponds to a Russian belt whose stiffness is K=98 [N/mm]

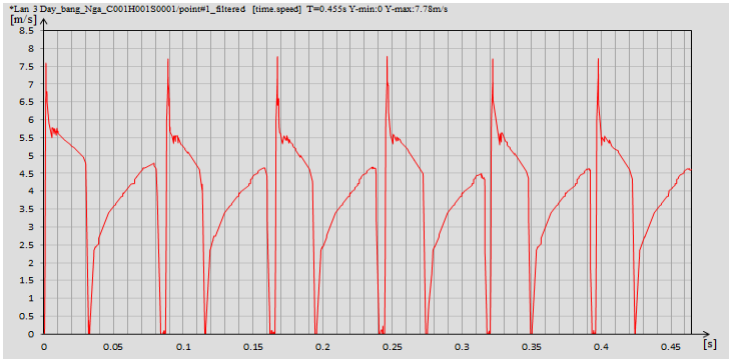

Figure 27 – Velocity of the bolt carrier corresponding to the Russian belt with K=98 [N/mm]

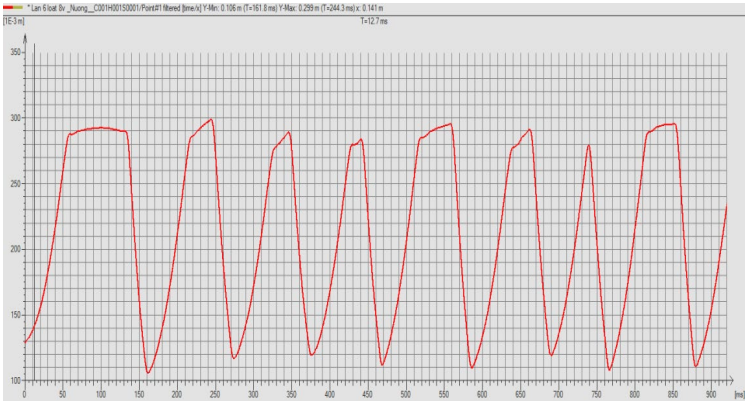

Figure 28 – Moving the bolt carrier with a Vietnamese belt with a stiffness of K=42 [N/mm]

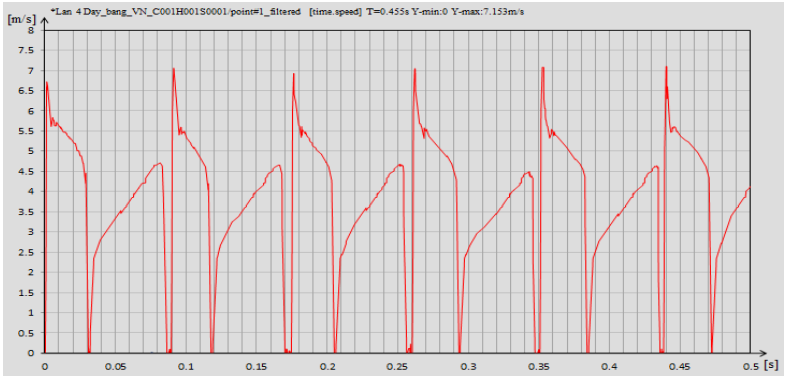

Figure 29 – Velocity of the bolt carrier with the Vietnamese belt with a stiffness of K=42 [N/mm]

Table 7 – Motion parameters of the bolt carrier corresponding to the Russian belt with a stiffness of K=98[N/mm]

Order of firing	Maximum recoil velocity of the bolt carrier [m/s]	Maximum push-up velocity of the bolt carrier [m/s]	Recoil time of the bolt carrier [s]	Working cycle of the bolt carrier [s]
1	7.59	4.748	0.0281	0.0865
2	7.71	4.755	0.0276	0.0869
3	7.76	4.752	0.0265	0.0845
4	7.78	4.698	0.0278	0.0878
5	7.71	4.731	0.0269	0.0881
6	7.72	4.741	0.0271	0.0855

Table 8 – Motion parameters of the bolt carrier corresponding to the Vietnamese belt with a stiffness of K=42 [N/mm]

Order of firing	Maximum recoil velocity of the bolt carrier [m/s]	Maximum push-up velocity of the bolt carrier [m/s]	Recoil time of the bolt carrier [s]	Working cycle of the bolt carrier [s]
1	6.722	4.739	0.0294	0.09045
2	7.068	4.725	0.0273	0.08937
3	6.931	4.729	0.0289	0.08955
4	7.057	4.498	0.0282	0.08955
5	7.080	4.631	0.0268	0.08972
6	7.153	4.684	0.0259	0.08969

Based on the results obtained, some comments are made as follows:

- With the Russian belt with a stiffness of K=98 [N/mm], the displacement of the bolt carrier remains relatively stable during a series of shots. However, there is a noticeable change in displacement at the top and bottom positions (see Figure 26). This can be attributed to various processes taking place at these positions, such as the closing of the bolt, the withdrawal and ejection of the cartridge case, and the firing process. In contrast, the maximum recoil velocity of the bolt carrier during the first shot is only 7.59 [m/s], which is lower than in subsequent shots (see Figure

27 and Table 7). This can be explained by the fact that the belt puller must initially overcome the weight of the entire ammunition belt, resulting in increased resistance in the automatic firing system. As a result, the first shot takes longer to complete compared to subsequent shots.

- With the Vietnamese belts of stiffness of K=42 [N/mm]: the period of each shot increases, which means the period of operation of the automatic firing system increases, see Figure 28, and Figure 29. However, this change only increases within certain limits shown in Table 8.

- The survey results have shown that variations in belt resistance directly affect the duty cycle of the automatic firing system, leading to a decrease in shooting accuracy. Specifically, when the stiffness of the bullet belt is increased, the shot cycle is reduced, resulting in a higher rate of fire (refer to Tables 7 and 8). It is important to note that this change can be influenced by various factors, but our findings confirm a clear correlation between the belt stiffness and the shot cycle, independent of other factors.

Conclusion

When researching the dynamic problem of the automatic firing system, taking into account the characteristics of the ammunition belt is extremely necessary. With the results obtained, some conclusions can be drawn as follows:

- The experiments described in this study provide an important theoretical foundation for determining kinematic parameters (displacement and displacement velocity) of the bullet belt and the bolt carrier of the automatic firing system which operates on the principle of gas extraction.

- High-speed cameras can be used to experimentally determine the motion parameters of objects with high moving speeds and complex working environments.

- The experimental determination of the elastic force between bullet belt links yields results that are relatively consistent with reality, making it an important parameter in the study of bullet belt dynamics.

- The use of measuring devices ensures high accuracy, reliability, and stability in the measurement of physical quantities.

- The method for determining dynamic parameters is reasonable, consistent, and reliable. The results obtained from this research can be used in design calculations to optimize the structure of the belt and automatic firing system, as well as to calculate the firing speed of the gun for the exploitation process. Additionally, these results can be used to verify corresponding mathematical models.

- The procedure used in this paper can serve as a reference for practical methods in other weapon systems.

The authors' next research will focus on surveying, analyzing, and evaluating the effects of changing the gap between ammunition belt links and the number of bullets in the ammunition feeding process. This will provide specific parameters for evaluating the impact on the reliable functioning of the automatic firing system.

References

Balla, J., Havlicek, M., Jedlicka, L., Krist, Z. & Racek, F. 2010. Dynamics of automatic weapon mounted on the tripod. In: Rogozea, L. (Ed.) *MACMESE'10: Proceedings of the 12th WSEAS international conference on Mathematical and computational methods in science and engineering*, Faro, Portugal, pp.122-127, November 3-5. Stevens Point, Wisconsin, USA: World Scientific and Engineering Academy and Society (WSEAS). Available at: https://dl.acm.org/doi/10.5555/1948857.1948881.

Balla, J., Havlicek, M., Jedlicka, L., Krist, Z., & Racek, F. 2011. Firing stability of mounted small arms. *International Journal of Mathematical Models and Methods in Applied Sciences,* 5(2), pp.412-422 [online]. Available at: https://www.naun.org/main/NAUN/ijmmas/19-818.pdf [Accessed: 01 November 2024].

Balla, J., Krist, Z. & Le, C.L. 2015. Experimental study of turret-mounted automatic weapon vibrations. *International Journal of Mechanics,* 9, pp.16-25 [online]. Available at: https://www.naun.org/main/NAUN/mechanics/2015/a062003-137.pdf [Accessed: 01 November 2024].

Balla, J. & Mach, R. 2007. Kinematics and dynamics of Gatling weapons. *Advances in Military Technology,* 2(2), pp.121-133 [online]. Available at: https://www.aimt.cz/index.php/aimt/article/view/1691 [Accessed: 01 November 2024].

Bien, V.V., Macko, M. & Hung, M.D. 2021a. Experimental Study of Automatic Weapons Vibrations When Firing Series. *Problems of Mechatronics. Armament, Aviation, Safety Engineering,* 12(4), pp.9-28. Available at: https://doi.org/10.5604/01.3001.0015.5984.

Bien, V.V., Phuc, T.V. & Macko, M. 2021b. Effect of Some Structural Parameters on Firing Stability of Shooter-Weapon System. *Advances in Military Technology,* 16(2), pp.235-251.Available at: https://doi.org/10.3849/aimt.01487.

Dingguo, Z. 1996. Computer simulation of the motion of the bullet belt of an airplane gun. *Applied Mathematics and Mechanics,* 17(11), pp.1059-1066. Available at: https://doi.org/10.1007/BF00119953.

Doan, D.V., Bien, V.V., Quang, M.A. & Phu, N.M. 2023. A Study on Multi-Body Modeling and Vibration Analysis for Twin-Barrel Gun While Firing on Elastic

Ground. *Applied Engineering Letters,* 8(1), pp.36-43. Available at: https://doi.org/10.18485/aeletters.2023.8.1.5.

Dung, D.T., Phu, M.N., Bien, V.V., Phon, D.N., Macko, M. & Vitek, M. 2023. Analysis of gas flow losses in a gas-operated gun. In: *2023 International Conference on Military Technologies (ICMT),* Brno, Czech Republic, pp.1-7, July 11. Available at: https://doi.org/10.1109/ICMT58149.2023.10171337.

Fiser, M., 2007. *Automatic weapons – design and testing*. Trencin, Slovak Republic: Alexander Dubček University of Trenčín. ISBN: 80-8575-089-0.

Fiser, M. & Popelinsky, L. 2007. *Small Arms*. Brno, Czech Republic: University of Defence. ISBN: 978-80-7231-475-1.

Goldberg, M.S. & Goldberg, D.M. 2019. Optimizing the Purchases of Military Air-To-Ground Weapons. *Military Operations Research,* 24(4), pp.37-52 [online]. Available at: https://www.jstor.org/stable/26853512 [Accessed: 01 November 2024].

Macko, M., Vo, B.V. & Mai, Q.A. 2021. Dynamics of Short Recoil-operated Weapon. *Problems of Mechatronics, Armament, Aviation, Safety Engineering,* 12(3), pp.9-26.Available at: https://doi.org/10.5604/01.3001.0015.2432.

Tien, V.D., Macko, M., Procházka, S. & Bien, V.V. 2022. Mathematical Model of a Gas-Operated Machine Gun. *Advances in Military Technology,* 17(1), pp.63-77. Available at: https://doi.org/10.3849/aimt.01449.

Tien, V.D., Procházka, S., Krist, Z. & Vo, B.V. 2021. Influence of Gas Port on Forces and Their Impulses Acting in an Automatic Weapon. In: *2021 International Conference on Military Technologies (ICMT),* Brno, Czech Republic, pp.1-8, June 08-11. Available at: https://doi.org/10.1109/ICMT52455.2021.9502832.

Van Hung, N., Van Dung, N., Van Minh, P., Van Ke, T., & Van Thom, D. 2024. Vibration Behavior Analysis of the Ammunition Belt of the Gas-Operated Machine Gun. *Journal of Vibration Engineering & Technologies,* 12, pp.1563-1575. Available at: https://doi.org/10.1007/s42417-023-00926-4.

Vitek, R. 2019. Analyses of the Measurement Accuracy of the Optical Light Gates. In: *2019 International Conference on Military Technologies (ICMT)*, Brno, Czech Republic, pp.1-11, May 30-31. Available at: https://doi.org/10.1109/MILTECHS.2019.8870114.

Vo, V.B., Macko, M. & Dao, H.M. 2021. Experimental Study of Automatic Weapon Vibrations when Burst Firing. *Problems of Mechatronics. Armament, Aviation, Safety Engineering*, 12(4), pp.9-28. Available at: https://doi.org/10.5604/01.3001.0015.5984.

Wang, G. & Jiang, T. 2008. Simulation and experiment of multi-body system dynamic model with clearance joint for ammunition belt system. *Journal of Mechanical Engineering,* 44(5), pp.238-241.

Investigación mediante métodos experimentales sobre el efecto de la rigidez de los cinturones de municiones en el funcionamiento de sistemas de disparo automático

Bien V. Vo[a], *Phon* D. Nguyen[a], **autor de correspondencia**,
Phu M. Nguyen[a], *Long* X. Vu[b]

[a] Universidad Técnica Le Quy Don, Facultad de Equipos Especiales, Hanoi, República Socialista de Vietnam

[b] Universidad Tran Dai Nghia, Ciudad Ho Chi Minh, República Socialista de Vietnam

CAMPO: matemáticas, ingeniería mecánica
TIPO DE ARTÍCULO: artículo científico original

Resumen:

Introducción/objetivo: Este artículo se centra en determinar mediante métodos experimentales las características dinámicas del sistema de disparo automático. Además, el estudio menciona el impacto de la rigidez del cinturón de municiones.

Métodos: Los resultados de la investigación incluyen los desplazamientos de la parte básica (portacerrojos) y del cinturón de municiones de armas automáticas durante series de disparos. Para medir y determinar estos parámetros se utilizó una cámara de alta velocidad modelo FASTCAM SA1.1, específicamente la variante 675K-C1. La fuerza elástica entre los eslabones de la correa se determinó mediante sellos de deformación equipados con sensores de medición de fuerza. Para validar la fiabilidad del método, se realizaron experimentos con la ametralladora PKMS.

Resultados: Los resultados obtenidos muestran que, cuando se utiliza una cinta con una rigidez de 42 [N/mm], las características cinemáticas del eslabón básico, como la velocidad de retroceso y el tiempo de retroceso, cambian significativamente en comparación con el uso de una cinta que tiene una rigidez de 98 [N/mm]. En particular, la velocidad máxima de retroceso del arma base se puede reducir en ~8% al disparar una serie de 6 balas. Estos resultados se pueden aplicar en cálculos y diseños para optimizar la estructura de la cinta de municiones y el sistema de disparo automático. Además, estos hallazgos pueden ayudar a calcular la velocidad de disparo del arma, facilitando así el funcionamiento de las armas automáticas.

Conclusión: El procedimiento de prueba desarrollado en este estudio sirve como base teórica crucial para evaluar y determinar las características dinámicas de otros sistemas de armas automáticas.

Palabras claves: sistema de disparo automático, cinturón de municiones, ametralladora PKMS de 7,62 mm.

Vo, B.V. et al, Research into the effect of ammunition belt stiffness on the operation of automatic firing systems using experimental methods, pp.469-495

Исследование влияния жесткости патронной ленты на эффективность системы серийной стрельбы экспериментальными методами

Биен В. Во[а], *Фон* Д. Нуиен[а], **корреспондент**,
Фу М. Нуиен[а], *Лонг* С. Ву[б]

[а] Технический университет имени Ле Куй Дона,
факультет специального оборудования,
г. Ханой, Социалистическая Республика Вьетнам

[б] Университет Тран Дай Нгиа,
г. Хошимин, Социалистическая Республика Вьетнам

РУБРИКА ГРНТИ: 55.68.00 Производство оружия
ВИД СТАТЬИ: оригинальная научная статья

Резюме:

Введение/цель: Данная статья посвящена определению динамических характеристик системы серийной стрельбы экспериментальными методами. Помимо того, в исследовании изучено влияние жесткости патронной ленты.

Методы: Результаты исследования выявили смещение затворной рамы и патронной ленты автоматического оружия во время серии выстрелов. Для измерения и определения этих параметров использовалась высокоскоростная камера модели FASTCAM SA1.1, в частности вариант 675K-C1. Усилие и предел упругости между звеньями патронной ленты измерялись с помощью тензодатчика. С целью валидации надежности метода были проведены эксперименты на пулемете ПКМС.

Результаты: Полученные результаты показали, что при использовании ленты с жесткостью 42 [Н/мм] кинематические характеристики основного звена, такие как скорость и время отдачи, значительно изменены по сравнению с использованием ленты с жесткостью 98 [Н/мм]. В частности, максимальная скорость отдачи может быть снижена на ~8% при серии из 6 выстрелов. Данные результаты могут быть использованы в расчетах и проектировании и оптимизации патронной ленты, а также системы серийной стрельбы. Кроме того, эти результаты могут помочь в расчете скорострельности, тем самым облегчая эксплуатацию автоматического оружия.

Вывод: Процедура испытаний, разработанная в ходе данного исследования, представляет важный теоретический фундамент для оценки и определения динамических характеристик других систем автоматического оружия.

Ключевые слова: система серийной стрельбы, патронная лента, 7,62-мм пулемет ПКМС.

Истраживање ефеката крутости реденика на функционисање система за рафалну паљбу помоћу експериманталних метода

Биен В. Во[а], *Фон* Д. Нуиен[а], **аутор за преписку**, *Фу* М. Нуиен[а], *Лонг* С. Ву[б]

[а] Технички универзитет „Ле Квај Дон", Факултет за специјалну опрему, Ханој, Социјалистичка Република Вијетнам

[б] Универзитет „Тран Дај Нгиа", Хо Ши Мин, Социјалистичка Република Вијетнам

ОБЛАСТ: математика, машинство
КАТЕГОРИЈА (ТИП) ЧЛАНКА: оригинални научни рад

Сажетак:

Увод/циљ: У овој студији се помоћу експерименталних метода одређују динамичке карактеристике система за рафалну паљбу. Такође, разматра се и утицај крутости реденика.

Методе: Резултати истраживања укључују померање основног дела (носача затварача) и реденика аутоматских оружја за време рафалне паљбе. За мерење и одређивање ових параметара коришћен је модел камере велике брзине FASTCAM SA1.1, варијанта 675K-C1. Сила еластичности између спојница реденика одређена је помоћу елемената за мерење деформације опремљених сензорима за мерење силе. Ради валидације поузданости метода експерименти су рађени на митраљезу ПКМС.

Резултати: Показано је да се при употреби траке крутости 42 N/mm, кинематичке карактеристике основне спојнице, као што су брзина трзања и време трзања, у знатној мери мењају у поређењу са употребом траке која има крутост од 98 N/mm. Конкретно, максимална брзина трзања може се редуковати за ~8% при опаљивању серије од 6 метака. Ови резултати могу да се примене у прорачунима и пројектовањима ради оптимизације структуре реденика и система за рафалну паљбу. Наведени налази могу да помогну и при израчунавању брзине паљбе, чиме се олакшава управљање аутоматским оружјем.

Закључак: Поступак испитивања развијен у овој студији суштински представља теоретску основу за процењивање и одређивање динамичких карактеристика других система аутоматског оружја.

Кључне речи: систем за рафалну паљбу, реденик, PKMS митраљез калибра 7,62 mm.

Paper received on: 05.11.2024.
Manuscript corrections submitted on: 26.03.2025.
Paper accepted for publishing on: 27.03.2025.

Planning vehicle routes to optimize fuel consumption

Predrag Grozdanović[a], *Miloš* Nikolić[b], *Milica* Šelmić[c]

University of Belgrade, Faculty of Transport and Traffic Engineering, Department of Operations Research in Transport and Traffic, Belgrade, Republic of Serbia

[a] e-mail: p.grozdanovic@sf.bg.ac.rs, **corresponding author**, ORCID iD: https://orcid.org/0009-0002-3401-5799

[b] e-mail: m.nikolic@sf.bg.ac.rs, ORCID iD: https://orcid.org/0000-0001-5892-8248

[c] e-mail: m.selmic@sf.bg.ac.rs, ORCID iD: https://orcid.org/0000-0003-2507-3663

https://doi.org/10.5937/vojtehg73-55998

FIELD: operations research, logistic, transport, traffic
ARTICLE TYPE: original scientific paper

Abstract:

Introduction/purpose: Models developed for routing transport vehicles with an environmental focus are predominantly dedicated to reverse logistics or transporting environmentally hazardous cargo. Few models in the relevant literature consider the ecological factors for routing vehicles involved in the distribution of consumer goods.

Methods: This paper presents a model for planning vehicle routes to optimize fuel consumption, considering the time windows required for service and payload capacity of vehicles. A heuristic algorithm was developed to minimize fuel consumption. A Simulated Annealing metaheuristic was applied to enhance the solutions obtained by the proposed heuristic.

Results: The results from the heuristic algorithm for fuel consumption minimization and the improved results using the Simulated Annealing metaheuristic are presented. All tests were conducted on Solomon's instances.

Conclusion: The developed approach to vehicle routing ensures a compromise between transport companies and ecology. The results show that applying this approach can simultaneously minimize the costs of the transport company and CO_2 emissions.

Key words: vehicle routing, fuel consumption, simulated annealing, heuristic algorithm.

ACKNOWLEDGMENT: This work was supported by the Ministry of Education, Science and Technological Development of the Republic of Serbia [grant number 451-03-68/2022-14].

Introduction

Environmental protection has become one of the most important factors in carrying out any activity. Road transport vehicles significantly impact the environment negatively, as they use fossil fuels, the combustion of which releases harmful gases that contribute to the greenhouse effect. However, road-transport vehicles remain irreplaceable for cargo distribution. It is crucial to recognize that one of the main contributors to the greenhouse effect is carbon dioxide (CO_2) emitted from fossil fuels by vehicles with internal combustion engines. Moreover, the amount of CO_2 released into the atmosphere is directly related to the fuel consumption of the vehicle; thus, reducing fuel consumption also reduces CO_2 emissions. Globally, there is a trend toward transitioning from fossil-fuel-powered transport to alternative fuels that pollute the atmosphere less.

If transitioning from one type of vehicle to another is not feasible, efforts should be focused on minimizing the harmful impacts of standard road transport vehicles that use fossil fuels. One effective approach is to apply vehicle routing models that also consider environmental factors (Asghari & Mirzapour Al-E-Hashem, 2021). Implementing these models to minimize fuel consumption is highly attractive to transport companies, as it reduces transportation costs while promoting environmentally responsible behavior.

Fuel consumption of a transport vehicle depends on numerous factors. These factors can be divided into those that can be optimized and included in the mathematical model and those that cannot be directly influenced by the optimization model, but can still be managed through appropriate measures.

Factors that cannot be optimized through a mathematical model include driver habits, vehicle age, and vehicle condition. Driver habits can significantly impact fuel consumption. Practical experience indicates that efficient driving can reduce fuel consumption by 1 to 2 liters per 100 km, resulting in substantial monthly fuel savings. To influence the habits of professional drivers, companies can organize training sessions on efficient driving and implement monitoring systems.

Vehicle age can also significantly affect fuel consumption. Truck manufacturers aim to reduce fuel consumption with each new series of trucks, so newer vehicles generally consume less fuel than older ones. Additionally, vehicle condition greatly influences fuel consumption. A well-maintained vehicle in good condition certainly consumes less fuel than a poorly maintained one. Therefore, older vehicles that are properly maintained can sometimes consume less fuel than newer vehicles that are

not well-maintained. Consequently, it is not always accurate to assume that newer vehicles have lower fuel consumption than older vehicles.

Factors influencing the minimization of fuel consumption, and amenable to optimization models, encompass cargo volume, distance traveled, journey duration, and vehicle utilization. Notably, fuel consumption varies significantly between an empty vehicle and one at maximum capacity, with differences of up to 10 liters per 100 km (Ćirković, 2018). Conversely, reducing time and distance typically aids in lowering fuel usage. However, many overlooked the importance of time, neglecting that a vehicle covering 100 km in 2 h consumes differently from one doing so in 3 h. Thus, minimizing either factor does not necessarily equate to a fuel reduction. Hence, developing an optimization model that considers distance, time, and cargo volume is imperative for fuel conservation. This study tackled this multifaceted problem, integrating these three factors.

The principal benefit of the mathematical model, which focuses on vehicle routing to reduce fuel consumption, lies in aligning the cost-saving objectives of transport companies with broader societal aims. While companies aim for cost reduction, societies, in general, aspire to curtail environmental pollution, attainable through meticulous route planning.

In this paper, the mathematical formulation of the Vehicle Routing Problem with Time Window (VRPTW) is modified in terms of the objective function. The objective function is an equation that determines the fuel consumption on the route depending on the amount of cargo in the vehicle and the distance traveled. In the paper, heuristic and metaheuristic algorithms designed to minimize fuel consumption are developed and used to solve the mentioned VRPTW problem. To improve the solution generated by the new heuristic algorithm, a Simulated Annealing metaheuristic is adapted and applied to the mentioned problem. Testing the developed heuristic and metaheuristic approaches was performed on Solomon instances, to validate the mentioned approaches. The main contribution of this paper is the application of heuristic and metaheuristic approaches adapted to solve the VRPTW problem, with the goal to minimize fuel consumption, and thus CO_2 emissions. Also, the test results show the possibility of direct practical application of the developed approaches.

The structure of the paper unfolds as follows. After introductory discussions, an extensive literature review is presented in the second section. The third section elaborates on the mathematical model addressing the vehicle routing problem, which incorporates both time windows required for delivery and vehicle capacity as significant factors contributing to increased fuel consumption. Section four delves into the

developed heuristic algorithm for fuel consumption minimization, while section five introduces the Simulated Annealing metaheuristic. The sixth section unveils the results of the testing, with the final, seventh section concluding with remarks and outlining ideas for future research.The introduction is an introductory part of the article.

Literature review

Vehicle routing problems that consider ecological factors, including carbon dioxide emissions, fuel consumption, and noise levels, aiming to minimize them through improved planning, fall within green logistic areas (Asghari & Mirzapour Al-E-Hashem, 2021). Considering that oil-fueled vehicles, known for their substantial environmental impact, are predominantly employed in road transport, it becomes imperative to prioritize ecological considerations in vehicle routing to ensure the sustainability of this sector in the future.

Routing is a routine task in the distribution and transportation sectors. Various software applications are used daily to define vehicle routes, aiming to boost company profits or cut costs. However, practical implementation of software that considers both economic factors and environmental protection is rare, largely owing to the recent development of optimization models with this objective. Additionally, environmental constraints further complicate the problem, hindering model formation and resolution.

Some authors have approached the routing problem from the perspective of "green" routing and schedules. Additionally, models related to sustainable logistics have been created (Asghari & Mirzapour Al-E-Hashem, 2021), such as:

- Waste collection problems;
- Transportation of hazardous materials;
- Time-dependent routing problems - indirectly influencing harmful gas emissions by aiming to reduce travel time by avoiding congested routes;
- enhancing the system in question, etc.

Models developed for routing transport vehicles with environmental considerations are mostly dedicated to reverse logistics or transportation of environmentally hazardous cargo. Few models have focused on the environmental concerns used for routing vehicles involved in the distribution of consumer goods. By developing such models, which strike a balance between societal aspects and the goals of transportation

companies, a real impact on the environment can be achieved. Another reason to pay attention to these models is that the number of vehicles involved in daily distribution far exceeds the number of vehicles used for cargo collection. By reducing the environmental impact of vehicles during both distribution and collection, significant environmental benefits can be achieved compared with considering environmental factors only in either distribution or collection. Therefore, models addressing environmental concerns and routing vehicles for both distribution and collection should be concurrently developed to achieve the best outcome.

Since the introduction of the first Vehicle Routing Problem (VRP) in 1959 (Dantzig & Ramser, 1959), numerous modifications and extensions to this problem have emerged. Various models have been developed for determining routes during goods distribution, aiming to minimize costs (Herdianti et al, 2021), time (Chen et al, 2021), and distance (Pan et al, 2021), while fewer models consider environmental criteria (CO_2 emissions, fuel consumption, etc.) (Tiwari & Chang, 2015). A detailed overview of VRP problems, solution methods, and objectives can be found in the review articles by Marinakis & Migdalas (2007), Braekers et al. (2016), and Konstantakopoulos et al. (2022).

Reducing fuel consumption and CO_2 emissions during goods distribution can be achieved by defining a set of routes to minimize fuel consumption in the case of internal combustion engine vehicles (Liu et al, 2020; Ramadhani & Garside, 2021; Song et al, 2020), introducing electric vehicles (Napoli et al, 2021), and combining drone and internal combustion engine vehicle operations (Huang et al, 2022). In the study by Liao et al. (2019), a detailed comparison of the advantages and disadvantages of internal combustion engine vehicles and electric vehicles can be found. Due to the insufficiently developed infrastructure for electric vehicle usage (locations of fast chargers) and the high costs of replacing internal combustion engine fleets with electric ones, exclusive use of electric vehicles for goods distribution remains unfeasible for many companies. Therefore, reducing CO_2 emissions is most easily achieved by reducing fuel consumption during goods distribution, which can be accomplished by developing new and improved algorithms. Ramadhani & Garside (2021) addressed the VRP problem using the Particle Swarm Optimization (PSO) metaheuristic to minimize fuel consumption, primarily to reduce costs for distribution companies due to frequent fuel price increases. Liu et al. (2020) solved the Time-Dependent Vehicle Routing Problem with Time Windows (TDVRPTW) problem by considering vehicle speed, travel time, waiting time, service time, time windows, and the influence of driving modes and speeds on CO_2 emissions. Liu et al. (2020) attempted to strike

a balance between company and societal goals by solving the stated problem by combining economic (vehicle fixed and driver costs) and environmental (fuel consumption, CO_2 emissions, noise level, etc.) criteria in the objective function. Opportunities to reduce fuel consumption during goods distribution are even more pronounced in cold chains. Song et al. (2020) solved the Vehicle Routing Problem with Time Windows (VRPTW) problem in the cold chain to reduce fuel consumption. In addition to the distance traveled and route completion time, the fuel consumption in the cold chain can be reduced by optimizing temperature maintenance device operations. The latest literature review on "green" VRP problems aimed at reducing fuel consumption, CO_2 emissions, noise levels, etc., was given by Asghari & Mirzapour Al-E-Hashem (2021).

Solving VRP problems to minimize only one environmental criterion is rare. Hence, the motivation for developing algorithms in this paper is to enable the determination of routes for wide-scale goods distribution, respecting time windows and vehicle capacity, to minimize only fuel consumption. Fuel consumption minimization falls under the category of economic criteria from the perspective of the distributing company, while from a societal perspective, minimizing fuel consumption affects CO_2 emissions, making it an environmental criterion. Unlike papers in the literature that exclusively combine economic or environmental criteria in the objective function, this paper focuses solely on minimizing fuel consumption, which simultaneously falls under both economic and environmental criteria, thus achieving the best compromise between the company's interests and those of the community.

Problem description and mathematical formulation

To present the mathematical formulation of the problem, it is necessary to first introduce certain notations. Let *G* (V*,* A) denote an oriented transport network, where V is the set of all nodes in the network V (0, 1, 2, 3, ..., *n*+1), and A is the set of edges (*i, j*). The nodes 0 and *n*+1 denote the depot, that is, the places where vehicles start and end their routes, respectively. Let N denote the set of nodes that must be serviced N (1, 2, 3, *…, n*), that is, the set of clients. The notation q_i represents the quantity of cargo demanded by the client *i*, and the notation [a_i, b_i] indicates the time window within which the required amount of cargo must be delivered to the client *i*.

Daily problems related to cargo distribution to facilities can be treated as vehicle routing problems with time windows - VRPTW (Desrochers et al, 1988).

The parameters:

t_{ij} – travel time from the node *i* to the node *j*;

M – a sufficiently large positive number;

w_i^k– variable indicating the start of service at the node *i* with the vehicle *k*;

Q – vehicle capacity;

c_{ij} – transportation cost from the node *i* to the node *j*

a_i – the earliest time when service can start at the node *i*

b_i – the latest time when service can start at the node *i*

S_i – service duration at the node *i*

q_i – demand at the node *i*

k – vehicle

The variable:

$$x_{ij}^k = \begin{cases} 1, \text{if the vehicle } k \text{ after visiting the node } i \text{ visits the node } j \\ 0, \quad otherwise \end{cases}$$

The mathematical formulation of the proposed problem (Desrochers et al, 1988):

Minimize

$$\sum_{k\in \mathrm{K}} \sum_{(i,j)\in \mathrm{A}} c_{ij} \cdot x_{ij}^k \tag{1}$$

with constraints:

$$\sum_{k\in \mathrm{K}} \sum_{j\in \delta^+(i)} x_{ij}^k = 1 \quad \forall i \in \mathrm{N} \tag{2}$$

$$\sum_{j\in \delta^+(0)} x_{0j}^k = 1 \quad \forall k \in \mathrm{K} \tag{3}$$

$$\sum_{i\in \delta^-(i)} x_{ij}^k - \sum_{i\in \delta^+(i)} x_{ij}^k = 0 \qquad \forall k \in \mathrm{K}, j \in \mathrm{N} \tag{4}$$

$$\sum_{i\in \delta^-(n+1)} x_{i,n+1}^k = 1 \qquad \forall k \in \mathrm{K} \tag{5}$$

$$w_j^k \geq w_i^k + S_i + t_{ij} - M\left(1 - x_{ij}^k\right) \qquad \forall k \in \mathrm{K}, (i,j) \in \mathrm{A} \tag{6}$$

$$a_i \leq w_i^k \leq b_i \qquad \forall k \in \mathrm{K}, i \in \mathrm{V} \tag{7}$$

$$\sum_{i \in \mathrm{N}} q_i \sum_{j \in \delta^+(i)} x_{ij}^k \leq Q \qquad \forall k \in \mathrm{K} \tag{8}$$

$$x_{ij}^k \in \{0,1\} \qquad \forall k \in \mathrm{K}, (i,j) \in \mathrm{A} \tag{9}$$

The objective function (1) is of a minimization type, representing either total costs or total distance traveled. Alternatively, it can minimize the total time required for the defined routes. Constraint (2) ensures that all clients are serviced, while constraints (3) and (5) guarantee that every vehicle departing from the depot also returns to it. Constraint (4) ensures that every vehicle arriving at a node to provide service also departs from that node. Constraints (6) and (7) pertain to time intervals, and constraint (8) ensures vehicle capacity. Constraint (9) indicates that x_{ij}^k is a binary variable.

As previously mentioned, decreasing fuel consumption not only mitigates emissions of harmful gases but also plays a pivotal role in reducing overall transportation costs. By decreasing fuel usage, we not only cut down on expenses but also contribute to the preservation of finite natural resources (Ćirković, 2018). Statistics indicate that fuel costs represent approximately 60% of total transportation expenses. (Xiao et al, 2012).

Xiao et al. (2012) introduced a modified model for the vehicle routing problem with capacity constraints, aiming to minimize the fuel costs required to visit all nodes within a network. Their model considers fuel consumption as dependent on both the cargo weight in the vehicle and the distances covered with this cargo weight. While accounting for various factors influencing fuel usage, such as driver habits and vehicle age, these are treated as constants within the model.

If Q_0 denotes the weight of the vehicle and Q_1 denotes the weight of the cargo in the vehicle, then the fuel consumption rate per unit length is ρ (Xiao et al, 2012):

$$\rho(Q_1) = \alpha(Q_0 + Q_1) + b \tag{10}$$

During vehicle routing, two extreme situations can arise. The first extreme situation occurs when the vehicle is empty, and the second when the vehicle is fully loaded. When the vehicle is empty, the fuel consumption rate is calculated as follows (Xiao et al, 2012):

$$\rho_0 = \alpha Q_0 + b \tag{11}$$

If Q denotes the maximum cargo capacity that can be loaded onto the vehicle, then the fuel consumption rate when the vehicle is fully loaded is calculated as follows (Xiao et al, 2012):

$$\rho^* = \alpha(Q_0 + Q) + b \tag{12}$$

The value of the coefficient α is obtained by dividing the difference in fuel consumption rates between the two extreme situations by the maximum amount of cargo that can be loaded onto the vehicle (Xiao et al, 2012):

$$\alpha = \frac{\rho^* - \rho_0}{Q} \tag{13}$$

When formula (13) is substituted for the coefficient α in equation (10), the fuel consumption rate is calculated as follows (Xiao et al, 2012):

$$\rho(Q_1) = \rho_0 + \frac{\rho^* - \rho_0}{Q} Q_1 \tag{14}$$

If y_{ij} denotes the quantity of cargo transported by the vehicle from the node i tothe node j, formula (14) is modified as follows (Xiao et al, 2012):

$$\rho_{ij} = \rho_0 + \frac{\rho^* - \rho_0}{Q} y_{ij} \tag{15}$$

The fuel consumption for transporting the cargo quantity y_{ij} over the distance d_{ij} is equal to (Xiao et al, 2012):

$$c_{ij}(y_{ij}) = \rho_{ij} \cdot d_{ij} = \left(\rho_0 + \frac{\rho^* - \rho_0}{Q} y_{ij}\right) \cdot d_{ij} \tag{16}$$

First, it is necessary to determine the cost of the fuel consumed along one edge, that is, when traversing the distance from the node i to the node j. The cost of the fuel consumed along the edge (i, j) is obtained using the following formula (Xiao et al, 2012):

$$c_{fuel}^{ij} = c_0 \cdot \rho_{ij} \cdot d_{ij} \tag{17}$$

where:

c_0 – fuel price;
ρ_{ij} – fuel consumption rate from the node i to the node j; and
d_{ij} – edge (i, j) length.

Given the method for calculating the fuel cost along one edge, the total fuel cost during the realization of a defined set of routes can be calculated as the sum of the products of the fuel cost per edge and a variable indicating whether the vehicle has traversed that edge. The formula for computing the fuel cost along the routes is:

$$C_{fuel} = \sum_{k \in \mathrm{K}} \sum_{(i,j) \in \mathrm{A}} c_{fuel}^{ij} \cdot x_{ij}^{k} = \sum_{k \in \mathrm{K}} \sum_{(i,j) \in \mathrm{A}} c_0 \cdot \rho_{ij} \cdot d_{ij} \cdot x_{ij}^{k} \qquad (18)$$

Applying formula (18) yields the fuel cost incurred during the service of n clients - nodes. If instead of fuel cost, the quantity of fuel consumed needs to be determined, this can be achieved by setting the unit fuel price to one, c0 =1. Thus, the resulting value of Cfuel represents the total fuel consumption when servicing n clients. Integrating the fuel consumption coefficient into the standard vehicle routing problem creates a new problem that may contribute to reducing fuel consumption compared to the standard problem.

Development of a heuristic algorithm for solving the given problem

A heuristic algorithm for minimizing fuel consumption developed in this paper was created to reduce fuel usage per vehicle route and consequently lower CO_2 emissions. This algorithm leverages the Nearest Neighbor Algorithm, considering time intervals, vehicle load capacity, and fuel consumption. Fuel consumption, calculated using formula (16), serves as the distance measure between nodes. Therefore, the nearest node is the one with the lowest fuel consumption.

The application of the heuristic algorithm for minimizing fuel consumption is outlined in five steps, and the implementation diagram is shown in Figure 1. The steps for the application are as follows:

Step 1: Calculate the fuel consumption for each pair of the nodes *i* and *j* using formula (16)**.**

Step 2: Begin forming a new route from the node representing the base. Set the departure time from the base to zero (D(0) = 0). Identify the nearest unserved node to the base based on fuel consumption. Include this node and add its demand to the partial route's total demand. Mark the added node as the current node and proceed to Step 3.

Step 3: Calculate the time when the vehicle departs from the current node after completing service. This is done by adding the travel time from the previous node to the current node to the departure time from the

previous node, and then taking the maximum of this value and the earliest start time of service at the current node. Finally, add the service time at the current node to this value. Proceed to the next step.

Step 4: Find the closest unserviced node concerning fuel consumption from the current node, ensuring that it complies with the vehicle's capacity and service-time constraints. If such a node is found, incorporate it into the partial route, add its demand to the existing partial route's demand, designate it as the current node, and revert to Step 3. Otherwise, conclude the route, return the vehicle to the base, and proceed to Step 5.

Step 5: Check if all nodes have been serviced. If all nodes have been serviced, calculate the total fuel consumption using formula (18), and terminate the algorithm. Otherwise, return to Step 2.

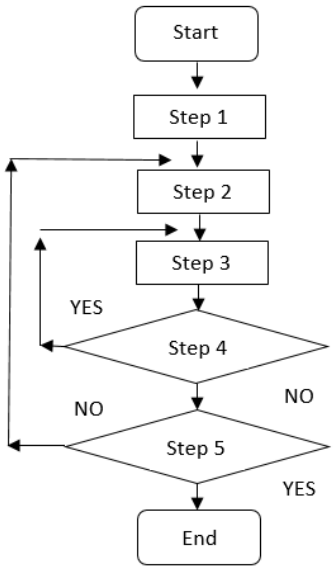

Figure 1 – Diagram illustrating the application steps of the heuristic algorithm for minimizing fuel consumption

Simulated Annealing metaheuristic

For solving combinatorial optimization problems, so-called specialized heuristic algorithms can be used. The heuristic algorithm for minimizing fuel consumption developed in this paper is a typical representative of this group of algorithms. Initially, the heuristic algorithm for minimizing fuel consumption was applied to obtain an initial solution. Subsequently, Simulated Annealing was applied to further improve the

solution, that is, further minimize fuel consumption. Simulated Annealing is one of the most commonly used metaheuristics for combinatorial optimization problems. In a large number of papers in the literature, the Simulated Annealing metaheuristic gives excellent results in solving routing problems.

Simulated Annealing, first introduced by Kirkpatrick et al. (1983), is a widely used metaheuristic algorithm for solving intricate combinatorial optimization problems. Its core idea revolves around iteratively applying small, random perturbations, and then assessing the change in the objective function value between iterations. If this change is negative, signifying an improvement, the new feasible solution becomes the initial one for further random perturbations. In cases where the change in the objective function value is positive, indicating that the new solution is worse than the previous one, it should not be discarded immediately. Instead, it undergoes evaluation to determine whether it should be rejected or accepted as a new starting point. This approach prevents getting trapped in local minima from which it is difficult to escape. When evaluating whether a solution should be accepted or not, it is necessary to first calculate the probability that increasing the objective function value by ΔF at a temperature T is acceptable. This probability is calculated as follows (Teodorović, 2007):

$$p = e^{-\frac{\Delta F}{T}} \tag{19}$$

After computing the probability of accepting a new initial solution with $\Delta F \geq 0$, the next step is to generate a random number within the range [0,1]. Comparing this randomly generated number, denoted as r, with the calculated probability (p), a decision is made. If $r < p$, then the new feasible solution is adopted as the new initial solution; otherwise, it is discarded.

If, after numerous iterations, there has been no decrease in the objective function value, thermal equilibrium is reached. Thermal equilibrium is associated with the concept of epochs. An epoch involves defining S feasible solutions, where the parameter S is predefined. The condition for reaching thermal equilibrium is when, after the defined S feasible solutions in one epoch, there is no decrease in the objective function. The number of epochs is denoted as E, with E being predefined. Upon reaching thermal equilibrium, the temperature T is lowered, and then the described process repeats at the new temperature.

In this paper, the Simulated Annealing algorithm has been adapted for solving the standard Vehicle Routing Problem with Time Windows. The developed algorithm is based on the paper of Teodorović & Pavković

(1992). The application of the Simulated Annealing algorithm involves the following steps:

Step 1: Define the initial temperature (*T*), the number of epochs (*E*), the number of solutions to be generated within one epoch (*S)*, and the number of small perturbations during the generation of one solution (*P*).

Step 2: Generate the initial solution using the heuristic algorithm for minimizing fuel consumption.

Step 3: Randomly select two nodes from different routes and swap their positions. When considering the node swaps, ensure adherence to vehicle load constraints and time intervals. Repeat this step as many times as the number of small perturbations defined in step 1.

Step 4: Calculate the objective function value using formula (18). Then, compute the difference ΔF between the value of the new objective function and the value of the old objective function (20), which represents the total fuel consumption during the execution of the defined set of routes.

$$\Delta F = NF - OF \tag{20}$$

where:

NF – total fuel consumption for executing the new set of routes, and

OF – total fuel consumption for executing the old set of routes.

If $\Delta F < 0$, proceed to step 6. Otherwise, proceed to step 5.

Step 5: Using a uniform distribution, generate a random number $r \in [0,1]$. Calculate the probability *p* of increasing the objective function value by *ΔF* using the formula (19). If $r < p$, proceed to Step 6. If $r \geq p$, retain the old set of routes and proceed to step 7.

Step 6: Save the new set of generated routes and the total fuel consumption required for executing this set of routes. Proceed to step 7.

Step 7: If the number of generated solutions in the current epoch is fewer than *S*, return to Step 3. Otherwise, the epoch is completed. If the number of generated epochs equals *E*, terminate the algorithm; otherwise, if the objective function has not been reduced in the current epoch, decrease the temperature (start a new epoch) and return to Step 3, and if the objective function has been reduced, keep the existing temperature (start a new epoch) and return to step 3.

After generating the predefined number of epochs, the resulting solution represents a set of routes with lower fuel consumption than any other set of routes generated during the Simulated Annealing process. An enhanced application of the Simulated Annealing technique has been developed to improve this solution further.

The key difference between the initial and the enhanced applications of the Simulated Annealing technique lies in the method of generating the route sets. In the initial approach, feasible solutions were generated by randomly selecting and swapping two nodes from different routes, considering the vehicle load capacities and time windows. This meant that the selected nodes always came from different routes. For instance, node 5 might initially belong to route 1, but be reassigned to route 3 after applying the Simulated Annealing technique. By the end of the predefined number of epochs, each node was assigned to a specific route.

In the enhanced application, the nodes' affiliation with specific routes remains unchanged. Instead, only the order of nodes within each route is modified (Teodorović, 2007). This approach involves randomly selecting two nodes within the same route and swapping their positions while considering the time windows. This reordering of nodes is performed a predefined number of times. By altering the order in which the nodes are visited within a route, the goal is to further optimize the initial solution.

The described Simulated Annealing algorithm for improving the initial solution consists of the following steps:

Step 1: The same as in the previous algorithm.

Step 2: Take the best solution found in the previous application of the Simulated Annealing metaheuristic and set it as the initial solution.

Step 3: Select a node randomly. Then, find the route to which that node belongs, and randomly choose another node from that route. Swap the positions of these nodes if possible, taking into account the time intervals. Repeat this step as many times as needed to make small perturbations when defining one feasible solution, as specified in Step 1. Then proceed to Step 4.

Steps 4, 5, 6, and 7: The same as in the previous algorithm.

Results of testing the proposed algorithms

The results of solving the vehicle routing problem with vehicle load constraints and time windows in the context of goods distribution are presented in this section. Two algorithms were used: one for obtaining the initial solution (using a heuristic algorithm) and the other for improving that initial solution (using the Simulated Annealing metaheuristic), both considering fuel consumption. To implement the proposed algorithms, Java programming language was used on a 64-bit ACER computer with an Intel(R) Core(TM) i5 2.50 GHz processor and 8 GB of RAM.

Solomon's instances from rc201 to rc208 were used to test these algorithms (Sintef, 2008). To use any of these Solomon instances, it is

necessary to determine the distance between nodes, the travel time between nodes, and the vehicle's load capacity. Regarding vehicle load capacity, the recommended value for these instances is 1000 units. The Euclidean distance is recommended for determining the distance between nodes, and the travel time is considered equal to the spatial distance. That is, traveling one unit of length requires one unit of time (Xiao et al, 2012). When applying these algorithms, the total fuel consumption for the defined set of routes is calculated using formula (18), where the price of fuel is set to one, $c_0 = 1$. To use this formula, it is necessary to predefine the empty vehicle fuel consumption rate, ρ_0, and the full vehicle fuel consumption rate, ρ^*. The empty vehicle consumption rate is set to 2, and the full vehicle consumption rate is set to 3. The fuel consumption of an empty vehicle is one-third lower than that of a full vehicle, hence these predefined values (Xiao et al, 2012). These values for ρ_0 and ρ^* are used to calculate the fuel consumption for the defined routes in both algorithms to enable a comparison of their results.

After determining the distance matrix, travel time, and vehicle load capacity, as described previously, vehicle route formation can begin. It is necessary to find routes that allow visiting all 100 nodes in the network and satisfying each node's demand, i.e., delivering the goods they require. Each route should start and end at node 1, which represents the base. When forming routes, the vehicle load capacity and predefined time intervals must be considered. The total demand on one route must not exceed the vehicle's load capacity of 1000 units. The calculation of the distance matrix and the general characteristics related to the instances (number of nodes, load capacity, relationship between time and spatial distance, full and empty vehicle consumption rates, etc.) are the same when implementing the heuristic algorithm for minimizing fuel consumption and the Simulated Annealing metaheuristic. For the Simulated Annealing algorithm, the number of epochs ($E = 15$), the number of new solutions generated within an epoch ($S = 20$), the number of small perturbations ($P = 2$), and the initial temperature ($T = 150$) must be defined. Additionally, during thermal equilibrium, the temperature decreases by multiplying the old temperature by 0.9 ($T_{new} = 0.9 \cdot T_{old}$).

The analysis of the test results for the heuristic algorithm and the Simulated Annealing metaheuristic, both aimed at minimizing fuel consumption, is shown in Table 1. The table reveals that both algorithms consistently generated the same number of routes. For each instance, the total distance required to complete the defined set of routes is greater with the heuristic algorithm than with the Simulated Annealing algorithm. Regarding time, for half of the instances, the total time required to

complete the defined routes is shorter with the heuristic algorithm, whereas for the other half, it is shorter with the Simulated Annealing algorithm. The most critical criterion is fuel consumption, and in each instance, less fuel is consumed using the Simulated Annealing algorithm. Based on these results, it can be concluded that using the Simulated Annealing metaheuristic to improve the solutions obtained by the heuristic algorithm is fully justified.

Table 1 – Analysis of the results of applying the heuristic algorithm and after their improvement using the Simulated Annealing algorithm

Inst.	Heuristic algorithm				Simulated Annealing			
	Fuel consumption	Distance	Time	No. of routes	Fuel consumption	Distance	Time	No. of routes
rc201	425.95	2054.01	6224.19	11	401.45	1930.26	6253.87	11
rc202	434.62	2095.97	6179.30	11	371.42	1782.85	6431.54	11
rc203	417.09	2001.85	5774.57	10	331.34	1569.49	5868.55	10
rc204	284.51	1313.99	4178.67	7	267.20	1218.21	3811.43	7
rc205	435.68	2106.45	6088.63	10	361.82	1732.57	6211.51	10
rc206	352.50	1656.66	3432.71	6	317.07	1474.44	3384.35	6
rc207	333.58	1563.46	3697.37	6	321.22	1506.71	3488.19	6
rc208	281.70	1248.24	2025.92	3	254.11	1116.31	1993.59	3

The developed approaches (Heuristic algorithm and Simulated Annealing) are suitable for solving routing problems of small, medium, and large dimensions. This is shown by testing the approach on Solomon instances. In these instances, the problem of distribution of goods up to 100 objects is considered. For this dimension of the problem, the developed approach reaches a very good solution in a very short CPU time.

Table 2 presents the percentage reduction in fuel consumption, distance traveled, and execution time for the defined set of routes for each instance when the Simulated Annealing algorithm is applied to the heuristic algorithm's solution. Additionally, Figure 2 provides a graphical representation of fuel consumption for each instance, first using the heuristic algorithm to minimize fuel consumption, and then using the Simulated Annealing algorithm. The average percentage reduction in fuel consumption achieved by applying the Simulated Annealing algorithm is

10.93% per instance. The average reduction in the distance traveled is 11.60%, while the average reduction in the total route completion time is 1.16%. These results suggest that using the Simulated Annealing technique in combination with a heuristic algorithm for the initial solution, which considers fuel consumption, can significantly reduce the environmental impact and transportation costs for a company.

Table 2 – Percentage reduction in fuel consumption, distance, and time achieved by the Simulated Annealing metaheuristic compared to the heuristic algorithm

Instance	Simulated Annealing vs heuristic algorithm [%]		
	Fuel consumption	Distance	Time
rc201	5.75	6.03	-0.48
rc202	14.54	14.94	-4.08
rc203	20.56	21.60	-1.63
rc204	6.08	7.29	8.79
rc205	16.95	17.75	-2.02
rc206	10.05	11.00	1.41
rc207	3.71	3.63	5.66
rc208	9.79	10.57	1.60
Average	**10.93**	**11.60**	**1.16**

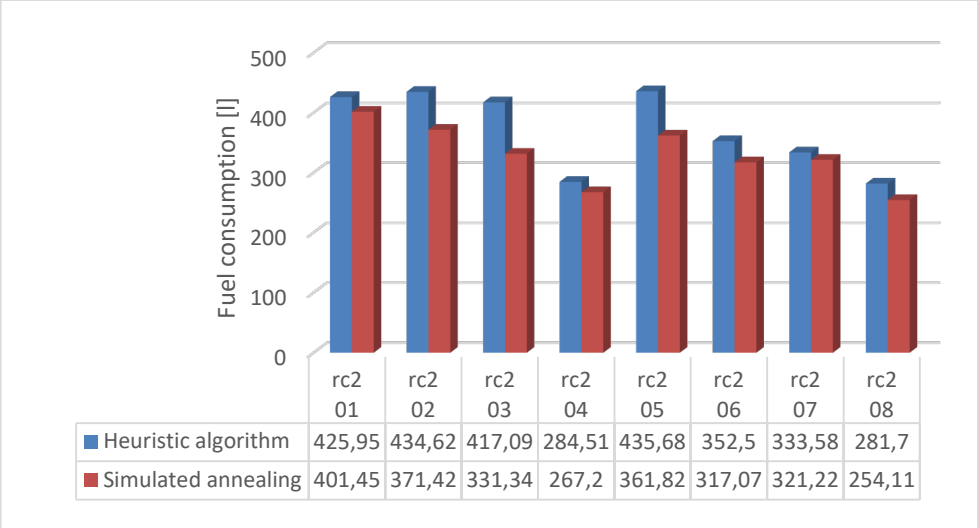

Figure 2 – Graphical representation of fuel consumption for each instance from rc201 to c208 using the heuristic algorithm and the simulated annealing metaheuristic

Conclusions

In-depth research on the standard vehicle routing problem dates back to the second half of the 20th century. At that time, the volume of transportation, and consequently the demand for it, was significantly lower than today. As a result, the harmful effects of vehicle emissions were not at the forefront of concern. However, with the global increase in population and rising living standards, both the need for transportation and customer demands have escalated. Consequently, in recent years, there has been a growing focus on environmental considerations, particularly in minimizing the adverse impacts of vehicle emissions during cargo distribution and collection.

The standard vehicle routing problem, which aims to optimize vehicle routes to reduce environmental impacts, is part of a relatively new research domain that has gained traction over the past decade. This paper demonstrates and substantiates the fact that a vehicle's fuel consumption is directly influenced by the volume of cargo it carries. For instance, when two clients are situated at comparable distances, priority should be given to the client with the larger cargo demand. This strategy ensures that the vehicle traverses the remaining route with a lighter load, consequently lowering fuel consumption, as vehicles with lighter loads consume less fuel.

To tackle this issue, a heuristic algorithm was developed to minimize fuel consumption. This algorithm builds upon the Nearest Neighbor Algorithm, aiming to minimize fuel consumption and, in turn, reduce environmental impact. Furthermore, to enhance the solutions provided by the heuristic, the Simulated Annealing metaheuristic was applied. The goal of Simulated Annealing is to make small changes to the initial solution, further reducing fuel consumption and, consequently, CO_2 emissions.

The analysis of the results after applying these two algorithms showed that using the Simulated Annealing algorithm results in an average fuel consumption reduction of 10.93% compared to using only the heuristic. Another advantage of combining the heuristic and the Simulated Annealing algorithm is the reduction in the total distance traveled and the overall time required for route completion. This approach leads to savings of 11.60% in total distance and 1.16% in total time compared with employing the heuristic alone. Based on these findings, it can be inferred that from both the environmental preservation and transportation company cost perspectives, employing a combination of a heuristic algorithm for fuel consumption minimization and the Simulated Annealing metaheuristic proves highly advantageous. Three directions for future research have been identified. The first relates to testing the developed approach on a

real example of a transport company. The second is to extend the model in a way that takes into account other factors that affect fuel consumption, such as: vehicle condition and age, vehicle utilization, etc. The third is to compare the developed approach with other metaheuristics such as Genetic Algorithms, Bee Colony Optimization, etc.

A potential problem when applying the developed approach may be that the fleet size is not considered. Therefore, it may happen that the observed fleet cannot implement all the generated routes. It should also be noted that a homogeneous fleet was observed when developing the approach. The mentioned limitations of the developed approach can be overcome with minor modifications.

References

Asghari, M. & Mirzapour Al-E-Hashem, S.M.J. 2021. Green vehicle routing problem: A state-of-the-art review. *International Journal of Production Economics*, 231, art.number:107899. Available at: https://doi.org/10.1016/j.ijpe.2020.107899.

Braekers, K., Ramaekers, K. & Van Nieuwenhuyse, I. 2016. The vehicle routing problem: State of the art classification and review. *Computers & Industrial Engineering*, 99, pp.300-313. Available at: https://doi.org/10.1016/j.cie.2015.12.007.

Chen, C., Demir, E. & Huang, Y. 2021. An adaptive large neighborhood search heuristic for the vehicle routing problem with time windows and delivery robots. *European Journal of Operational Research*, 294(3), pp.1164-1180. Available at: https://doi.org/10.1016/j.ejor.2021.02.027.

Ćirković, M. 2018. Ovo niste znali! Kolika je štetnost pogonskih goriva vozila. *Ekovest*, April 19 [online] Available at: www.eko-vest.com/ovo-niste-znali-kolika-je-stetnost-pogonskih-goriva-vozila/ (in Serbian) [Accessed: 10 January 2025].

Dantzig, G.B. & Ramser, J.H. 1959. The Truck Dispatching Problem. *Management science*, 6(1), pp.80-91. Available at: https://doi.org/10.1287/mnsc.6.1.80.

Desrochers, M., Lenstra, J., Savelsbergh, M.W.P., Soumis, F. 1988. Vehicle Routing with Time Windows: Optimization and Approximation. In: Golden, B.L. & Assad, A.A. (Eds.) *Vehicle Routing: Methods and Studies,* pp.65-84. Elsevier Science Publishers B.V. (North-Holland) [online]. Available at: https://ir.cwi.nl/pub/2036/2036D.pdf [Accessed: 10 January 2025].

Herdianti, W., Santoso Gunawan, A.A. & Komsiyah, S. 2021. Distribution cost optimization using pigeon inspired optimization method with reverse learning mechanism. *Procedia Computer Science*, 179, pp.920-929. Available at: https://doi.org/10.1016/j.procs.2021.01.081.

Huang, S.-H., Huang, Y.-H., Blazquez, C.A. & Chen, C.-Y. 2022. Solving the vehicle routing problem with drone for delivery services using an ant colony optimization algorithm. *Advanced Engineering Informatics*, 51, art.number:101536. Available at: https://doi.org/10.1016/j.aei.2022.101536.

Kirkpatrick, S., Gelatt Jr, C.D. & Vecchi, M.P. 1983. Optimization by Simulated Annealing. *Science,* 220(4598), pp.671-680. Available at: https://doi.org/10.1126/science.220.4598.671.

Konstantakopoulos, G.D., Gayialis, S.P. & Kechagias, E.P. 2022. Vehicle routing problem and related algorithms for logistics distribution: A literature review and classification. *Operational Research*, 22(3), pp.2033-2062. Available at: https://doi.org/10.1007/s12351-020-00600-7.

Liao, W., Liu, L. & Fu, J. 2019. A Comparative Study on the Routing Problem of Electric and Fuel Vehicles Considering Carbon Trading. *International Journal of Environmental Research and Public Health*, 16(17), art.number:3120. Available at: https://doi.org/10.3390/ijerph16173120.

Liu, C., Kou, G., Zhou, X., Peng, Y., Sheng, H. & Alsaadi, F.E. 2020. Time-dependent vehicle routing problem with time windows of city logistics with a congestion avoidance approach. *Knowledge-Based Systems*, 188, art.number:104813. Available at: https://doi.org/10.1016/j.knosys.2019.06.021.

Marinakis, Y. & Migdalas, A. 2007. Annotated bibliography in vehicle routing. *Operational Research*, 7, pp.27-46. Available at: https://doi.org/10.1007/BF02941184.

Napoli, G., Micari, S., Dispenza, G., Andaloro, L., Antonucci, V. & Polimeni, A. 2021. Freight distribution with electric vehicles: A case study in Sicily. RES, infrastructures and vehicle routing. *Transportation Engineering*, 3, art.number:100047. Available at: https://doi.org/10.1016/j.treng.2021.100047.

Pan, B., Zhang, Z. & Lim, A. 2021. Multi-trip time-dependent vehicle routing problem with time windows. *European Journal of Operational Research*, 291(1), pp.218-231. Available at:. https://doi.org/10.1016/j.ejor.2020.09.022.

Ramadhani, B.N.I.F. & Garside, A.K. 2021. Particle swarm optimization algorithm to solve vehicle routing problem with fuel consumption minimization. *JOSI Jurnal Optimasi Sistem Industri*, 20(1), pp.1-10 [online]. Available at: https://josi.ft.unand.ac.id/index.php/josi/article/view/140 [Accessed: 10 January 2025].

-Sintef. 2008. Solomon bechmark. *Sintef*, April 18 [online]. Available at: https://www.sintef.no/projectweb/top/vrptw/solomon-benchmark/ [Accessed: 10 January 2025].

Song, M.-x., Li, J.-q., Han, Y.-q., Han, Y.-y., Liu, L.-l. & Sun, Q. 2020. Metaheuristics for solving the vehicle routing problem with the time windows and energy consumption in cold chain logistics. *Applied Soft Computing*, 95, art.number:106561. Available at: https://doi.org/10.1016/j.asoc.2020.106561.

Teodorović, D. 2007. *Transportne mreže*, *4th Edition*. Belgrade: University of Belgrade, Faculty of Transport and Traffic Engineering (in Serbian). ISBN: 978-86-7395-239-0.

Teodorović, D. & Pavković, G. 1992. A simulated annealing technique approach to the vehicle routing problem in the case of stochastic demand. *Transportation Planning and Technology*, 16(4), pp.261-273. Available at: https://doi.org/10.1080/03081069208717490.

Tiwari, A. & Chang, P. 2015. A block recombination approach to solve green vehicle routing problem. *International Journal of Production Economics*, 164, pp.379-387. Available at: https://doi.org/10.1016/j.ijpe.2014.11.003.

Xiao, Y., Zhao, Q., Kaku, I. & Xu, Y. 2012. Development of a fuel consumption optimization model for the capacitated vehicle routing problem. *Computers & Operations Research*, 39(7), pp.1419-1431. Available at: https://doi.org/10.1016/j.cor.2011.08.013.

Planificación de rutas de vehículos para optimizar el consumo de combustible

Predrag Grozdanović, **autor de correspondencia**, *Miloš* Nikolić, *Milica* Šelmić

Universidad de Belgrado, Facultad de Ingeniería de Transporte y Tráfico, Departamento de Investigación Operativa en Transporte y Tráfico, Belgrado, República de Serbia

CAMPO: investigación de operaciones, logística, transporte, tráfico
TIPO DE ARTÍCULO: artículo científico original

Resumen:

Introducción/objetivo: Los modelos desarrollados para rutas de vehículos de transporte con un enfoque ambiental se dedican predominantemente a la logística inversa o al transporte de cargas ambientalmente peligrosas. Pocos modelos en la bibliografía relevante consideran los factores ecológicos para las rutas de vehículos involucrados en la distribución de bienes de consumo.

Métodos: Este artículo presenta un modelo de planificación de rutas vehiculares para optimizar el consumo de combustible, considerando las ventanas de tiempo requeridas para el servicio y la capacidad de carga útil de los vehículos. Se desarrolló un algoritmo heurístico para minimizar el consumo de combustible. Se aplicó una metaheurística de adaptación simulada para mejorar las soluciones obtenidas por la heurística propuesta.

Resultados: Se presentan los resultados del algoritmo heurístico para la reducción del consumo de combustible y los resultados mejorados utilizando la metaheurística de adaptación simulada. Todas las pruebas se realizaron en las instancias de Salomón.

Conclusión: El enfoque desarrollado para las rutas de vehículos garantiza un compromiso entre las empresas de transporte y la ecología. Los resultados muestran que la aplicación de este enfoque puede reducir simultáneamente los costes de la empresa de transporte y las emisiones de CO_2.

Palabras claves: rutas de vehículos, consumo de combustible, adaptación simulada, algoritmo heurístico.

Планирование маршрутизации транспортных средств с целью оптимизации расхода топлива

Предраг Грозданович, **корреспондент**, *Милош* Николич, *Милица* Шелмич

Белградский университет, факультет транспорта и организации движения, кафедра исследований операций на транспорте, г. Белград, Республика Сербия

РУБРИКА ГРНТИ: 27.47.19 Исследование операций,
73.47.12 Организация управления и автоматизированные системы управления транспортом
81.88.00 Материально-техническое снабжение. Логистика

ВИД СТАТЬИ: оригинальная научная статья

Резюме:

Введение/цель: Модели, разработанные для маршрутизации транспортных средств, ориентированных на охрану окружающей среды, в основном предназначены для обратной логистики или перевозки опасных для окружающей среды грузов. Однако лишь немногие модели в релевантной литературе учитывают экологические факторы для маршрутизации транспортных средств, участвующих в распределении товаров широкого потребления.

Методы: В данной статье представлена модель планирования маршрутизации транспортных средств для оптимизации расхода топлива с учетом временных интервалов, необходимых для обслуживания и грузоподъемности транспортных средств. Для минимизации расхода топлива был разработан эвристический алгоритм. Для улучшения решений, полученных с помощью предложенной эвристики, была применена имитационная метаэвристика отжига.

Результаты: В статье представлены результаты эвристического алгоритма для минимизации расхода топлива и улучшенные результаты с использованием метаэвристики имитационного отжига. Все испытания проводились на «Solomon instances».

Вывод: Разработанный подход к маршрутизации транспортных средств является компромиссным решением для транспортных компаний по отношению к экологии. Результаты показывают, что применение данного подхода позволяет одновременно минимизировать затраты транспортной компании и выбросы CO_2.

Ключевые слова: маршрутизация транспортных средств, расход топлива, имитация отжига, эвристический алгоритм.

Планирање рута возила ради оптимизације потрошње горива

Предраг Гроздановић, **аутор за преписку**,
Милош Николић, *Милица* Шелмић

Универзитет у Београду, Саобраћајни факултет,
Катедра за операциона истраживања у саобраћају,
Београд, Република Србија

ОБЛАСТ: операциона истраживања, логистика, транспорт, саобраћај
ВРСТА ЧЛАНКА: оригинални научни рад

Сажетак:

Увод/циљ: Модели развијени за рутирање транспортних возила, са фокусом на животну средину, претежно су посвећени повратној логистици или транспорту терета опасног по животну средину. У релевантној литератури неколико модела разматра еколошке факторе за усмеравање возила укључених у дистрибуцију робе широке потрошње.

Методе: У раду је представљен модел за планирање рута возила ради оптимизације потрошње горива, водећи рачуна о временским оквирима у којима се опслуга може извршити и носивости возила. Развијен је хеуристички алгоритам чији је циљ смањење потрошње горива. Такође, метахеуристика симулирано каљење примењена је да би се побољшала решења добијена предложеном хеуристиком.

Резултати: Приказани су резултати хеуристичког алгоритма за минимизацију потрошње горива и побољшани резултати применом метахеуристике симулирано каљење. Сви тестови су спроведени на Соломоновим инстанцама.

Закључак: Развијени приступ за рутирање возила обезбеђује компромис између транспортних компанија и екологије. Резултати показују да се применом овог приступа могу истовремено минимизирати трошкови транспортне компаније и емисија CO_2.

Кључне речи: рутирање возила, потрошња горива, симулирано каљење, хеуристички алгоритам.

Paper received on: 13.01.2025.
Manuscript corrections submitted on: 26.03.2025.
Paper accepted for publishing on: 27.03.2025.

Digital signal processing in MIMO radars with time-multiplexed transmit signals

Borko B. Đaković[a], *Slobodan* M. Simić[b],
Lidija M. Trivundža[c], *Aleksandar* G. Ristić[d]

[a] Serbian Armed Forces, General Staff,
Telecommunications and Information Technology Directorate (J-6),
Center for Applied Mathematics and Electronics,
Belgrade, Republic of Serbia,
e-mail: borkodj2001@gmail.com, **corresponding author**,
ORCID iD: https://orcid.org/0009-0000-4662-3981

[b] University of Defence in Belgrade, Military Academy,
Department for Military Electronic Systems,
Belgrade, Republic of Serbia,
e-mail: slobodan.simic@va.mod.gov.rs,
ORCID iD: https://orcid.org/0000-0002-6846-4886

[c] Serbian Armed Forces, General Staff,
Development and Equipment Directorate (J-5),
Technical Test Center, Belgrade, Republic of Serbia,
e-mail: lidija.trivundza@gmail.com,
ORCID iD: https://orcid.org/0009-0004-7040-8586

[d] Ministry of Defence of the Republic of Serbia,
Military Technical Institute, Belgrade, Republic of Serbia,
e-mail: ristic1504@gmail.com,
ORCID iD: https://orcid.org/0009-0003-1994-2815

https://doi.org/10.5937/vojtehg73-54972

FIELD: digital signal processing, telecommunications, electronic, electromagnetic
ARTICLE TYPE: original scientific paper

Abstract:

Introduction/purpose: A current topic of significant research and development efforts in the field of radar systems is MIMO (Multiple-Input-Multiple-Output) radar technology. MIMO radars represent a revolutionary step forward in radar technology, as the use of multiple transmitting antennas that emit orthogonal waveforms enables improved detection and angular resolution. To achieve effective results, high-quality digital signal processing and the application of advanced algorithms are essential for obtaining target information. This paper places special emphasis on coherent MIMO radars, with the objective of enhancing angular resolution. Time-multiplexing of transmit signals is applied as a primary method to achieve orthogonality between signals, utilizing a Frequency Modulated Continuous Wave (FMCW) signal as the foundation for the transmit waveform. The aim of this paper is to provide and explain the fundamentals

of digital signal processing in MIMO radars, present analytical expressions, and validate them through simulation and experimental verification.

Methods: The theoretical foundations are presented, with the Discrete Fourier Transform (DFT) used as a primary tool in digital signal processing to obtain information about the distance, velocity, and azimuth of the target. A simulation was developed in the MATLAB software package to analyze the performance of the radar system model. Experimental verification was conducted, where specific scenarios were recorded using the radar platform PUP_DUAL24P_T2R4, and the collected data was subsequently processed. The MATLAB functions MIMOFMCW and procDC were written to generate simulation samples of echo signals and to automate signal processing and the display of characteristic Range-Velocity and Range-Angle matrices.

Results: The simulation and experimental verification confirm the validity of the theoretical foundations related to digital signal processing in MIMO radars, and the target parameters can be clearly determined.

Conclusion: The Discrete Fourier Transform is a simple tool that provides satisfactory results for determining the range, velocity, and angle of targets. FMCW radars offer accuracy in determining range and velocity, while the MIMO mode enhances angular resolution. The DFT algorithm is capable of determining the target angle, but with a certain error, making the use of high-resolution methods necessary for more accurate angle determination.

Key words: MIMO, radar, TDM, FMCW, radar data cube, DFT, beat frequency, virtual antenna.

Introduction

MIMO radars are modern and advanced radar systems in which, unlike conventional radar systems, each transmitting antenna transmits an arbitrary waveform independently of other transmitting antennas. MIMO radars transmit uncorrelated signals in different directions or transmit mutually orthogonal signals in the same direction. Due to different waveforms and orthogonality between signals, receiving antennas can separate the echo signals originating from a target and assign them to a specific transmitter, which are then collected and further processed. This approach improves the probability of target detection and the accuracy of estimating the angle of arrival of echo signals (Stoica & Li, 2008; Wiesbeck et al, 2015).

MIMO technology has wide applications in telecommunications, significantly enhancing data transmission capacity and speed, particularly in 5G and 6G systems (Dessai & Patidar, 2024) through Massive MIMO technology (Wanga et al, 2021), which utilizes antenna arrays for spatial

diversity (Abdi & Rasheed, 2022). This technology improves angular resolution and accuracy in radar systems (Janoudi et al, 2023), which is especially important for automotive radars in the mm-wave range, enabling clear detection of objects and supporting the development of unmanned vehicles and their communication with one another (Han et al, 2024). Additionally, MIMO technology is increasingly used in Synthetic Aperture Radar (SAR) systems for terrain imaging (Wu et al, 2019) and in medicine for monitoring human vital signs (Alizadeh et al, 2019), detection glucose levels (Omer et al, 2018) and detecting tumors (Bliss & Forsythe, 2006) using the mm-Wave radar.

One of the primary classifications of MIMO radars is based on the antenna configuration. Accordingly, they can be divided into MIMO radars with widely spaced antennas, or statistical MIMO radars, and MIMO radars with collocated antennas, or coherent MIMO radars (Sun, 2023).

In statistical MIMO radars, the transmit and receive antennas are widely separated, providing independent scattering responses for each antenna pair (Figure 1a). By positioning antennas at different locations, the target is illuminated from various angles, mitigating the effects of a reduced radar cross-section and a poor electromagnetic wave scattering response. This results in more robust detection performance and reduces the likelihood of missing the target. In the other case, the transmit and receive antennas of a coherent MIMO radar are positioned relatively close together (Figure 1b).

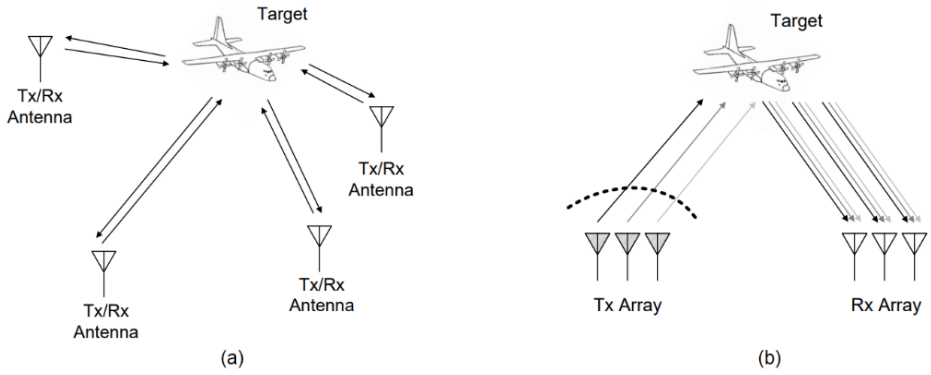

Figure 1 – Statistical MIMO radar (a) and coherent MIMO radar (b) (Sun,2023)

Here, it is assumed that the electromagnetic wave scattering response from the target is the same for each antenna pair, with minimal delay. The antennas of a MIMO radar transmit waveforms independently of each other. The goal is to use coherent signal processing to form a

virtual array of antennas, providing improved estimation of the signal's angle of arrival. This approach ensures that fewer antennas can achieve the effect of a larger antenna array on reception, enhancing the radar's angular resolution (Stoica & Li, 2008; Sun, 2023; Davis et al, 2014).

To prevent signal interference during transmission and ensure that receivers can successfully distinguish and assign signals to the correct transmitter, it is necessary for the signals to be orthogonal to each other. Signal orthogonality significantly simplifies further processing. Typical methods of achieving orthogonality include using time-division multiplexing (TDM) (Sun et al, 2014), frequency-division multiplexing (FDM) (Liu, 2009), and code-division multiplexing (CDM) (He et al, 2009).

In time-division multiplexed signals (TDM), orthogonality is achieved by having the transmitting antennas emit signals at different times. While one antenna is transmitting, the other antennas do not emit any signal. This method is simple to implement as it can use a single transmitter and a microwave switch, but it requires precise time synchronization and, in this way, the full transmission capacity is not utilized (Sun et al, 2014).

Formation of virtual antennas in MIMO radars

MIMO coherent radars, by emitting mutually orthogonal waveforms, can form a virtual antenna array and thereby increase angular resolution without increasing the number of receiving antennas. Virtual antennas are formed by combining signals from multiple transmitters and receivers. The number of virtual antennas that can be achieved is:

$$N_{\mathrm{R}} = N_{\mathrm{T_x}} \cdot N_{\mathrm{R_x}} \tag{1}$$

where N_{Tx} is the number of transmitting antennas, and N_{Rx} is the number of receiving antennas. In MIMO radar systems with a linear antenna array, the transmitting antennas must be spaced at a distance of $d_{\mathrm{T_x}} = N_{\mathrm{R_x}} \cdot d_{\mathrm{R_x}}$, where N_{Rx} is the number of receiving antennas and d_{Rx} is the distance between receiving antennas.

By measuring the phase delays $\Delta\phi$ of the signals at the elements of the receiving antenna array, the angle at which the target is located is determined. In the case shown in Figure 2a), the second transmitting antenna, due to its distance from the reference transmitting antenna, introduces an additional phase shift of $4\cdot\Delta\phi$. The signal from the first receiving antenna sent by the second transmitting antenna will be phase-shifted by $4\cdot\Delta\phi$, which would correspond to the fifth receiving antenna. Using this approach, eight virtual receiving antennas are formed, whose signal model is equivalent to a physical scenario with one transmitter and

eight receiver antennas (Figure 2b). This holds true assuming that the target is located in the far field relative to the antennas and that the reflected wave from the target reaches the receiving antennas as a plane wave (Rao, 2018).

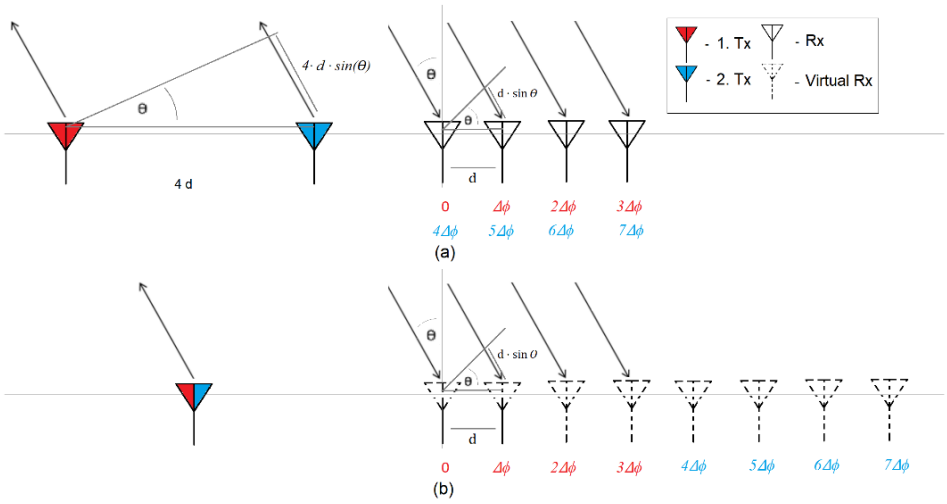

Figure 2 – MIMO Antenna Array (a) and Virtual Antenna Array(b)

Mathematical signal model in a coherent MIMO radar

The next chapter presents and explains the radar system model used in the research, as well as the form of the transmitted signal. The models were created based on the radar platform that was used at the end of the research for conducting experimental verification.

Model FMCW radar system

The signal generator generates the FMCW signal $x_T(t)$, which after the power amplifier (PA) is emitted from the transmitting antenna *T*x. After the signal hits the object, part of the signal energy is reflected from the object (echo signal) and returns back to the receiving antenna *R*x, where it is received as a signal $x_R(t)$ (Figure 3). After that, the signal $x_R(t)$ goes to the quadrature receiver, where it is mixed with the signal $x_T(t)$ and the signal $x_T(t)$ whose phase is shifted by 90º. In this way, two signals are obtained, one in phase (I Signal) and one in quadrature (Q Signal), which pass through a low-pass filter (LPF) after the mixer. In this way, an intermediate frequency (IF) signal is obtained, which after the analog-digital converter (ADC) is forwarded to digital signal processing (DSP),

where the range, velocity, and azimuth of the target are determined (Mahafza, 2013).

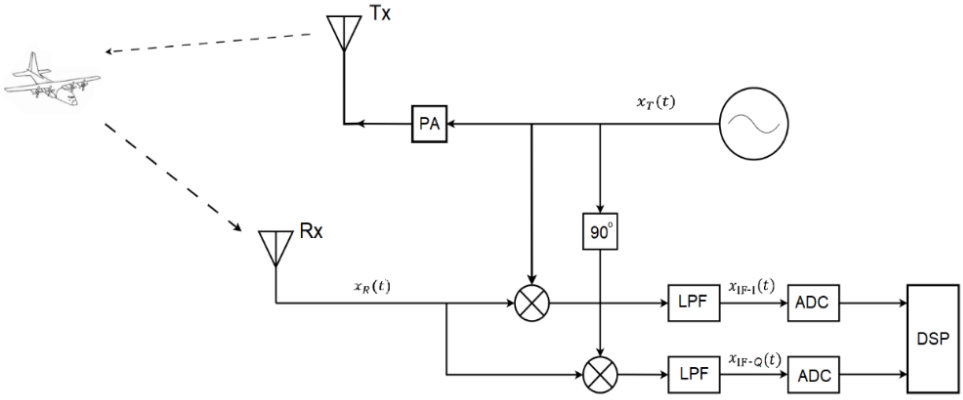

Figure 3 – Block diagram of the radar system

FMCW Signal

The radar system transmits a linearly increasing FMCW signal, which ensures a large product of signal duration and frequency bandwidth (*tB*), simultaneously enabling high range resolution and a high signal-to-noise ratio (Richards, 2014).

The characteristics of the FMCW signal are: the starting frequency f_c, the bandwidth *B,* the chirp signal duration T_C, and the ramp slope coefficient *S* (Figure 4). The ramp slope coefficient is calculated as (Iovescu & Rao, 2016):

$$S = \frac{B}{T_C}. \tag{2}$$

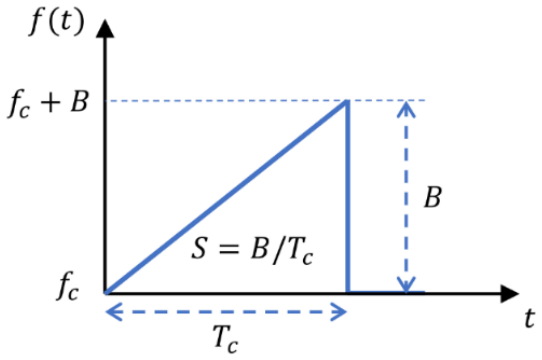

Figure 4 – FMCW chirp signal (Li et al, 2021)

The FMCW signal can be mathematically represented as (Li et al, 2021):

$$x_T = A_{\mathrm{T}} \cos(2\pi f_{\mathrm{C}}\, t \; + \; \pi S\, t^2), \tag{3}$$

while the instantaneous frequency is determined as (Li et al, 2021):

$$f(t) = \frac{1}{2\pi}\frac{d}{dt}(2\pi f_{\mathrm{c}}\, t \; + \; \pi S\, t^2) = f_{\mathrm{c}} + S\, t. \tag{4}$$

The radar system receives the echo signal $x_R(t)$ in its receiver and mixes it with the transmit signal $x_T(t)$ and $x_T(t)$ phase-shifted by π/2. As the frequency of the transmitted FMCW signal $x_T(t)$ increases linearly over time, at the moment when the echo signal $x_T(t)$ arrives at the receiver, the frequencies $f_T(t)$ and $f_R(t)$ of the transmitted and received signals will not be the same (Figure 5a). The difference in frequencies occurs because the transmitted signal changes frequency during the time as the signal is emitted, reflected from the object, and returned to the receiver. After the mixer, the signals is fed to a low-pass filter. The low-pass filter passes the lower sideband of the signals, i.e., the signal component located at the frequency $f_T(t)$-$f_R(t)$, and removes the signal component located at the frequency $f_T(t)$+$f_R(t)$ and the resulting signals are $x_{IF\text{-}I}(t)$ and $x_{IF\text{-}Q}(t)$. The signals can be represented (Iovescu & Rao, 2016) as:

$$x_{\mathrm{IF-I}}(t) = LPF\{x_{\mathrm{T}}(t) \cdot x_{\mathrm{R}}(t)\} = A_{\mathrm{IF-I}} \cos(2\pi f_{\mathrm{IF}}\, t \; + \; \phi_{\mathrm{IF-I}}) + n(t) \tag{5}$$

$$x_{\mathrm{IF-Q}}(t) = A_{\mathrm{IF-Q}} \cos\left(2\pi f_{\mathrm{IF}}\, t \; + \; \phi_{\mathrm{IF-Q}}\right) + n(t) \tag{6}$$

where A_I and A_Q are the amplitude, $\phi_{IF\text{-}I}$ and $\phi_{IF\text{-}Q}$ are the phases of the signal $x_{IF\text{-}I}(t)$ and $x_{IF\text{-}Q}(t)$, $f_{IF} = f_T(t)$-$f_R(t)$ is the frequency and is the same for both signals, and $n(t)$ is noise. The f_{IF} is constant in time(Figure 5b) and this frequency is called *beat frequency* (Li et al, 2021). Figure 5 refers to only one chirp and one target.

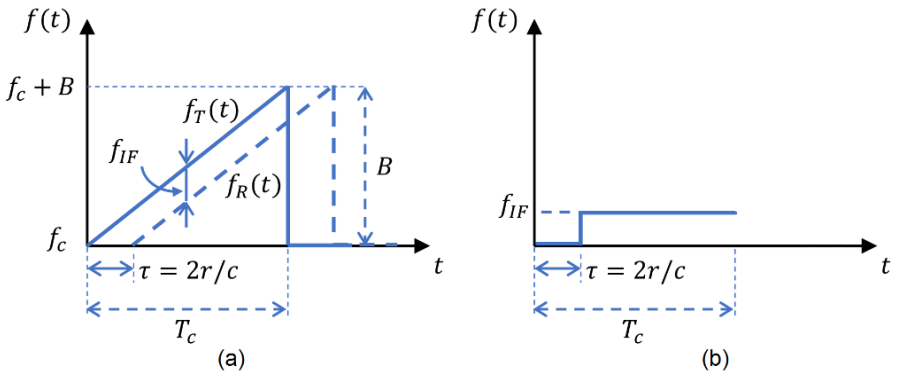

Figure 5 – Frequency of the transmitted and received chirp signal (a), frequency of the signal at the intermediate frequency (b) (Li et al, 2021)

The signals $x_{\mathrm{IF-I}}(t)$ and $x_{\mathrm{IF-Q}}(t)$ are sampled and form the signal $x_{\mathrm{IF}}[n] = x_{\mathrm{IF-I}}[n] + jx_{\mathrm{IF-Q}}[n]$. Viewed in the time domain, it can be observed that a complex exponential IF signal is obtained at the output of the quadrature receiver, which is equal to (Li et al, 2021; Ramasubramanian, 2017):

$$x_{\mathrm{IF}} = A\, e^{j(2\pi \cdot f_{\mathrm{IF}} \cdot t + \phi_{\mathrm{IF}})} + n(t)\ , \tag{7}$$

where is the amplitude $A = \sqrt{{A_{\mathrm{IF-I}}}^2 + {A_{\mathrm{IF-Q}}}^2}$, phase $\phi_{\mathrm{IF}} = tan^{-1}(\frac{\phi_{\mathrm{IF-Q}}}{\phi_{\mathrm{IF-I}}})$ and f_{IF} is the frequency of the signal x_{IF}.

The transmission signal is reflected from an object located at a range r and arrives at the receiving antennas with a delay τ , which is calculated as: $\tau = \frac{2r}{c}$, where c is the speed of light, that is the speed of electromagnetic wave propagation. If the target does not move, the frequency of the IF signal remains constant during the reception period, while the transmit and receive chirp signals overlap in time and are equal to: $f_{\mathrm{IF}} = f_T(t) - f_R(t) = S\,\tau$.

The phase of the IF signal can be determined at the moment of IF signal onset, when the reflected chirp signal arrives at the receiving antenna. Taking into account expression (3), the phase of the chirp signal is approximately equal to (Li et al, 2021): $\phi_{\mathrm{IF}} \approx 2\pi\, f_c\, \tau$.

It turns out that the frequency and phase of the IF signal, which is received from an object located at a range r, is equal to(Li et al, 2021):

$$f_{\mathrm{IF}} = S\,\tau = \frac{2\,S\,r}{c}, \tag{8}$$

$$\phi_{\mathrm{IF}} = 2\pi\, f_c\, \tau = \frac{4\pi\, r}{\lambda}. \tag{9}$$

When the chirp signal is bounced from multiple targets back to the radar, the received IF signal is a linear combination of multiple IF signals, each with a frequency and phase corresponding to the range of each individual target.

Digital processing of radar signals

This chapter explains the organization of radar data that is suitable for further processing. The standard flow of signal processing is shown and it is explained how to determine the DFT coefficients and thus obtain information about the target.

Radar signal sampling

A radar data cube is a three-dimensional data structure, which is a convenient way to conceptually represent the time-space processing of radar data. This way of organizing data is common to all modern radar systems, whether they are pulsed or continuous radars. The cube of radar data contains three axes and its cells contain the selected values of the reflected IF signal (Figure 6) (MathWorks, 2024). For MIMO radars and virtual antennas, the formation of a unified radar data cube is shown in Figure 11.

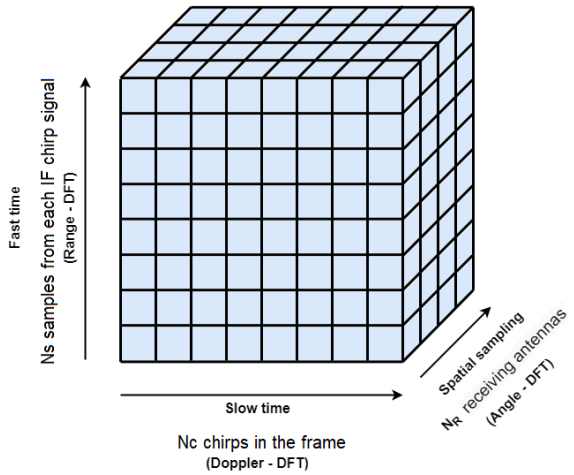

Figure 6 – Radar data cube

In the Fast Time Axis, signal samples are placed within a single chirp, i.e., within the repetition period of the radar signal (pulse) in pulse radars. This axis contains N_S samples, selected at a frequency F_S. The Slow Time Axis contains data from multiple chirp signals, with multiple chirps forming a single frame. In the Spatial Axis, samples of the signal received by all receiving antennas are placed. The spatial axis contains N_R samples, equal to the number of receiving antennas. In the case of MIMO radars, it contains a number of samples equal to the number of virtual receiving antennas (MathWorks, 2024).

The flow of digital radar signal processing

The digital radar signal processing flow includes a series of steps that involve processing the raw radar signal to obtain target information (Figure 7). As the output of the processing, the Range-Velocity and Range-Angle matrices are obtained, which provide all three important pieces of

information about the target. Later, the classification and tracking procedure can be entered (Li et al, 2021, p.167967).

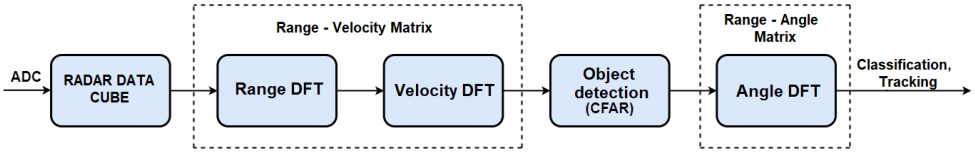

Figure 7 – Flow of digital processing of the radar signal

After AD conversion of the IF signal, the samples are organized into a radar data cube. Radar data cubes are formed, as explained in the chapter above, from samples of signals originating from different transmitting antennas. After organizing the data, the first step is to determine the Range DFT coefficients on each of the sampled IF chirp signals. The range DFT is applied along the columns to all chirps and from all virtual antennas. By applying the Discrete Fourier Transform (DFT) along the fast time axis, the *beat frequency* is observed and information about the distance of the targets is obtained. After the Range DFT, over the already calculated DFT coefficients, the Velocity DFT (Doppler DFT) is applied along all rows within the frames of all receiving virtual antennas. By applying the DFT along the slow time axis, the phase shift caused by the movement of the target is observed, Doppler processing is performed and information on the speed of the target's movement is obtained (Figure 8a). In this paper, all Range – Velocity DFT coefficients were calculated for the matrix representation, but in general, not all coefficients are used. By combining these two DFT algorithms, the Range-Velocity matrix is obtained for all virtual antennas (Li et al, 2021, p.167967).

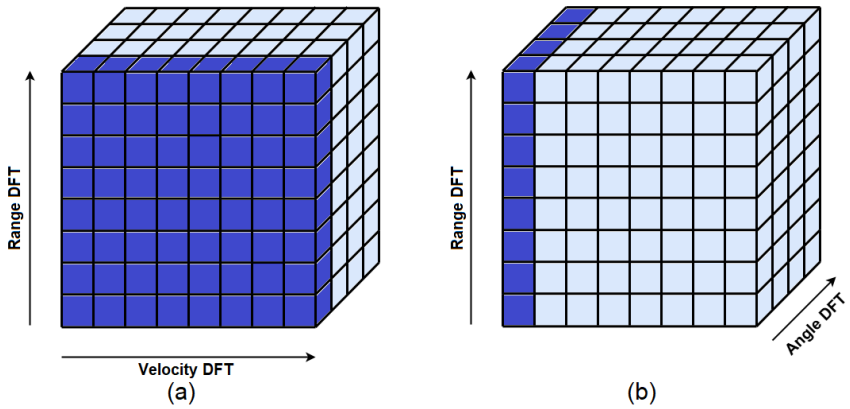

Figure 8 – Range and Velocity DFT (a), Range and Angle DFT (b)

Target detection is performed on the Range-Velocity matrices or CFAR (Constant False Alarm Rate) is applied in order to separate targets from noise. These algorithms are performed on the Range-Velocity matrices of all antennas. All matrices are summed into a single combined Range-Velocity matrix, where even targets with a low SNR (Signal-to-Noise Ratio), which were not detected in all matrices, will be observed.

After the detection of targets, or the application of CFAR and filtering in the frequency domain, the Angle DFT in the third dimension of the radar data cube is applied over the calculated DFT coefficients, over all virtual antennas (Figure 8b). Since the duration of the frame is a few milliseconds, it can be assumed that targets, due to their movement, will not change the resolution cell, and before the Angular DFT, it is not necessary to perform Doppler phase compensation. The Range-Angle matrices are obtained for each of the possible velocity of the targets. Finally, by adding all the amplitude characteristics of the Range-Angle matrices, one unified matrix is obtained that provides information about the distance and the angle at which the target is located. The amplitude characteristics of the matrices are displayed using a two-dimensional heat map or in a three-dimensional display. By observing the maximum of the functions, the distance, velocity, and azimuth of the target are determined (Li et al, 2021, p.167967).

Range DFT

By applying the DFT along the fast time axis, the N_S of the signal samples is obtained. According to the theory of the discrete Fourier transform, each cell of the DFT corresponds to the frequency $f_k = k\frac{f_S}{N_S}$ for $0 \leq k < N_S$. Based on expression (8), which describes the relationship between the *beat frequency* and the distance of the targets, and the calculation of the frequency in the DFT cells, it is concluded that the distance of the targets in relation to the DFT cell is equal to (Li et al, 2021):

$$r_k = f_k \frac{c}{2S} = k \frac{cf_S}{2SN_S} \tag{10}$$

for $0 \leq k < N_S$. By applying the Range DFT, and displaying the amplitude spectrum $|X[k]|$, a peak in the cell is observed on the range and by applying expression (10) the distance to the target corresponding to the reflected signal can be determined (Li et al, 2021).

In this application f_{IF} is positive, due to the assumed signal and system model. The use of a quadrature receiver the spectrum of a complex exponential signal (7) can be observed on the full spectrum from *0* to f_s, by considering the spectrum at negative frequencies, ranging from $-f_s/2$ to 0, as the spectrum at frequencis from $f_s/2$ to f_s. (Ramasubramanian, 2017). In

this regard, the maximum distance at which an object can be detected, with the condition that $f_{IF} < f_s$. is equal to (Li et al, 2021, p.167962):

$$r_{max} < \frac{c\, f_s}{2S}. \tag{11}$$

The received signal is a linear combination of several individually reflected signals from objects at different distances. As the DFT is a linear transform, the total signal spectrum is a linear combination of multiple individual spectra from each signal. Targets at different distances will appear in different cells of the spectrum and we can distinguish them if their mutual distance is greater than the resolution cell by the distance r_s. Therefore, the range resolution depends on the frequency detection resolution $f_{\mathrm{res}} = \frac{f_s}{N_s}$, so the range resolution is equal to (Li et al, 2021, p.167962):

$$r_{\mathrm{res}} = f_{\mathrm{res}} \frac{c}{2S} = \frac{c f_s}{2SN_s}. \tag{12}$$

Velocity DFT

The radar emits an N_c chirp signal of the duration T_c within the frame duration T_f (Figure 9). In order to measure the velocity of the target's movement, the radar must transmit a minimum of two separate chirp signals within the frame in order to detect the phase change due to the target's movement. If the target is moving at the radial speed v_r, during the time period until the next signal T_c is transmitted, the target travels the distance $\Delta r = v_r \cdot T_c$ (Li et al, 2021, p.167962).

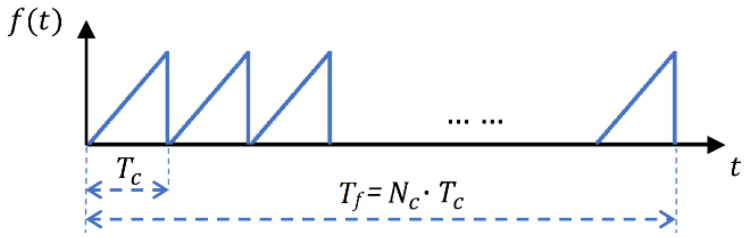

Figure 9 – Transmitted frame of the N_c chirp signal (Li et al, 2021)

The difference in the frequency of the two IF signals is negligible, while based on the signal model (9), the phase difference is equal to (Li et al, 2021):

$$\Delta\phi = \frac{4\pi\Delta r}{\lambda} = \frac{4\pi v_r T_c}{\lambda}. \tag{13}$$

Applying the DFT along the slow time axis gives the target velocity equal to (Li et al, 2021):

$$v_l = \omega_l \frac{\lambda}{4\pi T_c} = l \frac{\lambda}{2N_c T_c} = l \frac{\lambda}{2T_f}, \quad (14)$$

where $\omega_l = \frac{2\pi l}{N_c}$, N_c is the number of Velocity DFT samples and $-\frac{N_c}{2} \leq l < \frac{N_c}{2}$ assuming that N_c is an even number (Proakis & Manolakis, 2014). T_f is the frame duration or also known as the time on the target.

Unambiguous velocity measurement is performed in the range $-\pi \leq \omega < \pi$, so the unambiguous detectable velocity is equal to (Li et al, 2021):

$$-\frac{\lambda}{4T_c} \leq v < \frac{\lambda}{4T_c}, \quad (15)$$

where positive speed means a movement towards from the radar, and a negative movement occurs away from the radar.

The velocity resolution is equal to one resolution cell and amounts to (Li et al, 2021):

$$v_{res} = \frac{\lambda}{2N_c T_c} = \frac{\lambda}{2T_f}. \quad (16)$$

It is concluded that the longer the frame, the better the separation of two targets with similar velocity, with the condition that the target does not move to another resolution cell during that time.

Angle DFT

By using an array of receiving antennas, the angle of arrival of the echo signal can be estimated. The echo wave arrives at a certain angle to the receiving array and due to the mutual distance between the receiving antennas, a relative signal delay occurs between the two receiving antennas. Signal delay is reflected in the change in frequency and phase of the IF signal. The frequency change is negligibly small while the phase shift is equal to (Li et al, 2021):

$$\Delta\phi = 2\pi f_c \Delta\tau = \frac{2\pi d \sin(\theta)}{\lambda}, \quad (17)$$

where $\Delta\tau$ is the signal delay, due to the spacing between the receiver antennas and it is equal $\Delta\tau = d \sin(\theta) / c$ (Figure 2).

Applying the DFT to all antennas results in the angle under which the target is located being equal to (Li et al, 2021):

$$\theta u = sin^{-1}(\omega_u \frac{\lambda}{2\pi d}) = sin^{-1}(u \frac{\lambda}{Nd}), \quad (18)$$

where $\omega_u = \frac{2\pi u}{N}$ (Proakis & Manolakis, 2014), *N* is the number of Angle DFT samples, $-\frac{N}{2} \leq u < \frac{N}{2}$, assuming that *N* is an even number and *d* is the distance between the receiving antennas.
An unambiguous estimate of the angle can be determined in the range:

$$-sin^{-1}(\frac{\lambda}{2d}) \leq \theta < sin^{-1}(\frac{\lambda}{2d}). \quad (19)$$

In real applications, the distance between the antennas is often taken as the value $d = \frac{\lambda}{2}$, which corresponds to the fact that the angle can be estimated in the range *-90º ≤ θ < 90º,* where θ is defined in relation to broadside.

The angular resolution θ_{res} depends on the number of N_R receiving antennas and the central viewing angle of the target $\tilde{\theta}$ and is equal to (Li et al, 2021):

$$\theta\text{res} = |\Delta\theta| = 2 \cdot sin^{-1}(\frac{\lambda}{2N_R d\, cos(\tilde{\theta})}). \quad (20)$$

Assuming that $\tilde{\theta} = 0$ and $d = \frac{\lambda}{2}$, a rough estimate of the angular resolution is obtained, which is equal to (Li et al, 2021):

$$\theta\text{res} = \frac{2}{N_R}. \quad (21)$$

Improvement of angular resolution using the MIMO mode

A MIMO radar system has an antenna arrangement as shown in Figure 2 and by using the MIMO mode, virtual antennas are formed. By increasing the number of antennas, the angular resolution also improves. As the radar system works on the principle of time-multiplexed transmission signals, it first emits signals from one transmitter, and then from the other transmitter antenna (Figure 10). In this way, two radar data cubes are formed at reception (Li et al, 2021, p.167966).

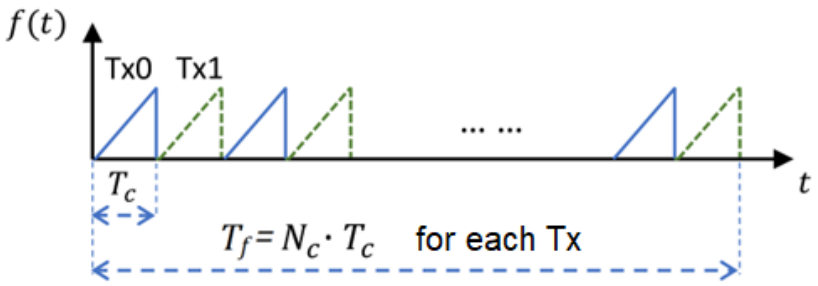

Figure 10 – Chirp signal frame with two transmitting MIMO antennas (Li et al, 2021)

Radar data cubes are formed for signals transmitted from different transmitting antennas. Since the condition of the distance between transmitting antennas in MIMO radars is met, a unified radar data cube (Figure 11) can be formed, which will have the properties as if there were 8 receiving antennas sent from one transmitting antenna.

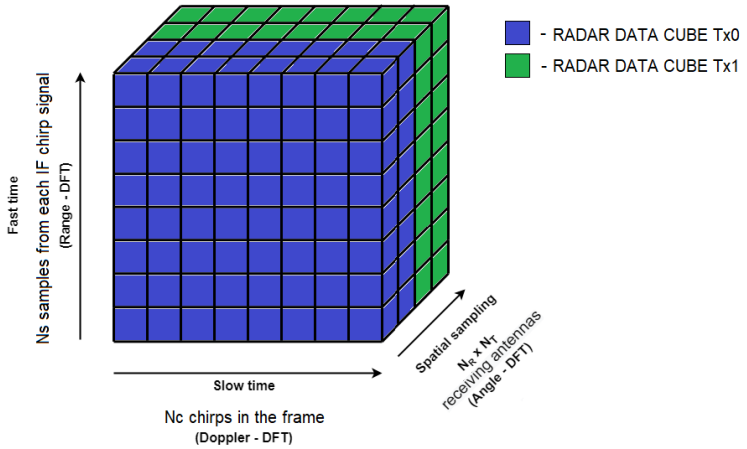

Figure 11 – Unified radar data cube

Simulation of a MIMO radar system

The Matlab functions for generating simulation and automated processing of the radar data cube are explained below. Te radar and target parameters for simulation purposes are defined and the simulation results are presented.

Generation of simulation echo signals of radar targets

In order to confirm the analytical claims in this paper, computer simulations were developed in the Matlab programming environment. The MIMOFMCW function was developed for simulation purposes. The mentioned function generates IF samples of the reception signal (7) that originated from the targets and were sent from one transmitting antenna. The output parameter is a three-dimensional radar data cube.

Processing of simulation radar data

In order to automate the process of digital processing of radar data, the procDC function was developed. The outputs of the function are two two-dimensional matrices RV - Range-Velocity matrix and RA - Range-Angle matrix. In addition to the matrices as an output, the function in the

command window prints the range of unique measurement of the range, velocity and angle of the radar for the given parameters and displays two three-dimensional views of the specified matrices with normalized axes, normalized in relation to the maximum value that appears in the matrix.

Simulation - Situation 1

The objective of situation 1 is to demonstrate the general operation of the radar for arbitrary parameters of the radar and targets. Table 1 shows the radar parameters adjusted for situation 1.

Table 1 – Simulation radar parameters - Situation 1

N_o	512	B	1 GHz
N_c	256	S	10 GHz/ms
T_c	0.1 ms	N_{Tx}	2
T_f	25.6 ms	N_{Rx}	4
f_s	5.12 MHz	d_{Rx}	λ/2
f_c	24 GHz	d_{Tx}	$4 \cdot d_{Rx}$

With the given parameters from Table 1, the radar achieves an unambiguous range of 76.80 m (11), unique speed measurement in the range from -31.25 m/s to 31.25 m/s (15) and the angle estimation from -90º to 90º (19). The distance between the transmitting antennas is satisfactory and allows the radar to work in the MIMO mode and behave as if it has 8 instead of 4 receiving antennas. In Table 2, the goal parameters adjusted for situation 1 are given.

Table 2 – Parameters of simulation targets - Situation 1

No	*A* (V)	*r* (m)	*v* (m/s)	*θ* (º)
1	1	70	-28	60
2	0.9	55	20	-30
3	0.85	40	-15	45
4	0.7	35	10	-45
5	0.6	20	5	0

Figure 12 shows the Range-Velocity matrix related to situation 1. In the image, peaks can be clearly observed, which correspond to the parameters set by the targets.

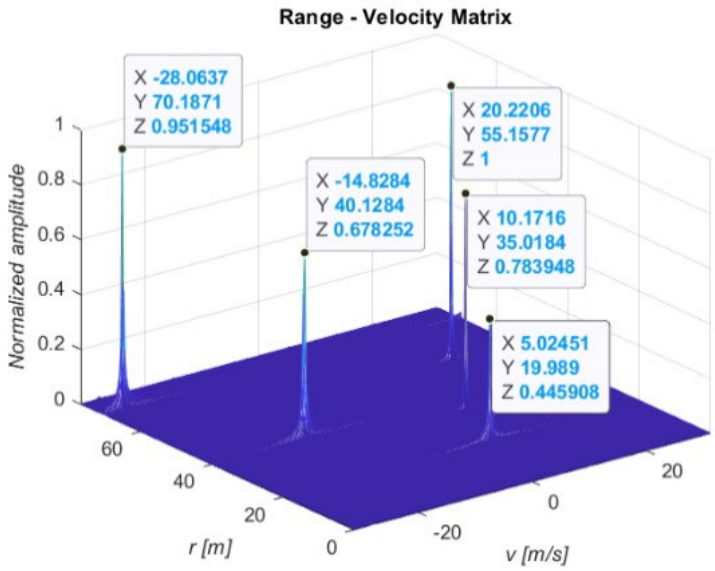

Figure 12 – Range-Velocity simulation matrix - Situation 1

In Figure 13a), the Range-Angle matrix is shown, simulating the operation of 1 transmitting and 4 receiving antennas. The radar data cube is padded along the angular axis with zeros to calculate the Angle DFT in 128 points. Zero-padding does not improve resolution but makes the signal spectrum more noticeable and easier to interpret. It can be concluded that due to the small number of receiving antennas, the angular resolution of the cell is considerable and that it is not possible to precisely determine the angle at which the target is in relation to the radar. Limited angular resolution causes a wide main lobe, but by finding the maximum values in the main lobes, one can come to the conclusion at which angle the target is located, but with a decision error. Also, due to the small angular resolution, the main lobes of the targets located at large angles are mirrored from one part of the range to another.

In Figure 13b), the Range-Angle matrix using 2 transmitting and 4 receiving antennas in the MIMO radar mode is shown. In this way, the effect is obtained as if there are 8 receiving antennas, which increases the angular resolution of the radar and narrows the main lobe. In this way, the error when measuring the angle is not drastically reduced, but it enables better separation of two close targets located at similar distances and at similar angles. It also reduces the aliasing effect. Using a single transmitting antenna gives the FWHP of 53.86º, while using the MIMO mode gives the FWHP (Full Width at Half Power) of 27.14º.

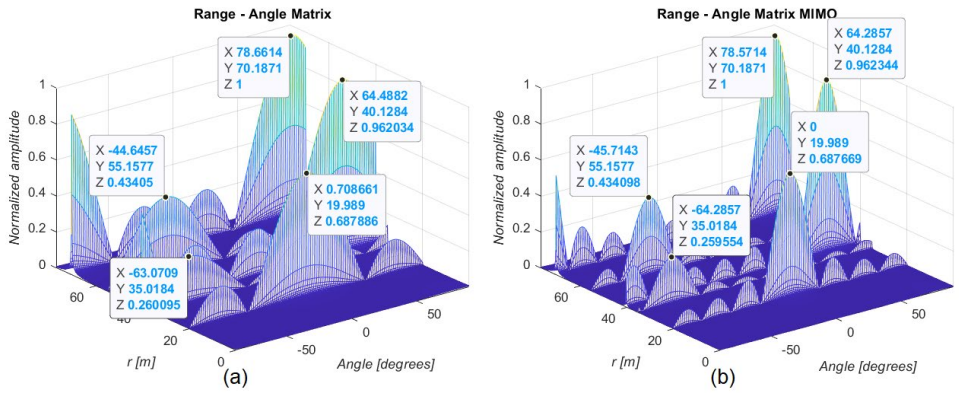

Figure 13 – Range-Angle simulation matrices - Situation 1, 1 Tx, 4 Rx (a); 2 Tx, 4 Rx (b)

Simulation - Situation 2

The purpose of simulation 2 is to show the angular resolution of the radar system and the improvement of the angular resolution using multiple transmit antennas, i.e., the MIMO mode of operation. Also, unlike simulation 1, which is shown under ideal conditions, simulation 2 includes noise where the SNR is -5 dB. Table 3 shows the parameters of the radar system for situation 2.

Table 3 – Simulation radar parameters - Situation 2

N_o	32	B	1 GHz
N_c	128	S	2 GHz/ms
T_c	0.5 ms	N_{Tx}	2
T_f	64 ms	N_{Rx}	4
f_s	64 KHz	d_{Rx}	λ/2
f_c	24 GHz	d_{Tx}	$4 \cdot d_{Rx}$

According to the parameters listed in Table 3, the radar has the following characteristics: the maximum unique range of 4.80 m; the unambiguous speed measurement range from -6.25 m/s to 6.25 m/s; and the angle measurement range from -90º to 90º with an angular resolution of 28.65º when using one transmitting antenna, or 14.32º when using two transmitting antennas.

Table 4 gives the parameters of the targets adjusted for situation 2. The targets are arranged in pairs to show the effect of separating the targets by angle. Targets one and two are at the same distance, moving at the same speed, but at different angles from the radar. Targets two and

three are at the same distance, but moving at different speeds and at different angles, clustered around 0º. For objectives five and six, similar conditions apply to the previous two objectives, except that they are grouped around 60º.

Table 4 – Parameters of simulation targets - Situation 2

No	*A* (V)	*r* (m)	*v* (m/s)	*θ* (º)
1	1	4,3	5	-40
2	0.9	4,3	5	30
3	0.8	2.5	-3	-10
4	0.8	2.5	4	10
5	0.6	0,5	-1	50
6	0.6	0,5	2	70

In Figure 14, one can see the Range-Velocity matrix related to situation 2. The Figure shows five peaks corresponding to five targets, although six targets are set in the simulation. Targets number one and two are located at the same distances and move at the same speeds, so they cannot be separated on the Range-Velocity matrix, while the other targets are clearly visible.

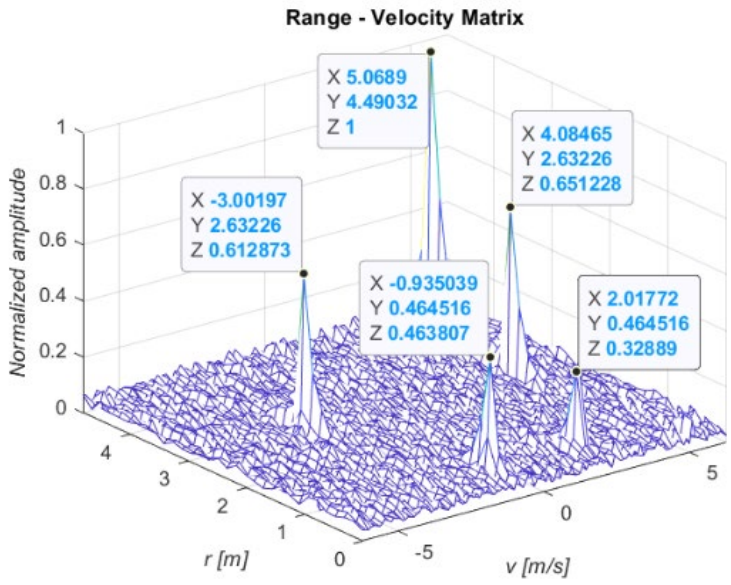

Figure 14 – Range-Velocity simulation matrices - Situation 2

In Figure 15a), there is a Range-Angle matrix that corresponds to the use of one transmitting and four receiving antennas. Although targets one and two are joined on the Range-Velocity matrix, it is observed that on the Range-Angle matrix the targets can be separated because they are at different angles. Targets three and four, as well as five and six are connected to each other and are located under one lobe. It cannot be concluded whether there is one or two targets. This happens because the angular distance between the targets is equal to 20º, and the angular resolution in this mode of operation is equal to 28.65º, and the targets are located in one resolution cell.

In Figure 15b), the Range-Angle matrix is shown when the radar is operating in the MIMO mode, where it uses two transmitting and four receiving antennas and forms a virtual antenna array on reception of eight receiving antennas. In this way, it increases the angular resolution and reduces the resolution cell to 14.32º (21). Targets three and four can be separated, while targets five and six remain under one main lobe - they cannot be separated even though they are at the same angular distance from each other as targets three and four.

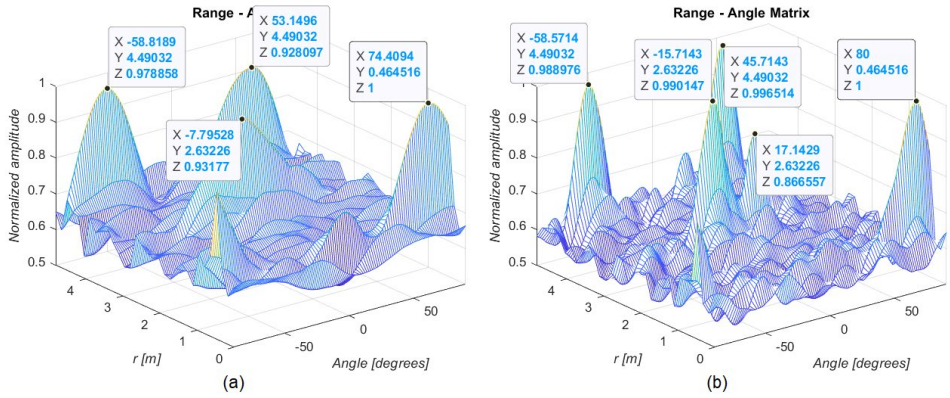

Figure 15 – Range-Angle simulation matrices - Situation 2, 1 Tx, 4 Rx (a); 2 Tx, 4 Rx (b)

It is observed that with the increase of the viewing angle, the angular resolution decreases, that is, the cell resolution increases, which leads to the fact that targets five and six cannot be separated angularly. Figure 16 shows the angular resolution for eight receiving antennas and an observation angle of 60º equal to 28.95º, which explains why targets five and six are not separated on the Range-Angle matrix.

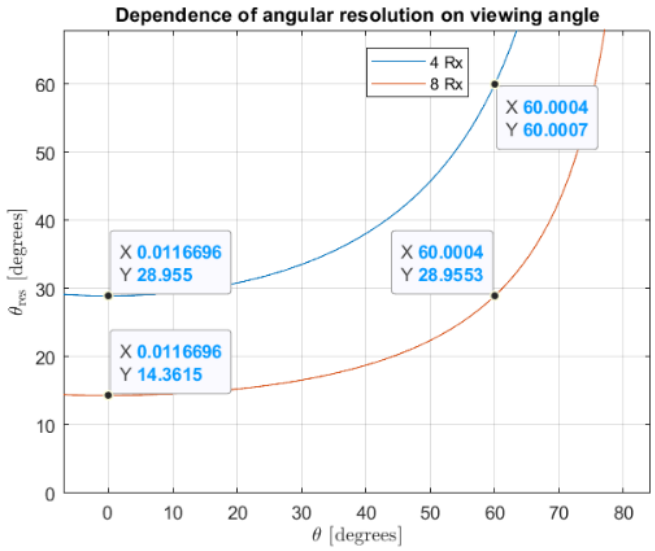

Figure 16 – Dependence of angular resolution on a viewing angle for 4 and 8 receiving antennas

Experimental verification of the MIMO radar model

During the experimental work, the MIMO radar platform PUP_DUAL24P_T2R4 (Figure 17a) from Luswave Technology (2020) was used. The radar platform operates in the K band and supports the continuous operation mode and th eFMCW modulation. The radar has two transmitting and four receiving antennas which enable the MIMO mode of operation and the creation of eight virtual antennas, resulting in a better angular resolution. In addition to the MIMO operating mode, the radar has the option of using only one transmitting antenna which behaves like a conventional radar. The radar comes with a Matlab graphical interface that allows setting the parameters of the radar. The parameters that can be adjusted are the number of transmitting and receiving antennas, the type of modulation, the operating frequency range, the duration of the chirp, the number of selections in the chirp and the length of data recording (Figure 17b) (Luswave, 2020).

The aforementioned radar from which the data was recorded onto the computer (Figure 18) was used in the experimental work. Through the computer, the parameters of the radar were set depending on the situation. The computer was later used to process and display the recorded data.

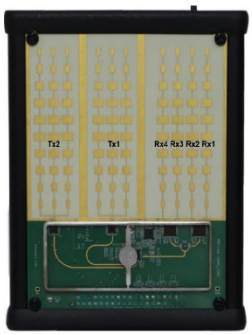

Specification	Minimum	Typical	Maximum
Channels		2x Transmitters, 4x Receivers	
Antennas		6x Onboard Patch Antennas	
Modulations		FMCW, CW	
Typical Frequency Range	24GHz		25GHz
Expandable Frequency Range	23.5GHz		26GHz
Sweep Time		0.5ms, 1ms, 2ms, 4ms, 8ms	
Samples per Sweep		128, 256, 512, 1024, 2048, 4096	
Tune Voltage	0		4V
Tuning Sensitivity		0.8GHz/V	
Transmit Power	16dBm	17dBm	18dBm
SSB Phase Noise @1MHz offset		-99dBc	
Noise Figure		12dB	
Maximum Input Power		5dBm	
IIP_1dB		-12dBm	
Supply Voltage	5.75V	6V	6.25V
Supply Current		1200mA	
Operating Tempreture	-40°C		85°C
Dimensions		L:130mm, W:108mm, H:32mm	

(a) (b)

Figure 17 – MIMO radar PUP_DUAL24P_T2R4 (a); Radar specifications (b) (Luswave, 2020)

Figure 18 – Radar and computer used for experimental imaging

For the purpose of the experiment, the recorded situations were those in which a person moves to and from the radar, to the left and to the right, while changing the speed of movement and the angle at which one is in relation to the radar (Figure 19a).

The person holds a reflector ball in the hands (Lunenberg lens) in order to increase the reflection and thus make the results more noticeable (Figure 19b).

(a) (b)

Figure 19 – Man as a radar target (a); Radar reflector (Lunenberg lens) (b)

Experiment - Situation 1

For the purpose of experimental verification, the radar parameters listed in Table 5 were used. According to the listed parameters, the radar has the following characteristics: the maximum unique range of 4.80 m; the unambiguous speed measurement range from -6.25 m/s to 6.25 m/s; and the angle measurement range from -90º to 90º with an angular resolution of 28.65º when using one transmitting antenna, or 14.32º when using two transmitting antennas.

Table 5 – Radar parameters of the experiment - Situation 1,2

N_o	32	f_c	24 GHz
N_c	128	B	1 GHz
T_c	0.5 ms	S	2 GHz/ms
T_f	64 ms	N_{Tx}	2
f_s	64 KHz	N_{Rx}	4

For situation 1 of the experiment, the person moves away from the radar from the right side of the radar. Figure 20 shows the Range-Velocity matrix of the experiment, where one intense peak is observed, which corresponds to the target. By reading the peak value, information is obtained about the distance and speed of the target.

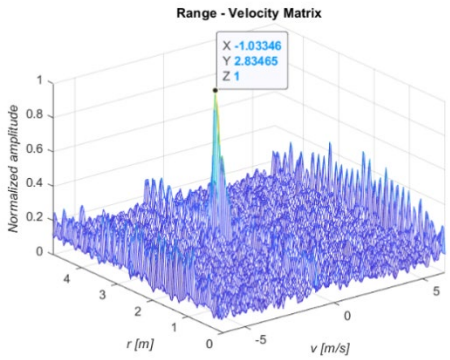

Figure 20 – Range- Velocity matrix of the experiment - Situation 1

When processing the data and displaying the Range-Velocity matrix, it is observed that the matrix contains unwanted components and a high level of noise. In order to reduce the influence of noise and make the results more obvious, before applying the Angle DFT algorithm, the observed object of interest is extracted using a 3x3 unit mask, in the center of which the object of interest is located. After the extraction of the object, the values in the matrix will remain only in the cells where the object is located, while the other cells will have a value of zero.

On the Range-Angle matrix, the main lobe is observed, and the search for its maximum determines the angle at which the target is located (Figure 21a). Using two transmitting antennas narrows the main lobe, which increases the angular resolution (Figure 21b). It is observed that the components at all other distances are suppressed, which is the result of extracting the object of importance by using a mask.

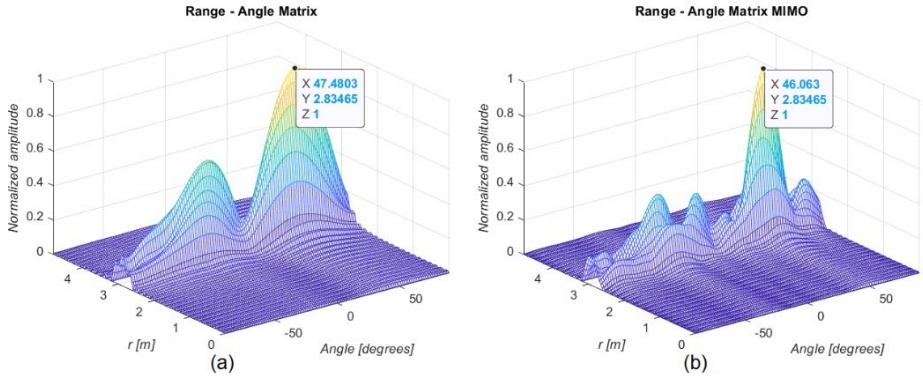

Figure 21 – Range-Angle matrices of the experiment - Situation 1, 1 Tx 4 Rx (a), 2 Tx4 Rx MIMO (b)

Experiment - Situation 2

For situation 2 of the experiment, the same radar parameters as those listed in Table 5 were used. Two people move away from the radar, from the same side and at similar angles (Figure 22).

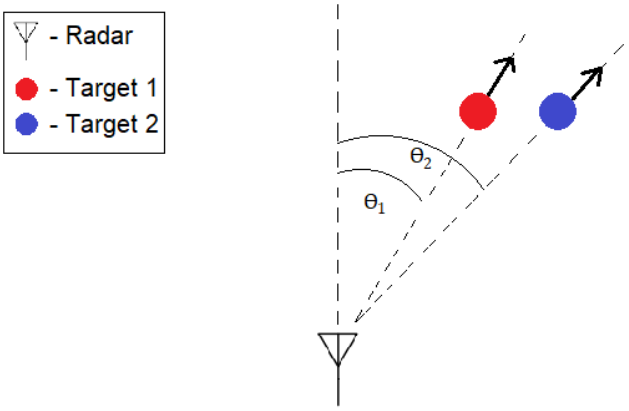

Figure 22 – Approximate sketch of the experiment situation 2

The aim of this experiment is to show better angular resolution using the MIMO mode and to confirm the claims shown in the simulation. By processing the signal, filtering and extracting the objects of interest, two peaks corresponding to two targets are observed, but it is difficult to separate them due to almost the same speed and mode of movement (Figure 23).

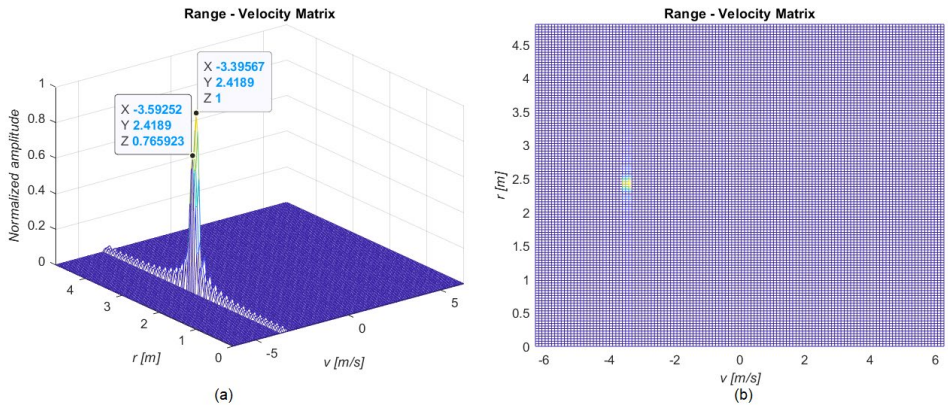

Figure 23 – Range-Velocity matrices of the experiment - Situation 2, 3D view (a), 2D heat map (b)

Since one transmitting and four receiving antennas are used and due to a small angular resolution and a large viewing angle, it is not possible to separate the targets which are both under a wide main lobe. The FWHP is 55.28º, which would lead to a wrong assessment of the situation (Figure 24a). By using two transmitting antennas in the MIMO mode of operation, the angular resolution is increased and is less than 34º. Two main lobes corresponding to the targets are distinguished, where the first FWHP is 25.51º and the second one is 22.68º (Figure 24b). By using an adequate decision-making threshold, a correct conclusion about the situation can be made.

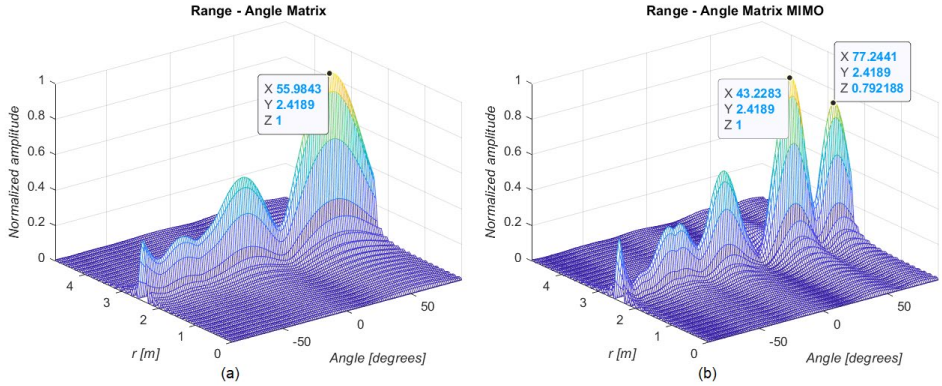

Figure 24 – Range-Angle matrices, - Situation 2, 1 Tx 4 Rx (a), 2 Tx 4 Rx MIMO (b)

Conclusion

In this paper, a model of an FMCW MIMO radar with time-multiplexed signals on transmission is presented, and the process of digital signal processing in this radar type, which primarily utilizes the Discrete Fourier Transform, is explained. The Discrete Fourier Transform has proven to be a straightforward tool that delivers satisfactory results. The theoretical foundations and mathematical models have been validated through simulation and experimental verification.

The resolution in the domains of range, velocity, and angle is limited by the use of the DFT algorithm. FMCW radars have been shown to provide accuracy in determining the range and velocity of targets, with the range resolution dependent on the signal sampling frequency f_S, the ramp slope coefficient S and the number of samples per chirp N_S, while the velocity resolution depends on the frame duration T_f. Since the angular resolution depends on the number of receiving antennas, it has been demonstrated that by introducing additional transmitting antennas, forming

a virtual receiving array, and operating the radar in the MIMO mode, the angular resolution and the ability to distinguish targets with similar angles are improved, as illustrated through simulations and experiments. In addition to the above, due to the limited number of receiving antennas, the DFT algorithm is characterized by wide main lobes. The algorithm determines the target angle, albeit with a certain error.

In this study, CFAR was not used, as target detection was trivial and performed manually. In this regard, the system can be improved by introducing an appropriate CFAR model which would automate the detection process. Future research will focus on the development and application of suitable algorithms for more precise target angle determination, such as MUSIC, Decorrelation Algorithms, and Spatial Smoothing. Additionally, research could be expanded to the design and implementation of planar MIMO radar structures, enabling target angle detection in both azimuth and elevation.

References

Abdi, A.H. & Rasheed, H. 2022. Performance Analysis of Outdoor Massive MIMO on Ultra-High Frequency Bands (73 GHz and 100 GHz). In: *2022 International Symposium on Networks, Computers and Communications (ISNCC),* Shenzhen, China, pp.1-6, July 19-22. Available at: https://doi.org/10.1109/ISNCC55209.2022.9851799.

Alizadeh, M., Shaker, G., De Almeida, J.C.M., Morita, P.P. & Safavi-Naeini, S. 2019. Remote Monitoring of Human Vital Signs Using mm-Wave FMCW Radar. *IEEE Access*, *7*, pp.54958-54968. Available at: https://doi.org/10.1109/ACCESS.2019.2912956.

Bliss, D.W. & Forsythe, K.W. 2006. MIMO Radar Medical Imaging: Self-Interference Mitigation for Breast Tumor Detection. In: *2006 Fortieth Asilomar Conference on Signals, Systems and Computers*, Pacific Grove, CA, USA, pp.1558-1562, October 29-November 01. Available at: https://doi.org/10.1109/ACSSC.2006.355020.

Davis, M.S., Showman, G.A. & Lanterman, A.D. 2014. Coherent MIMO radar: The phased array and orthogonal waveforms. *IEEE Aerospace and Electronic Systems Magazine*, 29(8), pp.76-91. Available at: https://doi.org/10.1109/MAES.2014.130148.

Dessai, S.N. & Patidar, H. 2024. Hardware software SoC co-design analysis and implementation of MIMO-OFDM for 4G/5G/6G eNodeB applications. *Transactions on Emerging Telecommunications Technologies*, 35(7), e5012. Available at: https://doi.org/10.1002/ett.5012.

Han, K., Bauduin, M., & Bourdoux, A. 2024. Beamspace Matrix Completion in Subarray-Based Sparse Linear Array for High-Resolution Automotive MIMO Radar. In: *2024 IEEE Radar Conference (RadarConf24)*, Denver, CO, USA, pp.1-6, May 06-10. Available at: https://doi.org/10.1109/RadarConf2458775.2024.10549360.

He, H., Stoica, P. & Li, J. 2009. Designing Unimodular Sequence Sets With Good Correlations—Including an Application to MIMO Radar. *IEEE Transactions on Signal Processing*, 57(11), pp.4391-4405. Available at: https://doi.org/10.1109/tsp.2009.2025108.

Iovescu, C. & Rao, S. 2016. The fundamentals of millimeter wave sensors. *Texas Instruments* [online]. Available at: https://www.ti.com/lit/wp/spyy005a/spyy005a.pdf?ts=1736646797336 [Accessed: 10 May 2024].

Janoudi, V., Schoeder, P., Grebner, T., Schwarz, D., Waldschmidt, C., Dickmann, J. & Appenrodt, N. 2023. Antenna Array Design for Coherent MIMO Radar Networks. In: *2023 IEEE Radar Conference (RadarConf23)*, San Antonio, TX, USA, pp.1-6, May 01-05. Available at: https://doi.org/10.1109/RadarConf2351548.2023.10149789.

Li, X., Wang, X., Yang, Q. & Fu, S. 2021. Signal Processing for TDM MIMO FMCW Millimeter-Wave Radar Sensors. *IEEE Access*, 9, pp.167959-167971. Available at: https://doi.org/10.1109/ACCESS.2021.3137387.

Liu, B. 2009. Orthogonal Discrete Frequency-Coding Waveform Set Design with Minimized Autocorrelation Sidelobes. *IEEE Transactions on Aerospace and Electronic Systems*, 45(4), pp.1650-1657. Available at: https://doi.org/10.1109/taes.2009.5310326.

-Luswave Technology. 2020. *PUP_DUAL24P_T2R4 Datasheet* [online]. Available at: https://luswave.com/PUP_EN24P_T2R4 [Accessed: 1 June 2024].

Mahafza, B.R. 2013. *Radar Systems Analysis and Design using MATLAB*, 2nd Edition. New York: Chapman and Hall/CRC. Available at: https://doi.org/10.1201/9781420057072.

-MathWorks. 2024. *Radar Data Cube* [online]. Available at: https://www.mathworks.com/help/phased/gs/radar-data-cube.html [Accessed: 24 May 2024].

Omer, A.E., Shaker, G., Safavi-Naeini, S., Murray, K. & Hughson, R. 2018. Glucose Levels Detection Using mm-Wave Radar. *IEEE Sensors Letters*, 2(3), pp.1-4. Available at: https://doi.org/10.1109/LSENS.2018.2865165.

Proakis, J.G. & Manolakis, D.G. 2014. *Digital Signal Processing, Fourth Edition*. Harlow, Essex, UK: Pearson. ISBN: 978-1-292-02573-5.

Ramasubramanian, K. 2017. Using a complex-baseband architecture in FMCW radar systems. *Texas Instruments* [online]. Available at: https://www.ti.com/lit/wp/spyy007/spyy007.pdf [Accessed: 5 May 2024].

Rao, S. 2018. MIMO Radar. *Texas Instruments*, July [online]. Available at: https://www.ti.com/lit/an/swra554a/swra554a.pdf?ts=1736649852855 [Accessed: 3 May 2024].

Richards, M.A. 2014. *Fundamentals of Radar Signal Processing, 2nd Edition.* New York: McGraw-Hill Education [online]. Available at: https://www.accessengineeringlibrary.com/content/book/9780071798327 [Accessed: 3 May 2024]. ISBN: 9780071798327.

Stoica, P. & Li, J. 2008. *MIMO Radar Signal Processing*. John Wiley & Sons, Inc. Available at: https://doi.org/10.1002/9780470391488.

Sun, H. 2023. Introduction to MIMO Radar Waveforms. *IEEE AESS,* 13 April [online]. Available at: https://ieee-aess.org/presentation/lecture/introduction-mimo-radar-waveforms [Accessed: 25 April 2024].

Sun, H., Brigui, F. & Lesturgie, M. 2014. Analysis and comparison of MIMO radar waveforms. In: *2014 International Radar Conference,* Lille, France, pp.1-6, October 13-17. Available at: https://doi.org/10.1109/radar.2014.7060251.

Wang, Z., Shi, D. & Wu, H. 2021. The Role of Massive MIMO and Intelligent Reflecting Surface in 5G/6G Networks. In: *2021 International Conference on Wireless Communications and Smart Grid (ICWCSG)*, Hangzhou, China, pp.309-312, August 13-15. Available at: https://doi.org/10.1109/ICWCSG53609.2021.00067.

Wiesbeck, W., Sit, L., Younis, M., Rommel, T., Krieger, G. & Moreira, A. 2015. Radar 2020: The future of radar systems. In: *2015 IEEE International Geoscience and Remote Sensing Symposium (IGARSS),* Milan, Italy, pp.188-191, July 26-31. Available at: https://doi.org/10.1109/igarss.2015.7325731.

Wu, C., Zhang, Z., Chen, L. & Yu, W. 2019. The Same Range Line Cells Based Fast Two-Dimensional Compressive Sensing For Airborne MIMO Array SAR 3-D Imaging. In: *IGARSS 2019 - 2019 IEEE International Geoscience and Remote Sensing Symposium*, Yokohama, Japan, pp.3653-3656, July 28-August 02. Available at: https://doi.org/10.1109/IGARSS.2019.8900050.

Procesamiento de señales digitales en radares MIMO con señales de transmisión multiplexadas en el tiempo

Borko B. Đaković[a], *Slobodan* M. Simić[b],
Lidija M. Trivundža[c], *Aleksandar* G. Ristić[d]

[a] Fuerzas Armadas de Serbia, Estado Mayor,
Dirección de Telecomunicaciones y Tecnologías de la Información (J-6),
Centro de Matemáticas Aplicadas y Electrónica,
Belgrado, República de Serbia, **autor de correspondencia**

[b] Universidad de Defensa de Belgrado, Academia Militar,
Departamento de Sistemas Electrónicos Militares,
Belgrado, República de Serbia

[c] Fuerzas Armadas de Serbia, Estado Mayor,
Dirección de Desarrollo y Equipamiento (J-5),
Centro de pruebas técnicas, Belgrado, República de Serbia,

[d] Ministerio de Defensa de la República de Serbia,
Instituto Técnico Militar, Belgrado, República de Serbia

CAMPO: procesamiento de señales digitales, telecomunicaciones, electrónica, electromagnética
TIPO DE ARTÍCULO: artículo científico original

Resumen:

Introducción/objetivo: Un tema actual de importantes esfuerzos de investigación y desarrollo en el campo de los sistemas de radar es la tecnología de radar MIMO (múltiple entrada-múltiple salida). Los radares MIMO representan un avance revolucionario en la tecnología de radar, ya que el uso de múltiples antenas transmisoras que emiten formas de onda ortogonales permite una mejor detección y resolución angular. Para lograr resultados efectivos, el procesamiento de señales digitales de alta calidad y la aplicación de algoritmos avanzados son esenciales para obtener información del objetivo. Este artículo pone especial énfasis en los radares MIMO coherentes, con el objetivo de mejorar la resolución angular. La multiplexación en el tiempo de las señales de transmisión se aplica como método principal para lograr la ortogonalidad entre señales, utilizando una señal de onda continua de frecuencia modulada (FMCW) como base para la forma de onda de transmisión. El objetivo de este artículo es proporcionar y explicar los fundamentos del procesamiento digital de señales en radares MIMO, presentar expresiones analíticas y validarlas mediante simulación y verificación experimental.

Métodos: Se presentan los fundamentos teóricos, utilizando la Transformada Discreta de Fourier (DFT) como herramienta principal en el procesamiento de señales digitales para obtener información sobre la distancia, velocidad y azimut del objetivo. Se desarrolló una simulación en el paquete de software MATLAB para analizar el desempeño del modelo del sistema radar. Se realizó una verificación experimental, donde se registraron escenarios específicos utilizando la plataforma de radar PUP_DUAL24P_T2R4 y posteriormente se procesaron los datos recopilados. Las funciones de MATLAB MIMOFMCW y procDC se escribieron para generar muestras de simulación de señales de eco y para automatizar el procesamiento de señales y la visualización de matrices características de rango-velocidad y rango-ángulo.

Resultados: La simulación y la verificación experimental confirman la validez de los fundamentos teóricos relacionados con el procesamiento de señales digitales en radares MIMO, y los parámetros objetivo se pueden determinar claramente.

Conclusión: La Transformada Discreta de Fourier es una herramienta sencilla que proporciona resultados satisfactorios para determinar el alcance, la velocidad y el ángulo de los objetivos. Los radares FMCW ofrecen precisión para determinar el alcance y la velocidad, mientras que el modo MIMO mejora la resolución angular. El algoritmo DFT es capaz de determinar el ángulo objetivo, pero con un cierto error, lo que hace

necesario el uso de métodos de alta resolución para una determinación más precisa del ángulo.

Palabras claves: MIMO, radar, TDM, FMCW, cubo de datos de radar, DFT, frecuencia de pulsación, antena virtual.

Цифровая обработка сигналов в радарах MIMO с мультиплексированием по времени сигналов передачи

Борко Б. Джакович[а], *Слободан* М. Симич[б],
Лидия М. Тривунджа[в], *Александар* Г. Ристич[г]

[а] Вооруженные силы Республики Сербия, Генеральный штаб,
Управление телекоммуникаций и информационных технологий (J-6),
Центр прикладной математики и электроники,
г. Белград, Республика Сербия, **корреспондент**

[б] Университет обороны, Военная академия,
кафедра военных электронных систем,
г. Белград, Республика Сербия

[в] Вооруженные силы Республики Сербия, Генеральный штаб,
Управление развития и оснащения (J-5),
Центр технических испытаний, г. Белград, Республика Сербия

[г] Министерство обороны Республики Сербия,
Военно-технический институт , г. Белград, Республика Сербия

РУБРИКА ГРНТИ: 47.05.17 Методы приема и обработки сигналов,
47.49.29 Радиолокационные системы, станции,
47.47.29 Радиопередающие устройства,
47.47.31 Радиоприемные устройства,
78.25.00 Вооружение и военная техника,
78.21.49 Военная электроника и кибернетика
ВИД СТАТЬИ: оригинальная научная статья

Резюме:

Актуальной темой важных исследований и разработок в области радиолокационных систем является радиолокационная технология MIMO (множественный вход-множественный выход). Радары MIMO представляют собой революционный прогресс в радиолокационной технологии, поскольку использование нескольких передающих антенн, излучающих ортогональные сигналы, позволяет улучшить обнаружение и угловое разрешение. Для достижения эффективных результатов необходимы качественная цифровая обработка сигналов и применение передовых алгоритмов получения целевой информации. В данной статье особое внимание уделяется когерентным MIMO-радарам с целью улучшения углового разрешения. Временное мультиплексирование сигналов передачи применяется в качестве основного метода

достижения ортогонализации между сигналами с использованием сигнала непрерывной волны с частотной модуляцией (FMCW) в качестве основы формирования сигнала передачи. Цель данной статьи — предоставить и объяснить основы цифровой обработки сигналов в радарах MIMO, представить аналитические выражения и проверить их посредством моделирования и экспериментальной верификации.

Методы: В статье представлены теоретические основы использования дискретного преобразования Фурье (ДПФ) в качестве основного инструмента цифровой обработки сигналов для получения информации о расстоянии, скорости и азимуте цели. В пакете программ MATLAB было разработано моделирование для анализа производительности модели радиолокационной системы. Была проведена экспериментальная проверка, в ходе которой с помощью радиолокационной платформы PUP_DUAL24P_T2R4 зафиксированы конкретные сценарии, а в дальнейшем были обработаны собранные данные. Функции MATLAB, MIMOFMCW и procDC были разработаны для генерирования образцов моделирования эхо-сигналов, а также для автоматизации обработки сигналов и отображения характеристических матриц «Диапазон-Скорость» и «Диапазон-Угол».

Результаты: Моделирование и экспериментальная верификация подтверждают справедливость теоретических основ, связанных с цифровой обработкой сигналов в радарах MIMO, и позволяют четко определить целевые параметры.

Выводы: Дискретное преобразование Фурье — это простой инструмент, который дает удовлетворительные результаты для определения расстояния, скорости и целевого угла. Радарные системы FMCW обеспечивают точность в определении расстояния и скорости, в то время как режим MIMO улучшает угловое разрешение. Алгоритм DFT способен определять целевой угол, но с определенной погрешностью, что делает необходимым применение методов высокой разрешающей способности для более точного определения угла.

Ключевые слова: MIMO, радар, TDM, FMCW, куб данных радара, DFT, частота биений, виртуальная антенна.

Дигитална обрада сигнала у радарима МИМО са временски мултиплексираним сигналима на предаји

Борко Б. Ђаковић[а], *Слободан* М. Симић[б],
Лидија М. Тривунца[в], *Александар* Г. Ристић[г]

[а] Војска Србије, Генералштаб, Управа за телекомуникације и информатику (J-6), Центар за примењену математику и електронику, Београд, Република Србија, **аутор за преписку**

[б] Универзитет одбране у Београду, Војна академија, Катедра војноелектронског инжењерства, Београд, Република Србија

[в] Војска Србије, Генералштаб, Управа за развој и опремање (J-5), Технички опитни центар, Београд, Република Србија

[г] Министарство одбране Републике Србије, Војнотехнички институт, Београд, Република Србија

ОБЛАСТ: обрада дигиталних сигнала, телекомуникације, електроника, електромагнетика
КАТЕГОРИЈА (ТИП) ЧЛАНКА: оригинални научни рад

Сажетак:

Увод/циљ: Актуелну тему значајних истраживачких и развојних напора из области радарских система представља радарска технологија MIMO (енг. Multiple-Input-Multiple-Output). Радари MIMO представљају револуционаран искорак у домену радаске технологије, јер употребом више предајних антена које емитују ортогоналне таласне облике омогућавају бољу детекцију и угаону резолуцију. За постизање ефикасних резултата од кључног значаја је квалитетна дигитална обрада сигнала и примена напредних алгоритама како би се добиле информације о циљу. У фокусу овог рада су кохерентни радари MIMO, јер повећавају угаону резолуцију. Примењено је временско мултиплексирање сигнала на предаји, као један од основних начина постизања ортогоналности између сигнала, при чему је коришћен континуални фреквенцијски модулисани сигнал (енг. FMCW – Frequency Modulated Continuous Wave) као основа за формирање предајног таласног облика. Циљ овог рада јесте да пружи и објасни основе дигиталне обраде сигнала у радарима MIMO, изнесе аналитичке изразе и потврди их кроз симулацију и експерименталну верификацију.

Методе: Изнете су теоријске основе при чему је коришћена дискретна Фуријеова трансформација као основни алат у дигиталној обради сигнала и добијању информација о даљини, брзини и азимуту под којим се циљ налази. Развијена је симулација у софтверском пакету МАТЛАБ ради анализе перформанси модела радарског система. Спроведена је експериментална верификација, при чему су специфични сценарији снимљени помоћу радарске платформе PUP_DUAL24P_T2R4, а прикупљени подаци су накнадно

обрађени. Написане су МАТЛАБ функције MIMOFMCW и procDC за генерисање симулационих одбирака ехо сигнала и за аутоматизовану обраду сигнала и приказане карактеристичне матрице даљина-брзина и даљина-угао.

Резултати: Симулација и експериментална верификација потврђују исправност теоријских основа које се односе на дигиталну обраду сигнала у MIMO радарима, при чему се јасно могу одредити параметри циљева.

Закључак: Дискретна Фуријеова трансформација је једноставан алат који даје задовољавајуће резултате за одређивање даљине, брзине и угла циљева. FMCW пружају тачност при одређивању даљине и брзине, а режим МИМО повећава угловну резолуцију. Алгоритам DFT успева да одреди угао циља, али са одређеном грешком, па је за тачније одређивање угла потребно користити високорезолуционе методе.

Кључне речи: MIMO, радар, TDM, FMCW, радарска коцка података, DFT, фреквенција избијања, виртуелна антена.

Paper received on: 25.11.2024.
Manuscript corrections submitted on: 26.03.2025.
Paper accepted for publishing on: 27.03.2025.

Study of the impact of various supplies on the quality of surface water

Hocine Chibane[a], *Mohamed Redha* Menani[b], *Kamel-eddine* Bouhidel[c]

[a] University of Batna 2,
Institute of Earth and Universe Sciences, Department of Geology,
Mobilization and Management of Water Resources Laboratory
LMMWR, Batna, People's Democratic Republic of Algeria,
e-mail: h.chibane@univ-batna2.dz, **corresponding author**,
ORCID iD: https://orcid.org/0009-0009-8894-3225

[b] University of Batna 2,
Institute of Earth and Universe Sciences, Department of Geology,
Mobilization and Management of Water Resources Laboratory
LMMWR, Batna, People's Democratic Republic of Algeria,
e-mail: redha.menani@univ-batna2.dz,
ORCID iD: https://orcid.org/0000-0001-7261-9417

[c] University of Batna 1, Faculty of Material Sciences,
Department of Chemistry, Chemistry and Environmental Chemistry
Laboratory LCEC, Batna, People's Democratic Republic of Algeria,
e-mail: ke.bouhidel@gmail.com,
ORCID iD: https://orcid.org/0009-0004-1956-7733

https://doi.org/10.5937/vojtehg73-50508

FIELD: environmental chemistry
ARTICLE TYPE: original scientific paper

Abstract:

Introduction purpose: As population growth and industrial expansion continue, surface freshwater reservoirs such as dams have become increasingly vital due to their accessibility and ease of treatment. However, the quality of these water sources has significantly deteriorated, primarily due to the discharge of domestic and industrial wastewater. The proliferation of extensive algal blooms has led to significant challenges in maintaining drinking water quality and raised concerns about public health. This study investigates the impact of various water sources on the physicochemical quality of an Algerian dam over four seasons (December 2020 – October 2021) and explores the factors influencing the occurrence of cyanobacterial blooms to better understand and manage this excessive growth.

ACKNOWLEDGMENT: This work was supported by the PNR (National Research Projects)/DGRSDT Program of the Algerian Ministry of Higher Education and Scientific Research. The authors are grateful to ANBT (National Agency for Dams and Transfers) Batna–Algeria and ONA (National Office for Sanitation) for facilitating the access to sampling sites. The authors are grateful also to ADE (Algerian water company) Batna–Algeria for facilitating the analysis and using their equipment.

Methods: Physicochemical properties and algal composition of the dam water were analyzed monthly to determine nutrient sources and environmental factors affecting cyanobacterial proliferation.

Results: The analysis revealed that the Timgad stream and Reboua valley are notable sources of nutrient enrichment. Elevated temperatures and high nutrient loads, particularly total phosphorus (TP), in Timgad dam water facilitate the proliferation of blue-green algae. Additionally, limited nitrogen content favors the dominance of nitrogen-fixing cyanobacteria such as Aphanizomenon and Oscillatoria. The study also highlights that the low flow rate and high nutrient load of the Timgad stream create favorable conditions for cyanobacterial growth.

Conclusions: Nutrient inputs, temperature, and hydrological conditions significantly influence cyanobacterial blooms. Understanding these factors is crucial for implementing effective water management strategies to reduce algal proliferation and protect freshwater quality.

Key words: Koudiet Medouar water dam, blue-green algae, cyanobacteria, nutrient pollution, Timgad.

Introduction

The availability of fresh water is one of the necessities of life. Although it represents 2.5% of all the water on our planet, less than 1.2% is in lakes, rivers, and dams, while 68.7% is in form of glaciers and ice caps, and 30.1% is under ground (Gleick, 1993).

With demographic growth and industrial development, surface fresh water such as that from dams has become more and more important because of its ease of access and treatment (Berga et al, 2006; Loucks et al, 2017). However, the quality of such water resources has suffered serious deterioration, principally because of domestic and industrial wastewater effluents (Quesada et al, 2019; Segerson & Walker, 2002; Walker et al, 2019).

Surface water pollution has been made the principal objective of several studies during the last years, indeed because of their serious health and environmental risks. Pollutants such as heavy metals, nitrates, phosphorus, dissolved organic matter (DOM) and others are well-studied (Adimalla et al, 2020; Karaouzas et al, 2021; Pivokonsky et al, 2016; Qu & Fan, 2010), but in fact, they still make a real challenge for water producers. Nutrient pollution which includes nitrogen (N) and phosphorus (P) is the leading type of contamination in water sources such as dams (Segerson & Walker, 2002). While plants and animals need these nutrients to grow, they have become a major pollutant due to fertilizer runoffs and effluents of domestic and industrial wastewater. Nutrient pollution typically

stimulates phytoplankton growth in dams (Dzialowski et al, 2005; Marra et al, 1990). Unfortunately, some genera of phytoplankton named cyanobacteria or blue-green algae (B-G Algae) usually break out and stand stably, leading to problems with hypoxia, toxins, and changes in the structure of biological communities (Carmichael, 2008; Havens, 2008; Dobricic et al, 2016)

The excessive proliferation of blue-green algae not only creates ecological problems but can also affect the ability of water treatment plants (Gitis & Hankins, 2018; Wurtsbaugh et al, 2019). This includes poor settling, clogging sand filters, and breakthrough of small-size algae through sand filters, the fouling of membranes, and ion-exchange resins (Cheng & Chi, 2003; Hoeger et al, 2005). In addition, algae can also serve as precursors to form disinfection by-products (DBPs) during chlorination (Richardson & Postigo, 2011).

The Koudiet Medouar dam (Timgad, Batna, NE Algeria) is one of the most important freshwater resources in the area; it is used mainly to produce drinking water for one million inhabitants of the cities of Batna and Khenchla as well as for irrigation (Amrane & Bouhidel, 2019). Timgad's water dam receives water from three principal supplies: Reboua valley, the Timgad stream, and the water transfer from the Bni Haron water dam (Mila/Algeria).

The plant of this dam uses a conventional treatment based on the use of the coagulation/flocculation CF technique since it has been widely used for the treatment of surface water due to its several advantages such as the removal of organic, suspended, and colloidal matters. It can also be effective in removing many protozoa, bacteria, and viruses; it has been also found to be cost-effective, easy to operate and it is an energy-saving treatment alternative (Feihrmann et al, 2017; Mhamdi et al, 2016).

Recently, the treatment plant in the Timgad dam has faced serious problems with water quality caused by cyanobacteria blooms. Based on the reports, algae concentration reached 600×10^3 cells cm^{-3} in the summer which causes an increase in the chemicals during water treatment and affects the organoleptic quality of the produced drinking water. While the dam plant uses chlorination as a pretreatment, a lot of concerns have been raised about DBPs formation and its risks to public health.

Since this dam is of recent origin and little research has been carried out about it, except for a few studies (Bouslah et al, 2017; Labed, 2015; Smatti-Hamza et al, 2020; Tiri et al, 2017) on the water quality and water pollution, this research work aimed to study the impact of different water supplies on the physicochemical quality of the dam water, as well as the

factors affecting the presence of cyanobacterial blooms in this important Algerian reservoir for better environmental monitoring.

In this work, the physicochemical parameters (especially nutrients), blue-green algae count, and identification have been followed during four seasons in the water reservoir and its water supplies. To the best of our knowledge, no study has so far been reported on the nutrient pollution, blue green algae presence and their effect on the Timgad dam water quality.

Study materials and methods

Study area

The Koudiet Medouar watershed is located northeast of the city of Batna in the eastern part of Algeria (Figure 1). The water from its reservoir is used for drinking and irrigation supply with a 69 million m^3 total capacity, 44 m depth, and 59.000 m^2 surface area (Amrane & Bouhidel, 2019). The flow goes from south to north, and it is supplied by rainwaters that come through Reboua valley by purified sewage of bordering cities and villages that come through the Timgad stream, and by water transfer that comes from the Bni Haroun watershed. The area lies between the longitude of 35°30′57″ N and the latitude of 6°30′48″ E (Figure 1).

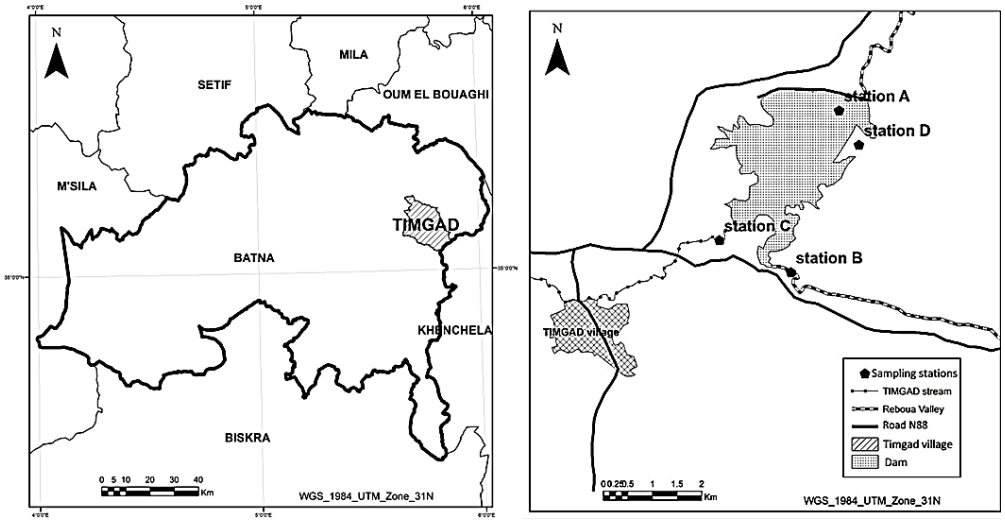

Figure 1 – Geographic map for the study area. The Koudiet Medouar dam, Timgad-Batna-Algeria (software used ArcGIS 10.3.1)

The Koudiat Medouar watershed is characterized by a semi-arid climate, characterized by cold and wet winters, warm and dry summers, and the rainfall between 300 and 450 mm per year. The extreme is marked by a climate known as a mountain climate with abundant rainfall (over 600 mm per year), especially in spring and late fall. It is sometimes characterized by violent storms. Generally, the regional rainfall exhibits three maxima during the year: January, May, and November. The annual average temperature is between 12 and 13 °C, with January as the coldest month and August as the hottest month (average between 26 and 34 °C) (Bouslah et al, 2017).

Sampling

Four sampling sites were chosen, each one from the dam and its supplies:

- Station A - The intake tower of the dam: the samples in this station were collected from different depths using a Niskin bottle attached to an electric hoist winch.
- Station B - Reboua valley (a source of rainwater that comes from the mountains).
- Station C – The Timgad stream (a source of purified wastewater that comes from the purification stations of the bordering cities).
- Station D - The water transfer comes from the Bni Haroun dam water (Mila-Algeria) which was put into service in 2013 (this supply was out of service during the period of study).

Samples were collected monthly from December 2020 to October 2021. They were collected at about 30 cm in depth and 1m away from the shore (APHA, 1999). For physicochemical analysis, Polyethylene bottles (1 dm^3) were used to collect water samples. The measurement of the pH, turbidity, temperature, and conductivity was performed on-site. Afterwards, samples were immediately transported to the laboratory and maintained at 4 °C in darkness for no more than 48 h before analysis.

The samples of the algae were collected. These samplings were carried out using a 20 to 100 µm mesh plankton net; the samples were fixed in a LUGOL solution and stored in glass jars (1 dm^3).

Analytical methods

Chemicals and materials

All chemicals used in this work, such as $K_2Cr_2O_7$ (≥99.5%), HCl (36.5–38%), NaOH (≥98%), H_2SO_4 (95–98%), potassium hydrogen phthalate

(KHP) (≥99.95%), ammonium persulfate (≥98%), potassium antimonyl tartrate (≥99%), ammonium molybdate (99.98%) and ascorbic acid (99%), anhydrous sodium tetra borat $Na_2B_4O_7$ (≥99.5%), phenol (≥99%), disodium ethylenediamine-tetraacetic acid EDTA (≥97%), and others, were purchased from Sigma-Aldrich, Algeria.

Analysis of the physicochemical parameters

Temperature, pH, and conductivity were measured in situ using a Hanna Instrument (Portable pH/EC/TDS/ Temperature) Model No. H1991300. Also, the dissolved oxygen (DO) was measured in situ using a portable oxygen meter (Hanna HI 9142). Turbidity was measured in the laboratory using a HACH 2100N turbid meter. Calcium (Ca^{2+}), and total hardness were determined by the volumetric method using ethylene diamine tetraacetic acid (EDTA) while orthophosphates (PO_4^{3-}) and nitrate (NO^{3-}) were determined by colorimetric assay using a Shimadzu UV-1601 spectrophotometer (Rodier et al, 2009).

Organic matter analysis

The COD of the dam water and deferent supplies was measured following the chemical oxygen demand index small scale sealed-tube method (ST-COD) (Rodier et al, 2009). Standards of 0, 5, 10, 15, 20, and 25 mg dm^{-3} of dissolved oxygen were prepared with potassium hydrogen phthalate (KHP) using ultra-pure water for all dilutions. After 2 h in a normalized thermo-reactor (WTW) at 150 °C, the dichromate excess absorbance of samples and standards was measured using a UV-visible spectrophotometer (Shimadzu, PharmaSpec 1700 UV/Vis) at 444 nm with a quartz cell of a 1 cm path length. The instrument was calibrated using ultrapure water as a blank.

Total phosphorus (TP) analysis

In a typical procedure for neutral digestion, 1 cm^3 of sulfuric acid solution and 0.4 g of ammonium persulfate were added to a 125 cm^3 Erlenmeyer flask containing 50 cm^3 of the aqueous sample (or the standard), and mixed. Then these flasks were placed on a pre-heated hot plate for approximately 30-40 min. After digestion, the samples were cooled and diluted to 50 cm^3 and 8 cm^3 of a combined reagent (H_2SO_4 solution, potassium antimonyl tartrate solution, ammonium molybdate solution, and ascorbic acid solution) was added and mixed thoroughly.

The characteristic blue color fully developed within 10 min at room temperature. The absorbance of the formed compound was measured at

880 nm with a spectrophotometer using a 1 cm quartz cuvette (APHA, 1992).

Total nitrogen (TN) analysis

The TN is analyzed following the Kjeldahl digestion method using an automated system of digestion/distillation/titration (U.S. Environmental Protection Agency, 2001).

Algae analysis

The collected samples of algae were fixed using a LUGOL solution of 15%, and the species were counted and identified using an inverted microscope OPTIKA IM-2 Trinocular according to the method of UTERMÖL (British Standards Institute, 2006).

Results and discussion

Physico-chemical quality of the studied water

Samples were taken from 3 different locations, at about 30 cm in depth. Table 1 shows that most physicochemical parameters are in normal values except for Reboua Valley which gives high levels of turbidity reaching 60.4 NTU during the rainy season due to the high flow rate.

Figure 2 shows that the TP concentration is extremely high ranging between 0.92 and 15.76 mg dm^{-3} in the Timgad stream (throughout the study period). These results are unexpected for the Timgad stream, which is considered purified wastewater. And on the contrary, the results of TN ranged between 150 and 300 µg dm^{-3} laid as to confirm that the purification plan used needs improvement.

Reboua valley has also shown high levels of TP ranging between 0.59 and 15.77 mg dm^{-3} during the rainy season; this may be due to an erosion of agricultural lands. The TN values ranged between 500 and 625 µg dm^{-3}.

On the other hand, the TP concentration in the dam water varies between 0.59 and 6.48 mg dm^{-3} (below the Algerian standards of 10 mg of P dm^{-3}), which shows a clear impact of the Timgad stream and Reboua valley on the dam water quality. The TN results ranged between 105 and 223 µg dm^{-3}.

The organic matter concentration in the water between summer and winter has also been investigated in this study. The maximum value of 25 mg O_2 dm^{-3} was recorded during May in the dam water and 27 mg O_2 dm^{-3} in the Timgad stream. A good stratification and aeration in the dam

water was shown by the DO analysis; the mean average is 6.54 and 6.30 mg dm^{-3} at the top and bottom, respectively.

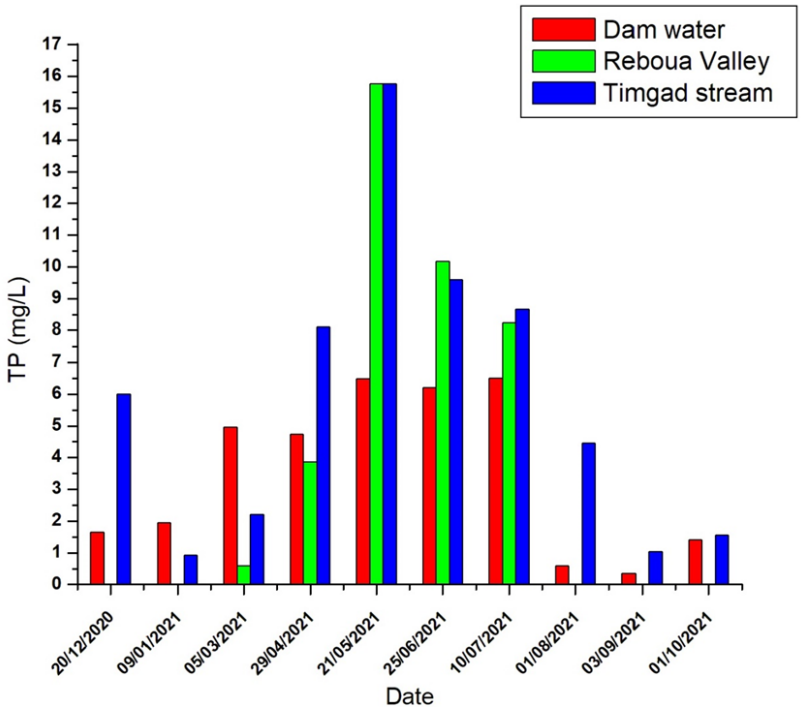

Figure 2 – Results of total phosphorus between December 2020 and October 2021

Algae analysis

In this study, two water supplies have been investigated and compared with the dam water. The maximum values of the total algae concentration were 428.5×10^3 cells cm^{-3} (recorded during October 2021) and 344×10^3 cells cm^{-3} (recorded during July 2021) in the Timgad stream and the dam water, respectively, as shown in Figure 3 and Figure 4.

It seems that the low flow rate, the high load of nutrients (TP especially), and the lighting conditions in the Timgad stream give the perfect conditions for algae proliferation (Lv et al, 2011; Mitrovic et al, 2011). Since the maximum values of the blue-green algae (B-G Algae) concentration were recorded in July 2021 (360×10^3 cells cm^{-3}) and May 2021 (217×10^3 cells cm^{-3}) in the Timgad stream and the dam water respectively, a probable reason was the ideal conditions of temperature, light, and nutrients (Giannuzzi, 2018). The percentage of blue-green algae shows values superior to 50% between March and August 2021 (spring

and summer). The possible explanation for these results is the nutrients load (TP in particular) as well as the temperature that can control the domination of algae species (Journey et al, 2013; Lv et al, 2011). During the period of study, no algae proliferation is found in Reboua valley, probably due to the high flow rate.

Table 1 – Results of physicochemical analysis between December 2020 and Ocobert 2021

Location	T (°C)		pH		EC (µs cm^{-3})		DO (mg dm^{-3})		TP (mg dm^{-3})		TN (µg dm^{-3})		DCO (mg O_2 dm^{-3})	
	Min	Max	Min	Max	Min	Max	Min	Max	Min	Max	Min	Max	Min	Max
Station A (The dam water)	8.4	26.2	7.44	8.58	919	1432	4.7	8.61	0.59	6.48	105	223	12	25
	Dec	Jul	Apr	Dec	Dec	Apr	Apr	Mar	Sep	May	Aug	Jan	Sep	May
Station B (Reboua valley)	-	-	7.47	7.83	703	1542	-	-	0.59	15.7	500	625	8	9.44
	-	-	May	Apr	Jun	Mar	-	-	Dec	Apr	Jun	Dec	Mar	Apr
Station C (Timgad stream)	9.5	27.3	7.38	8.69	1182	1508	-	-	0.92	15.7	150	300	14	27
	Dec	Jul	Apr	Dec	Jun	Apr	-	-	Sep	May	May	Jan	Oct	May

The dominant algal species identified in the dam water and the Timgad stream between March and August 2021 were Planktothrix (Cyanobacteria), and Aphanizomenon flos-aquae (Cyanobacteria). Cylindrospermopsis (Cyanobacteria), Euglena sp (Cyanobacteria), Nodularia spumigena (Cyanobacteria). These species are often considered a type of "nuisance algae" because they can form dense blooms that can affect the appearance, odor, and taste of the water, as well as interfere with the growth of other aquatic plants and animals (Havens, 2008). They can also produce potent toxins that are harmful to humans and animals (Codd et al, 2005). For this reason, monitoring and management strategies are necessary to control the proliferation of these species.

The dominance of some cyanobacteria like Aphanizomenon and Oscillatoria is possible due to the low nitrogen content in the dam water and the Timgad stream, whereas in a similar situation this genera of cyanobacteria called N2-fixing can fix atmospheric nitrogen, which can lead to a lack of nitrates or ammonia (Issa et al, 2014).

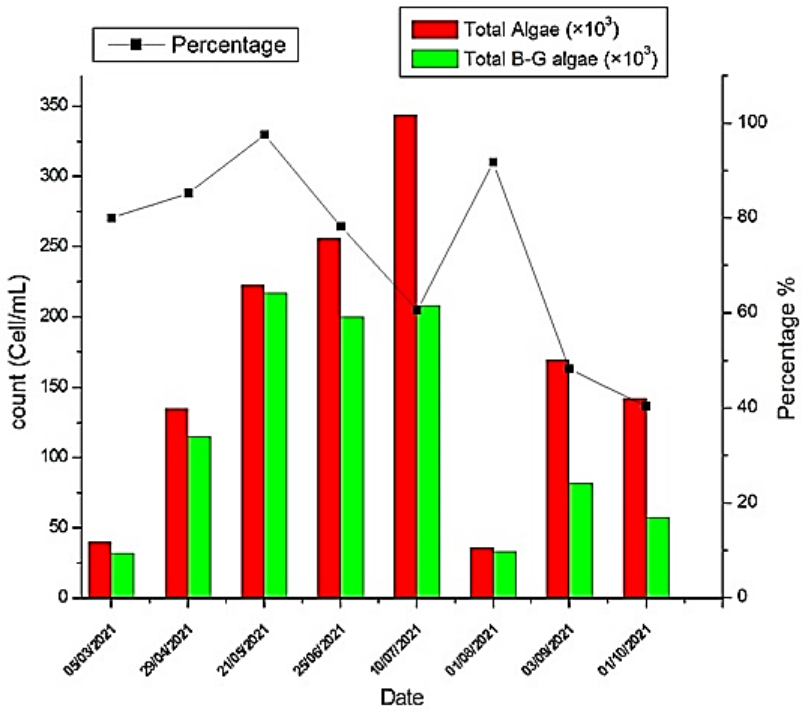

Figure 3 – Count of Algae and B-G algae in the dam water (Station A)

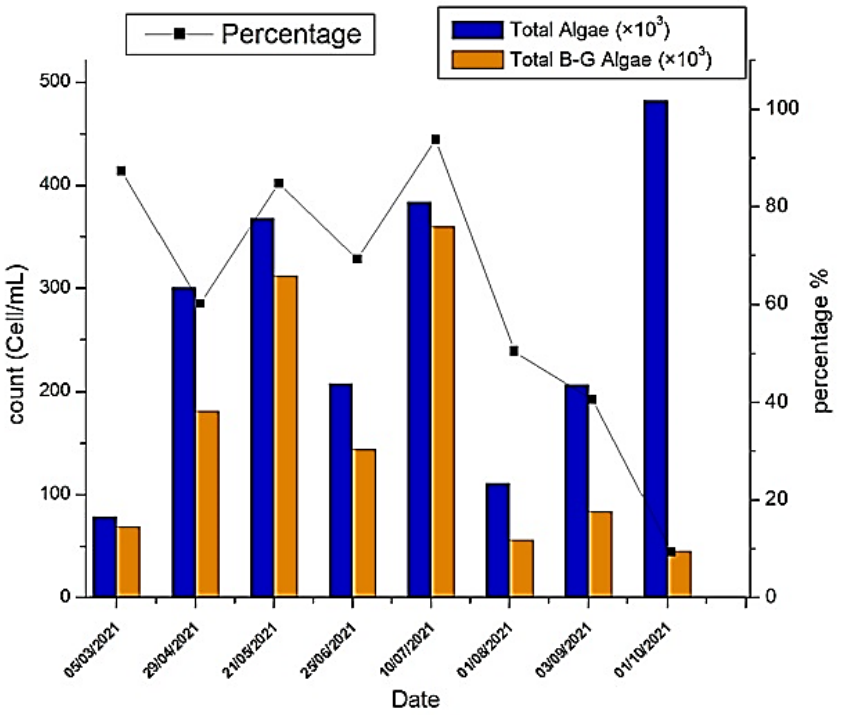

Figure 4 – Count of Algae and B-G algae in the Timgad stream (Station C)

Effects of TP on blue-green algae dominance

The combined results of the physicochemical analysis and the algae analysis show a positive correlation between the TP and blue-green algae concentration in the dam water (R^2=0.85) (Figure 5), and in the Timgad stream (R^2=0.48) (Figure 6).

The strong positive correlation in the dam water compared with the Timgad stream is possibly due to the difference in homogeneity and mixing conditions (Whitton, 2012).

However, in general, these results have been in agreement with the conclusion of a recent study that considered the TP to be the limiting nutrient in freshwater ecosystems (Li et al, 2018; O'Neil et al, 2012).

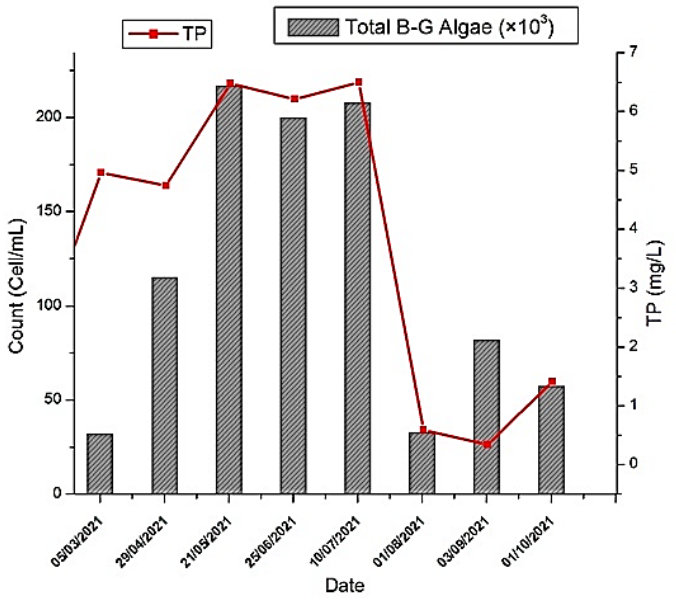

Figure 5 – Correlation between the TP and Cyanobacteria count in the dam water between March 2021 and October 2021

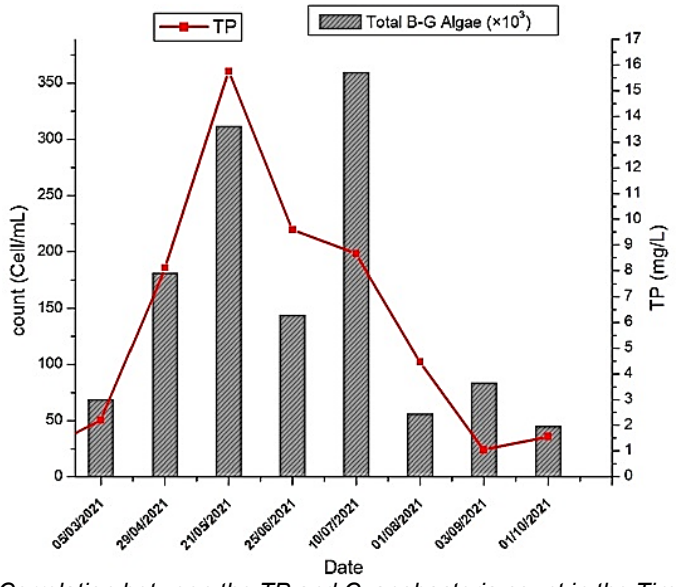

Figure 6 – Correlation between the TP and Cyanobacteria count in the Timgad stream between March 2021 and October 2021

Effects of temperature on blue-green algae dominance

A positive correlation has been recorded between temperature and blue-green algae concentration in the dam water (R^2=0.83) (Figure 7), and in the Timgad stream (R^2=0.84) (Figure 8) in the period between March and August 2021. These results show that temperature is an important factor that controls blue-green algae dominance in freshwater ecosystems (Beaulieu et al, 2013; Konopka & Brock, 1978).

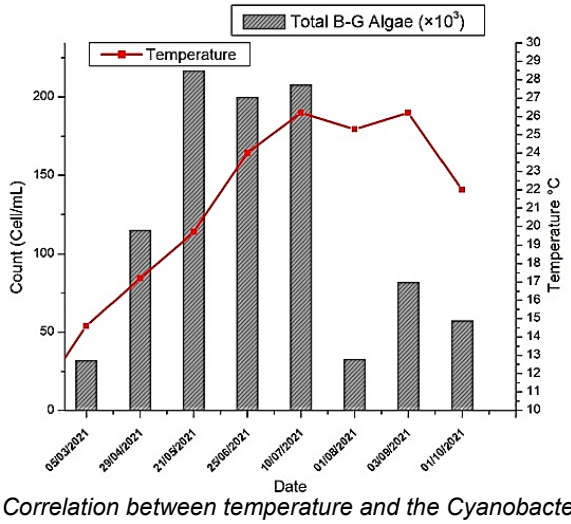

Figure 7 – Correlation between temperature and the Cyanobacteria count in the dam water between March 2021 and October 2021

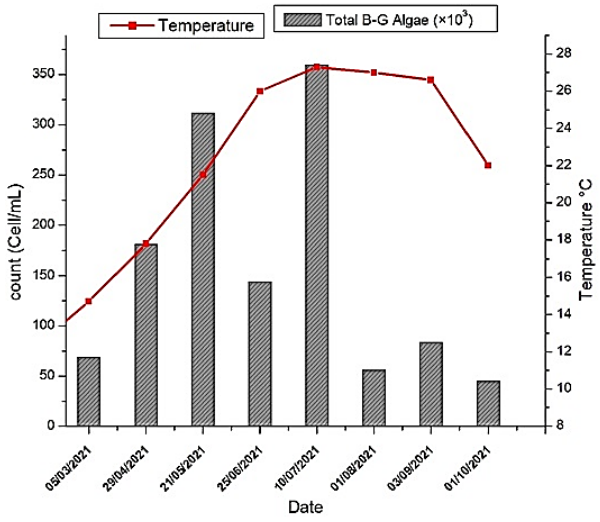

Figure 8 – Correlation between temperature and the Cyanobacteria count in the Timgad stream between March 2021 and October 2021

Effects of blue-green algae on DO

The DO results negatively correlated with the blue-green algae concentration in the dam water (Figure 9). The excessive proliferation of algae leads to oxygen depletion (Dobricic et al, 2016). However, the results show that the eutrophication phenomenon has not yet been reached.

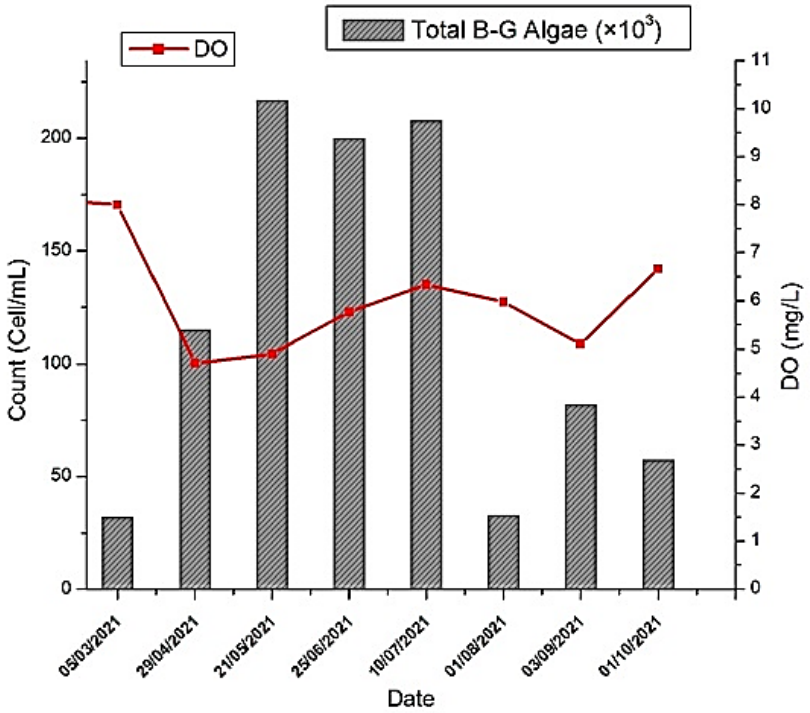

Figure 9 – Correlation between DO and the cyanobacteria count in the dam water between March 2021 and October 2021

Conclusion

This paper delves into the impact of various water supplies on the physicochemical quality of the Timgad dam water and the factors influencing the presence of cyanobacteria blooms. The findings reveal that the Timgad stream and Reboua valley contribute significantly to nutrient levels. Elevated temperatures and nutrient loads, particularly those of total phosphorus (TP), in the Timgad dam water facilitate the growth of blue-green algae. Conversely, the limited nitrogen content favors the predominance of nitrogen-fixing cyanobacteria such as Aphanizomenon

and Oscillatoria. Moreover, the study highlights that the low flow rate and high nutrient load of the Timgad stream create favorable conditions for cyanobacterial growth. Importantly, the study confirms that eutrophication has not yet occurred, underscoring the critical need for controlling nutrient levels to enhance the efficiency of water treatment plants, maintain potable water quality, and safeguard the aquatic ecosystem from further deterioration.

References

Adimalla, N., Chen, J. & Qian, H. 2020. Spatial characteristics of heavy metal contamination and potential human health risk assessment of urban soils: A case study from an urban region of South India. *Ecotoxicology and Environmental Safety*, 194, art.number:110406. Available at: https://doi.org/10.1016/j.ecoenv.2020.110406.

-APHA (American Public Health Association). 1992. Standards Methods for the Examination of Water And Wastewater, 18th Edition. Washington DC: American Public Health Association, American Water Works Association, Water Environment Federation. ISBN: 0-87553-207-1.

-APHA (American Public Health Association). 1999. Standards Methods for the Examination of Water And Wastewater, 20th Edition. Washington DC: American Public Health Association, American Water Works Association, Water Environment Federation. ISBN: 0-87553-235-7.

Amrane, C. & Bouhidel, K.E. 2019. Analysis and speciation of heavy metals in the water, sediments, and drinking water plant sludge of a deep and sulfate-rich Algerian reservoir. *Environmental Monitoring and Assessment*, 191, art.number:73. Available at: https://doi.org/10.1007/s10661-019-7222-9.

Beaulieu, M., Pick, F. & Gregory-Eaves, I. 2013. Nutrients and water temperature are significant predictors of cyanobacterial biomass in a 1147 lakes data set. *Limnology and Oceanography*, 58(5), pp.1736-1746. Available at: https://doi.org/10.4319/lo.2013.58.5.1736.

Berga, L., Buil, J.M., Bofill, E., De Cea, J.C., Garcia Perez, J.A., Mañueco, G., Polimon, J., Soriano, A. & Yagüe, J. (Eds.). 2006. Dams and Reservoirs, Societies and Environment in the 21st Century, Two Volume Set, 1st ed. In: *Proceedings of the International Symposium on Dams in the Societies of the 21st Century, 22nd International Congress on Large Dams (ICOLD)*, Barcelona, Spain, 18 June. CRC Press. Available at: https://doi.org/10.1201/b16818.

Bouslah, S., Djemili, L. & Houichi, L. 2017. Water quality index assessment of Koudiat Medouar Reservoir, northeast Algeria using weighted arithmetic index method. *Journal of Water and Land Development*, 35(X-XII), pp.221-228. Available at: https://doi.org/10.1515/jwld-2017-0087.

-British Standards Institute. 2006. *BS EN 15204:2006 Water quality. Guidance standard on the enumeration of phytoplankton using inverted microscopy (Utermoehl technique)*. London, UK: British Standards Institute. Available at: https://doi.org/10.3403/30085818.

Carmichael, W. 2008. A world overview — One-hundred-twenty-seven years of research on toxic cyanobacteria — Where do we go from here?. In: Hudnell, H.K. (Eds.) *Cyanobacterial Harmful Algal Blooms: State of the Science and Research Needs. Advances in Experimental Medicine and Biology*, 619. New York, NY: Springer. Available at: https://doi.org/10.1007/978-0-387-75865-7_4.

Cheng, W.P. & Chi, F.-H. 2003. Influence of eutrophication on the coagulation efficiency in reservoir water. *Chemosphere*, 53(7), pp.773-778. Available at: https://doi.org/10.1016/S0045-6535(03)00510-1.

Codd, G.A., Lindsay, J., Young, F.M., Morrison, L.F. & Metcalf, J.S. 2005. Harmful Cyanobacteria. In: Huisman, J., Matthijs, H.C., Visser, P.M. (Eds.) *Harmful Cyanobacteria. Aquatic Ecology Series*, 3. Dordrecht: Springer. Available at: https://doi.org/10.1007/1-4020-3022-3_1.

Dobricic, S., Pozzoli, L., Sanseverino, I., Conduto, D. & Lettieri, T. 2016. *Algal bloom and its economic impac*t. Joint Research Centre (European Commission). Available at: https://doi.org/10.2788/660478.

Dzialowski, A.R., Wang, S.-H., Lim, N.-C., Spotts, W.W. & Huggins, D.G. 2005. Nutrient limitation of phytoplankton growth in central plains reservoirs, USA. *Journal of Plankton Research*, 27(6), pp.587-595. Available at: https://doi.org/10.1093/plankt/fbi034.

Feihrmann, A.C., Baptista, A.T.A., Lazari, J.P., Silva, M.O., Vieira, M.F. & Vieira, A.M.S. 2017. Evaluation of Coagulation/ Floculation Process for Water Treatment using Defatted Cake from Moringa oleifera. *Chemical Engineering Transactions*, 57, pp.1543-1548. Available at: https://doi.org/10.3303/CET1757258.

Giannuzzi, L. 2018. Cyanobacteria Growth Kinetics. In. Wong, Y.K. (Ed.) *Algae*. IntechOpen. Available at: https://doi.org/10.5772/intechopen.81545.

Gitis, V. & Hankins, N. 2018. Water treatment chemicals: Trends and challenges. *Journal of Water Process Engineering*, 25, pp.34-38. Available at: https://doi.org/10.1016/j.jwpe.2018.06.003.

Gleick, P.H. 1993. *Water in Crisis: A Guide to the World's Fresh Water Resources*. Oxford University Press. ISBN: 9780195076288.

Havens, K.E. 2008. Cyanobacteria blooms: effects on aquatic ecosystems. In: Hudnell, H.K. (Eds.) *Cyanobacterial Harmful Algal Blooms: State of the Science and Research Needs. Advances in Experimental Medicine and Biology*, 619. New York, NY: Springer. Available at: https://doi.org/10.1007/978-0-387-75865-7_33.

Hoeger, S.J., Hitzfeld, B.C. & Dietrich, D.R. 2005. Occurrence and elimination of cyanobacterial toxins in drinking water treatment plants. *Toxicology and Applied Pharmacology*, 203(3), pp.231-242. Available at: https://doi.org/10.1016/j.taap.2004.04.015.

Issa, A.A., Abd-Ala, M.H. & Ohyama, T. 2014. Nitrogen Fixing Cyanobacteria: Future Prospect. In: Ohyama, T. (Ed.) *Advances in Biology and Ecology of Nitrogen Fixation*. IntechOpen. Available at: https://doi.org/10.5772/56995.

Journey, C.A., Beaulieu, K.M. & Bradley, P.M. 2013. Environmental Factors that Influence Cyanobacteria and Geosmin Occurrence in Reservoirs. In: Bradley, P.M. (Ed.) *Current Perspectives in Contaminant Hydrology and Water Resources Sustainability*. IntechOpen. Available at: https://doi.org/10.5772/54807.

Karaouzas, I., Kapetanaki, N., Mentzafou, A., Kanellopoulos, T.D. & Skoulikidis, N. 2021. Heavy metal contamination status in Greek surface waters: A review with application and evaluation of pollution indices. *Chemosphere*, 263, art.number:128192. Available at: https://doi.org/10.1016/j.chemosphere.2020.128192.

Konopka, A. & Brock, T.D. 1978. Effect of Temperature on Blue-Green Algae (Cyanobacteria) in Lake Mendota. *Applied and Environmental Microbiology*, 36(4), pp.572-576. Available at: https://doi.org/10.1128/aem.36.4.572-576.1978.

Labed, A. 2015. *Biodiversité et dynamique spatio-temporelle de la communauté phytoplanctonique de la zone humide artificielle du barrage*. MA thesis. Algeria: University of Oum el Bouaghi [online]. Available at: https://www.ccdz.cerist.dz/admin/notice.php?id=000000000000081602500063 2 [Accessed: 15 April 2024].

Li, J., Hansson, L.-A. & Persson, K.M. 2018. Nutrient Control to Prevent the Occurrence of Cyanobacterial Blooms in a Eutrophic Lake in Southern Sweden, Used for Drinking Water Supply. *Water*, 10(7), art.number:919. Available at: https://doi.org/10.3390/w10070919.

Loucks, D.P. & van Beek, E. 2017. Water Resources Planning and Management: An Overview. In: *Water Resource Systems Planning and Management*. Cham: Springer. Available at: https://doi.org/10.1007/978-3-319-44234-1_1.

Lv, J., Wu, H. & Chen, M. 2011. Effects of nitrogen and phosphorus on phytoplankton composition and biomass in 15 subtropical, urban shallow lakes in Wuhan, China. *Limnologica*, 41(1), pp.48-56. Available at: https://doi.org/10.1016/j.limno.2010.03.003.

Marra, J., Bidigare, R.R. & Dickey, T.D. 1990. Nutrients and mixing, chlorophyll and phytoplankton growth. *Deep Sea Research Part A. Oceanographic Research Papers*, 37(1), pp.127-143. Available at: https://doi.org/10.1016/0198-0149(90)90032-Q.

Mhamdi, F., Khouni, I. & Ghrabi, A. 2016. Diagnosis and characteristics of water quality along the Wadi El Bey river (Tunisia). Coagulation/flocculation essays of textile effluents discharged into the Wadi. *Desalination and Water Treatment*, 57(46), pp.22166-22188. Available at: https://doi.org/10.1080/19443994.2016.1147378.

Mitrovic, S.M., Hardwick, L. & Dorani, F. 2011. Use of flow management to mitigate cyanobacterial blooms in the Lower Darling River, Australia. *Journal of Plankton Research*, 33(2), pp.229-241. Available at: https://doi.org/10.1093/plankt/fbq094.

O'Neil, J.M., Davis, T.W., Burford, M.A. & Gobler, C.J. 2012. The rise of harmful cyanobacteria blooms: The potential roles of eutrophication and climate

change. *Harmful Algae*, 14, pp.313-334. Available at: https://doi.org/10.1016/j.hal.2011.10.027.

Pivokonsky, M., Naceradska, J., Kopecka, I., Baresova, M., Jefferson, B., Li, X. & Henderson, R.K. 2016. The impact of algogenic organic matter on water treatment plant operation and water quality: a review. *Critical Reviews in Environmental Science and Technology*, 46(4), pp.291-335. Available at: https://doi.org/10.1080/10643389.2015.1087369.

Qu, J. & Fan, M. 2010. The Current State of Water Quality and Technology Development for Water Pollution Control in China. *Critical Reviews in Environmental Science and Technology*, 40(6), pp.519-560. Available at: https://doi.org/10.1080/10643380802451953.

Quesada, H.B., Baptista, A.T.A., Cusioli, L.F., Seibert, D., de Oliveira Bezerra, C. & Bergamasco, R. 2019. Surface water pollution by pharmaceuticals and an alternative of removal by low-cost adsorbents: A review. *Chemosphere*, 222, pp.766-780. Available at: https://doi.org/10.1016/j.chemosphere.2019.02.009.

Richardson, S.D. & Postigo, C. 2011. Drinking Water Disinfection By-products. In: Barceló, D. (Ed.) *Emerging Organic Contaminants and Human Health. The Handbook of Environmental Chemistry*, 20. Berlin, Heidelberg: Springer. Available at: https://doi.org/10.1007/698_2011_125.

Rodier, J., Legube, B., Merlet, N. & Brunet, R. 2009. *L'analyse de l'eau - 9e éd.* Dunod. ISBN: 9782100541799.

Segerson, K. & Walker, D. 2002. Nutrient pollution: An economic perspective. *Estuaries*, 25(4), pp.797-808. Available at: https://doi.org/10.1007/BF02804906.

Smatti-Hamza, I., Afri-Mehennaoui, F., Keddari, D. & Mehennaoui, S. 2020. Evaluation du niveau de contamination par le Cuivre et le Chrome des sédiments du barrage Koudiat Medouar de Timgad Batna (Algérie). *Algerian Journal of Environmental Science and Technology*, 6(2), pp.1348-1353 [online]. Available at: https://www.aljest.net/index.php/aljest/article/view/261. [Accessed: 15 April 2024].

Tiri, A., Lahbari, N. & Boudoukha, A. 2017. Assessment of the quality of water by hierarchical cluster and variance analyses of the Koudiat Medouar Watershed, East Algeria. *Applied Water Science*, 7, pp.4197-4206. Available at: https://doi.org/10.1007/s13201-014-0261-z.

-U.S. Environmental Protection Agency. 2001. *Method 1687 Total Kjeldahl Nitrogen in Water and Biosolids by Automated Colorimetry with Preliminary Distillation/Digestion*. Washington, D.C: U.S. Environmental Protection Agency, Office of Water, Office of Science and Technology Engineering and Analysis Division [online]. Available at: https://www.epa.gov/sites/default/files/2015-10/documents/method_1687_draft_2001.pdf [Accessed: 15 April 2024].

Walker, D.B, Baumgartner, D.J., Gerba, C.P. & Fitzsimmons, K. 2019. Chapter 16 - Surface Water Pollution. In: *Environmental and Pollution Science (Third Edition)*, pp.261-292. Academic Press. Available at: https://doi.org/10.1016/B978-0-12-814719-1.00016-1.

Whitton, B.A. 2012. *Ecology of Cyanobacteria II: Their Diversity in Space and Time*. Springer Dordrecht. Available at: https://doi.org/10.1007/978-94-007-3855-3.

Wurtsbaugh, W.A., Paerl, H.W. & Dodds, W.K. 2019. Nutrients, eutrophication and harmful algal blooms along the freshwater to marine continuum. *WIREs Water*, 6, e1373. Available at: https://doi.org/10.1002/wat2.1373.

Estudio del impacto de diversos suministros sobre la calidad de las aguas superficiales

Hocine Chibane[a], **autor de correspondencia**,
Mohamed Redha Menani[a], *Kamel-eddine* Bouhidel[b]

[a] Universidad de Batna 2, Instituto de Ciencias de la Tierra y del Universo, Departamento de Geología, Movilización y Gestión de Recursos Hídricos, Laboratorio LMMWR, Batna, República Argelina Democrática y Popular

[b] Universidad de Batna 1, Facultad de Ciencias de los Materiales, Departamento de Química, Laboratorio de Química y Química Ambiental LCEC, Batna, República Argelina Democrática y Popular

CAMPO: química ambiental
TIPO DE ARTÍCULO: artículo científico original

Resumen:

Introducción/objetivo: Con el continuo crecimiento poblacional y la expansión industrial, los reservorios superficiales de agua dulce, como las presas, se han vuelto cada vez más vitales debido a su accesibilidad y facilidad de tratamiento. Sin embargo, la calidad de estas fuentes de agua se ha deteriorado significativamente, principalmente debido al vertido de aguas residuales domésticas e industriales. La proliferación de floraciones extensas de algas ha generado importantes desafíos para mantener la calidad del agua potable y ha suscitado preocupación por la salud pública. Este estudio investiga el impacto de diversas fuentes de agua en la calidad fisicoquímica de una presa argelina durante cuatro temporadas (diciembre de 2020 a octubre de 2021) y explora los factores que influyen en la aparición de floraciones de cianobacterias para comprender mejor y gestionar este crecimiento excesivo.

Métodos: Se analizaron mensualmente las propiedades fisicoquímicas y la composición algal del agua de la presa para determinar las fuentes de nutrientes y los factores ambientales que afectan la proliferación de cianobacterias.

Resultados: El análisis reveló que el arroyo Timgad y el valle de Reboua son fuentes importantes de enriquecimiento de nutrientes. Las temperaturas elevadas y las altas cargas de nutrientes, en particular el fósforo total (PT) en el agua de la presa de Timgad facilitan la proliferación

de algas verdeazuladas. Además, el contenido limitado de nitrógeno favorece el predominio de cianobacterias fijadoras de nitrógeno, como Aphanizomenon y Oscillatoria. El estudio también destaca que el bajo caudal y la alta carga de nutrientes del arroyo Timgad crean condiciones favorables para el crecimiento de cianobacterias.

Conclusión: El aporte de nutrientes, la temperatura y las condiciones hidrológicas influyen significativamente en las floraciones de cianobacterias. Comprender estos factores es crucial para implementar estrategias eficaces de gestión del agua que reduzcan la proliferación de algas y protejan la calidad del agua dulce.

Palabras claves: presa de agua Koudiet Medouar, algas verdeazuladas, cianobacterias, contaminación por nutrientes, Timgad.

Изучение влияния различных форм водоснабжения на качество поверхностных вод

Хусейн Шибана[а], **корреспондент**,
Мухаммед Реза Менани[а], *Камел-еддин* Бухайдал[б]

[а] Университет Батны 2,
Институт наук о Земле и космосе, факультет геологии,
лаборатория мобилизации и управления водными ресурсами MMWR,
г. Батна, Алжирская Народная Демократическая Республика

[б] Университет Батны 1, факультет материаловедения, кафедра химии,
лаборатория химии и химии окружающей среды LCEC,
г. Батна, Алжирская Народная Демократическая Республика

РУБРИКА ГРНТИ: 61.01.94 Охрана окружающей среды
ВИД СТАТЬИ: оригинальная научная статья

Резюме:

Введение/цель: В связи с ростом населения и развитием промышленности поверхностные водоемы с пресной водой, такие как плотины, приобретают все большее значение из-за простоты эксплуатации и очистки. Однако качество этих источников водоснабжения значительно ухудшилось, в первую очередь из-за сброса бытовых и промышленных сточных вод. Распространение бурного цветения водорослей привело к серьезным проблемам в сохранении качества питьевой воды и вызвало обеспокоенность по поводу общественного здравоохранения. В данном исследовании изучается влияние различных источников воды на физико-химическое качество воды в одной алжирской плотине в течение четырех времен года (декабрь 2020 г. - октябрь 2021 г.). В статье также исследуются факторы, влияющие на возникновение цветения цианобактерий,

с целью лучшего понимания и предотвращения их чрезмерного роста.

Методы: В ходе исследования ежемесячно анализировались физико-химические свойства и водорослевый состав воды плотины для определения источников питательных веществ и факторов окружающей среды, влияющих на размножение цианобактерий.

Результаты: Анализ показал, что водоем Тимгад и долина Румбура являются важными источниками питательных веществ. Повышенные температуры и высокая концентрация питательных веществ, особенно общего фосфора в воде плотины Тимгад способствуют размножению сине-зеленых водорослей. Помимо того, ограниченное содержание азота способствует преобладанию азотфиксирующих цианобактерий, таких как афанизоменон и осциллатория. Исследование также показало, что медленное, богатое питательными веществами течение реки Тимгад создает подходящую среду для роста цианобактерий.

Выводы: Поступление питательных веществ, температура и гидрологические условия существенно влияют на цветение цианобактерий. Понимание этих факторов имеет ключевое значение в применении эффективных стратегий управления водными ресурсами, направленных на предотвращение распространения водорослей и защиту качества пресной воды.

Ключевые слова: плотина Кудиат-Медуар, сине-зеленые водоросли, цианобактерии, биогенное загрязнение, Тимгад.

Испитивање утицаја различитих облика снабдевања на квалитет површинских вода

Хусеин Шибан[а], **аутор за преписку**,
Мухамед Реза Менани[а], *Камел-един* Бухајдал[б]

[а] Универзитет у Батни 2,
Институт за науке о Земљи и свемиру, Департман за геологију,
Лабораторија за мобилизацију и управљање водним ресурсима
ЛММВР, Батна, Народна Демократска Република Алжир

[б] Универзитет у Батни 1, Факултет наука о материјалима,
Департман за хемију, Лабораторија за хемију и хемију животне
средине ЛЦЕЦ, Батна, Народна Демократска Република Алжир

ОБЛАСТ: хемија животне средине
КАТЕГОРИЈА (ТИП) ЧЛАНКА: оригинални научни рад

Chibane, H. et al, Study of the impact of various supplies on the quality of surface water, pp.553-574

Сажетак:

Увод/циљ: С растом популације и ширењем индустрије резервоари површинских слатких вода, као што су бране, постају све значајнији због своје приступачности и лакоће прераде. Међутим, квалитет ових водоизворишта постаје све лошији, пре свега због испуштања комуналних и индустријских отпадних вода. Пролиферација екстензивног цветања алги довела је до значајних проблема у одржавању квалитета пијаће воде, као и до забринутости за јавно здравље. Ова студија бави се утицајем различитих извора воде на физичко-хемијски квалитет воде у једној брани у Алжиру током четири годишња доба (децембар 2020 – октобар 2021), а испитује и факторе који утичу на појаву цветања цијанобактерија како би се боље разумео и контролисао њихов прекомерни раст.

Методе: Физичко-хемијска својства воде у брани, као и састав алги у њој, анализирани су на месечном нивоу како би се одредили извори нутријената и фактори животне средине који утичу на ширење цијанобактерија.

Резултати: Анализа је показала да су водоток Тимгада и долина Ребоуа значајни извори обогаћивања хранљивим материјама. Високе температуре и висока засићеност воде хранљивим материјама (нарочито укупним фосфором) у брани Тимгад олакшавају ширење плавозелених алги. При томе, ограничени садржај азота подстиче доминацију азотофиксирајућих цијанобактерија као што су Aphanizomenon и Oscillatoria. Такође, у студија се истиче да спори ток Тимгада богатог хранљивим материјама представља погодну средину за раст цијанобактерија.

Закључак: Доток хранљивих материја, температура и хидролошки услови знатно утичу на цветање цијанобактерија. Познавање ових фактора од суштинске је важности за примену ефикасних стратегија управљања водом како би се смањила пролиферација алги и заштитио квалитет слатких вода.

Кључне речи: водена брана Коудиет Медоуар, плавозелене алге, цијанобактерије, загађење нутријентима, Тимгад.

Paper received on: 17.04.2024.
Manuscript corrections submitted on: 27.03.2025.
Paper accepted for publishing on: 28.03.2025.

Assessment of the environmental impact of urban wastewater and the treatment capacity of the Saida activated sludge plant (North-western Algeria) on the occasion of Eid Al-Adha

Souad Zairi[a], *Boumediene* Meddah[b], *Miloud* Slimani[c], *Asmaa* Rahmani[d]

[a] Mustapha Stambouli University, Faculty of Natural and Life Sciences, Department of Biology, Biology Laboratory, Mascara, People's Democratic Republic of Algeria, e-mail: soufark74@gmail.com, **corresponding author**, ORCID iD: https://orcid.org/0000-0001-8119-7033

[b] Mustapha Stambouli University, Faculty of Natural and Life Sciences, Department of Biology, Biology Laboratory, Mascara, People's Democratic Republic of Algeria, e-mail: meddah19@yahoo.fr, ORCID iD: https://orcid.org/0000-0001-7946-012X

[c] Dr. Tahar Moulay University of Saida, Faculty of Sciences, Department of Biology, Biology Laboratory, Saida, People's Democratic Republic of Algeria, e-mail: mslimani20@gmail.com, ORCID iD: https://orcid.org/0000-0003-1191-3924

[d] Dr. Tahar Moulay University of Saida, Faculty of Technology, Department of Civil Engineering and Hydraulics, Modeling and Calculation Methods Laboratory, Saida, People's Democratic Republic of Algeria, e-mail: ra.hydrau@outlook.com, ORCID iD: https://orcid.org/0000-0003-3267-4862

https://doi.org/10.5937/vojtehg73-55420

FIELD: chemical technology, environmental science
ARTICLE TYPE: original scientific paper

Abstract:

Introduction/purpose: The slaughter of livestock during Eid Al-Adha generates significant quantities of wastewater rich in organic pollutants. However, the specific impact of these effluents on water quality remains poorly documented. This study aimed to assess the pollutant loads discharged into the Saida Valley during Eid Al-Adha and evaluate the treatment capacity of the local activated sludge wastewater treatment plant (WWTP).

Methods: Water samples were collected from different points in the sewerage system at various times throughout the day during three Eid Al-

Adha events (2017, 2018, and 2019). Several physico-chemical parameters were analyzed, including temperature, pH, electrical conductivity, chemical oxygen demand (COD), five-day biochemical oxygen demand (BOD_5), total suspended solids (TSS), ammonium, nitrates, nitrites, and phosphorus. The measured pollution levels were compared to the Algerian regulatory standards to assess compliance.

Results: The analyses revealed a sharp increase in pollution levels in the morning, followed by a gradual decline in the evening. High pollutant loads from slaughter effluents significantly degraded the water quality of the Saïda River. The organic pollution index classified these discharges as very high pollution. The excessive input of organic matter and nutrients resulted in oxygen depletion and eutrophication risks.

Conclusion: The discharge of untreated slaughter wastewater poses serious environmental and public health risks. Strengthening wastewater management strategies during Eid Al-Adha, enhancing treatment processes at the Saïda WWTP, and enforcing strict environmental regulations are essential to mitigating these impacts.

Key words: Eid Al-Adha, activated sludge WWTP, biodegradability, pollutant load, receiving environment, wastewater.

Introduction

The protection of the environment is an objective in policies of most countries in terms of preserving natural resources and ecosystems, as well as protecting public health (Chennaoui, 2003). In this context, wastewater, excreta, and greywater could be considered costly by-products of the urbanization process, requiring significant investments in treatment plants and disposal mechanisms (Asibor et al, 2020). Freshwater resources are being depleted at an alarming rate due to increasing water consumption. Consequently, the volume of wastewater discharges increases considerably (Bhave et al, 2020). In recent years, the scarcity of fresh water and the treatment of wastewater are among the main environmental challenges (MWR 2017). Algeria ranks 29th among the countries most vulnerable to water stress. It is thus classified in the category of “high” water stress, the second largest category behind that of “extremely high” water stress. The anchoring of Algeria in the path of sustainable development has prompted the public authorities to resume the policy of sanitation and wastewater treatment. Thus, a special fund has been set up to support the management and recovery of treated wastewater. It is a pioneer on the African scale in the construction of wastewater treatment plants. A number of 172 stations operate throughout the national territory, providing approximately one billion cubic meters of treated water for

agricultural irrigation (MWR 2019). Hydrous environments and aquatic ecosystems must be protected against all forms of pollution likely to alter water quality and harm its various uses (JORA, 2003). Thus, uncontrolled wastewater discharges, loaded with organic matter and mixed with chemicals, are therefore a fundamental element in terms of pollution because they are the site of many chemical reactions and the reproduction of many disease vectors (De Anda et al, 2018; Gautam et al, 2013). This uncontrolled disposal of untreated sewage is the main cause of water contamination which causes waterborne diseases such as cholera, typhoid, and infectious hepatitis. This leads to a high risk of disease transmission due to the presence of pathogens in irrigation water (Kokkinos et al, 2015).

In August 2018, the Ministry of Health and Population revealed contamination of water by the "cholera vibrio" virus, which was the main cause of the spread of a virulent infection, resulting in two deaths in the central regions (Algiers, Blida, Tipasa and Bouira) two days after the 2018 Eid holiday. The return of cholera, which last appeared in 1996, reminds Algerians of certain bitter truths. It reveals major dysfunctions. This is due to the evacuation of effluents on the day of Eid Al-Adha into the receiving environment without any prior treatment and to the use of this water for the irrigation of vegetables and fruits (melon, watermelon, tomato, salad, etc.). The U.S. Environmental Protection Agency has ranked slaughterhouse discharges (Identical to Eid Day sacrifice discharges) among the most environmentally damaging (Walter et al, 1974). Raw water quality assessment and treatment at the station inlet are widely preferred (Bayo & López-Castellanos, 2016).

Muslims around the world celebrate the occasion of Eid Al-Adha which marks the end of the period of pilgrimage to Mecca. All the slaughtering, skinning and evisceration operations are carried out in the same place. From a symbolic viewpoint, this celebration is "the feast of sacrifice", translated in Algeria, by the slaughter of an average of 4 million animals (sheep, cattle, goats or camelids). Domestic drinking water consumption peaks on the first day of Eid, the average daily quantity of 9 million cubic meters of water distributed nationally is consumed within 6 hours, thus generating an average of 7.5 million cubic meters of waste water. For the capital of Saida region, average production is 1300 tons of slaughtered carcasses (producing approximately an average of 710 tons of waste/day and an average of 10608.39 m^3/day of wastewater, an average of 8 liters per kg of carcass. The operator of the Saida wastewater treatment plant bypasses the wastewater discharges today directly into the Saida river without any treatment on the pretext that such events cause a

significant accumulation of mineral sludge in the structures, which would further delay the resumption of normal operation of the plant. Moreover, the pollution load of these waters exceeds the capacity of the plant; this would create various problems of fouling of the structures and organs operation of the installation (NHO, 2017).

The present study consists, initially, of monitoring certain major pollution parameters generated by the discharge of wastewater on this occasion and then estimating the polluting loads brought. Finally, the impact of discharges on this occasion on the purification capacity of the Saida station was assessed.

Materials and methods

Study area

The city of Saida is located in northwestern Algeria (Figure 1), it covers an area of 6 613 km^2. In this region, conventional water resources are mainly underground. Water availability is around 230 m^3/inhabitant/year (ratio of 47% of the national average). The city is 98% connected to the sanitation network. All of this wastewater drained by the districts of the city is directed to the treatment plant.

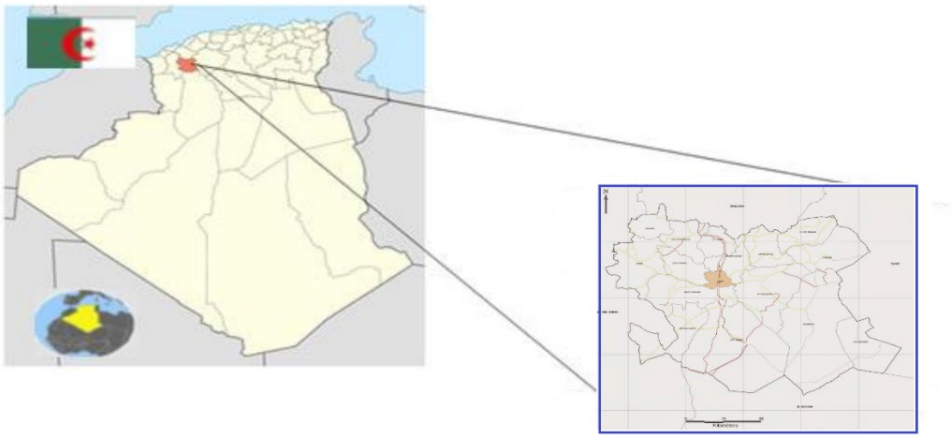

Figure 1 – Location of the study area

The Saida region wastewater treatment plant is located in the northwestern part of the city. It is located near the Saida River in the municipality of Rebahia. This station covers an area of 11.47 ha. It is designed by the Spanish company (SACOM DIESA Algeria sector) to treat

a nominal flow rate of waste water of 30 000 m^3/day with a capacity of 150 000 equivalents/inhabitant.

The collection system connected to the treatment plant is unitary. The pollution that the station receives comes from urban domestic discharges and certain industrial discharges. As shown in Figure 2, the main collectors of the station are A, B, and C. The culmination of the collectors A and C is done by gravity. Wastewater from the collector B is routed to the pumping station and then crosses the river to reach the collector A.

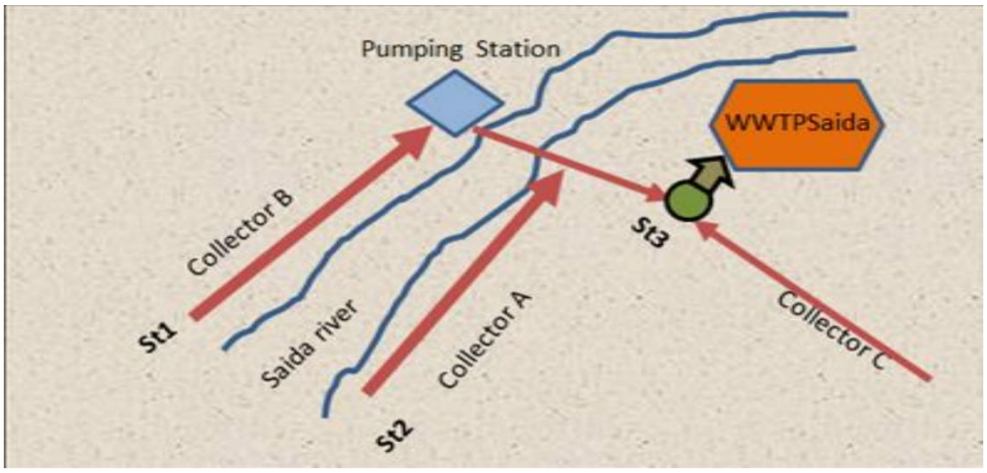

Figure 2 – Main sewers of the Saida sewerage network

The Saida wastewater treatment plant operates with a low-load activated sludge process. It has two parallel biological treatment lines. Each line is composed of a biological reactor followed by a clarifier. The biological reactor is the first link in secondary treatment.

The station's two basins are rectangular with a total volume of 13 068 m^3 for each basin. Mixing and oxygenation are ensured by six vertical axis surface aerators having a total nominal power of 900 kw, total oxygen supply of 1296 kg O_2/h and a specific mixing power of 34.4 w/m^3.

It also has two parallel cylindrical-conical settling tanks, equipped with a scraper and a suction bridge and two sludge extraction pumps, with a volume of 5800 m^3 for each basin, a horizontal surface of 1452 m^2 and a peripheral height of 3 m (Figure 3).

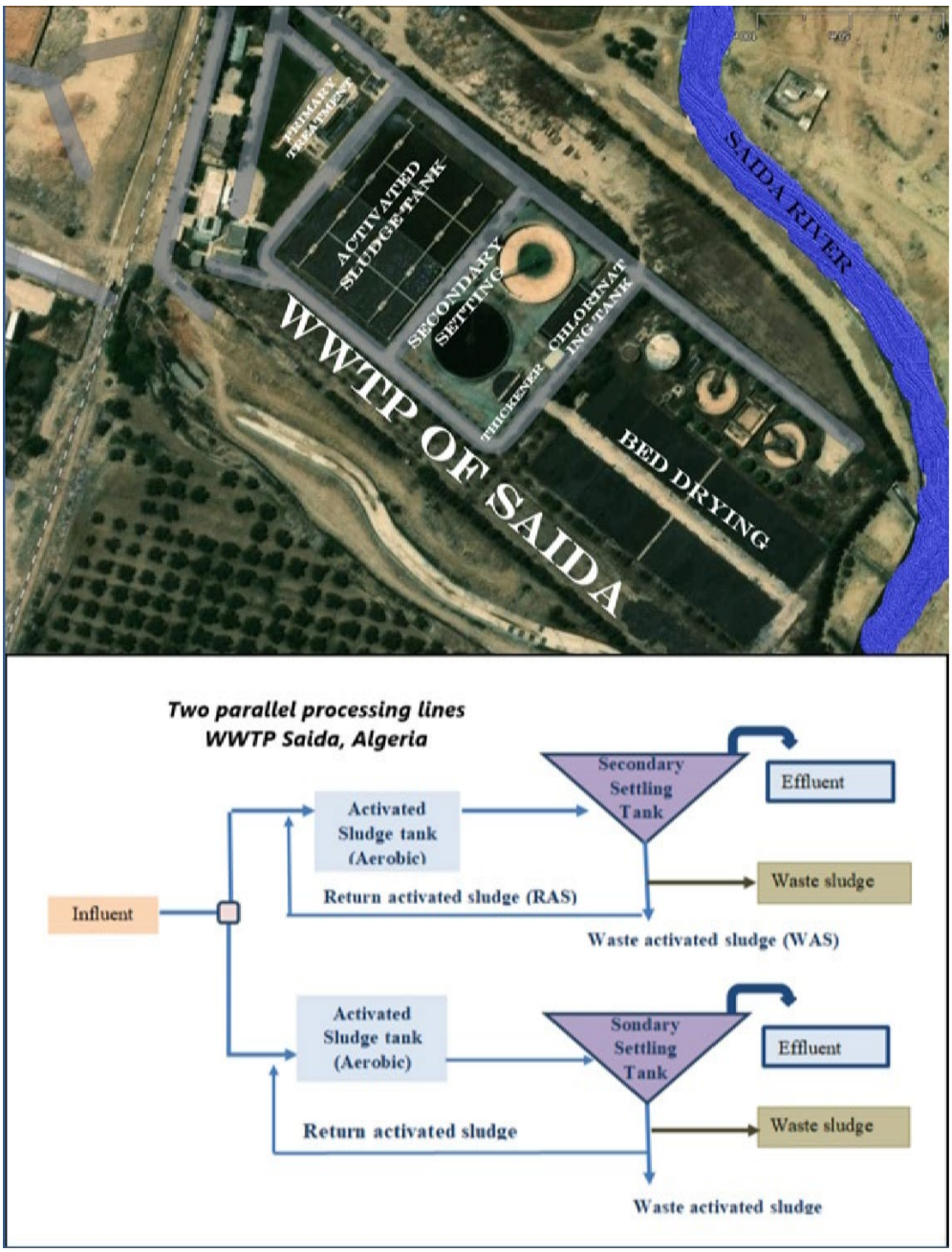

Figure 3 – Schematic presentation of the biological treatment of the Saida WWTP

The technical characteristics of the station are summarized in Table 1.

Table 1 – Technical characteristics of the Saida WWTP (NHO, 2017)

Type of sewerage network.	unit	
Average daily flow	30 000 m^3 /d	
Daily load in BOD5	9 000 kg/d	
Daily load in TSS	12 000 kg/d	
Purification objective	Inlet (mg/l)	Outlet (mg/l)
BOD5Concentration	300	30
TSS Concentration	400	30
COD Concentration	/	120
Concentration of NH4+	/	5

Sampling and physical-chemical analysis

During the occasion of Eid Al-Adha, all wastewater is directed to the receiving environment (Saida River) without any treatment. Three sampling points (St_1, St_2, and St_3) were identified (Figure 4).

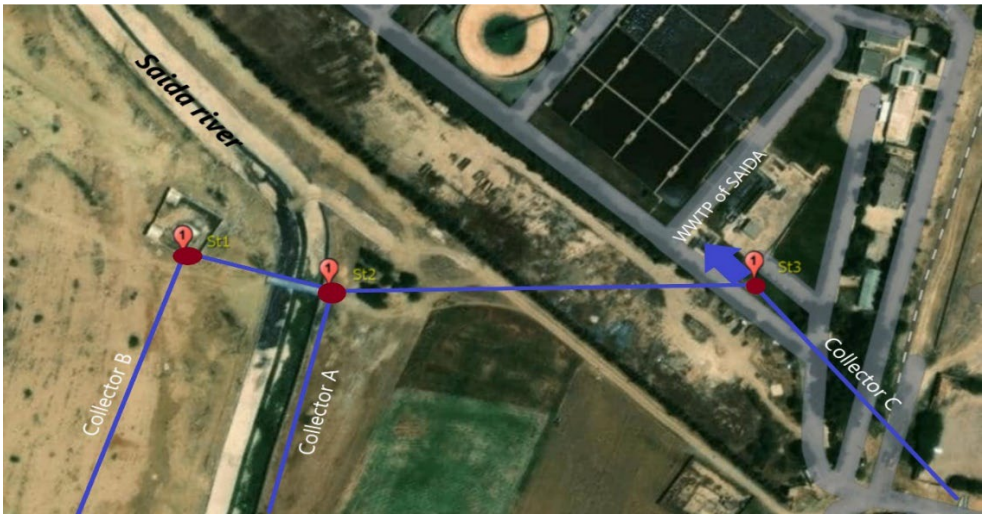

Figure 4 – Locations of the sampling sites

The samples were taken on the day of Eid Al-Adha on three consecutive occasions - August 31, 2017, August 20, 2018, and August 10, 2019. The geographical location of the three sampling sites is given in Table 2.

Table 2 – Details of the sampling locations

N°	Location name	Coordinates	Description
1	St1	N34°52'18.7783" E0°08'39.2476"	B upper part manifold of the Saida city
2	St2	N34°52'18.2713" E0°08'41.7581"	A collector of the lower part of the Saida city
3	St3	N34°52'18.3980" E0°08'49.0967"	Upstream of the WWTP

Wastewater samples were collected using a wide-mouth container. The container is placed on a stick to fill a 3-liter bucket. The bucket used is made of plastic material free of pollutants and preservatives. The bucket was rinsed with wastewater for sampling. Samples are taken a few centimeters below the water surface without approaching the bottom. Then, the samples were covered and labeled with their origin and time of collection. The samples were stored and transported in a cooler at a temperature close to 4°C.

The monitoring of physical-chemical parameters was carried out with a frequency of one sample every half hour in the time intervals from 08h:00 to 20h:00.

In the present study, the physical-chemical parameters analyzed are temperature, pH, electrical conductivity, dissolved oxygen, five-day biological oxygen demand (BOD_5), chemical oxygen demand (COD), suspended matter (TSS), and the concentration of ammonium, nitrite, nitrate and total phosphorus (Pt). All the tests are carried out in the ONA laboratory at the Saida STEP, according to the methods described in the ISO standard (ISO, 2025). Temperature, pH and electrical conductivity measurements were taken "in situ".

Table 3 shows the different parameters measured. The analytical methods used are based on the principles of the NF-EN-ISO standards while respecting the required quality assurance/control rules.

Table 3 – Principles of measurement of the different parameters studied (Rodier, 1975)

Parameter	Abbreviation	Standards
Suspended matter	TSS	NF T90-105
Biochemical oxygen demand	BOD_5	NF T90-103
Chemical oxygen demand	COD	NF T90-101
Nitrates	NO3-	NF T90-012
Nitrites	NO2-	NF T90-013
Ammonium	NH4+	NF T90-015
Total phosphorus	Pt	NF T90-023
Conductivity	Cond	NFT90-31

Temperature, pH, and electrical conductivity are measured using a thermometer (Checktemp Dip - HI98539), a conductivity meter (HACH HQ 1110,) and a pH meter (HACH HQ 1110, IP67), respectively. For suspended solids, the analysis is based on filtration and drying at 105°C for 2 hours. The BOD_5, using a BOD-meter (OXITOP112), was determined. The COD was measured with a mineralization station (Hach, DRB 200). For the measurement of nitrate, ammonium, nitrite, and phosphorus content, a digestion block (BUCHI Speed Digester K-436) and a distillation unit (BUCHI K-350) were used. The results were read with a spectrophotometer.

Pollution indices

The calculation of the Organic Pollution Index (IPO) is based on the distribution of the values of the polluting elements into 5 classes (Table 4). Then, the class number is determined according to its measurements BOD_5 (mg O_2/l)), ammonium (mg N/l), nitrite (µg N/l), phosphate (µg P/l) and finally used to achieve the mean (Table 5).

The calculation principle of the Lisec-index is the same as the IPO index, but replacing the average of the classes by the sum of the classes. The principle of calculation of the Index of the Institute of Hygiene and Epidemiology IHE is the same as the IPO, but with other classes and other

parameters (dissolved oxygen %, COD (mg O_2/l), BOD_5 (mg O_2/l), Ammonium (mg N/l), Phosphate (µg P/l), and Phosphorus (µg P/l)).

Table 4 – Class limits of the organic pollution index (Al-Hejuje et al, 2017)

Parameters / Classes	BOD5 (mg/l)	NH4+ (mg/l)	NO2- (µg/l)	PO4- (µg/l)
5	< 2	< 0.1	5	15
4	2 - 5	0.1 – 0.9	6 - 10	16 - 75
3	5.1 - 10	1 – 2.4	11 - 50	76 - 250
2	10.1 - 15	2.5 – 6.0	51 - 150	251 - 900
1	>15	>6	>150	>900

OPI = Average class number of 4 parameters

Table 5 – OPI classes, pollution degrees

Classes average	Organic pollution level
5.0 – 4.6	Null
4.5 - 4.0	Low
3.9 – 3.0	Moderate
2.9 – 2.0	High
1.9 – 1.0	Very high

Results and discussion

Flow estimation

The increase in population, as well as in water consumption, leads to an increase in the production of wastewater. In Table 1, the average flow of collected wastewater is calculated taking into account the increase in population corresponding to the sanitation master plans. The average flow treated is measured at the entrance to the treatment plant. The average flow discharged into the receiving medium without treatment is the difference between the two flow rates collected and measured. Eid Al-Adha's occasional wastewater flow is calculated by multiplying the number of carcasses slaughtered by the average volume used per carcass (8 l/carcass). The average flow of water discharged without treatment on the day of Eid Al-Adha is the sum between the average flow discharged into the receiving environment without treatment and the occasional discharge of Eid Al-Adha.

More than 98% of homes are connected to sewers. In 2017, only 72% of waste collected was treated without danger. The 28% untreated present risks to the environment and public health. The results show that the rate of water discharged without treatment into the receiving environment decreases from 27% in 2018 to 23% for 2019 (Table 6).

Table 6 – Monitoring of wastewater in the city of Saida

Wastewater rate	Values (m3/d)		
	2017	2018	2019
Average flow rate of collected wastewater	28679.8	28812.9	29537.8
Average flow rate treated in the WWTP	19110	21050.4	22644.1
Average flow rate released into the receiving environment without treatment	9569.8	7762.5	6893.7
Percentage of connection to the WWTP	33%	27%	23%
Occasional flow of wastewater on Eid Al-Adha without treatment	10474.58	10447.74	10902.86
Average flow of water discharged without treatment on the day of Eid Al-Adha	20044.38	18210.24	17796.56

This shows the interest that local authorities attach to the collection of wastewater discharges. During Eid, all wastewater is directed to the receiving environment (Saida River) without any treatment .

Influent flow

The analysis of the curve shape in Figure 5a shows a variation in the flow of wastewater throughout the day of sacrifice. The average rejection on that day did not change much for the three occasions. It varies between 10 447.73 m^3/d and 10 902.86 m^3/d. The volume of wastewater varies

significantly. It is related to the number of slaughtered animals and the nature of the slaughtered animals.

The volume of wastewater increases in the morning from 9 a.m. until noon. The examination of the daily variation reveals the presence of three peaks which appear around 10 a.m., 11 a.m., and 2 p.m. The peaks of 10 a.m. and 11 a.m. are due to the use of water for cleaning after slaughter. It decreases during the lunch hour, between noon and 1:00 p.m. The peak at 2:00 p.m. is due to water consumption linked to the lunch break, which lasts from 30 min to 2 h. The average total discharge of urban wastewater on the days of Eid on the three occasions (2017, 2018, and 2019) varies from 39 154.32 to 40 440.66 m^3/d with an average of 39 618.54 m^3/d (Figure 5b).

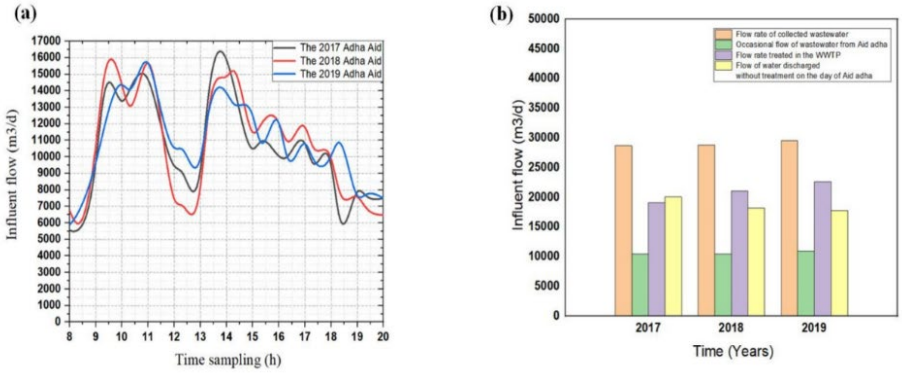

Figure 5 – (a) Variation of waste water from the slaughter on the day of the sacrifice. (b) Variation in the average daily flow of urban wastewater from Saida on Eid day

This average flow is higher than the regulatory dry weather capacity of the treatment plant, which is 30 000 m^3/d. It is influenced by the mode of use of drinking water which is inevitably accompanied by increasing production of polluting discharges.

Physical-chemical characteristics of the Eid effluents

These effluents have a reddish appearance, an unpleasant odor and are heavily loaded with figurative elements, trimming debris, blood clots, pieces of horns and claws, stomach contents, feces, straw, and possibly other organic constituents. They are drained through the collectors towards the Saida river without treatment. Table 7 gives the average of the results of the physical-chemical parameters of the effluents of the three sampling stations for three Eid occasions. The bacteriological analysis of the discharges will be the subject of another work.

Table 7 – Average of the parameters on the day of sacrifice

	Year 2017	Year 2018	Year 2019	Threshold values
Temperature(°c)	24.0	23.5	22.5	25
pH	7.7	7.7	7.5	6.5 - 8.5
Cond (µs/ cm)	1406.7	1377.5	1487.9	2700
TSS (mg/l)	866.9	668.0	686.2	40
BOD5 (mg/l)	485.6	397.0	387.9	40
COD (mg/l)	740.8	741.9	687.8	130
NO3- (mg/l)	54.0	64.6	65.1	50
NO2- (mg/l)	1.8	2.5	1.8	< 01
NH4+ (mg/l)	126.1	108.1	117.9	< 02
Pt (mg/l)	23.3	33.9	22.4	< 02
Cl- (mg/l)	567.6	547.5	650.5	/
COD/BOD5	1.5	1.9	1.8	/

Temperature and hydrogen potential

The results show that the water temperature values fluctuate between 23°C and 24°C limit values for direct discharge into the receiving environment (JORA, 2006). For the three occasions, the samples taken show high temperatures from 9:00 a.m. until 6:00 p.m. This is due to the influence of air temperature over 45°C in August and the usage of hot water for grease cleaning (Figure 6).

The pH is an important parameter that represents the degree of ionization of the studied medium. It gives an indication of the level of water pollution. It should be closely monitored during sampling. The analysis of the pH evolution of the water shows that the average pH values recorded for the different stations studied and on the three Eid occasions are relatively similar. These values range from 7.65 to 7.66 (Figure 7). It is within the acceptable range for wastewater discharge which is between 6.5 and 8.5 according to the Algerian regulations. The values obtained are comparable with those of other places of slaughterhouse wastewater, which generally have a neutral to slightly basic pH (Belghyti et al. 2009).

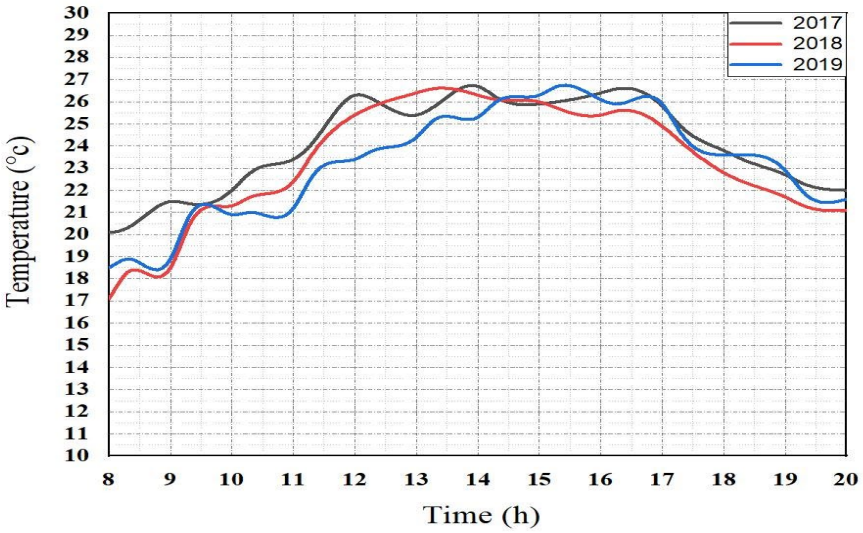

Figure 6 – Temperature for the three occasions of Eid

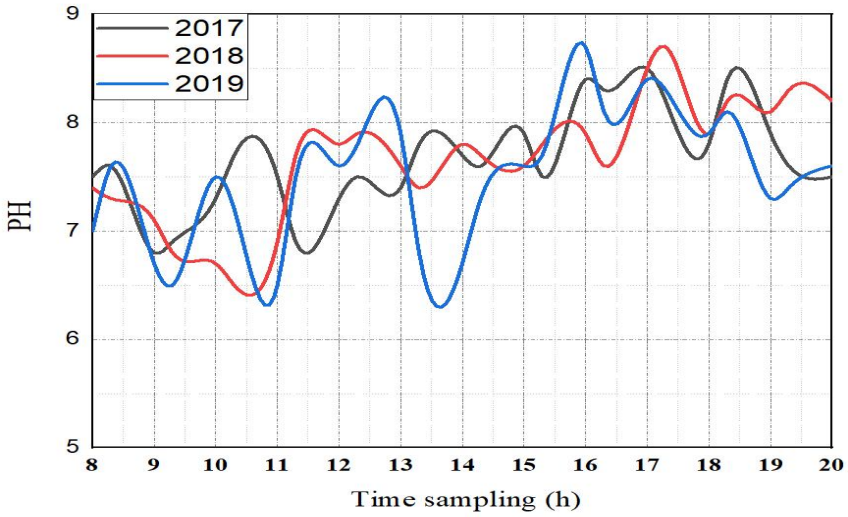

Figure 7 – PH for the three occasions of Eid

Conductivity and chlorine

The electrical conductivity of water reflects its ability to allow an electric current to pass. This ability is due to the presence of ions in the water, which transport the charges. Therefore, higher mineralization of

water increases its conductivity. Conductivity measurement is thus a quick and effective way to assess water mineralization (Rodier, 1975).

Any polluted discharge typically leads to an increase in conductivity (Rejsek, 2002). The observed results, ranging from 1377.44 µs/cm to 1487.9 µs/cm, indicate significant variance in mineralization as reflected in the average conductivity. This can be attributed to the discharge of highly mineralized wastewater. These values comply with the Algerian standards for wastewater discharge into natural environments, such as surface or groundwater, which require conductivity to be ≤ 2700 µs/cm.

After the slaughtering of the Eid sacrifices, the chlorine values range between 547.55 mg/l and 650.52 mg/l. The use of bleach for cleaning is the main reason for the high chlorine concentration. These results can be explained, on the other hand, by the formation of wastewater discharge rich in minerals rich in fertilizers and nutrients (N.C.P).

From Figure 8a, there is a clear association between variations in conductivity and chlorine concentrations. The variation in conductivity follows the variation in chlorine concentration for the three Eid occasions (Figure 8b). Chlorine contributes to high discharge conductivity.

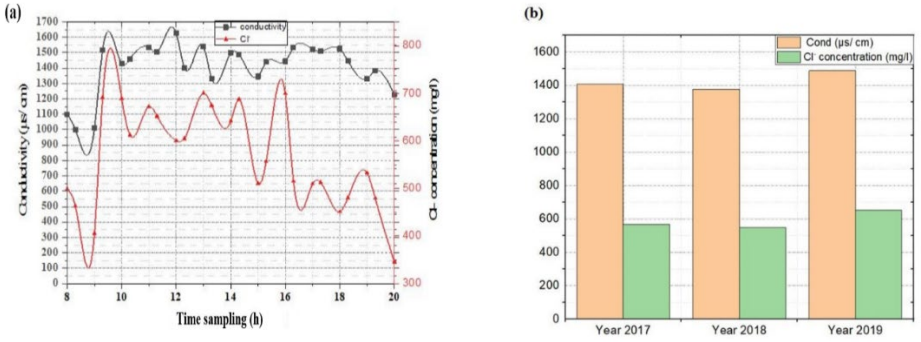

Figure 8 – (a) Variations in conductivity and chlorine concentrations after slaughtering (b) Conductivity and Cl - concentration for the three occasions of Eid

A good statistically significant correlation is observed between conductivity and chlorine (R^2=0.41) (Figure 9).

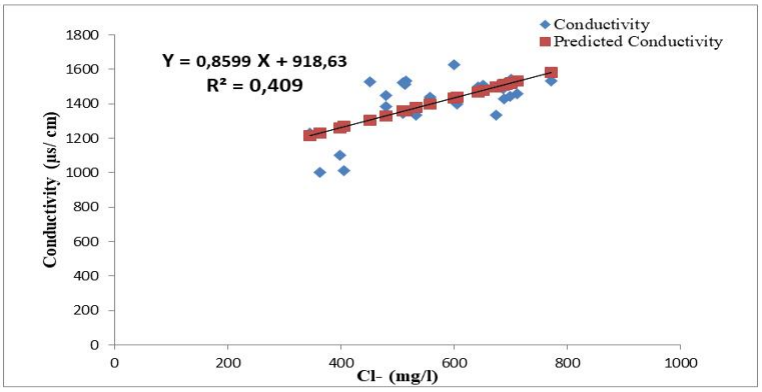

Figure 9 – Correlation between conductivity and chlorine of waste water on the day of Eid Al-Adha

Ammonium, nitrates and nitrites

Ammonium, nitrates, and nitrites are all types of nitrogen compounds. These variables were included because they have an impact on the eutrophication process. Proteins, polypeptides, amino acids, and urea are the principal sources of nitrogen organic. The majority of total nitrogen is mineral nitrogen, which contains ammonium ($NH4^+$), nitrite ($NO2^-$), and nitrates ($NO3^-$). The released effluent had extremely high levels of ammonium and nitrate, with average concentrations of 117.41 mg/l and 61.26 mg/l, respectively (Figure 10a).

The comparison of the average concentrations of ammonium and nitrate in the wastewater analyzed with the discharge threshold values shows that these concentrations vary respectively from 54.03 m/l to 65.12 mg/l, which makes it possible to conclude that these effluents represent a high pollution load in terms of pollution of the receiving environment by nitrogen. These rates are almost identical for the three years studied due to the particular nature of the releases on this occasion (blood and debris). One liter of blood provides 25 grams of NTK (Peiffer, 2002). For nitrites, which constitute an important step in the metabolization of nitrogen compounds, it is a transitional phase between ammonium and nitrates. Nitrites generally come either from an incomplete degradation of ammonia or from a reduction of nitrates.

The low concentrations of nitrites, average 2.01 mg/l encountered in the wastewater from the effluent studied (Figure 10a) are explained by the fact that the nitrite ion ($NO2^-$) is an intermediate compound, unstable in the presence of oxygen, and generally has a lower concentration of both forms, nitrate and ammonium ions.

A statistically significant correlation is observed with conductivity (R^2 = 0.4) (Figure 10b).

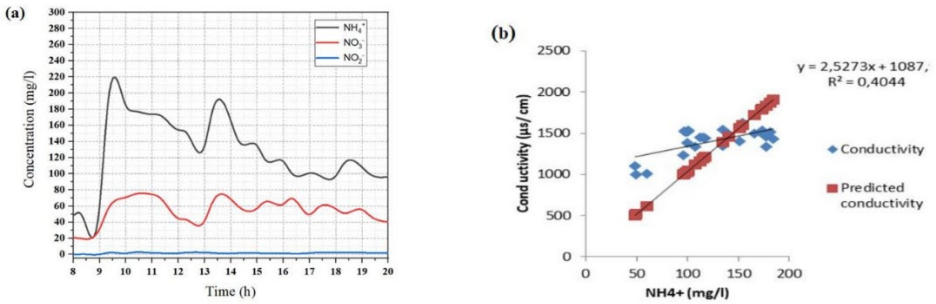

Figure 10 – (a) Evolution of the nitrogen pollution for the three occasions of Eid. (b) Statistically significant correlation is observed with conductivity (R2 = 0.4)

Total phosphorus

Phosphorus compounds exist in natural waters and wastewater in different forms, namely soluble orthophosphates, water-soluble phosphates, and organophosphate derivatives. The average total phosphorus value of 26.52 mg/l is well above the limit value of 2 mg/l (Figure 11). This content is due to the nature of the wastewater (urine and animal faces), and to the use of detergents for cleaning. Indeed, many detergents contain phosphates; the sodium tripolyphosphate (STPP) content of some detergents can exceed 50%.

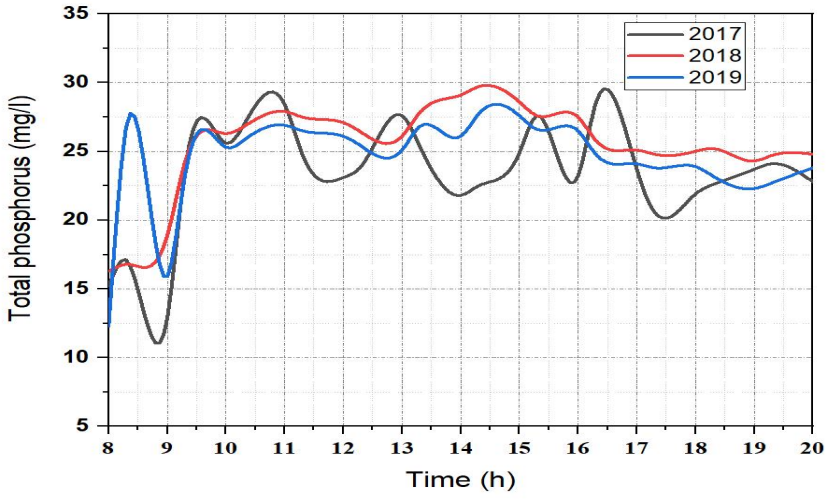

Figure 11 – Evolution of the total phosphorus

Suspended matter

TSS represent all the mineral and organic particles contained in water. They depend on the nature of their releases. In general, TSS are involved in the composition of water through their effect of ion exchange or absorption on both trace chemical elements and microorganisms. Variations of this parameter are shown in Figure 12. According to the results, it is noted that the sacrificial wastewater is more loaded than the Algerian urban wastewater for which the SS concentrations are between 350 mg/l and 570 mg/l (NSO 2018). Moreover, these average SS values in the analyzed wastewater vary between 668.07 and 866.83; they are clearly higher than the value set by the Algerian standards (JORA, 2006). The peak of the day appears from 9:30 a.m. to 11:00 a.m. for the three occasions studied (Figure 12). These concentrations are caused by the washing of the slaughter areas containing blood, the washing waters of the guts and the digestive contents, the debris discharged with the waters. The Algerian national standards (Executive Decree 06-141 of April 19, 2006/JORADP/23-04-2006) set a concentration of 40mg/l in TSS as a limit value in liquid effluents (domestic, industrial and agricultural).

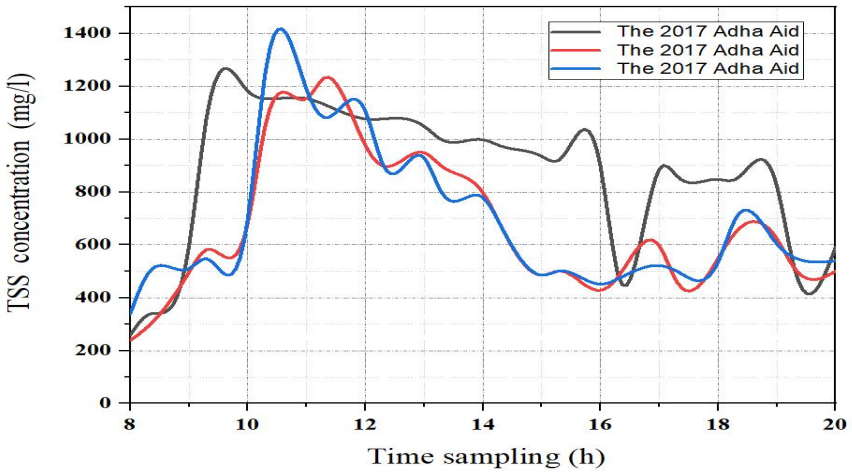

Figure 12 – Variation of suspended solids of waste water from slaughtering

Chemical and biochemical oxygen demand

Although COD should be considered an independent test of BOD_5 and will generate a higher concentration reading than BOD_5 for a particular wastewater sample, it is generally accepted that COD and BOD_5 share an empirical relationship.

The BOD_5 varies between 387.96 and 485.56 mg/l; these values could be explained by the fact that the share of biodegradable organic matter in this wastewater comes from the abundance of organic matter (rumen debris), by the concentration of this effluent by the blood of slaughter waste. COD makes it possible to assess the concentration of organic or mineral matter, dissolved or suspended in the water, through the quantity of oxygen necessary for their total chemical oxidation. The staining of slaughterhouse rejects is caused by blood from the slaughterhouse. Blood represents the major part of the COD of these liquid wastes. (Khennoussi et al, 2013).

The non-biodegradable organic matter is found in large quantities in this wastewater (high COD value) and comes mainly from various external sources with variable compositions of these non-biodegradable elements towards the network through the sacrificial waters. The variation of COD shows peaks, with a profile almost similar to that of BOD_5 (Figure 13). The first peak appears around 9:30 a.m. while the second (very pronounced) is observed around 10 a.m. and 11 a.m. during the day, the time of slaughter after the Eid prayer. The values observed are between 687.81 mg/l and 741.93 mg/l.

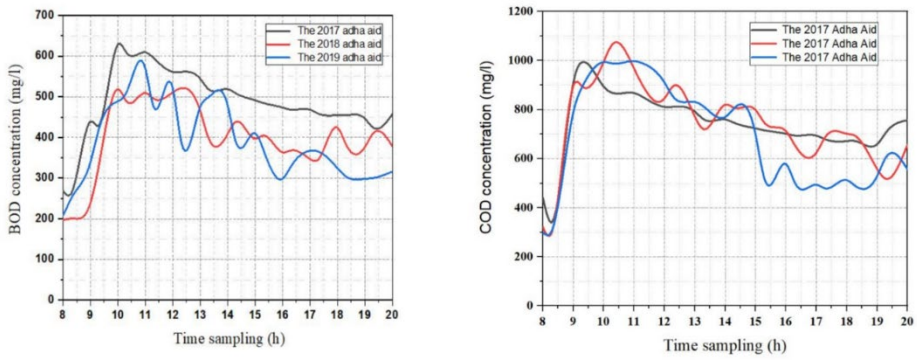

Figure 13 – Evolution of the organic pollution of waste water from slaughtering

There is a relationship between COD and BOD_5 because suspended solids include volatiles and ash, where the volatile part contributes to BOD_5. On the other hand, BOD_5 correlates very well with COD ($R^2 = 0.98$) (Figure 14) because the latter contributes to the oxidation of organic and inorganic matter, while BOD_5 contributes to organic matter (bacteria).

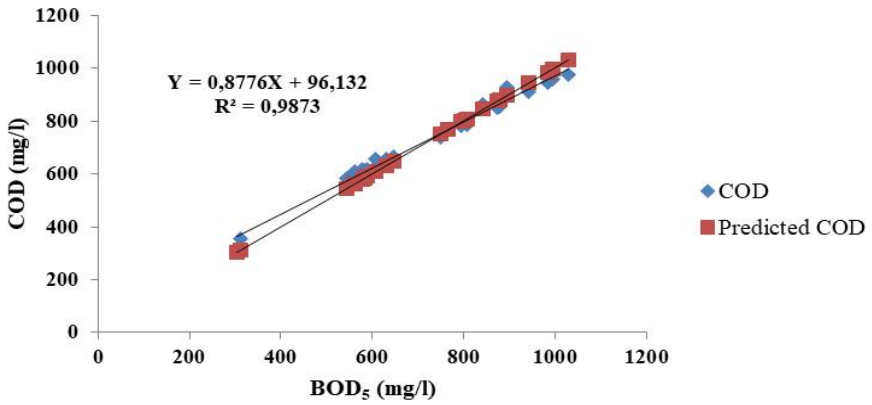

Figure 14 – Correlation between COD and BOD5 on the day of Eid Al-Adha

The results of the samples showed that for the various parameters analyzed, the pollution is very high in the morning. It reaches its peak around 11:00 a.m. and decreases between 12:00 p.m. and 1:00 p.m. during the lunch break, then it increases in the afternoon. This is due to cleaning operations.

Ratios

The use of these characterization parameters is a good way to give an image of the degree of pollution due to raw effluents and also to optimize the physicochemical parameters of wastewater to propose a suitable mode of treatment. The values of different ratios are given in Table 8.

Biodegradability is measured by the COD/BOD_5 ratio, which is used to assess raw water and determine the effluent biodegradability. The COD/BOD_5 ratio is important for determining an effluent purification cycle. Indeed, a low COD/BOD_5 ratio indicates the presence of a substantial fraction of biodegradable components, allowing a biological therapy to be considered. A high value of this ratio, on the other hand, shows that a major portion of the organic matter is not biodegradable, and it is advisable to pursue physical-chemical treatment in this scenario.

Observing the COD and BOD_5 levels on the same wastewater showed that the COD to BOD_5 ratio of the sacrificial wastewater will remain constant over time. The three Eid occasions have an average COD/BOD ratio of around 1.71.

In conclusion, the wastewater from this occasion has a high organic load. It is easily biodegradable and can be treated in the activated sludge treatment plant of Saida (Figure 15).

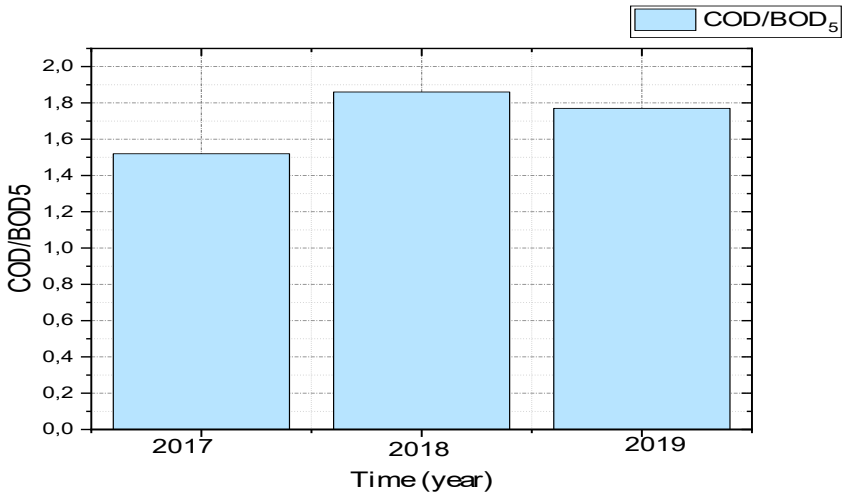

Figure 15 – Variation of biodegradability for the three occasions of Eid

The BOD_5/COD ratio gives a very interesting indication of the origin of pollution and its treatment options (Karefa et al, 2017). It is around 0.60; this effluent is biodegradable and confirms that these waters are loaded with organic (60%) and inorganic (40%) matter.

According to Rejsek (2002), this organic load makes this wastewater quite unstable; it rapidly evolves towards “digested” forms with the risk of releasing odors.

TSS/COD: The increase in the TSS/COD ratio is an index allowing one to suspect a phenomenon of resuspension of the deposits (during transport in the network). The found value of this ratio is between 0.90 and 1.16.

TSS/BOD5: The typical value for domestic wastewater for this ratio is between 1.65 and 1.75 and provides information on the production of sludge, a “natural” fraction provided by the TSS already present in the raw water. It indicates the distribution of particulate pollution and dissolved pollution. The average value of 1.72 indicates that the pollution is more granular than dissolved, which characterizes an essentially unitary network.

The index of organic pollution

According to the values of the organic pollution index (IPO) (Table 8), the pollution flow is classified as very strong organic pollution, as measured by the average of the number of classes of the four criteria (IPO = 1), owing primarily to discharges of very organic-rich sacrificial waters.

Table 8 – Relation between the pollution parameters

Ratios	2017	2018	2019
COD/BOD_5	1.54	1.90	1.75
BOD_5/COD	0.66	0.55	0.59
TSS/COD	1.16	0.90	1.09
TSS/BOD_5	1.75	1.65	1.75
BOD_5/TSS	0.60	0.64	0.59

Estimation of pollution loads

The polluting loads in (kg/d) are calculated from the concentrations in (mg/l) of the physical-chemical parameters, and an average of the occasional sacrifice flow and the wastewater flow discharged into the receiving environment (Saida river) without processing (Table 9).

Table 9 – Polluting loads in carbon, nitrogen and phosphorus pollution

	BOD5 (kg/d)	TSS (kg/d)	COD (kg/d)	NO_3^- (kg/d)	NH_4^+ (kg/d)	P_t (kg/d)
2017	9732.75	17375.07	14848.68	1082.99	2528.40	466.83
2018	7230.19	12165.71	13510.72	1176.93	1969.26	617.87
2019	6904.35	12211.82	12240.65	1158.91	2099.10	397.93

The calculated pollutant loads give an idea of the importance of the pollution brought to the receiving environment that day. The pollutant loads revealed that the samples are highly loaded with the organic matter in COD (Average = 13533.35 kg/d), in BOD_5 (Average= 7955.76 kg/d), in TSS (Average = 13917. 54 kg/d), the polluting loads of ammonium, nitrates, and total phosphorus Pt respectively of the order of 2198.92 kg/d, 1139.61 kg/d and 494.21 kg/d (Figure 16).

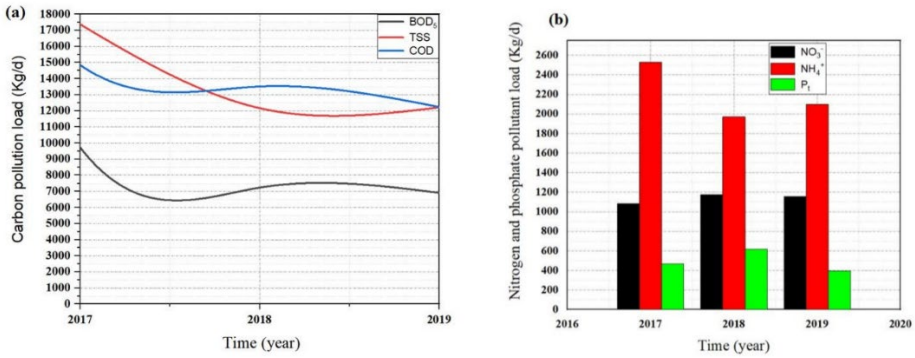

Figure 16 – Untreated polluting loads

Compared to the national and international standards for the discharge of wastewater into the natural environment (25 mg/l ≤ BOD_5 ≤ 100 mg/l and 125 mg/l ≤ COD ≤ 500 mg/l), loads of BOD_5 and COD in the Saida sacrifice wastewater exceed the permissible limits for the discharge of wastewater into the natural environment (surface water).

Conclusion

The quality of wastewater changes according to the sudden change in the inflow. The importance of identifying the problem of waste water discharges on the day of Eid Al-Adha is today an emergency measure. It is time for this issue to be among Algeria's national strategic concerns. Steps should be taken to better manage liquid waste and waste on the day of the sacrifice.

The discharge of wastewater on the day of Eid poses a serious environmental problem since it is highly loaded with organic matter. It is charged with blood, tripe contents, washing water, as well as solid particles such as animal hair, bones, offal, leather, etc., presenting panoply of pollutants which include proteins, fats, suspension, as well as pathogenic germs.

Both quantitatively and qualitatively, the monitoring of the wastewater studied shows that all the pollutants characterizing the pollution (BOD_5, COD, TSS, NH_4^+, NO_2^-, NO_3^- and P_t) show an increasing gradient in the morning for all samples taken, and a decreasing gradient at the end of the day. This increase in pollution is due to the nature of discharges after slaughter, inducing pollution which contributes to the total degradation of the quality of the receiving environment (Saida river).

After the assessment of the degree of organic pollution, the organic pollution index (IPO) of all the parameters studied (in particular with BOD5, COD, and SS) classifies the wastewater analyzed in the category of very strong organic pollution.

The Saida region is characterized by the presence of two types of aquifers, a superficial aquifer, and a Karstic aquifer. The presence of faults and cracks contribute to the contamination of the aquifers by these releases.

It is crucial for public health that these effluents be properly treated by an appropriate method to obtain a risk-free affluent. As the sanitation network is unitary, it is recommended to provide a buffer basin for this event, which could be useful in the event of heavy rainfall. The latter must be installed upstream of the WWTP for the recovery of blood to reduce the pollution load and treat water in the Saida WWTP that has sufficient capacity to treat this water before its discharge into the environment.

These recommendations open prospects that must be confirmed through intensification of local studies and further pathological analyses.

Nomenclature

pH Hydrogen potential
TSS Suspended Matter
COD Chemical Oxygen Demand
BOD Biochemical Oxygen Demand
MWR Ministry of Water Resources
NHO National Health Office
NH_4^+ Ammonium
NO_3^- Nitrates
NO_2^- Nitrites
Pt Total Phosphorus
Cl^- Chlorine
EC Electrical Conductivity
OPI Organic Pollution Index
WWTP Wastwater Treatement Plant

References

Al-Hejuje, M.M., Al-Saad, H.T. & Hussain, N.A. 2017. Assessing the Organic Pollution and Aquaculture Activity of Surface water at Shatt-Al-Arab Estuary Southern of Iraq. *ILMU KELAUTAN: Indonesian Journal of Marine Sciences (IJMS)*, 22(4), pp.161-168. Available at: https://doi.org/10.14710/ik.ijms.22.4.161-168.

Asibor, G., Edjere, O. & Azubuike, C. 2020. Status of discharged abattoir effluent and its effects on the physico-chemical characteristics of Orogodo river, delta state, Nigeria. *WIT Transactions on Ecology and the Environment,* 242, pp.51-60. Available at: https://doi.org/10.2495/WP200051.

Bayo, J. & López-Castellanos, J. 2016. Principal factor and hierarchical cluster analyses for the performance assessment of an urban wastewater treatment plant in the Southeast of Spain. *Chemosphere*, 155, pp.152-162. Available at: https://doi.org/10.1016/j.chemosphere.2016.04.038.

Belghyti, D., Guamri, Y.E., Ztit, G., Ouahidi, M., Joti, M., Harchrass, A., Amghar, H., Bouchouata, O., Kharrim, K.E. & Bounouira, H. 2009. Caractérisation physico-chimique des eaux usées d'abattoir en vue de la mise en oeuvre d'un traitement adéquat : Cas de Kénitra au Maroc. *Afrique Science: Revue Internationale des Sciences et Technologie*, 5(2), pp.199-216. Available at: https://doi.org/10.4314/afsci.v5i2.61730.

Bhave, P.P., Naik, S. & Salunkhe, S.D. 2020. Performance Evaluation of Wastewater Treatment Plant. *Water Conservation Science and Engineering*, 5, pp.23-29. Available at: https://doi.org/10.1007/s41101-020-00081-x.

Chennaoui, M. 2003. *Rejets d'abattoir des viandes rouges de la ville d'El Jadida : Caractérisation, impact sur la qualité du milieu marin récepteur et essai de valorisation en aliment animale*. PhD thesis. El Jadida, Morocco: Université Chouaib Doukkali, Faculté des Sciences [online]. Available at: https://toubkal.imist.ma/handle/123456789/6065?show=full [Accessed: 12 December 2024].

De Anda, J., López-López, A., Villegas-García, E. & Valdivia-Aviña, K. 2018. High-Strength Domestic Wastewater Treatment and Reuse with Onsite Passive Methods. *Water*, 10(2), art.number:99. Available at: https://doi.org/10.3390/w10020099.

Gautam, S.K., Sharma, D., Tripathi, J.K., Ahirwar, S. & Singh, S.K. 2013. A study of the effectiveness of sewage treatment plants in Delhi region. *Applied Water Science*, 3, pp.57-65. Available at: https://doi.org/10.1007/s13201-012-0059-9.

-ISO. 2025. *ICS 13.060.60 Détermination des propriétés physiques de l'eau* [online]. Available at: https://www.iso.org/fr/ics/13.060.60/x/p/1/u/1/w/0/d/0 [Accessed: 12 December 2024].

-JORA. 2003. Décret exécutif n° 03-451 du 7 Chaoual 1424 correspondant au 1er décembre 2003 définissant les règles de sécurité applicables aux activités portant sur les matières et produits chimiques dangereux ainsi que les récipients de gaz sous pression. *JORA Journal officiel de la Republique Algerienne Democratique et Populaire*, 42(75), décembre 7, pp.4-7. Alger: Direction et redaction secretariat general du gouvernement [online]. Available at: https://www.joradp.dz/FTP/jo-francais/2003/F2003075.pdf (in French) [Accessed: 12 December 2024].

-JORA. 2006. Décret exécutif n° 06-141 du 20 Rabie El Aouel 1427 correspondant au 19 avril 2006 définissant les valeurs limites des rejets d'effluents liquides industriels. Journal officiel de la République algérienne

Democratique et populaire. *JORA Journal officiel de la Republique Algerienne Democratique et Populaire*, 45(26), avril 23, pp.4-9. Alger: Direction et redaction secretariat general du gouvernement [online]. Available at: https://www.joradp.dz/FTP/jo-francais/2006/F2006026.pdf (in French) [Accessed: 12 December 2024].

Karef, S., Kettab, A., Loudyi, D., Bruzzoniti, M., Del Bubba, M., Nouh, F., Boujelben, N. & Mandi, L. 2017. Pollution parameters and identification of performance indicators for wastewater treatment plant of Medea (Algeria). *Desalination and Water Treatment,* 65, pp.192-198. Available at: https://doi.org/10.5004/dwt.2017.20290.

Khennoussi, A., Chaouch, M. & Chahlaoui, A. 2013. Treatment of the effluent from a red meat slaughterhouse by electrocoagulation flotation with iron electrodes. *Revue des sciences de l'eau/Journal of Water Science*, 26(2), pp.81-171. Available at: https://doi.org/10.7202/1016064ar.

Kokkinos, P., Mandilara, G., Nikolaidou, A., Velegraki, A., Theodoratos, P., Kampa, D., Blougoura, A., Christopoulou, A., Smeti, E., Kamizoulis, G., Vantarakis, A. & Mavridou, A. 2015. Performance of three small-scale wastewater treatment plants. A challenge for possible re use. *Environmental Science and Pollution Research International*, 22, pp.17744-17752. Available at: https://doi.org/10.1007/s11356-015-4988-3.

-NHO National Health Office. 2017. *Management and operating report of the wastewater treatment plant in the city of Saida*. Saida, Algeria: NHO National Health Office.

Peiffer, G. 2002. *Impact environnemental des effluents d'abattoirs : Actualités techniques et réglementaires.* Médecine vétérinaire et santé animale [online]. Available at: https://dumas.ccsd.cnrs.fr/dumas-04655172v1 [Accessed: 12 December 2024].

Rejsek, F. 2002. *Analyse des eaux: Aspects réglementaires et techniques*, *Broché – 1*. Canopé - CRDP de Bordeaux. ISBN: 978-2866174200.

Rodier, J. 1975. *Analysis of Water*. John Wiley & Sons. ISBN: 978-0470729342.

Walter, R.H., Sherman, R.M. & Downing, D.L. 1974. Reduction in oxygen demand of abattoir effluent by precipitation with metal. *Journal of Agricultural and Food Chemistry*, 22(6), pp.1097-1099. Available at: https://doi.org/10.1021/JF60196A015.

Evaluación del impacto ambiental de las aguas residuales urbanas y de la capacidad de tratamiento de la planta de lodos activados de Saida (noroeste de Argelia) con motivo del Eid Al-Adha

Souad Zairi[a], **autor de correspondencia**, *Boumediene* Meddah[a], *Miloud* Slimani[b], Asmaa Rahmani[c]

[a] Universidad Mustapha Stambouli,
Facultad de Ciencias Naturales y de la Vida,
Departamento de Biología, Laboratorio de Biología,
Mascara, República Argelina Democrática y Popular

[b] Dr. Tahar Moulay Universidad de Saida, Facultad de Ciencias, Departamento de Biología, Laboratorio de Biología, Saida, República Argelina Democrática y Popular

[c] Dr. Tahar Moulay Universidad de Saida, Facultad de Tecnología, Departamento de Ingeniería Civil e Hidráulica, Laboratorio de Métodos de Cálculo y Modelado, Saida, República Argelina Democrática y Popular

CAMPO: tecnología química, ciencia ambiental
TIPO DE ARTÍCULO: artículo científico original

Resumen:

Introducción/objetivo: La matanza de ganado durante el Eid Al-Adha genera cantidades significativas de aguas residuales ricas en contaminantes orgánicos. Sin embargo, el impacto específico de estos efluentes en la calidad del agua sigue estando poco documentado. Este estudio tuvo como objetivo evaluar las cargas contaminantes vertidas en el valle de Saida durante el Eid Al-Adha y evaluar la capacidad de tratamiento de la planta de tratamiento de aguas residuales (PTAR) local con lodos activados.

Métodos: Se recogieron muestras de agua de diferentes puntos del sistema de alcantarillado en distintos momentos del día durante tres eventos de Eid Al-Adha (2017, 2018 y 2019). Se analizaron varios parámetros fisicoquímicos, entre ellos temperatura, pH, conductividad eléctrica, demanda química de oxígeno (DQO), demanda bioquímica de oxígeno a cinco días (DBO_5), sólidos suspendidos totales (SST), amonio, nitratos, nitritos y fósforo. Para evaluar el cumplimiento, Los niveles de contaminación medidos se compararon con las normas reglamentarias argelinas.

Resultados: Los análisis revelaron un aumento brusco de los niveles de contaminación por la mañana, seguido de una disminución gradual por la tarde. Las altas cargas contaminantes procedentes de los efluentes de matanza degradaron significativamente la calidad del agua del río Saïda. El índice de contaminación orgánica clasificó estos vertidos como muy contaminantes. El aporte excesivo de materia orgánica y nutrientes provocó un agotamiento del oxígeno y riesgos de eutrofización.

Conclusión: El vertido de aguas residuales de matanza sin tratar plantea graves riesgos para la salud pública y el medio ambiente. Para mitigar estos impactos es esencial reforzar las estrategias de gestión de las aguas residuales durante el Eid al-Adha, mejorar los procesos de tratamiento en la planta de tratamiento de aguas residuales de Saïda y aplicar normas ambientales estrictas.

Palabras claves: Eid Al-Adha, EDAR de lodos activados, biodegradabilidad, carga contaminante, medio receptor, aguas residuales.

Оценка воздействия городских сточных вод на окружающую среду и эффективности очистки активного ила очистным сооружением в городе Саида на северо-западе Алжира во время праздника Курбан-Байрам

Суад Заири[а], **корреспондент**, *Бумедин* Мейда[а],
Милуд Слимани[б], *Асма* Рамани[в]

[а] Университет им. Мустафы Стамбули, факультет естественных наук, кафедра биологии, биологическая лаборатория, г. Маскара, Алжирская Народная Демократическая Республика

[б] Университет им. Доктора Мулая Тахара в Саиде, факультет естественных наук, кафедра биологии, биологическая лаборатория, г. Саида, Алжирская Народная Демократическая Республика

[в] Университет им. Доктора Мулая Тахара в Саиде, технологический факультет, кафедра гражданского строительства и гидравлики, Лаборатория моделирования и расчетных методов, г. Саида, Алжирская Народная Демократическая Республика

РУБРИКА ГРНТИ: 61.01.94 Охрана окружающей среды
ВИД СТАТЬИ: оригинальная научная статья

Резюме:

Введение/цель: При убое скота во время праздника Курбан-Байрам образуется значительное количество сточных вод, содержащих органические загрязнители. Однако конкретное воздействие этих сточных вод на качество воды остается недостаточно исследованным. В данной статье представлена оценка количества загрязняющих веществ, сбрасываемых в долину Сайда во время праздника Курбан-Байрам, и оценку мощности местной станции очистки сточных вод от активного ила (WWTP).

Методы: Образцы воды трижды были отобраны из разных точек канализационной системы в разное время суток во время праздника Курбан-Байрам (2017, 2018 и 2019). Были проанализированы несколько физико-химических параметров, включая температуру, pH, электропроводность, химическое потребление кислорода (ХПК), пятидневное биохимическое потребление кислорода ($БПК_5$), общее содержание взвешенных веществ, аммония, нитратов, нитритов и фосфора. Измеренные уровни загрязнения были сопоставлены с алжирскими нормативными стандартами с целью оценки соответствия.

Результаты: Анализ результатов выявил резкое повышение уровня загрязнения в утренние часы, за которым последовало

постепенное снижение к вечеру. Высокое содержание загрязняющих веществ в сточных водах, образующихся при убое скота, значительно ухудшило качество воды в реке Сайда. По индексу органического загрязнения эти выбросы классифицированы как экстремально высокие загрязнители. Чрезмерное поступление органических и питательных веществ привело к истощению запасов кислорода и риску от эвтрофикации.

Вывод: Сброс неочищенных сточных вод со скотобойни представляет серьезную угрозу для окружающей среды и здоровья населения. Для смягчения таких последствий необходимы совершенствование стратегий управления сточными водами во время праздника Курбан-Байрам, совершенствование процессов очистки на станции очистки сточных вод в Саиде и соблюдение строгих экологических стандартов.

Ключевые слова: Курбан-байрам, очистное сооружение, активный ил, биоразлагаемость, нагрузка загрязняющих веществ, водоприемник, сточные воды.

Процена утицаја градских отпадних вода на животну средину и капацитет пречишћавања активираног муља у постројењу за пречишћавање отпадних вода у граду Саиди на северозападу Алжира током Курбан-бајрама

Суад Заири[а], **аутор за преписку**, *Бумедин* Мејда[а],
Милуд Слимани[б], Асма Рамани[в]

[а] Универзитет „Мустафа Стамболи”, Факултет природних наука,
Одсек за биологију, Биолошка лабораторија,
Маскара, Народна Демократска Република Алжир

[б] Универзитет у Саиди „др Тахар Мулаи”,
Природно-математички факултет,
Одсек за биологију, Биолошка лабораторија,
Саида, Народна Демократска Република Алжир

[в] Универзитет у Саиди „др Тахар Мулаи”, Технолошки факултет,
Департман за грађевинарство и хидраулику,
Лабораторија за моделирање и методе прорачуна,
Саида, Народна Демократска Република Алжир

ОБЛАСТ: хемијске технологије, заштита животне средине
КАТЕГОРИЈА (ТИП) ЧЛАНКА: оригинални научни рад

Сажетак:

Увод/циљ: Клање стоке током Курбан-бајрама доводи до стварања великих количина отпадне воде богате органским загађивачима. Међутим, специфични утицај ових комуналних отпадних вода на квалитет воде још није довољно истражен. Циљ ове студије јесте

да процени контаминацију загађивачима који се испуштају у долину Саиде током Курбан-бајрама, као и да процени капацитет пречишћавања активираног муља локалног постројења за пречишћавање отпадних вода (wastewater treatment plant -WWTP).

Методе: Узорци воде су прикупљани са различитих места у канализационом систему током различитих делова дана за време одржавањаКурбан-бајрама 2017, 2018. и 2019. године. Анализирано је неколико физичко-хемијских параметара као што су температура, pH вредност, електрична проводљивост, хемијска потрошња кисеоника (chemical oxygen demand – COD), петодневна биохемијска потрошња кисеоника (biochemical oxygen demand – BOD_5), укупне суспендоване честице, амонијак, нитрати, нитрити и фосфор. Измерени нивои загађености упоређени су са алжирским законским стандардима како би се утврдило да ли и у којој мери одступају од њих.

Резултати: Анализе су показале да ниво загађености нагло расте током јутра, а постепено се смањује током вечери. Велики садржај загађивача из отпадних вода након клања знатно је умањио квалитет воде у реци Саиде. Индекс органског загађења класификује ове отпадне воде као изузетно загађене. Прекомерни унос органских материја и нутријената довео је до смањивања количине кисеоника и до ризика од цветања воде.

Закључак: Испуштање непречишћене отпадне воде од клања стоке представља озбиљан ризик по животну средину и јавно здравље. Побољшавање стратегија управљања отпадним водама током Курбан-бајрама, унапређивање процеса пречишћавања у постројењу за пречишћавање отпадних вода у Саиди, као и спровођење строгих прописа у заштити животне средине од суштинске су важности за смањење ових негативних утицаја.

Кључне речи: Курбан-бајрам, постројење за пречишћавање активираног муља из отпадних вода, биоразградивост, оптерећење загађујућим материјама, водопријемник, отпадне воде.

Paper received on: 14.12.2024.
Manuscript corrections submitted on: 26.03.2025.
Paper accepted for publishing on: 27.03.2025.

Effect of crushed limestone sand and dust on the mechanical behaviour of river sand mixtures: an experimental study

Ahmed Bilal Benyahia[a], *Ilyes* Irki[b], *Ahmed* Djafar Henni[c], *Mohammed* Ezziane[d], *Zine el abidine* Laidani[e]

[a] University of Hassiba Ben Bouali,
Laboratory of Structures, Geotechnics and Risks (LSGR),
Chlef, People's Democratic Republic of Algeria,
e-mail: ab.benyahia@univ-chlef.dz,
ORCID iD: https://orcid.org/0009-0000-9349-5468

[b] University centre of Tipaza,
Laboratory of Materials and Environment (LME),
Medea, People's Democratic Republic of Algeria,
e-mail: Irki.ilyes@cu-tipaza.dz, **corresponding author**,
ORCID iD: https://orcid.org/0000-0003-0152-2559

[c] University of Hassiba Ben Bouali,
Laboratory of Structures, Geotechnics and Risks (LSGR),
Chlef, People's Democratic Republic of Algeria,
e-mail: a.djafarhenni@univ-chlef.dz,
ORCID iD: https://orcid.org/0009-0000-1340-3173

[d] University of Hassiba Ben Bouali,
Laboratory of Structures, Geotechnics and Risks (LSGR),
Chlef, People's Democratic Republic of Algeria,
e-mail: m.ezziane@univ-chlef.dz,
ORCID iD: https://orcid.org/0000-0001-9550-206X

[e] University Blida1, Civil Engineering Department,
Blida, People's Democratic Republic of Algeria,
e-mail: laidani_z@univ-blida.dz,
ORCID iD: https://orcid.org/0000-0002-8502-9819

https://doi.org/10.5937/vojtehg73- 56170

FIELD: materials
ARTICLE TYPE: original scientific paper

Abstract:

Introduction: The present study aims to investigate the effect of crushed limestone sand (CLS) and limestone crushed sand dust (LCSD) on the physical and mechanical behaviour of reconstituted river sand (RS) using the volumetric substitution method.

ACKNOWLEDGEMENTS: All tests were carried out at the Civil Engineering Laboratory - University of Medea, Algeria. The authors express their gratitude to the engineer who contributed to this experimental program; this work was supported by the General Directorate for Scientific Research and Technological Development (DGRSDT) in Algeria.

Methods: The study involved conducting direct shear tests on two substitution series to evaluate the effect of CLS sand with incremental increases of 0, 10, 20, 30, and 40%, and LCSD dust ranging from 0 to 35% in 5% steps on the mechanical behaviour of reconstituted river sand. All samples are prepared with 50% relative density and tested under three different normal stresses of 100, 200, and 300 kPa, respectively.

Results: The results show that the substitution of river sand with CLS up to 30% enhances its mechanical properties; the peak shear strength reached a maximum value of 29% under 200 kPa of normal stress. The substitution of river sand for LSCD leads to a decrease in mechanical properties. However, a more in-depth analysis of the results obtained reveals an improvement in residual parameters, with up to 15% of substitution.

Conclusion: Following a rigorous analysis of the obtained results, it was determined that sand reconstituted from a combination of 30% CLS and 15% LCSD offers optimal performance in terms of enhanced mechanical properties. This solution aligns significantly with the sustainable development of the Algerian government strategy promoting improved characteristics and preserving natural resources while meeting the stringent requirements of the geotechnical sector.

Key words: river sand, crushed limestone sand, limestone crushed sand dust, substitution, shear strength, sustainable development.

Introduction

Recently, Algeria has seen a notable expansion of its road and railway infrastructure, which has occurred in parallel with advancements in the urban sector. Therefore, the demand for fundamental construction materials in terms of aggregates and raw materials has increased considerably; aggregates, being one of the most extensively utilised resources in this sector, are responsible for the generation of approximately 20% of waste products (equivalent to 13.5 million tonnes) due to their high fines content (15-25%) (Guemmadi & Houari, 2009).

On the other hand, a substantial amount of waste is generated, along with the production of additional dust. Research indicates that these by-products can pose serious environmental and health risks, posing a risk to both human populations and the country's biodiversity (Safiddine et al, 2017, 2021).The use of this particular type of aggregate, which contains a high level of fine limestone, necessitates a series of washing and other treatment procedures. Several studies were conducted with the objective of recovering this particular industrial by-product in Algeria as crushed sand and limestone crushed sand dust in concrete technology (Safiddine

et al, 2017, 2021; Abbou et al, 2020; Skender et al, 2021; Logbi et al, 2023).

Recycling this type of waste could be a way of improving the mechanical properties of sandy soils, according to other researchers (Abbou et al, 2020; Ibrahim et al, 2020). Soils containing more angular grains have higher shear strengths than soils based on more rounded river sand (Holtz & Gibbs, 1956). Furthermore, the maximum shear stress and the angle of internal friction were improved by varying the shape of soil grains and increasing their roughness (Cho et al, 2006; Altuhafi et al, 2016; Kandasami & Murthy, 2017). The presence of angular particles in soils can favour the rearrangement of grains and develop additional friction between particles, thus enhancing mechanical resistance under variable and high loads (Holtz & Gibbs, 1956; Holtz et al, 2022; Santamarina & Cho, 2001; Guo & Su, 2007; Li, 2013; Yang & Wei, 2014; Borhani & Fakharian, 2016).

The incorporation of fine content led to a decrease in the mechanical properties of granular soil (Belkhatir et al, 2010; Monkul et al, 2016; Monkul et al, 2017; Cherif Taiba et al, 2018; Benessalah et al, 2021; Ezziane et al, 2025); the fine content effect becomes significant at rates of up to 20%, particularly in the behaviour of undrained mixtures, leading to a linear decrease in the shear strength of silty sand (Belkhatir et al, 2010). It is important to note that the optimum percentage of fine limestone used to enhance the volume change of clay soils is 18%; otherwise, up to 12% of limestone powder amount, the initial void index is significantly reduced (Ibrahim et al, 2020). In accordance with the findings of preceding research (Brooks et al, 2011; Sabat & Muni, 2015; Ibrahim et al, 2020; Cabalar & Omar, 2023), it was determined that two parameters previously examined, namely grain shape and fine content, are present in the used sand from aggregate production quarries, represented by crushed limestone sand (CLS) and limestone crushed sand dust (LCSD).

The present study aims to investigate the incorporation of crushed sands and their limestone fines on the physical and mechanical behaviour of reconstituted river sands and to align with the Algerian sustainable development strategy.

Experimental materials and methods

Materials

In the present study, two different types of clean sand presented in Figure 1 were used. The first is the river sand (RS) from the M'zi River (Laghouat city), 400 km south of Algiers, and the second one is the

crushed limestone sand (CLS) from the Montgorno quarry (Medea city) situated 90 km south of Algiers. Both RS and CLS were characterized by a continuous particle size distribution between 0.08 and 2mm. LCSD is obtained from CLS sieving through an 80 μm sieve.

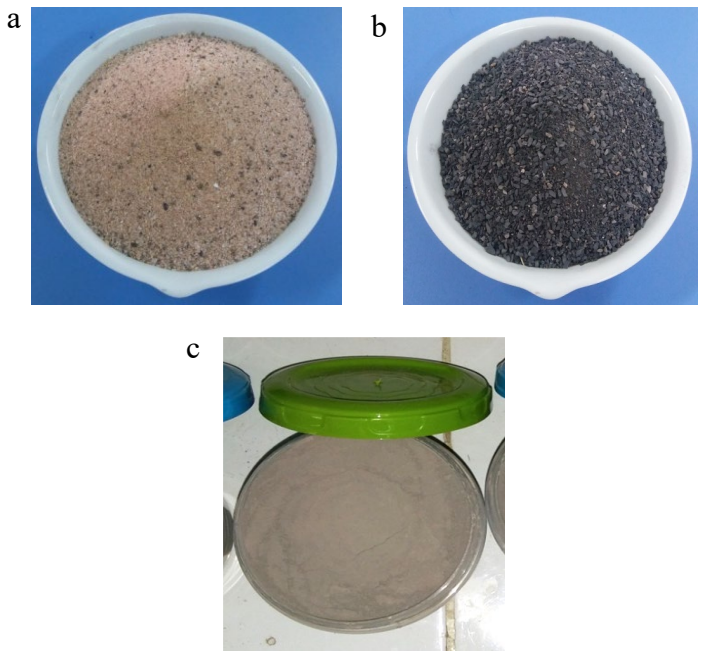

Figure 1 – (a) river sand (RS), (b) crushed limestone sand (CLS) and (c) limestone crushed sand dust (LCSD)

Figure 2 shows the grain size distribution curves of clean river and clean crushed limestone sands and limestone crushed sand dust (LCSD); river sand (RS) is characterized by rounded particles with smooth surfaces, classified as poorly graded (SP) according to the Unified Soil Classification System. It is medium-sized sand with a wide grain size distribution. On the other hand, crushed limestone sand (CLS) is well-known by angular particles with rough surfaces. It is classified as well-graded (SW) and exhibits a more dispersed grain size distribution compared to RS. LCSD particle sizes predominantly smaller than 80 μm are characterized by a wide particle size distribution. The particle size distributions of sands and LCSD were determined according to the AFNOR (1992, 1996) standards, respectively.

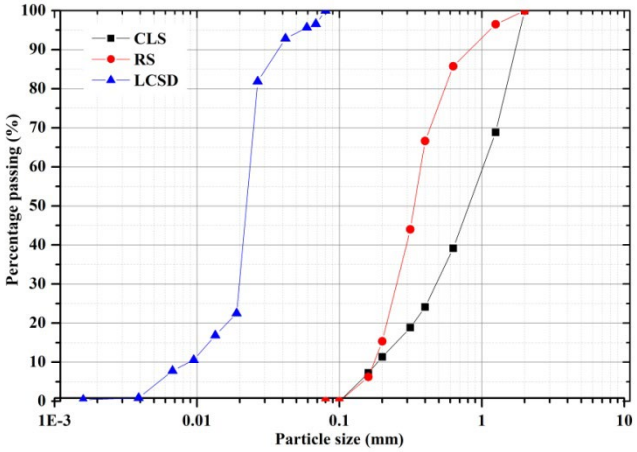

Figure 2 – Grain size distribution curve for sands and CLS dust used

The physical characteristics of the used sands and LCSD are presented in Table 1.

Table 1 – Physical properties of clean sands used in the experimental program

Sands	**RS**	**CLS**	**LCSD**
G_s **(g/cm3)**	2.646	2.741	2.741
e_{max} **(-)**	0.904	1.097	-
e_{min} **(-)**	0.607	0.722	-
D_{50} **(mm)**	0.330	0.790	0.022
D_{60} **(mm)**	0.394	0.987	0.023
D_{30} **(mm)**	0.259	0.390	0.020
D_{10} **(mm)**	0.177	0.120	0.010
Cu **(-)**	2.226	8.225	2.300
Cc **(-)**	0.962	1.284	1.739
W_L ***(%)***	-	-	26.25
W_P ***(%***	-	-	21.11
I_P ***(%)***	-	-	5.14

Specimen preparation

In the first part of this experimental program, five clean sand mixtures were formulated; river sand (RS) was used as a base material, with crushed limestone sand (CLS) incorporated in various volumetric proportions of 0, 10, 20, 30, and 40% to investigate their effect on the properties of reconstituted clean sand (RCS).The second part of the study

involves an investigation of the effect of fine limestone on the mechanical behaviour of the best-reconstituted sand from the first part, with reference to its mechanical properties. These mixtures are obtained by replacing RCS with a volumetric percentage of fine limestone ranging from 0 to 35%, with an increment of 5%.

Physical properties

A series of three tests was conducted in order to characterise the physical parameters of the various mixtures: granulometry analysis, specific gravity measurement, and void ratio determination according to the (AFNOR, 1991, 1996, 2000) standards, respectively. The grain size distributions of the reconstituted sand mixtures are illustrated in Figure 3 (a, b).

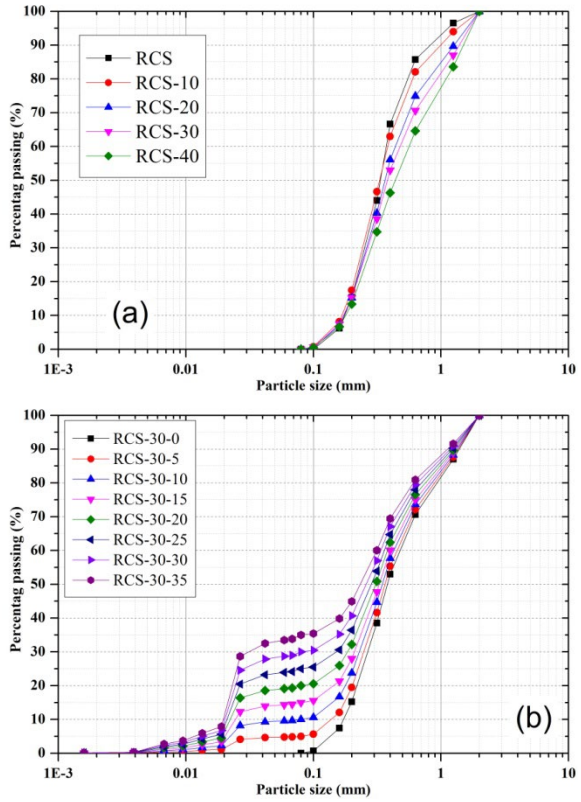

Figure 3 – Grain size distribution curve for the sands used in the experimental program: (a) RCS mixture, (b) RCS with LCSD

As illustrated in Figure 4 below, the reconstituted void ratios (e_{min} and e_{max}) are presented. It has been observed that both maximum and minimum void ratios underwent a linear decrease with increasing CLS content up to 40%. This phenomenon could be explained by a change in particle size, resulting in increased dispersion. However, beyond this content level (40%), an increase in void ratio values was observed with increasing the CLS content. This behavior can be attributed to the fact that as particle angularity rises, voids between particles also increase, thereby reducing particle mobility and leading to a decrease in the sample's potential density. In contrast, rounded particles tend to minimize voids and enhance density. These findings are consistent with previous studies (Youd, 1973; Cho et al, 2006; Al-Tuhafi et al, 2016).

The second part deals with the effect of limestone crushed sand dust (LCSD) where the variation of the void ratios of the reconstituted silty sands is illustrated in Figure 4(b). The more the dust amount is increased, the more the void ratio decreased up to 20% - this can be explained by the filling role of fine particles until saturation. Following this percentage, an increase in the void ratio was observed (Cubrinovski & Ishihara, 2002; Belkhatir et al, 2011; Monkul et al, 2016; Cherif Taiba et al, 2018; Ezziane et al, 2025).

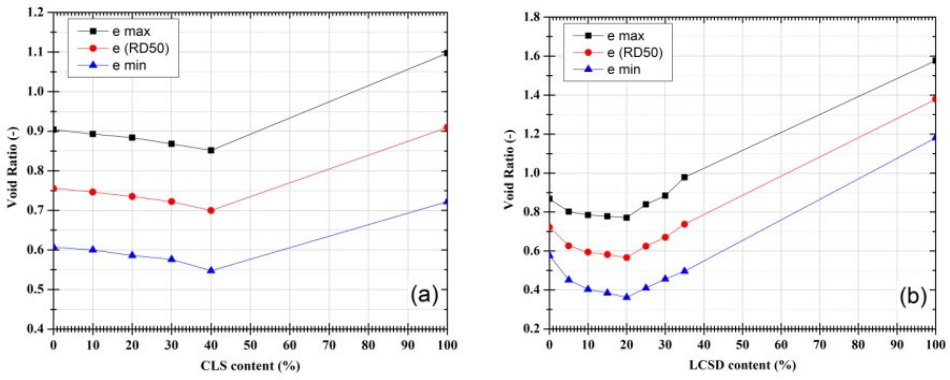

Figure 4 – Variation of the maximum and minimum void ratio of sand mixtures: (a) with different CLS content, (b) with different LCSD content

The physical characteristics of the sand mixtures used in this experimental program are represented in Tables 2 and 3.

Table 2 – Physical characteristics of the reconstituted clean sand mixtures

Reconstituted clean sands mixtures									
CLS **(%)**	G_s (-)	e_{max} (-)	e_{min} (-)	D_{50} (mm)	D_{60} (mm)	D_{30} (mm)	D_{10} (mm)	Cu (-)	Cc (-)
0	2.646	0.904	0.607	0.330	0.394	0.259	0.177	2.226	0.962
10	2.656	0.893	0.600	0.345	0.381	0.241	0.164	2.323	0.930
20	2.663	0.884	0.586	0.362	0.434	0.258	0.168	2.583	0.913
30	2.674	0.868	0.576	0.391	0.479	0.267	0.172	2.785	0.865
40	2.682	0.852	0.547	0.451	0.562	0.285	0.179	3.139	0.807
100	2.741	1.097	0.722	0.790	0.987	0.390	0.120	8.225	1.284

Table 3 – Physical characteristics of the reconstituted silty-sand mixtures

RCS%+LCSD% mixtures									
LCSD **(%)**	G_s (-)	e_{max} (-)	e_{min} (-)	D_{50} (mm)	Cu (-)	Cc (-)	W_L (%)	W_P (%)	I_P (%)
0	2.674	0.868	0.576	0.391	2.785	0.865	-	-	-
5	2.675	0.801	0.452	0.362	3.290	0.982	-	-	-
10	2.681	0.784	0.403	0.350	5.338	1.535	-	-	-
15	2.682	0.778	0.384	0.333	12.62	3.478	-	-	-
20	2.689	0.770	0.362	0.311	14.38	3.390	-	-	-
25	2.693	0.839	0.410	0.297	14.70	2.620	-	-	-
30	2.694	0.884	0.456	0.270	14.51	0.813	-	-	-
35	2.699	0.978	0.496	0.243	14.00	0.221	-	-	-
100	2.741	1.369	0.854	0.029	16.84	0.087	26.25	21.11	5.14

Experimental setup

The effect of incorporating CLS and LCSD on the mechanical behaviour of reconstituted sands was investigated in 36 direct shear test series.

All experiments were performed in accordance with the standard (AFNOR, 1994) ensuring a relative density of 50% under 100, 200, and 300 kPa of normal stress, with a constant displacement speed of 1.00 mm/min.

The shear box dimensions were 25 mm for the height of the sample and 60 x 60 mm² for the surface area of the horizontal section. The study's experimental program is illustrated in Table 4.

Table 4 – Testing program of mixtures

Tests (RCS-CLS %-LCSD %)	RS (%)	CLS (%)	LCSD (%)	Normal stress (kPa)
RCS	100	0		
RCS-10	90	10		
RCS-20	80	20	0	
RCS-30	70	30		
RCS-40	60	40		
RCS-30-5	67.5	27.5	5	100, 200, and 300 kPa
RCS-30-10	65.0	25.0	10	
RCS-30-15	62.5	22.5	15	
RCS-30-20	60.0	20.0	20	
RCS-30-25	57.5	17.5	25	
RCS-30-30	55.0	15.0	30	
RCS-30-35	52.5	12.5	35	

Experimental results and discussion

Effect of crushed limestone sand (CLS) on the river sand (RS) parameters

Effect of the CLS content on shear strength

Figure 5 shows the shear strength behaviour of reconstituted clean sand-based 0, 10, 20, 30, and 40% of CLS under different normal stresses (100, 200, and 300 kPa) prepared with a relative density of 50%. The test results indicate that the shear strength of all samples increases rapidly against the shear displacement to reach a peak value, followed by a partial decrease that could reflect the failure behaviour; then, a stabilisation segment is observed until the end of the shear test, which represents the typical behaviour of soils. This pattern can be attributed to the materials' strain-softening behaviour exhibited, whereby a peak shear strength is achieved at small displacements, followed by gradual strength reductions as displacement increases (Gilbert & Byrne, 1996; Igwe, 2018).

It is clear that the use of higher amounts of CLS (30 and 40%) exhibits better stability compared to lower percentages. Additionally, higher normal stress (300 kPa) enhances the stability of the shear stress curves, showing improved soil failure resistance. Furthermore, an increase in shear strength with the CLS content up to 30% is indicated by the test result; a more detailed analysis of this parameter shows that the shear strength increased by approximately 18, 29, and 17% under normal stress of 100, 200, 300kPa, respectively.

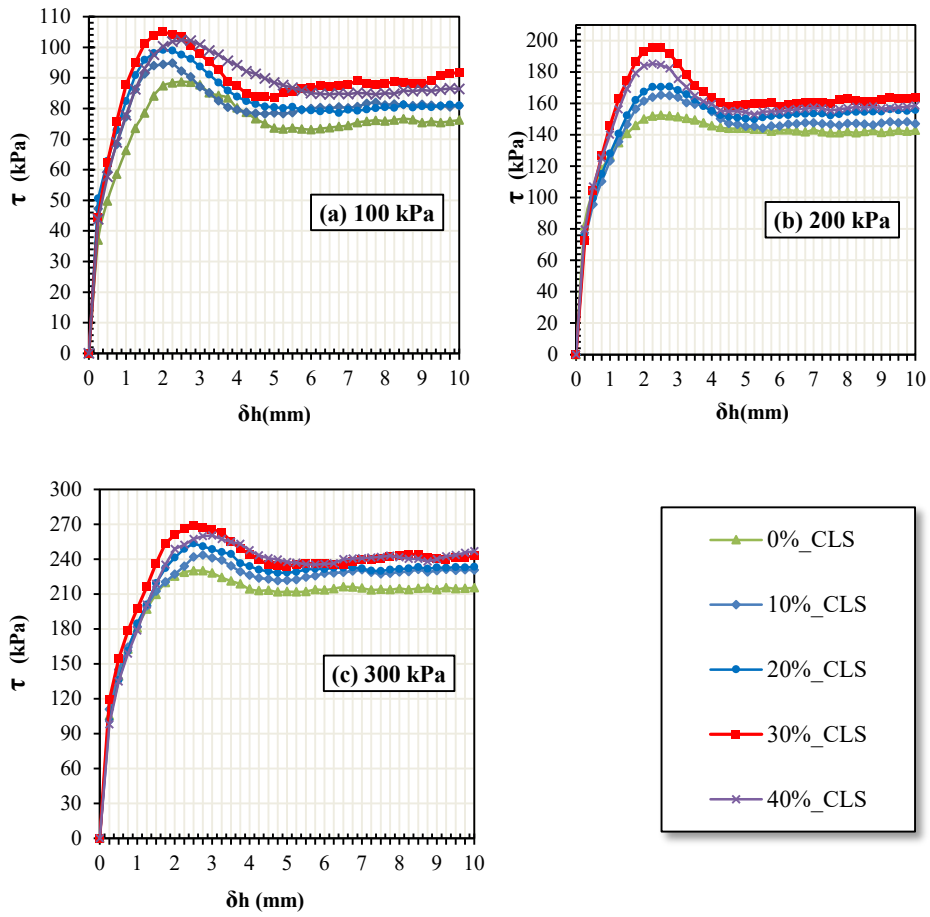

Figure 5 – Variation of shear *strength versus horizontal shear displacement for RS mixed with various contents of CLS at normal stress: (a) 100 kPa, (b) 200kPa, and (c) 300 kPa*

The enhancement in shear strength can be attributed to the influence of the angular particles of CLS, by enhancing interparticle interlocking, and contributes to developing shear resistance (Schanz & Vermeer, 1996; Hamidi et al, 2009; Nafisi et al, 2018; Nie et al, 2022; Daghistani & Abuel-Naga, 2023). However, at 40% CLS content, a slight decrease in the shear strength was observed; this is due to the increased void ratio between the particles at this stage because the increase in eccentricity leads to an increase in the e_{max} and e_{min} ratios and thus the density becomes lower, which is the reason for the decrease in resistance (Cho et al, 2006; Shabong et al, 2023).

Effect of the CLS content on the peak friction angle of RS

The results in Figure 6 present the influence of the CLS incorporation on the river sand friction angle (φ). It was observed that the more the CLS content is increased, the more the friction angle is improved, reaching its maximum value of approximately 43° at 30% CLS content, corresponding to an enhancement rate of 12%; beyond a 30% amount, a decrease of the friction angle is observed.

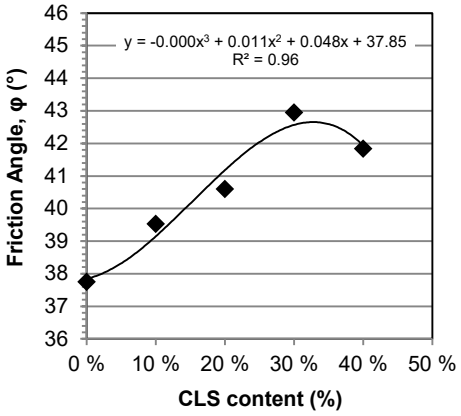

Figure 6 – Effect of the CLS content on the friction angle

The enhancement in the friction angle is attributed to the angularity of the CLS particles. These particular shapes of angular grains could enhance the interlocking and frictional resistance between particles up to a critical threshold (Been & Jefferies, 1985; Thevanayagam et al, 2002; Cho et al, 2006; Guo & Su, 2007; Li, 2013, Abbireddy & Clayton, 2015). Following this percentage, the friction angle decrease can be attributed to the excess of fine particles generated by higher CLS content, reducing the effective interparticle interactions and limiting the beneficial effects of angularity (Vallejo, 2001; Shabong et al, 2023).

Effect of the CLS content on the volume change behaviour

Figure 7 illustrates the effect of the CLS content on the volume change behaviour of RS, under 100, 200, and 300 kPa of normal stresses. The vertical displacement versus horizontal shear displacement curves reveal three primary phases during shearing: initial contraction, dilation to vertical displacement peak, and subsequent contraction until failure.

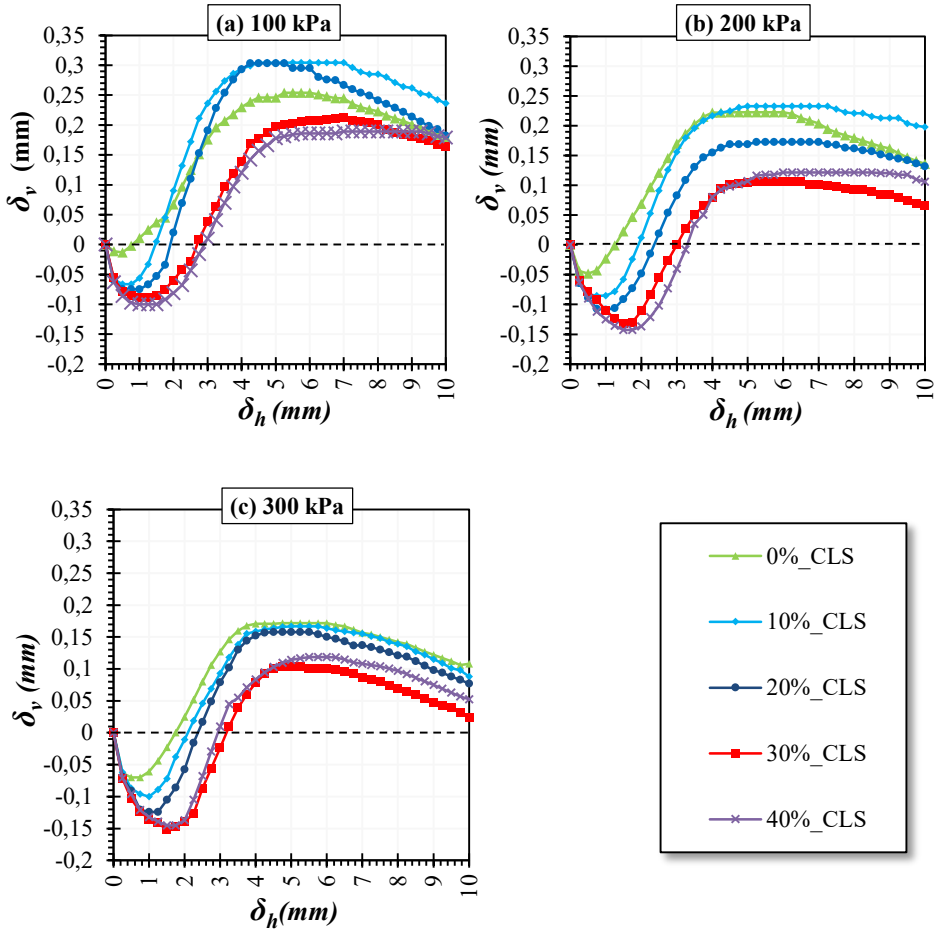

Figure 7 –Vertical displacement/horizontal shear displacement curve for RS mixed with various contents of CLS at normal stress: (a) 100 kPa, (b) 200kPa, and (c) 300 kPa

At low normal stresses (100 kPa), sands containing 10 and 20% of the CLS content exhibit greater dilation compared to RS, which is attributable to the theoretical capacity of sands containing irregular particle shape to form a lower minimum void ratio compared to sands with rounded particles, allowing particle rearrangement during shearing (Lu et al, 2019). In contrast, when the CLS content exceeds 30%, the dilation level is notably decreased, signifying the predominance of angular particle effects in constraining expansive movements through enhanced interlocking and prevention of particle rearrangement during shear resulting from the incorporation of angular particles (Cho et al, 2006).

Furthermore, the contraction phase in the samples containing 30 and 40% CLS is observed to intensify under 200 and 300 kPa of normal stresses, in particular.

This behaviour underscores the critical role of angular grains in constraining the interparticle rotation and promoting interlocking, thereby diminishing the potential for expansion (Bolton, 1986; Lu et al, 2019).

The interaction between particle shape, content and stress illustrates the importance of optimising the CLS content to balance expansion and contraction to improve mechanical performance, thus justifying the use of up to 30% CLS content in technical applications requiring high load-bearing capacity.

Effect of the LCSD content on the mechanical properties of the optimum reconstructed clean sands (RCS)

Based on the results obtained in the first stage, the mixture that developed the best resistance and friction angle is the reconstituted sand containing 30% of crushed sand.

Therefore, the investigation in the second stage will be based on studying the effect of limestone crushed sand dust (LCSD) on the mechanical properties of the optimum reconstructed clean sands (RCS). RCS is substituted by LCSD with various volumetric contents (from 0 to 35%) and sheared under different normal stresses of 100, 200, and 300 kPa at 50% of relative density.

Effect of the LCSD content on shear strength

Figure 8 represents the variation of shear strength versus horizontal shear displacement for reconstituted clean sand (RCS) mixed with various contents of LCSD. Clearly visible in the figures is that the shear strength of clean sand is significantly greater than that of the mixtures containing fine particles.

Furthermore, the shear strength of clean sand increases considerably with the advancement of horizontal displacement. Consequently, an increase in fine content leads to a gradual decrease in shear strength, especially during the initial stage of horizontal displacement (from 0 to 2 mm).

This reduction can be attributed to fine particles enhancing the contractiveness phase during the test, thereby filling the voids as well as reducing internal friction between the resulting sand particles (Arab et al, 2008; Belkhatir et al, 2010; Monkul et al, 2016; Monkul et al, 2017; Bouri et al, 2019; Aouali et al, 2019; Nougar et al, 2021).

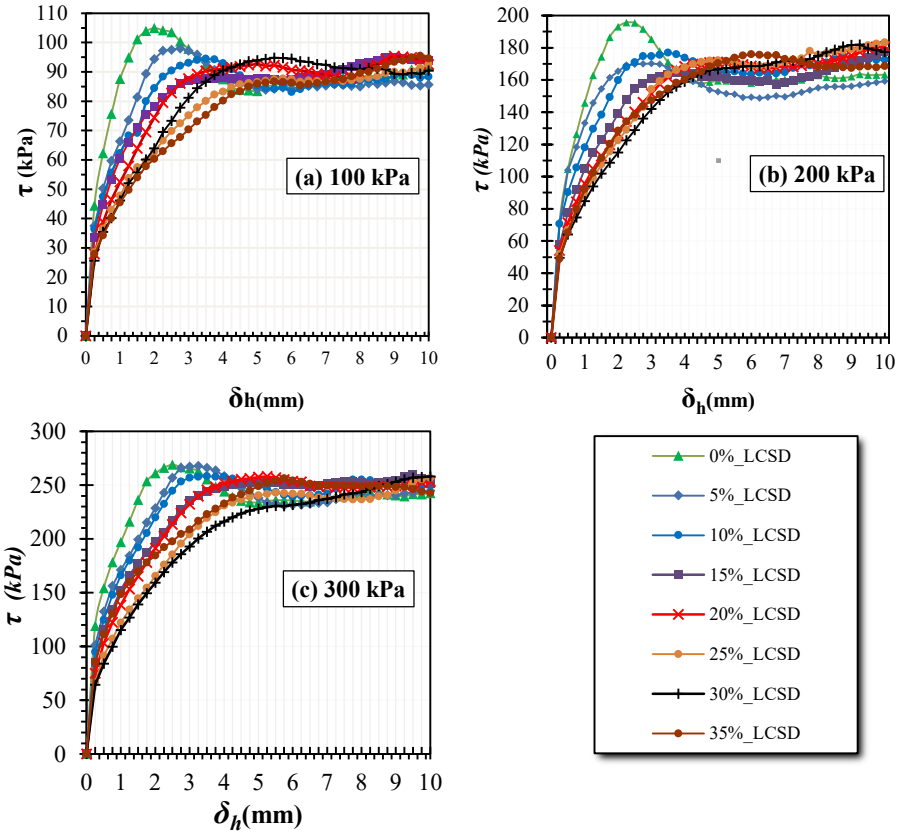

Figure 8 – Variation of shear strength versus horizontal shear displacement for reconstituted clean sand (RCS) mixed with various contents of LCSD, under normal stress: (a) 100 kPa, (b) 200 kPa, and (c) 300 kPa

In particular, the stabilisation of shear strength at large displacements was observed for higher proportions of LCSD (>15%), while lower proportions (≤15%) exhibited lower strength and less stability in comparison. High fines content enhances the phenomenon of "soil softening" or "stable cohesion", ultimately leading to relative stability after reaching maximum shear strength values (Ishihara, 1996; Lade & Yamamuro, 1997).

The effect of the LCSD content on the maximum shear resistance (τ_{Peak}) and the residual shear resistance (τ_{res}) under different normal stresses (100, 200, and 300 kPa) is shown in Figure 9. The maximum shear strength (τ_{Peak}) is linearly decreased with increasing the LCSD content under all levels of normal stress, as shown in Figure 9(a). The

decrease is attributed to the effect of fines on reducing the interlocking between sand particles, which reduces the ability of the mixture to resist external loads (Shen et al, 2021; Ouici et al, 2024; Li et al, 2023).

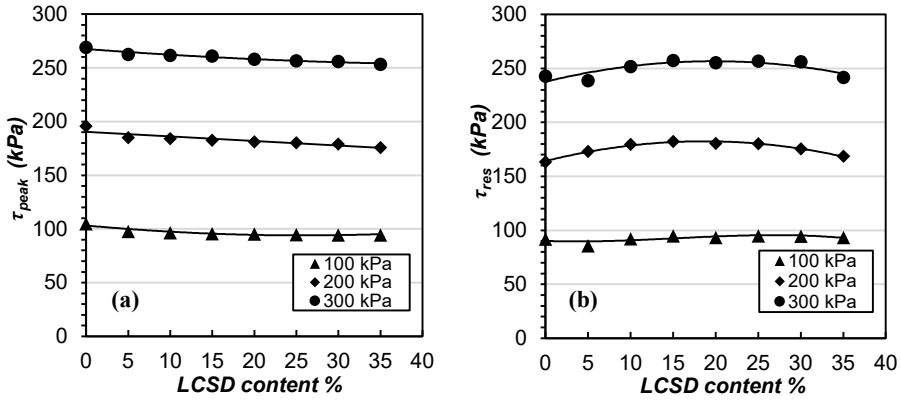

Figure 9 – Effect of the LCSD content on the peak and residual shear strength, under normal stresses of 100, 200, and 300 kPa

A different trend is shown in Figure 9(b) - as the LCSD content increases up to 15%, the residual shear strength (τ_{Res}) is improved. However, beyond this threshold, the residual shear strength is decreased gradually with an increase in the LCSD content. This performance at this range of substitution (less than 15%) can be attributed to the interlocking effect between fine and soil particles during shearing, which significantly enhances the overall structure and increases the residual shear strength (Shi et al, 2024).

Once the value exceeds 15%, the interparticle content becomes sufficient to destabilize the sand particles' cohesion.

This study reflects a dual effect of the LCSD content on shear strength - fine particles improve the residual shear strength within a certain range, while their increase leads to a negative effect on the maximum and residual shear strength when the critical percentage is exceeded (15%).

Effect of the LCSD content on the friction angle

The influence of the limestone sand dust content (LCSD) on the maximum friction angle (φ_{Peak}) and the residual friction angle (φ_{Res}) of reconstituted clean sand (RCS) is shown in Figure 10. The test results show that the maximum friction angle gradually decreased as the LCSD content increased, indicating the effect of fine particles in reducing the

interaction between coarse grains; this result agrees with those of (Bouri et al, 2019; Monkul & Ozden, 2007; Najjar et al, 2015) concluding that the addition of fines to granular materials decreases the friction angle. This decrease is attributed to fine particles by the voids filling effect, limiting the structural cohesion and reducing the friction angle (Been & Jefferies, 1985). In addition, the results showed an almost linear relationship between the LCSD content and the maximum friction angle.

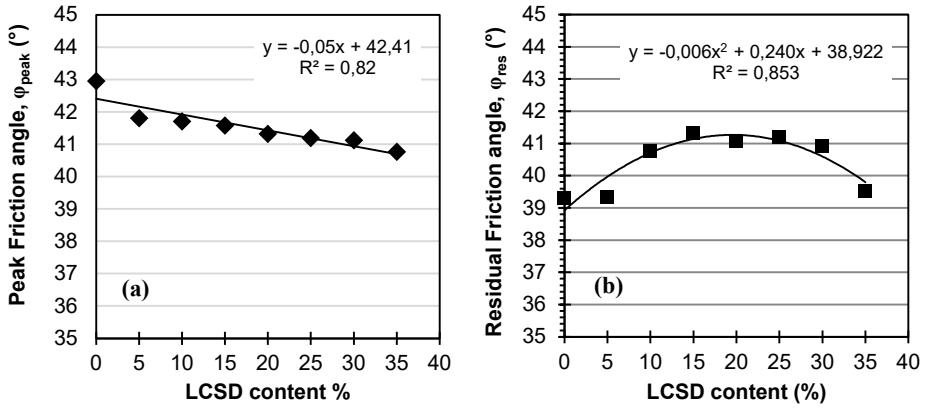

Figure 10 – Effect of the LCSD content on: (a) peaks friction angle (φ_{Peak}) and (b) residual friction angle (φ_{Res})

On the other hand, the residual friction angle (φ_{res}) shows a clear improvement as the LCSD content increases until reaching 15%; at this threshold, the interstices between sand grains are completely filled by fine particles, without significantly altering the interaction between the coarse grains, thereby enhancing the residual friction characteristics (Thevanayagam et al, 2002). However, when the substitution exceeds 15%, the residual friction angle begins to diminish due to the increased content of fine particles, leading to the failure of structural cohesion and the reduction of the positive effect of these particles (Vallejo, 2001).

Effect of the LCSD content on the volume change behaviour

The effect of the LCSD content on the volume change behaviour of the reconstituted clean sand specimens, incorporating different LCSD ratios ranging from 0 to 35% by sand volume, under normal stresses of 100, 200, and 300 kPa, is shown in Figure 11.

The analysis reveals a typical volumetric deformation of medium-density samples, where three primary phases are observed. Firstly, there

is the initial contraction phase, where the specimens begin to contract as the shearing process begins due to the rearrangement of sand grains and the void filling by fine particles (Xiao et al, 2017). Moreover, the results illustrate that increases in normal stress lead to a greater initial contraction behaviour of the specimens.

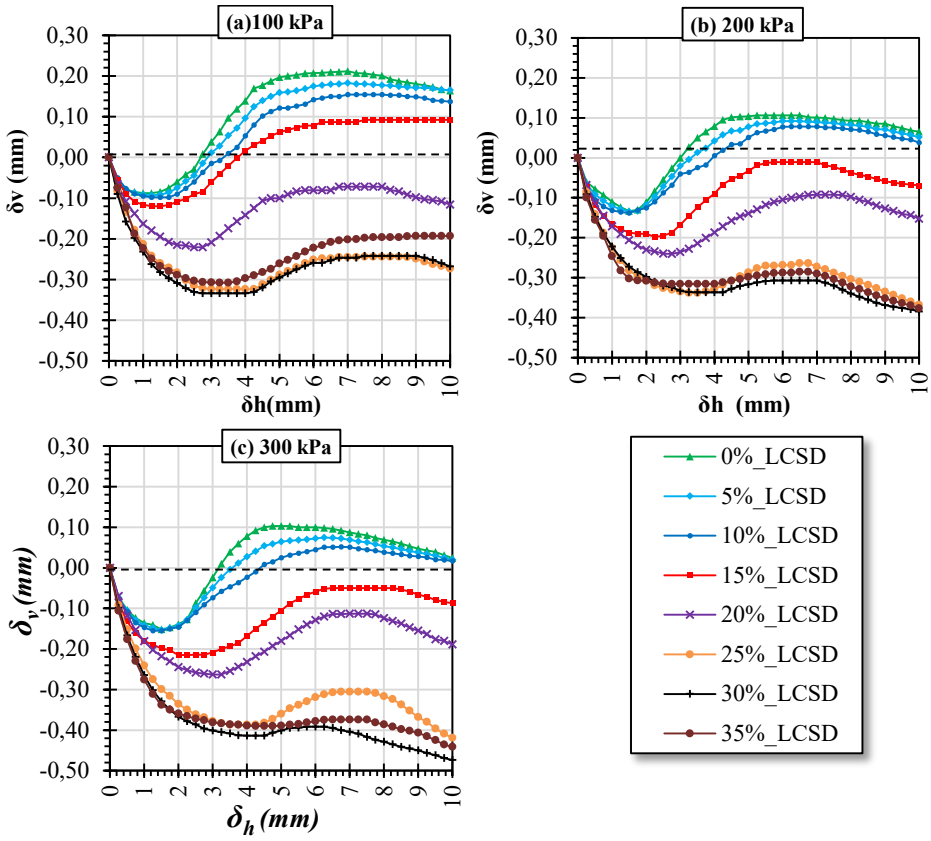

Figure 11 – Vertical displacement / horizontal shear displacement curve for RCS mixed with various contents of LCSD, at normal stress: (a)100 kPa, (b)200 kPa and (c)300 kPa

The second stage is expansion: the samples begin to expand significantly at low pressures compared to high pressures and with the increase in the LCSD content, especially within the range of 0 to 15%, the expansion becomes more pronounced. Meanwhile, at an amount exceeding or equal to 20%, the expansion gradually decreases due to the effect of fine content in increasing the sphericity and roundness of the samples (Nguyen et al, 2021). The final phase is indicative of the secondary contraction under normal stresses of 200 and 300 kPa.

Subsequent to the expansion phase, the samples begin to contract once more under a high LCSD content. The fine particles start to create internal saturation of the voids, thereby reducing the void ratio. Consequently, the interlocking increases, weakening the significance of the expansion (Liu et al, 2023).

Moreover, when the fine content (FC) is low (FC ≤ 10%), the values of the volume change are very similar to each other, indicating that the influence of the LCSD content on volumetric deformation is negligible. In this case, coarse particles dominate the mechanical properties of the soil, while fine particles occupy the voids between them. Nevertheless, a substantial decrease in the volume change values is observed when the FC is greater than or equal to 15%. This decline can be ascribed to fine particles starting to fill the voids between coarse particles. Consequently, the porosity and compressibility of the soil are reduced, thus limiting the volume change that occurs under loading condition (Gong et al, 2019). The distribution of fine particles in the soil plays a critical role in the phenomenon of contraction and expansion during the shearing process. The increase in the percentage of fines in the soil leads to an enhancement in its contraction, concurrent with a reduction in its expansion, resulting from an increase in internal friction between the grains (Been & Jefferies, 1985; Schanz et al, 1999). Furthermore, the results of (Thevanayagam et al, 2002) indicate that the optimum percentage of fines, varying between 15 to 20%, improves the behaviour of mixed sands through the filling void without disturbing the fundamental interaction of sand grains. These results confirm that the optimum LCSD ratio obtained in this study to balance contraction and expansion is estimated at 15% of LSCD substitution.

Conclusion

This experimental study investigates the effect of crushed limestone sand (CLS) and limestone crushed sand dust (LCSD) on the mechanical behaviour of river sand (RS). Based on the obtained results, the following conclusions can be drawn:

– The substitution of RS with 30% CLS resulted in an enhancement of the peak shear strength by 18, 28, and 17% under normal stresses of 100, 200, and 300 kPa, respectively. Furthermore, the friction angle is improved to 43° (representing a 12% improvement).
– At low normal stresses (100 kPa), sands with 10% and 20% CLS showed greater dilation compared to river sands. However, as the content of CLS is increased to 30% or more, the dilation is reduced,

and the contraction is increased, especially under higher normal stresses of 200 and 300 kPa.

– The findings demonstrate a gradual decrease in the peak shear strength values, exhibiting a linear relationship with the increasing LCSD content. Moreover, the residual shear strength increased by 12%, 14%, and 9.5% at 100, 200, and 300 kPa normal stresses, respectively, up to 15% LCSD content.
– The incorporation of up to 15% LCSD content enhanced the residual shear strength without compromising the peak shear strength; beyond this threshold, a decline in residual shear strength is observed.
– The optimum amount of the LCSD content is considered to be 15%.The peak friction angle (φ_{peak}) regularly decreased as the LCSD content increased.
– The residual friction angle (φ_{res}) achieved the optimum value for 15% of LCSD substitution.
– The substitution of sand with 15% to 20% LCSD resulted in enhanced dilation under low stresses and balanced contraction under high normal stresses.

The mechanical behaviour of river sands from the M'zi River was significantly improved when substituted with crushed limestone sand at a percentage of 30%, with the incorporation of fines from the same limestone rock estimated at 15%. The waste from the aggregate production quarries in the Montgorno region (Medea, Algeria) contains a limestone fines content ranging between 15 and 20%, which allows it to be used directly without any treatment. These findings are highly promising for the field of sustainable development, as they demonstrate the potential to enhance soil properties and valorise quarry by-products.

The results presented in this paper are part of a research project focusing on the valorisation and reuse of construction and road wastes and industrial by-products.

References

-AFNOR. 1991. *NF-P94-054: Sols: reconnaissance et essais–Détermination de la masse volumique des particules solides des sols–Méthode du pycnomètre à eau* [online]. Available at: https://www.boutique.afnor.org/fr-fr/norme/nf-p94054/sols-reconnaissance-et-essais-determination-de-la-masse-volumique-des-parti/fa020767/11077 [Accessed: 19 January 2025].

-AFNOR. 1992. *NF P94-057: Soils investingation and testing. Granulometric analysis. Hydrometer method* [online]. Available at:

https://www.boutique.afnor.org/en-gb/standard/nf-p94057/soils-investingation-and-testing-granulometric-analysis-hydrometer-method/fa020768/11074 [Accessed: 19 January 2025].

-AFNOR. 1994. *NF-P94-071-1: Soil investigation and testing. Direct shear test with shearbox apparatus. Part 1: direct shear* [online]. Available at: https://www.boutique.afnor.org/en-gb/standard/nf-p940711/soil-investigation-and-testing-direct-shear-test-with-shearbox-apparatus-pa/fa029769/11060 [Accessed: 19 January 2025].

-AFNOR. 1996. NF-P94-056: Sols: reconnaissance et essais - Analyse granulométrique - Méthode par tamisage à sec après lavage [online]. Available at: https://www.boutique.afnor.org/fr-fr/norme/nf-p94056/sols-reconnaissance-et-essais-analyse-granulometrique-methode-par-tamisage-/fa026936/11075 [Accessed: 19 January 2025].

-AFNOR. 2000. *NF-P94-059: Sols: reconnaissance et essais - Détermination des masses volumiques minimale et maximale des sols non cohérents* [online]. Available at: https://www.boutique.afnor.org/fr-fr/norme/nf-p94059/sols-reconnaissance-et-essais-determination-des-masses-volumiques-minimale-/fa106659/17780 [Accessed: 19 January 2025].

Abbireddy, C.O.R. & Clayton, C.R.I. 2015. The impact of particle form on the packing and shear behaviour of some granular materials: an experimental study. *Granular Matter,* 17**,** pp.427-438. Available at: https://doi.org/10.1007/s10035-015-0566-0.

Abbou, M., Semcha, A. & Kazi-Aoual, F. 2020. Stabilization of compressed earth block clayey materials from Adrar (Algeria) by lime and crushed sand. *Journal of Building Materials and Structures,* 7(1)**,** pp.42-50. Available at: https://doi.org/10.34118/jbms.v7i1.137.

Altuhafi, F.N., Coop, M.R. & Georgiannou, V.N. 2016. Effect of Particle Shape on the Mechanical Behavior of Natural Sands. *Journal of Geotechnical and Geoenvironmental Engineering,* 142(12). Available at: https://doi.org/10.1061/(ASCE)GT.1943-5606.0001569.

Aouali, N., Benessalah, I., Arab, A., Ali, B. & Abed, M. 2019. Shear Strength Response of Fibre Reinforced Chlef (Algeria) Silty Sand: Laboratory Study. *Geotechnical and Geological Engineering,* 37(2)**,** pp.1047-1057. Available at: https://doi.org/10.1007/s10706-018-0641-5.

Arab, A., Hamoudi, S., Shahrour, I. & Lancelot, L. 2008. Influence of fines fraction on the behaviour of a silty sand. *Revue Française de Géotechnique*, 122, pp.37-43. Available at: https://doi.org/10.1051/geotech/2008122037.

Been, K. & Jefferies, M.G. 1985. A state parameter for sands. *Géotechnique,* 35(2)**,** pp.99-112. Available at: https://doi.org/10.1680/geot.1985.35.2.99.

Belkhatir, M., Arab, A., Della, N., Missoum, H. & Schanz, T. 2010. Influence of inter-granular void ratio on monotonic and cyclic undrained shear response of sandy soils. *Comptes Rendus. Mécanique,* 338(5)**,** pp.290-303. Available at: https://doi.org/10.1016/j.crme.2010.04.002.

Belkhatir, M., Arab, A., Schanz, T., Missoum, H., Della, N. 2011. Laboratory study on the liquefaction resistance of sand-silt mixtures: effect of grading

characteristics. *Granular Matter*, 13(5), pp.599-609. Available at: https://doi.org/10.1007/s10035-011-0269-0.

Benessalah, I., Arab, A. & Meziane, E.-H. 2021. Intergranular void ratio and undrained monotonic behavior of Chlef sand containing low plastic fines. *Acta Mechanica,* 232(4)**,** pp.1621-1640. Available at: https://doi.org/10.1007/s00707-020-02923-0.

Bolton, M. 1986. The strength and dilatancy of sands. *Geotechnique,* 36(1)**,** pp.65-78. Available at: https://doi.org/10.1680/geot.1986.36.1.65.

Borhani, A. & Fakharian, K. 2016. Effect of Particle Shape on Dilative Behavior and Stress Path Characteristics of Chamkhaleh Sand in Undrained Triaxial Tests. *International Journal of Civil Engineering,* 14**,** pp.197-208. Available at: https://doi.org/10.1007/s40999-016-0048-8.

Bouri, D., Krim, A., Brahim, A. & Arab, A. 2019. Shear strength of compacted Chlef sand: effect of water content, fines content and others parameters. *Studia Geotechnica et Mechanica,* 42(1)**,** pp.18-35. Available at: https://doi.org/10.2478/sgem-2019-0027.

Brooks, R., Udoeyo, F.F. & Takkalapelli, K.V. 2011. Geotechnical Properties of Problem Soils Stabilized with Fly Ash and Limestone Dust in Philadelphia. *Journal of Materials in Civil Engineering,* 23(5)**,** pp.711-716. Available at: https://doi.org/10.1061/(ASCE)MT.1943-5533.0000214.

Cabalar, A.F. & Omar, R.A. 2023. Stabilizing a silt using waste limestone powder. *Bulletin of Engineering Geology and the Environment,* 82(8)**,** art.number:300. Available at: https://doi.org/10.1007/s10064-023-03302-4.

Cherif Taiba, A., Mahmoudi, Y., Belkhatir, M. & Schanz, T. 2018. Experimental Investigation into the Influence of Roundness and Sphericity on the Undrained Shear Response of Silty Sand Soils. *Geotechnical Testing Journal,* 41(3), pp. 619-633. Available at: https://doi.org/10.1520/GTJ20170118.

Cho, G.-C., Dodds, J. & Santamarina, J.C. 2006. Particle Shape Effects on Packing Density, Stiffness, and strength Natural and Crushed sands. *Geotechnical and Geoenvironmental Engineering,* 132(5)**,** pp.591-602. Available at: https://doi.org/10.1061/(ASCE)1090-0241(2006)132:5(591).

Cubrinovski, M. & Ishihara, K. 2002. Maximum and Minimum Void Ratio Characteristics of Sands. *Soils and Foundations,* 42(6)**,** pp.65-78. Available at: https://doi.org/10.3208/sandf.42.6_65.

Daghistani, F. & Abuel-Naga, H. 2023. Evaluating the Influence of Sand Particle Morphology on Shear Strength: A Comparison of Experimental and Machine Learning Approaches. *Applied Sciences,* 13(14)**,** art.number:8160. Available at: https://doi.org/10.3390/app13148160.

Ezziane, M., Henni, A.D., Denine, S., Benyahia, B.A. & Boumezerane, D. 2025. Effect of silt fines on the undrained monotonic behavior of compacted tuff soil. *Arabian Journal of Geosciences*, 18(1), art.number:9. Available at: https://doi.org/10.1007/s12517-024-12149-2.

Gilbert, R.B. & Byrne, R.J. 1996. Strain-Softening Behavior of Waste Containment System Interfaces. *Geosynthetics International,* 3(2)**,** pp.181-203. Available at: https://doi.org/10.1680/gein.3.0059.

Gong, J., Nie, Z., Zhu, Y., Liang, Z. & Wang, X. 2019. Exploring the effects of particle shape and content of fines on the shear behavior of sand-fines mixtures via the DEM. *Computers and Geotechnics,* 106**,** pp.161-176. Available at: https://doi.org/10.1016/j.compgeo.2018.10.021.

Guemmadi, Z. & Houari, H. 2009. Utilizing crushed limestone fine wastes in Algeria as fillers in cement. *Sciences & Technologie. B, Sciences de l'ingénieur***,** 29, pp.17-22 [online]. Available at: https://revue.umc.edu.dz/b/article/view/252 [Accessed: 19 January 2025].

Guo, P. & Su, X. 2007. Shear strength, interparticle locking, and dilatancy of granular materials. *Canadian Geotechnical Journal,* 44(5)**,** pp.579-591. Available at: https://doi.org/10.1139/t07-010.

Hamidi, A., Yazdanjou, V. & Salimi, N. 2009. Shear strength characteristics of sand-gravel mixtures. *International Journal of Geotechnical Engineering,* 3(1)**,** pp.29-38. Available at: https://doi.org/10.3328/IJGE.2009.03.01.29-38.

Holtz, R.D., Kovacs, W.D. & Sheahan, T.C. 2022. *An Introduction to Geotechnical Engineering, 3rd edition.* Pearson. ISBN: 9780135619254.

Holtz, W.G. & Gibbs, H.J. 1956. Engineering Properties of Expansive Clays. *Transactions of the American Society of Civil Engineers,* 121(1)**,** pp.641-663. Available at: https://doi.org/10.1061/TACEAT.0007325.

Ibrahim, H.H., Alshkane, Y.M., Mawlood, Y.I., Noori, K.M.G. & Hasan, A.M. 2020. Improving the geotechnical properties of high expansive clay using limestone powder. *Innovative Infrastructure Solutions,* 5(3)**,** art.number :112. Available at: https://doi.org/10.1007/s41062-020-00366-z.

Igwe, O. 2018. The Combined Effect of Particle Size Distribution and Relative Density on the Large Strain Behavior of Sandy Soils. *Geotechnical and Geological Engineering,* 36(2)**,** pp.1037-1048. Available at: https://doi.org/10.1007/s10706-017-0372-z.

Ishihara, K. 1996. *Soil Behaviour in Earthquake Geotechnics*. Oxford Academic. Available at: https://doi.org/10.1093/oso/9780198562245.001.0001.

Kandasami, R.K. & Murthy, T.G. 2017. Manifestation of particle morphology on the mechanical behaviour of granular ensembles. *Granular Matter,* 19**,** art.number:21. Available at: https://doi.org/10.1007/s10035-017-0703-z.

Lade, P.V. & Yamamuro, J.A. 1997. Effects of non-plastic fines on static liquefaction of sands. *Canadian Geotechnical Journal,* 34(6)**,** pp.918-928. Available at: https://doi.org/10.1139/t97-052.

Li, X., Liu, J. & Sun, Z. 2023. Shear strength-dilation characteristics of coral sand contained fines. *Bulletin of Engineering Geology and the Environment,* 82(9)**,** art.number:349. Available at: https://doi.org/10.1007/s10064-023-03349-3.

LI, Y. 2013. Effects of particle shape and size distribution on the shear strength behavior of composite soils. *Bulletin of Engineering Geology and the Environment,* 72**,** pp.371-381. Available at: https://doi.org/10.1007/s10064-013-0482-7.

Liu, Y., Liu, X. & Hu, W. 2023. Competition mechanism between dilation and interlocking in granular soils: DEM simulation and constitutive modeling. *Acta*

Geotechnica, 18(1)**,** pp.149-169. Available at: https://doi.org/10.1007/s11440-022-01552-2.

Logbi, A., Mani, M., Choungara, T. & Kriker, A. 2023. Comparative study of the effect of crushed dune sand and limestone fillers on mortar properties in aggressive environment. *World Journal of Engineering,* 20(1)**,** pp.85-92. Available at: https://doi.org/10.1108/WJE-09-2020-0437.

Lu, Z., Yao, A., Su, A., Ren, X., Liu, Q. & Dong, S. 2019. Re-recognizing the impact of particle shape on physical and mechanical properties of sandy soils: A numerical study. *Engineering Geology,* 253**,** pp.36-46. Available at: https://doi.org/10.1016/j.enggeo.2019.03.011.

Monkul, M.M., Etminan, E. & Şenol, A. 2016. Influence of coefficient of uniformity and base sand gradation on static liquefaction of loose sands with silt. *Soil Dynamics and Earthquake Engineering,* 89**,** pp.185-197. Available at: https://doi.org/10.1016/j.soildyn.2016.08.001.

Monkul, M.M., Etminan, E. & Senol, A. 2017. Coupled influence of content, gradation and shape characteristics of silts on static liquefaction of loose silty sands. *Soil Dynamics and Earthquake Engineering,* 101**,** pp.12-26. Available at: https://doi.org/10.1016/j.soildyn.2017.06.023.

Monkul, M.M. & Ozden, G. 2007. Compressional behavior of clayey sand and transition fines content. *Engineering Geology,* 89(3-4)**,** pp.195-205. Available at: https://doi.org/10.1016/j.enggeo.2006.10.001.

Nafisi, A., Khoubani, A., Montoya, B.M. & Evans, M. 2018. The effect of grain size and shape on mechanical behavior of MICP sand I: experimental study. In: *Proceedings of the 11th National Conference on Earthquake Engineering,* Los Angeles, CA, USA, June 25-29. Earthquake Engineering Research Institute (EERI). ISBN: 9781510873254.

Najjar, S., Yaghi, K., Adwan, M. & Jaoude, A. 2015. Drained shear strength of compacted sand with clayey fines. *International Journal of Geotechnical Engineering,* 9(5)**,** pp.513-520. Available at: https://doi.org/10.1179/1939787915Y.0000000001.

Nguyen, H.B.K., Rahman, M.M. & Fourie, A.B. 2021. How particle shape affects the critical state, triggering of instability and dilatancy of granular materials–results from a DEM study. *Géotechnique,* 71(9)**,** pp.749-764. Available at: https://doi.org/10.1680/jgeot.18.P.211.

Nie, J., Zhao, S., Cui, Y. & Wang, Y. 2022. Coupled effects of particle overall regularity and sliding friction on the shear behavior of uniformly graded dense sands. *Journal of Rock Mechanics and Geotechnical Engineering,* 14(3)**,** pp.873-885. Available at: https://doi.org/10.1016/j.jrmge.2021.10.014.

Nougar, B., Brahimi, A., Bouri, D.E., Arab, A. & Benessalah, I. 2021. Laboratory Investigation into the Effect of Fines Plasticity on the Mechanical Behavior of Sand/Fines Mixtures. *Transportation Infrastructure Geotechnology***,** 8(3), pp.438-451. Available at: https://doi.org/10.1007/s40515-020-00144-5.

Ouici, A.A., Taiba, A.C., Mahmoudi, Y. & Belkhatir, M. 2024. Influence of fines and gravel particles on strength-dilatancy of river sand: Effect of depositional

conditions. *Marine Georesources & Geotechnology*, pp.1-15. Available at: https://doi.org/10.1080/1064119X.2024.2409411.

Sabat, A.K. & Muni, P.K. 2015. Effects of Limestone Dust on Geotechnical Properties of an Expansive Soil. *International Journal of Applied Engineering Research,* 10(17), pp.377724-37730.

Safiddine, S., Amokrane, K., Debieb, F., Soualhi, H., Benabed, B. & Kadri, E.-H. 2021. How quarry waste limestone filler affects the rheological behavior of cement-based materials. *Applied Rheology,* 31**,** pp.63-75. Available at: https://doi.org/10.1515/arh-2020-0118.

Safiddine, S., Debieb, F., Kadri, E.-H., Menadi, B. & Soualhi, H. 2017. Effect of crushed sand and limestone crushed sand dust on the rheology of cement mortar. *Applied Rheology,* 27(1)**,** pp.12-20. Available at: https://doi.org/10.3933/applrheol-27-14490.

Santamarina, J.C. & Cho, G.C. 2001. Determination of Critical State Parameters in Sandy Soils—Simple Procedure. *Geotechnical Testing Journal,* 24(2)**,** pp.185-192. Available at: https://doi.org/10.1520/GTJ11338J.

Schanz, T. & Vermeer, P. 1996. Angles of friction and dilatancy of sand. *Géotechnique,* 46(1)**,** pp.145-151. Available at: https://doi.org/10.1680/geot.1996.46.1.145.

Schanz, T., Vermeer, P.A. & Bonnier, P.G. 1999. The hardening soil model: Formulation and verification. In: *Beyond 2000 in Computational Geotechnics, 1st Edition.* Routledge [online]. Available at: https://www.taylorfrancis.com/chapters/edit/10.1201/9781315138206-27/hardening-soil-model-formulation-verification-schanz-vermeer-bonnier [Accessed: 19 January 2025]. ISBN: 9781315138206

Shabong, R.A., Sonowal, A.J., Pukhrambam, A., Das, R., Anand, A., Bobing, S. & Deka, S. 2023. An experimental study on the effect of particle size and non-homogeneity on the shear strength of soil. In: *IOP Conference Series: Materials Science and Engineering, Volume 1282, 3rd International Conference on Sustainable Construction Technologies & Advancements in Civil Engineering. (ScTACE 2022),* Bhimavaram, India, art.number:012021, December 15-17. Available at: https://doi.org/10.1088/1757-899X/1282/1/012021.

Shen, J., Wang, X., Wang, X., Yao, T., Wei, H. & Zhu, C. 2021. Effect and mechanism of fines content on the shear strength of calcareous sand. *Bulletin of Engineering Geology and the Environment,* 80**,** pp.7899-7919. Available at: https://doi.org/10.1007/s10064-021-02398-w.

Shi, Y., Li, S., Zhang, T., Liu, J. & Zhang, J. 2024. Compaction and shear performance of lime-modified high moisture content silty clay. *Case Studies in Construction Materials,* 21**,** e03529. Available at: https://doi.org/10.1016/j.cscm.2024.e03529.

Skender, Z., Bali, A. & Kettab, R. 2021. Self-compacting concrete (SCC) behaviour incorporating limestone fines as cement and sand replacement. *European Journal of Environmental and Civil Engineering,* 25(10)**,** pp.1852-1873. Available at: https://doi.org/10.1080/19648189.2019.1607564.

Thevanayagam, S., Shenthan, T., Mohan, S. & Liang, J. 2002. Undrained Fragility of Clean Sands, Silty Sands, and Sandy Silts. *Journal of Geotechnical and Geoenvironmental Engineering,* 128(10)**,** pp.849-859. Available at: https://doi.org/10.1061/(ASCE)1090-0241(2002)128:10(849).

Vallejo, L.E. 2001. Interpretation of the limits in shear strength in binary granular mixtures. *Canadian Geotechnical Journal,* 38(5)**,** pp.1097-1104. Available at: https://doi.org/10.1139/t01-029.

Xiao, Y., Liu, H., Chen, Q., Long, L. & Xiang, J. 2017. Evolution of particle breakage and volumetric deformation of binary granular soils under impact load. *Granular Matter,* 19, art.number:71. Available at: https://doi.org/10.1007/s10035-017-0756-z.

Yang, J. & Wei, L.M. 2014. Static Liquefaction of Granular Soils: The Role of Grain Shape and Size. In: Chau, KT. & Zhao, J. (Eds.) *Bifurcation and Degradation of Geomaterials in the New Millennium. IWBDG 2014. Springer Series in Geomechanics and Geoengineering,* pp.199-205. Cham: Springer. Available at: https://doi.org/10.1007/978-3-319-13506-9_29.

Youd, T.L. 1973. Factors Controlling Maximum and Minimum Densities of Sands. In: Selig, E.T. & Ladd, R.S. (Eds.) *Evaluation of Relative Density and its Role in Geotechnical Projects Involving Cohesionless Soils*, pp.98-112. ASTM International. Available at: https://doi.org/10.1520/STP37866S.

Efecto de la arena y el polvo de caliza triturados sobre el comportamiento mecánico de mezclas de arena de río: un estudio experimental

Ahmed Bilal Benyahia[a], *Ilyes* Irki[b], **autor de correspondencia**,
Ahmed Djafar Henni[a], *Mohammed* Ezziane[a], *Zine el abidine* Laidani[c]

[a] Universidad de Hassiba Ben Bouali, Laboratorio de Estructuras, Geotecnia y Riesgos (LSGR), Chlef, República Argelina Democrática y Popular

[b] Centro Universitario de Tipaza, Laboratorio de Materiales y Medio Ambiente (LME), Medea, República Argelina Democrática y Popular

[c] Universidad Blida1, Departamento de Ingeniería Civil, Blida, República Argelina Democrática y Popular

CAMPO: materiales
TIPO DE ARTÍCULO: artículo científico original

Resumen:

Introducción/objetivo: El presente estudio tiene como objetivo investigar el efecto de la arena caliza triturada (CLS) y el polvo de arena caliza triturada (LCSD) sobre el comportamiento físico y mecánico de la arena de río reconstituida (RS) utilizando el método de sustitución volumétrica.

Métodos: El estudio implicó la realización de pruebas de corte directo en dos series de sustitución para evaluar el efecto de la arena CLS con incrementos incrementales de 0, 10, 20, 30 y 40%, y del polvo LCSD que varía de 0 a 35% en pasos del 5% sobre el comportamiento mecánico de

la arena de río reconstituida. Todas las muestras se preparan con una densidad relativa del 50% y se prueban bajo tres tensiones normales diferentes de 100, 200 y 300 kPa, respectivamente.

Resultados: Los resultados muestran que la sustitución de arena de río por CLS hasta un 30% mejora sus propiedades mecánicas; la resistencia máxima al corte alcanzó un valor máximo del 29% bajo 200 kPa de tensión normal. La sustitución de arena de río por LSCD conduce a una disminución de las propiedades mecánicas. Sin embargo, un análisis más profundo de los resultados obtenidos revela una mejora en los parámetros residuales, con hasta un 15% de sustitución.

Conclusión: Tras un análisis riguroso de los resultados obtenidos, se determinó que la arena reconstituida a partir de una combinación de 30% de CLS y 15% de LCSD ofrece un rendimiento óptimo en términos de propiedades mecánicas mejoradas. Esta solución se alinea significativamente con la estrategia de desarrollo sostenible del gobierno argelino que promueve la mejora de las características y la preservación de los recursos naturales, al tiempo que cumple con los estrictos requisitos del sector geotécnico.

Palabras claves: arena de río, arena caliza triturada, polvo de arena caliza triturada, sustitución, resistencia al corte, desarrollo sostenible.

Влияние дробленого известнякового песка и пыли на физико-механические свойства речного песка: экспериментальное исследование

Ахмед Билал Беньяхиа[а], *Елис* Ирки[б], **корреспондент**,
Ахмед Джафар Хенни[а], *Мухаммед* Еззиан[а], *Зин Ел Абидин* Леидани[в]

[а] Университет Хассибы Бен Буали,
Лаборатория структур, геотехники и рисков (LSGR),
г. Шлеф, Алжирская Народная Демократическая Республика

[б] Университетский центр Типазы,
Лаборатория материалов и окружающей среды (LME),
г. Медеа, Алжирская Народная Демократическая Республика

[в] Университет Блида 1, факультет гражданского строительства,
г. Блида, Алжирская Народная Демократическая Республика

РУБРИКА ГРНТИ: 81.09.00 Материаловедение
ВИД СТАТЬИ: оригинальная научная статья

Резюме:

Введение/цель: Целью настоящего исследования является изучение влияния дробленого известнякового песка и известняковой пыли на физические и механические свойства восстановленного речного песка с использованием метода объемного замещения.

Методы: Исследование включало проведение испытаний на прямой сдвиг с использованием двух серий заменителей для оценки влияния дробленого известнякового песка с постепенным увеличением содержания на 0, 10, 20, 30 и 40% и известняковой пыли в диапазоне от 0 до 35% с шагом в 5% на механические свойства восстановленного речного песка. Все образцы были подготовлены с относительной плотностью 50% и испытаны под тремя различными нормальными напряжениями 100, 200 и 300 кПа.

Результаты: Результаты показывают, что замена речного песка на дробленый известняковый песок на 30% улучшает его механические свойства; максимальная прочность на сдвиг при этом достигла максимального значения в 29% при нормальном напряжении 200 кПа. В то время как замена речного песка на известняковую пыль приводит к снижению механических свойств. Однако более тщательный анализ полученных результатов показывает улучшение остаточных параметров, достигающее 15% при замене.

Вывод: После тщательного анализа полученных результатов установлено, что песок, восстановленный из комбинации 30% дробленого известнякового песка и 15% известняковой пыли, обладает оптимальными эксплуатационными характеристиками с точки зрения улучшенных механических свойств. Это решение в значительной степени соответствует стратегии устойчивого развития правительства Алжира, направленной на улучшение характеристик и сохранение природных ресурсов при одновременном соблюдении жестких требований геотехнического сектора.

Ключевые слова: речной песок, дробленый известняковый песок, известняковая дробленая песчаная пыль, замещение, прочность на сдвиг, устойчивое развитие.

Утицај издробљеног кречњачког песка и праха на механичко понашање мешавина речног песка: експериментална студија

Ахмед Билал Бенјахиа[а], *Елис* Ирки[б], **аутор за преписку**,
Ахмед Џафар Хени[а], *Мухамед* Езиан[а], *Зин Ел Абидин* Леидани[в]

[а] Универзитет „Хассиба Бен Боуали”,
Лабораторија за конструкције, геотехнику и ризике (ЛСГР),
Шлеф, Народна Демократска Република Алжир

[б] Универзитетски центар Типаза,
Лабораторија за материјале и животну средину (ЛМЕ),
Медеа, Народна Демократска Република Алжир

[в] Универзитет Блида 1, Грађевински одсек,
Блида, Народна Демократска Република Алжир

ОБЛАСТ: материјали
КАТЕГОРИЈА (ТИП) ЧЛАНКА: оригинални научни рад

Сажетак:

Увод/циљ: Циљ ове студије јесте да испита утицај издробљеног кречњачког песка (crushed limestone sand –CLS) и кречњачког праха (limestone crushed sand dust – LCSD) на физичко и механичко понашање реконституисаног речног песка помоћу методе волуметријске супституције.

Методе: У студији су изведени тестови директног смицања на две серије супституције како би се проценио ефекат песка CLS са повећањима у инкрементима од 0, 10, 20, 30, и 40%, као и ефекат праха LCSD од 0 до 35% у корацима од 5% на механичко понашање реконституисаног речног песка. Сви узорци су припремљени са 50% релативне густине и тестирани под три различита нормална напона, тј. под напонима од 100, 200 и 300 kPa.

Резултати: Резултати показују да замена речног песка издробљеним кречњачким песком повећава његова механичка својства до 30%. Чврстоћа смицања достигла је максималну вредност од 29% под нормалним напоном од 200 kPa. Замена речног песка прахом издробљеног кречњачког песка доводи до смањивања механичких својстава. Међутим, детаљнија анализа добијених резултата открива побољшање у резидуалним параметрима до 15% супституције.

Закључак: Након ригорозне анализе добијених резултата, утврђено је да песак реконституисан комбинацијом 30% издробљеног кречњачког песка и 15% кречњачког праха нуди оптималне перформансе када је реч о побољшаним механичким својствима. Ово решење у великој мери одговара одрживом развоју стратегије алжирске владе јер промовише побољшане карактеристике и очување природних ресурса, док у исто време испуњава строге захтеве геотехничког сектора.

Кључне речи: речни песак, издробљени кречњачки песак, прах издробљеног кречњачког песка, супституција, чврстоћа смицања, одрживи развој.

Paper received on: 20.01.2025.
Manuscript corrections submitted on: 26.03.2025.
Paper accepted for publishing on: 27.03.2025.

Analytical investigation of the interfacial behavior of a prestressed concrete beam strengthened with a prestressed FRP-bonded plate

Hanane Mebsout[a], *Mohamed Atif* Benatta[b], *Baghdad* Krour[c], *Oussama* Benachour[d], *Mohamed* Bachir Bouiadjra[e], *Nacer* Rahal[f]

[a] Mustapha Stambouli University, Mascara, People's Democratic Republic of Algeria, e-mail: mebsouthanane@gmail.com, ORCID iD: https://orcid.org/0009-0003-5837-4144

[b] University of Djillali Liabes, Structures and Advanced Materials in Civil Engineering and Public Works Laboratory (LSMAGCTP), Sidi Bel Abbes, People's Democratic Republic of Algeria, e-mail: bematif@gmail.com, ORCID iD: https://orcid.org/0009-0007-5854-9054

[c] University of Djillali Liabes, Structures and Advanced Materials in Civil Engineering and Public Works Laboratory (LSMAGCTP), Sidi Bel Abbes, People's Democratic Republic of Algeria, e-mail: baghdad.krour@univ-sba.dz, **corresponding author**, ORCID iD: https://orcid.org/0000-0002-8265-9807

[d] University of Djillali Liabes, Structures and Advanced Materials in Civil Engineering and Public Works Laboratory (LSMAGCTP), Sidi Bel Abbes, People's Democratic Republic of Algeria, e-mail: dr.oussama.benachour@gmail.com, ORCID iD: https://orcid.org/0009-0003-3792-7424

[e] University of Djillali Liabes, Structures and Advanced Materials in Civil Engineering and Public Works Laboratory (LSMAGCTP), Sidi Bel Abbes, People's Democratic Republic of Algeria + Thematic Agency for Research in Science and Technology, Algiers, People's Democratic Republic of Algeria, e-mail: mohamedbachirbouiadjra@gmail.com, ORCID iD: https://orcid.org/0009-0008-4814-6187

[f] Mustapha Stambouli University, Department of Civil Engineering, Mascara, People's Democratic Republic of Algeria + University of Sciences and Technology, Laboratory of Mechanical Structure and Construction Stability, Oran, People's Democratic Republic of Algeria, e-mail: n.rahal@univ-mascara.dz, ORCID iD: https://orcid.org/0009-0002-0400-8360

https://doi.org/10.5937/vojtehg73-54215

ACKNOWLEDGMENT: The authors acknowledge the financial support received from the Algerian Ministry of Higher Education and Scientific Research. A grateful acknowledgement is also addressed to the Thematic Agency for Research in Science and Technology (ATRST) of Algeria.

FIELD: civil engineering, materials
ARTICLE TYPE: original scientific paper

Abstract:

Introduction/purpose: Utilizing composite materials to reinforce reinforced concrete structures is now a very prevalent practice in the field of civil engineering. However, prestressed concrete construction does not usually use this method. The principal purpose of the present study is to extend the use of composite materials to reinforce prestressed concrete beams by taking into account the effect of interfacial stresses concentration on the global behavior of such structures.

Methods: A new analytical model is suggested taking into account how changes in the RC beam's prestress affect the interface stresses. A polynomial function expressing the variation of the geometrical shape of the cable as well as the instantaneous and non-instantaneous losses of the prestressed concrete beam is considered in order to address the issue of stress concentration at the adhesive-plate-concrete interface.

Results: The main findings of the present investigation demonstrate that, in the presence of cable prestress, the interface stresses decrease non-significantly; but, as the prestressing force applied to the FRP plate increases, a more substantial increase of interfacial stresses is observed.

Conclusion: Because of a high degree of contact stresses at the plate end the debonding risk becomes greater and an anchoring mechanism is recommended at the edge of the plate.

Key words: prestressed concrete beam, FRP composites, interfacial stresses, fibers orientations, strengthening.

Introduction

The necessity for public works and civil engineering infrastructures to be improved has grown significantly in recent years, to the point that heritage preservation is one of the requirements that must be fulfilled to ensure ecologically responsible, sustainable growth. One of the ways to increase the safety and durability of these structures is reinforcement using several methods. Thus, many theoretical and experimental scientific studies have been carried out to recommend the best solutions for reinforcing existing reinforced concrete structures. One of these solutions is the use of composite material plates such as carbon fiber reinforced polymer (CFRP) plates due to their high stiffness and light weight.

A review paper on the use of prestressed composite materials in the strengthening of reinforced concrete beams was published by (Aslam et al, 2015) illustrating the benefits and drawbacks of several strengthening procedures, including external reinforcement (EBR), surface

reinforcement (NSM), and externally post-tensioned techniques (EPT). Prestressed Near Surface Mounted Carbon Fiber Reinforced Polymer laminates (NSM-CFRP) were used in an experimental and numerical investigation by (Mostakhdemin Hosseini et al, 2016) to strengthen low resistance reinforced concrete slabs. The results indicate an intriguing improvement in the bearing capacity of slabs. The impact of a prestressed CFRP laminate on the fatigue performance of steel plates was investigated by (Emdad & Al-Mahaidi, 2015). It is shown in this experimental and numerical work that prestressed CFRP laminates dramatically reduce strain in steel plate specimens. A new experimental and numerical study on the bending behavior of reinforced concrete beams reinforced with prestressed CFRP laminates has been developed by Gao et al. (2016); this study's primary contribution is the application of a novel CFRP laminate prestressing method. An analytical method for a bending study of reinforced concrete beams reinforced by prestressed CFRP plates was proposed by (Rezazadeh et al, 2015). This method takes into account the maximum capacity of CFRP plate reinforced beams in cases when the first mode of delamination predominates. A moment-curvature connection is created based on three linear branches that correspond to the pre-cracking, post-cracking, and post-plastification stages. In a study given by (Bansal et al, 2016), the FRP laminates are swapped out for FRP sheets in an attempt to solve the issue of the debonding of laminates prior to fiber breakage.

A number of studies conducted by various experts indicate that the presence of shear and normal stresses at the plate–core interface is an important component. Researchers have devised numerous closed-form solutions for the interfacial stresses since they can, in fact, lead to brittle fracture of the concrete layer supporting the composite laminate and early collapse of the reinforced beam. The interfacial stresses are accurately estimated using Smith & Teng's solution (Smith & Teng, 2001); however, it ignores the fiber orientation of the FRP plate. To enhance the solution created by (Smith & Teng, 2001), further solutions have been put forth. (Tounsi et al, 2009) have suggested a novel method that ignores the orientation influence of fibers while also accounting for adherend shear deformations. A novel approach has been provided by (Tounsi & Benyoucef, 2007), which takes into account the fiber orientation of the FRP plate while keeping the flexural stiffness of composite plates in mind. A sensitivity analysis that takes into account various combinations of fiber orientations has been considered. An analytical analysis was conducted by (Krour et al, 2010, 2011) to provide a more precise solution for the interfacial stress problem by taking into account the mean curvature at the

interface between the RC beam and the FRP plate and adjusting fiber spacing according to its thickness. Following that, an analytical and numerical investigation was carried out by (Krour et al, 2013) to determine the optimal approach for determining bearing capacity and interfacial stresses.

To achieve the time-dependent impact, numerous research studies were conducted. For example, Mohamed et al. (2009) carried out a theoretical interfacial stress analysis for simply supported RC beams with thin FRP composite plates, taking into account the laminate theory, the interface slip effect on the structural performance, and the same assumptions as (Smith & Teng, 2001). The analysis included both the creep and shrinkage effects. Similarly to this, (Fahsi et al, 2011) carried out an analytical analysis for interfacial adhesive stresses, including creep, shrinkage, and thermal deformation, using the mean curvature assumption between the two addends. Both investigations were carried out using the Fib-international model (1990).

Recently, prestressed laminates have been applied to bridge girders and other types of constructions in the field, with both theoretical and empirical investigations conducted. The analyses produced closed-form formulas that could be used to determine peeling stress and interfacial shear in beams that had laminates or bonded, non-prestressed plates. (Al-Emrani & Kliger, 2006) have addressed the issue of interfacial stress in the context of prestressed laminates used for strengthening and repair. The examined beam was not loaded throughout this experiment; only interfacial shear stress was examined. These investigations were all conducted on steel or reinforced concrete beams that were strengthened with CFRP plates, either prestressed or not. Using the laminate theory and altering the fiber orientation, (Benachour et al, 2008) conducted an analytical analysis of the interface steel beam reinforced by a prestressed CFRP plate.

Due to the significance of prestressed concrete, many studies have concentrated on the estimation of time-dependent losses. Indeed, (Páez & Sensale-Cozzano, 2021) proposed a theoretical analysis of simply supported and continuous unbonded prestressed concrete beams, taking into account concrete creep and shrinkage as well as pre-stressing steel relaxation. In order to ascertain the prestress loss and time-dependent deflection in cracked prestressed concrete elements, prestressed with fiber reinforced polymers or steel tendons, (Páez, 2023) carried out a novel, simplified method based on the creep-transformed section method. Artificial Intelligence has been applied to civil engineering challenges as a new contribution. Indeed, (Zhang et al, 2023) predicted the long-term

prestress loss for prestressed concrete cylinder structures using machine learning. Using a numerical model calibrated against experimental data, (Lou & Karavasilis, 2018) gave an evaluation of the time-dependent behavior and the prediction of the long-term deflection of concrete beams prestressed with internal unbonded carbon fiber reinforced polymer (CFRP) tendons.

Because composite material plates are an effective way to reinforce steel or reinforced concrete structures, researchers are now concentrating their efforts on employing this technique to prestressed concrete, which is commonly used in civil engineering. An analytical study by (Mebsout et al, 2017) amply demonstrated the benefits of using prestressed FRP plates to enhance the behavior of prestressed concrete section beams. The study showed that it is possible to remove tensile stress by applying a prestressed CFRP plate transforming the cross-sectional area from Class II to Class I according to Eurocode 2 (Le Delliou, 2003).

This paper focuses on an analytical analysis of prestressed composite FRP plates used in conjunction with prestressed concrete beams for reinforcement. Based on the model developed by (Smith & Teng, 2001), the study consists of the analysis of normal and shear interfacial stresses for a prestressed concrete beam strengthened by a prestressed FRP composite plate, where (Smith & Teng, 2001) deal with RC beams reinforced with FRP plates. The beam is simply supported, and three load cases are considered. As a new contribution, the proposed model considers the immediate and time-dependent losses of the prestressed concrete beam in addition to the geometrical shape of the cable. This leads to a random fluctuation in the prestress losses along the span beam. However, this variation of the prestress can be approximated by a simple polynomial function necessary to facilitate the integration of the governing equations of interfacial stresses.

Interfacial shear and normal stresses governing equation

Previous research has shown that high stress concentration at the interface between the composite plate and concrete may compromise this type of reinforcement and cause the debonding of the composite plate. To estimate these contact stresses, an analytical model based on strain compatibility is developed in this section. Let us consider a simply supported prestressed beam represented in Figure 1 and Figure 2.

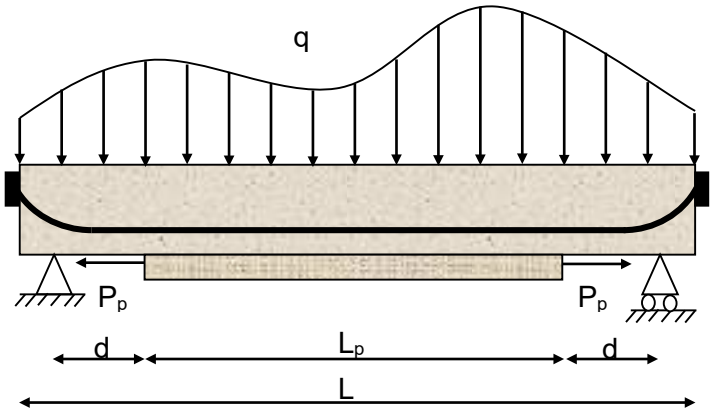

Figure 1 – Simply supported prestressed concrete beam strengthened with a bonded FRP plate

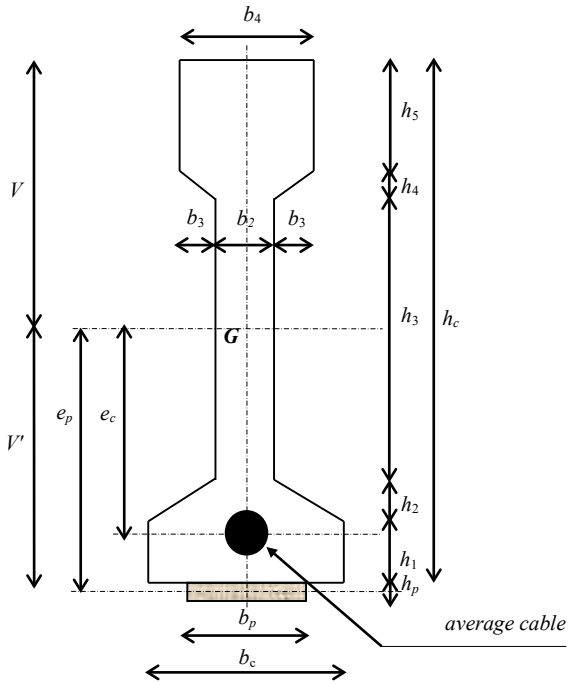

Figure 2 – Shape of the cross section

Figure 3 displays a differential segment, or dx, of the plated beam, with all forces and stresses indicated by their corresponding signs.

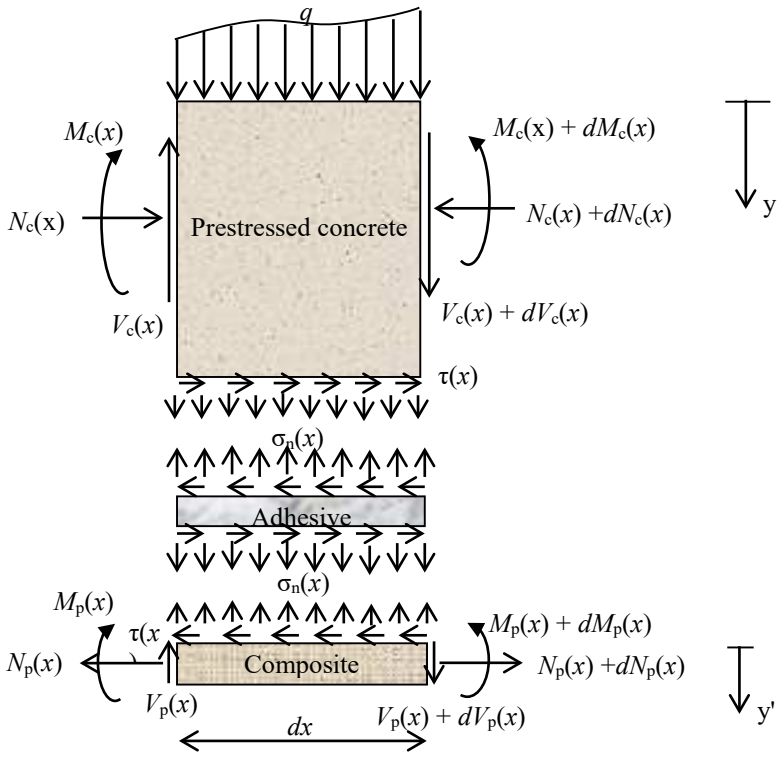

Figure 3 – Forces in the infinitesimal element of a soffit-plated beam

The interfacial shear and the normal stresses are represented by the symbols $\tau(x)$ and $\sigma(x)$, respectively.

The assumptions listed below are made:

1. The concrete, adhesive, and FRP materials behave elastically and linearly.

2. No slip is allowed at the interface of the bond (i.e., there is a perfect bond at the adhesive–concrete interface and at the adhesive–plate interface).

3. Stresses in the adhesive layer do not change with the thickness.

4. Deformations of adherends 1 and 2 are due to bending moments and axial forces.

5. Since the shear and normal stress equations can be uncoupled by assuming identical curvatures in the beam and the plate, the shear stress analysis makes this assumption due to a high stiffness of the concrete beam. Nevertheless, the peel stress solution does not make this assumption. Many authors, including (Smith & Teng, 2001), make advantage of this assumption.

The shear strain in the adhesive layer is expressed as:

$$\gamma_{xy} = \frac{\partial u(x,y)}{\partial y} + \frac{\partial w(x,y)}{\partial x} \approx \frac{u_p(x) - u_c(x)}{h_a}, \tag{1}$$

Consequently, the shear stress in the adhesive layer is given by:

$$\tau(x) = G_a \left[\frac{u_p(x) - u_c(x)}{h_a} \right], \tag{2}$$

where, G_a, t_a, u_p, and u_c indicate, in that order, the shear modulus, the thickness of the adhesive layer, the horizontal displacement at the top of the externally bonded FRP plate, and the horizontal displacement at the bottom of the concrete beam. The formula for shear stress in terms of the mechanical strain of the FRP plate $\varepsilon_p(x)$ and the concrete $\varepsilon_c(x)$ is obtained by differentiating Eq. (2) with regard to x.

$$\frac{d\tau(x)}{dx} = G_a \left[\frac{\varepsilon_p(x) - \varepsilon_c(x)}{h_a} \right], \tag{3}$$

The strain at the bottom of the prestressed concrete beam is given by:

$$\varepsilon_c(x) = \frac{du_c(x)}{dx} = \frac{y_c}{E_c I_c} M_c(x) - \frac{1}{E_c A_c} N_c(x), \tag{4}$$

where:

E_c is the elastic modulus, M_c is the bending moment, N_c is the axial force and y_c is the distance from the bottom of the concrete beam to its centroid.

The bending moment $M_c(x)$ results from the external loading and the prestress force applied with eccentricity from the centroid of the prestressed concrete beam. Then the bending moment $M_c(x)$ may be written as follows:

$$M_c(x) = M_q(x) + M_{pc}(x), \tag{5}$$

where:

$M_{pc}(x)$ is the bending moment due to the prestress force which can be written as follows:

$$M_{pc}(x) = P_c(x,\infty) \times e_c(x), \tag{6}$$

The present investigation employs the laminate theory (Herakovich, 1997) to underscore the impact of fiber orientation on the behavior of the externally bonded composite plate. Applying this theory to a symmetrical composite plate yields the following values for the composite plate curvature k_x and the mid-plane strain ε_x^0:

$$\begin{cases} \varepsilon_x^0 = A'_{11} N_x \dfrac{1}{b_2}, \\ k_x = D'_{11} M_x \dfrac{1}{b_2}, \end{cases} \tag{7}$$

where:

$[A'] = [A]^{-1}$ is the inverse of the extensional matrix $[A]$; $[D'] = [D]^{-1}$ is the inverse of the flexural matrix $[D]$; and b_2 is the width of the FRP plate.

The terms of the matrices $[A]$ and $[D]$ are written as:

$$\begin{cases} A_{mn} = \sum_{j=1}^{N} \bar{Q}_{mn}(h_j - h_{j-1}), \\ D_{mn} = \sum_{j=1}^{N} \bar{Q}_{mn}(h_j^3 - h_{j-1}^3), \end{cases} \tag{8}$$

where

$$\begin{cases} \overline{Q}_{11} = \left[\dfrac{E_{11}}{1-\nu_{12}\nu_{21}}\right]\cos^4(\theta_j) + \left[\dfrac{E_{22}}{1-\nu_{12}\nu_{21}}\right]\sin^4(\theta_j) \\ +2\left[\dfrac{\nu_{12}E_{22}}{1-\nu_{12}\nu_{21}} + 2G_{12}\right]\cos^2(\theta_j)\sin^2(\theta_j), \\ \overline{Q}_{22} = \left[\dfrac{E_{11}}{1-\nu_{12}\nu_{21}}\right]\sin^4(\theta_j) + \left[\dfrac{E_{22}}{1-\nu_{12}\nu_{21}}\right]\cos^4(\theta_j) \\ +2\left[\dfrac{\nu_{12}E_{22}}{1-\nu_{12}\nu_{21}} + 2G_{12}\right]\cos^2(\theta_j)\sin^2(\theta_j), \\ \overline{Q}_{12} = \dfrac{\nu_{12}E_{22}}{1-\nu_{12}\nu_{21}}\left[\cos^4(\theta_j) + \sin^4(\theta_j)\right] \\ +\left[\dfrac{E_{11}}{1-\nu_{12}\nu_{21}} + \dfrac{E_{22}}{1-\nu_{12}\nu_{21}} - 4G_{12}\right]\cos^2(\theta_j)\sin^2(\theta_j), \\ \overline{Q}_{33} = G_{12}, \end{cases} \tag{9}$$

where j is the number of the layer; h; $\left[\overline{Q}\right]$ and θ_j are respectively the thickness, the Hooke's elastic tensor and the fibers orientation of each layer.

Using the classical laminate theory (Herakovich, 1997), the strain at the top of CFRP plate is given by:

$$\varepsilon_p(x) = \frac{du_p(x)}{dx} = \varepsilon_x^0 - \frac{h_p}{2}k_x, \tag{10}$$

Substituting Eq. (7) in (10) gives the following equation:

$$\varepsilon_p(x) = A'_{11}\frac{N_p(x)}{b_p} - D'_{11}\frac{h_p}{2b_p}M_p(x), \tag{11}$$

The horizontal forces equilibrium gives:

$$\frac{dN_c(x)}{dx} = \frac{dN_p(x)}{dx} = b_p\tau(x), \tag{12}$$

And then:

$$N_c(x) = N_p(x) = b_p\int_0^x \tau(x)dx, \tag{13}$$

From the second assumption below (perfect bond), we obtain:

$$\frac{d^2w_p(x)}{dx^2} = \frac{d^2w_c(x)}{dx^2}, \tag{14}$$

The relationship between the moments in the two adherends can be written as follows:

$$M_c(x) = \Psi M_p(x), \tag{15}$$

with:

$$\Psi = -\frac{E_c I_c D'_{11}}{b_p}, \tag{16}$$

The moment equilibrium gives:

$$M_T(x) = M_c(x) + M_p(x) + N(x)\left[y_c + h_a + \frac{h_p}{2}\right], \tag{17}$$

where, $M_T(x)$ is the total applied moment.

In the case of the prestressed concrete beam, the bending moment is given by:

$$M_c(x) = M_q(x) + M_{Pc}(x) + M_{Pp}(x), \tag{18}$$

$$M_c(x) = M_q(x) + P_c(x,\infty) \times e_c(x) + P_p\left(y_c + h_a + \frac{h_p}{2}\right), \tag{19}$$

As a function of the total applied moment and the interfacial shear stress, the bending moments in each adherend are expressed as follows:

$$M_c(x) = -\frac{\Psi}{\Psi+1}\left[b_p \int_0^x \tau(x)(y_c + \frac{h_p}{2} + h_a)dx\right] + \frac{\Psi}{\Psi+1} M_T(x), \tag{20}$$

and

$$M_p(x) = -\frac{1}{\Psi+1}\left[b_p \int_0^x \tau(x)(y_c + \frac{h_p}{2} + h_a)dx\right] + \frac{1}{\Psi+1} M_T(x), \tag{21}$$

The first derivative of the bending moment in each adherend gives:

$$\frac{dM_c(x)}{dx} = \frac{\Psi}{\Psi+1}\left[V_T(x) - b_p\tau(x)(y_c + \frac{h_p}{2} + h_a)\right] \tag{22}$$

$$\frac{dM_p(x)}{dx} = \frac{1}{\Psi+1}\left[V_T(x) - b_p\tau(x)(y_c + \frac{h_p}{2} + h_a)\right], \tag{23}$$

Substituting Eqs. (4) and (11) into Eq. (3) and differentiating the resulting equation once yields:

$$\begin{aligned}\frac{d^2\tau(x)}{dx^2} &= \frac{G_a}{h_a}\left(\frac{A'_{11}}{b_p}\frac{dN_p(x)}{dx} - D'_{11}\frac{h_p}{2b_p}\frac{dM_p(x)}{dx}\right) \\ &+ \frac{G_a}{h_a}\left(\frac{1}{E_cA_c}\frac{dN_c(x)}{dx} - \frac{y_c}{E_cI_c}\frac{dM_c(x)}{dx}\right),\end{aligned} \tag{24}$$

Substituting Eqs. (22), (23) and Eq. (12) into Eq. (24) gives the following governing differential equation for the interfacial shear stress:

$$\frac{d^2\tau(x)}{dx^2}+\frac{G_a}{t_a}\left(\frac{\left(y_c+\frac{h_p}{2}\right)}{E_cI_cD'_{11}+b_p}D'_{11}\right)V_T(x)-\frac{G_a}{t_a}A'_{11}$$
$$-\frac{G_a}{t_a}\left(\frac{b_p}{E_cA_c}+\frac{\left(y_c+\frac{h_p}{2}\right)\left(y_c+h_a+\frac{h_p}{2}\right)}{E_cI_cD'_{11}+b_p}b_2D'_{11}\right)\tau(x)=0, \quad (25)$$

$$V_T(x)=\frac{dM_T(x)}{dx}=\frac{dM_q(x)}{dx}+\frac{dM_{cp}(x)}{dx}+\frac{dM_{Pp}(x)}{dx}, \quad (26)$$

Due to the losses of the prestressing force and the variable eccentricity of the mean cable along the beam span, the induced bending moment may be approximated by a polynomial function of the forth degree.

$$M_{cp}(x)=P_1x^4+P_2x^3+P_3x^2+P_4x+P_5, \quad (27)$$

Then the shear effort induced by this moment is written as follows:

$$V_{cp}(x)=\frac{dM_{cp}(x)}{dx}=4P_1x^3+3P_2x^2+2P_3x+P_4, \quad (28)$$

The coefficients P_i are determined by fitting the fluctuation of immediate and time-dependent losses and are specific to each case.

The general solutions presented below are limited to loading which is either concentrated or uniformly distributed, or both. For such loading $d^2V_q(x)/dx^2=0$, and the general solution to Eq. (26) is given by:

$$\tau(x)=C_1\cosh(\alpha x)+C_2\sinh(\alpha x)+\beta V_c(x)+\frac{\beta}{\alpha^2}\frac{d^2V_c(x)}{dx^2}, \quad (29)$$

where:

$$\begin{cases} \alpha^2 = \dfrac{G_a}{h_a}\left(A'_{11} + \dfrac{b_p}{E_c A_c} + \dfrac{\left(y_c + \dfrac{h_p}{2}\right)\left(y_c + h_a + \dfrac{h_p}{2}\right)}{E_c I_c D'_{11} + b_p} b_p D'_{11} \right), \\ \beta = \dfrac{G_a}{h_a}\left(\dfrac{\left(y_c + \dfrac{h_p}{2}\right)}{E_c I_c D'_{11} + b_p} D'_{11} \right) \end{cases} \tag{30}$$

$$\begin{cases} V_c(x) = V_q(x) + V_{cp}(x) + V_{P_0}(x) \\ \dfrac{d^2 V_c(x)}{dx^2} = \dfrac{d^2 V_{cp}(x)}{dx^2} = 24P_1 x + 6P_2 \end{cases}, \tag{31}$$

C_1 and C_2 are constant coefficients determined from the boundary conditions.

Adhesive normal stress: governing differential equations

The strain in the adhesive layer is given by:

$$\varepsilon_y = \frac{\partial w(x,y)}{\partial y} \approx \frac{w_p(x) - w_c(x)}{h_a}, \tag{32}$$

where $w_c(x)$ and $w_p(x)$ are the vertical displacements of the prestressed concrete beam and the CFRP plate, respectively.

The normal stress in the adhesive layer is expressed as follows:

$$\sigma_n(x) = \frac{E_a}{h_a}\left[w_p(x) - w_c(x) \right], \tag{33}$$

Differentiating Eq. (33) two times gives:

$$\frac{d^2\sigma_n(x)}{dx^2} = \frac{E_a}{h_a}\left[\frac{d^2w_p(x)}{dx^2} - \frac{d^2w_c(x)}{dx^2}\right], \tag{34}$$

The moment-curvature relationship for the two adherends is expressed as follows:

$$\begin{cases} \dfrac{d^2w_c(x)}{dx^2} = -\dfrac{M_c(x)}{E_cI_c} \\ \dfrac{d^2w_p(x)}{dx^2} = -\dfrac{D'_{11}M_p(x)}{b_p} \end{cases}, \tag{35}$$

The moment equilibrium of the prestressed concrete beam and the CFRP plate gives:

The prestressed concrete beam:

$$\begin{cases} \dfrac{dM_c(x)}{dx} = V_c(x) - b_p y_c \tau(x) \\ \dfrac{dV_c(x)}{dx} = -b_p\sigma_n(x) - q \end{cases}, \tag{36}$$

The CFRP plate:

$$\begin{cases} \dfrac{dM_p(x)}{dx} = V_p(x) - b_p\dfrac{t_p}{2}\tau(x) \\ \dfrac{dV_p(x)}{dx} = b_p\sigma_n(x) \end{cases}, \tag{37}$$

Using the above equilibrium equations, the governing differential equations for the deflection of each adherend are given by:

The prestressed concrete beam:

$$\frac{d^4w_c(x)}{dx^4} = \frac{1}{E_cI_c}b_p\sigma_n(x) + \frac{y_c}{E_cI_c}b_p\frac{d\tau(x)}{dx} + \frac{q}{E_cI_c}, \tag{38}$$

The CFRP plate:

$$\frac{d^4 w_p(x)}{dx^4} = -D'_{11}\sigma_n(x) + D'_{11}\frac{h_p}{2}\frac{d\tau(x)}{dx}, \tag{39}$$

Substituting both Eqs. (38) and (23) as well as Eq. (39) into the fourth derivation of the interfacial normal stress obtained from Eq. (33) gives the following governing differential equation for the interfacial normal stress:

$$\begin{aligned}&\frac{d^4\sigma_n(x)}{dx^4} + \frac{E_a}{h_a}\left(D'_{11} + \frac{b_p}{E_c I_c}\right)\sigma_n(x)\\ &-\frac{E_a}{h_a}\left(D'_{11}\frac{h_p}{2} - \frac{y_c b_p}{E_c I_c}\right)\frac{d\tau(x)}{dx} + \frac{qE_a}{E_c I_c} = 0,\end{aligned} \tag{40}$$

The general solution of Eq. (40) which is a fourth-order differential equation is:

$$\begin{aligned}&\sigma(x) = e^{-\gamma x}\left[C_3\cos(\gamma x) + C_4\sin(\gamma x)\right] + e^{\gamma x}\left[C_5\cos(\gamma x) + C_6\sin(\gamma x)\right]\\ &-\eta_1\frac{d\tau(x)}{dx} - \eta_2 q,\end{aligned} \tag{41}$$

For large values of x, the normal interfacial stress is assumed to be zero, and so $C_5 = C_6 = 0$.

The general equation becomes:

$$\sigma_n(x) = e^{-\gamma x}\left[C_3\cos(\gamma x) + C_4\sin(\gamma x)\right] - \eta_1\frac{d\tau(x)}{dx} - \eta_2 q, \tag{42}$$

where:

$$\begin{cases} \gamma = \sqrt[4]{\dfrac{E_a}{4h_a}\left(D'_{11} + \dfrac{b_p}{E_c I_c}\right)} \\ \eta_1 = \dfrac{y_c b_p - E_c I_c D'_{11}\left(\dfrac{h_p}{2}\right)}{E_c I_c D'_{11} + b_p}, \\ \eta_2 = \dfrac{1}{E_c I_c D'_{11} + b_p} \end{cases} \quad (43)$$

The constant coefficients C_3 and C_4 are determined by the boundary conditions.

Application of the boundary conditions and closed-form solutions

The following boundary conditions are thus considered:

$$\begin{cases} N_c(0) = P(d,t) \\ N_p(0) = P_p \\ M_p(0) = 0 \\ \tau\left(L_p/2\right) = 0 \end{cases}, \quad (44)$$

These boundary conditions give the interfacial shear stress described by (Smith & Teng, 2001) and written as:

Uniformly distributed load

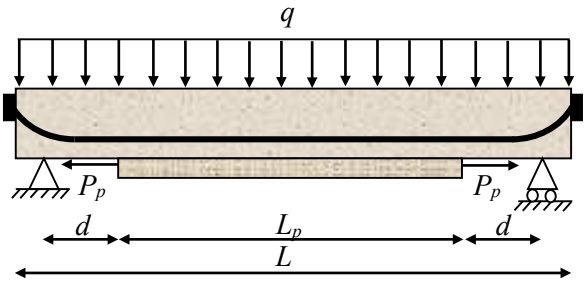

Figure 9 – Uniformly distributed load

$$\begin{cases} C_2 = \dfrac{G_a}{\alpha t_a}\left(\dfrac{A'_{11}}{b_p}P_p + \dfrac{1}{E_c A_c}P(d) - \dfrac{y_c}{E_c I_c}M_c(d)\right) - \dfrac{\beta}{\alpha}\dfrac{dV_c(d)}{dx} - \dfrac{\beta}{\alpha^3}\dfrac{d^3V_c(d)}{dx^2} \\ M_c(d) = \left(L-d\right)\dfrac{qd}{2} + P_p\left((y_c + h_a + \dfrac{h_p}{2}\right) + P_1 d^4 + P_2 d^3 + P_3 d^2 + P_4 d + P_5 \\ \dfrac{dV_c(d)}{dx} = \dfrac{dV_{cp}(d)}{dx^2} = 12P_1 d^2 + 6P_2 d + 2P_3 \\ \dfrac{d^3V_c(d)}{dx^2} = \dfrac{d^3V_{cp}(d)}{dx^2} = 24P_1 \\ C_1 = -C_2 \end{cases}, \quad (45)$$

Single point load

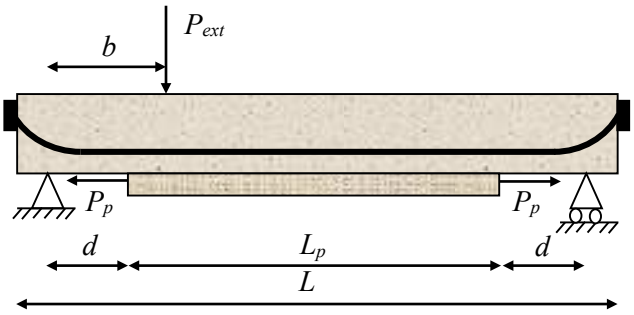

Figure 10 – Single point load

For such a loading type, two cases are possible: the first considers that the left edge of the plate is located to the left of the load application point $d < b$, and the second considers that the left edge of the plate is placed to the right of the load application point $d > b$.

Based on the general solution of Equation (45), applying the same boundary conditions as for the uniformly distributed load, and taking into account the continuity of the interface tangential stress and its first derivative at the application load point, we obtain:

For $d < b$:

$$\begin{cases} C_2 = \dfrac{G_a}{\alpha t_a}\left(\dfrac{A'_{11}}{b_p}P_p + \dfrac{1}{E_c A_c}P(d) - \dfrac{y_c}{E_c I_c}M_c(d)\right) - \dfrac{\beta}{\alpha}\dfrac{dV_c(d)}{dx} - \dfrac{\beta}{\alpha^3}\dfrac{d^3V_c(d)}{dx^2} \\ M_c(d) = P_{ext}d\left(1-\dfrac{b}{L}\right) + P_1 d^4 + P_2 d^3 + P_3 d^2 + P_4 d + P_5 \\ \dfrac{dV_c(d)}{dx} = \dfrac{dV_{cp}(d)}{dx^2} = 12P_1 d^2 + 6P_2 d + 2P_3 \\ \dfrac{d^3V_c(d)}{dx^2} = \dfrac{d^3V_{cp}(d)}{dx^2} = 24P_1 \\ C_1 = -C_2 \end{cases}, \quad (46)$$

For $d > b$:

$$\begin{cases} C_2 = \dfrac{G_a}{\alpha t_a}\left(\dfrac{A'_{11}}{b_p}P_p + \dfrac{1}{E_c A_c}P(d) - \dfrac{y_c}{E_c I_c}M_c(d)\right) - \dfrac{\beta}{\alpha}\dfrac{dV_c(d)}{dx} - \dfrac{\beta}{\alpha^3}\dfrac{d^3V_c(d)}{dx^2} \\ M_c(d) = P_{ext}d\left(1-\dfrac{b}{L}\right) + P_p\left((y_c + h_a + \dfrac{h_p}{2}\right) \\ + P_1 d^4 + P_2 d^3 + P_3 d^2 + P_4 d + P_5 \\ \dfrac{dV_c(d)}{dx} = \dfrac{dV_{cp}(d)}{dx^2} = 12P_1 d^2 + 6P_2 d + 2P_3 \\ \dfrac{d^3V_c(d)}{dx^2} = \dfrac{d^3V_{cp}(d)}{dx^2} = 24P_1 \\ C_1 = -C_2 \end{cases}, \quad (47)$$

Two symmetrical point loads

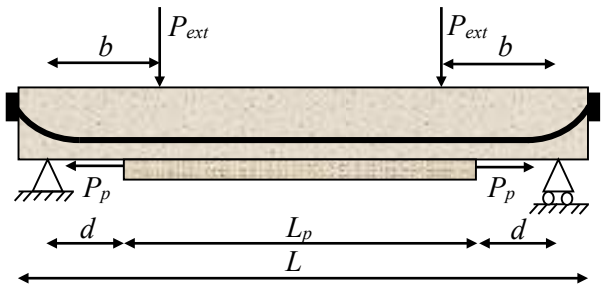

Figure 11 – Two symmetrical point loads

In the same way as for a single concentrated load, it is possible to obtain the expression of the tangential interface stress for two concentrated loads, taking into account the symmetry. The expression of the tangential stress is given by:

$d < b$:

$$\begin{cases} C_2 = \dfrac{G_a}{\alpha t_a}\left(\dfrac{A'_{11}}{b_p}P_p + \dfrac{1}{E_c A_c}P(d) - \dfrac{y_c}{E_c I_c}M_c(d)\right) - \dfrac{\beta}{\alpha}\dfrac{dV_c(d)}{dx} - \dfrac{\beta}{\alpha^3}\dfrac{d^3V_c(d)}{dx^2} \\ M_c(d) = P_{ext}d + P_1 d^4 + P_2 d^3 + P_3 d^2 + P_4 d + P_5 \\ \dfrac{dV_c(d)}{dx} = \dfrac{dV_{cp}(d)}{dx^2} = 12P_1 d^2 + 6P_2 d + 2P_3 \\ \dfrac{d^3V_c(d)}{dx^2} = \dfrac{d^3V_{cp}(d)}{dx^2} = 24P_1 \\ C_1 = -C_2 \end{cases}, \quad (48)$$

$d > b$:

$$\begin{cases} C_2 = \dfrac{G_a}{\alpha t_a}\left(\dfrac{A'_{11}}{b_p}P_p + \dfrac{1}{E_c A_c}P(d) - \dfrac{y_c}{E_c I_c}M_c(d)\right) - \dfrac{\beta}{\alpha}\dfrac{dV_c(d)}{dx} - \dfrac{\beta}{\alpha^3}\dfrac{d^3V_c(d)}{dx^2} \\ M_c(d) = P_{ext}d + P_p\left((y_c + h_a + \dfrac{h_p}{2}\right) \\ +P_1 d^4 + P_2 d^3 + P_3 d^2 + P_4 d + P_5 \\ \dfrac{dV_c(d)}{dx} = \dfrac{dV_{cp}(d)}{dx^2} = 12P_1 d^2 + 6P_2 d + 2P_3 \\ \dfrac{d^3V_c(d)}{dx^2} = \dfrac{d^3V_{cp}(d)}{dx^2} = 24P_1 \\ C_1 = -C_2 \end{cases}, \quad (49)$$

The constant coefficients C_3 and C_4 for the normal interfacial stress are given by:

$$\begin{cases} C_3 = \dfrac{E_a}{2\gamma^3 t_a E_c I_c}\left[V_T(0) + \gamma M_T(0)\right] - \dfrac{\eta_3}{2\gamma^3}\tau(0) + \dfrac{\eta_1}{2\gamma^3}\left(\dfrac{d^4\tau(0)}{dx^4} + \gamma\dfrac{d^3\tau(0)}{dx^3}\right) \\ C_4 = \dfrac{E_a}{2\gamma^2 t_a E_c I_c}M_T(0) - \dfrac{\eta_1}{2\gamma^2}\dfrac{d^3\tau(0)}{dx^3} \\ \eta_3 = \dfrac{E_a b_2}{t_a}\left(\dfrac{y_c}{E_c A_c} - \dfrac{D'_{11}t_2}{2b_2}\right) \end{cases}, \quad (50)$$

The aforementioned constant expressions C_3 and C_4 have been left in terms of the bending moment $M_T(0)$ and the shear force $V_T(0)$ at the end of the soffit plate. With the constants C_3 and C_4 calculated, Eq. (42) may be used to calculate the adhesive normal stress for all three load scenarios.

Results and discussions

As part of the present work on strengthening existing prestressed concrete beams using composite materials, a demonstration study on a prestressed bridge girder is conducted to examine potential practical

problems that could occur from applying strengthening technologies to already-existing structures. The main goal is to demonstrate the existence of a high level of interfacial stresses leading to early debonding failure of laminates especially at their ends.

Additionally, it was noted that there is a knowledge gap regarding the best way to choose the adhesives and material properties for prestressed composite materials to minimize the amount of shear and normal stresses at the laminate ends without compromising the effectiveness of the strengthening technique.

For these reasons, a real case is examined. A simply supported bridge girder having a free span of 26 meters, is considered. The data used in this study are summarized in Table 1 and Figure 12. The laminate is kept at a constant width of 200 mm and a constant length of 24.6 m, with 0.7 m remaining between the end of the laminate and each support. The maximum shear and normal stress values in the bonding region depend on a number of factors. The prestressing force and the fiber orientation in various laminate layers are two most crucial factors for retrofitting beams.

Table 1 – Geometric characteristics of the cross section

h_c (mm)	h_1 (mm)	h_2 (mm)	h_3(mm)	h_4(mm)	h_5 (mm)	h_p (mm)	e_c (mm)
1300	270	150	700	100	80	1.2	476
b_c(mm)	b_2 (mm)	b_3 (mm)	b_4 (mm)	b_p (mm)	V (mm)	V' (mm)	e_p (mm)
500	150	100	350	200	674	626	627.1

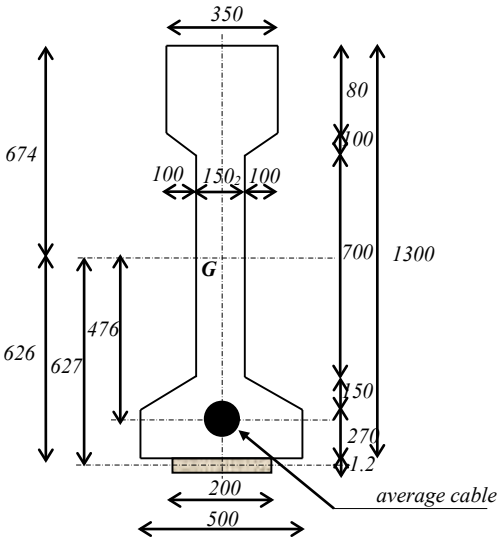

Figure 12 – Cross section sketch

Adhesive stresses with respect to the prestressing force P_p

Three example problems are taken into consideration. The first problem involves a beam that is simply supported and subjected to a uniformly distributed load (UDL), while the second problem involves a single point load and the third problem involves two symmetric point loads.

The UDL is taken to be equal to 100kN/m, the single point load is 500kN and the two symmetric point loads are P_{ext}=250kN and P_{ext}=250kN. Four values of P_p are considered in this study (0, 50, 100 and 150kN). For all the three problems, a unidirectional composite plate is used and the instantaneous elastic modulus of concrete is considered.

By way of comparison, we considered the work of (Benachour et al, 2008), which deals with the problem of interface stresses for a reinforced concrete beam. This will allow us to distinguish the effect of a prestressing cable on interface stresses.

Shear and normal interfacial stresses for UDL

The variation of normal stress and interfacial shear for the prestressed concrete beam reinforced with a bonded prestressed FRP plate along its span for the UDL scenario is shown in Figs. 13 and 14. The numerical values at the plate end are summarized in Table 2.

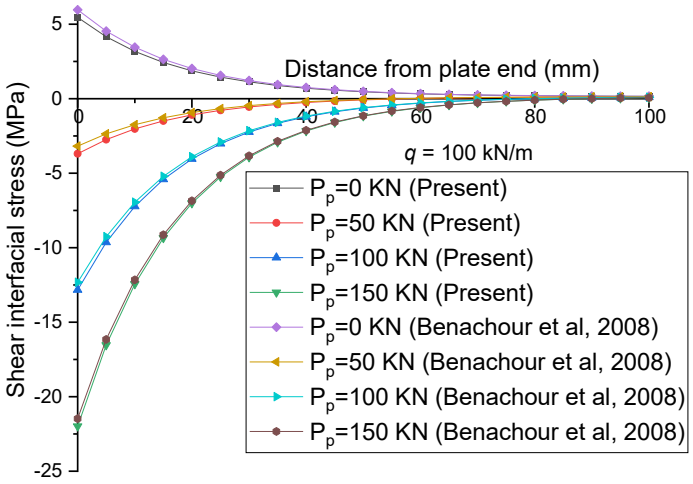

Figure 13 – Adhesive shear stress at the bond line for the FRP-strengthened beam under various prestressing forces Pp (the beam is under UDL)

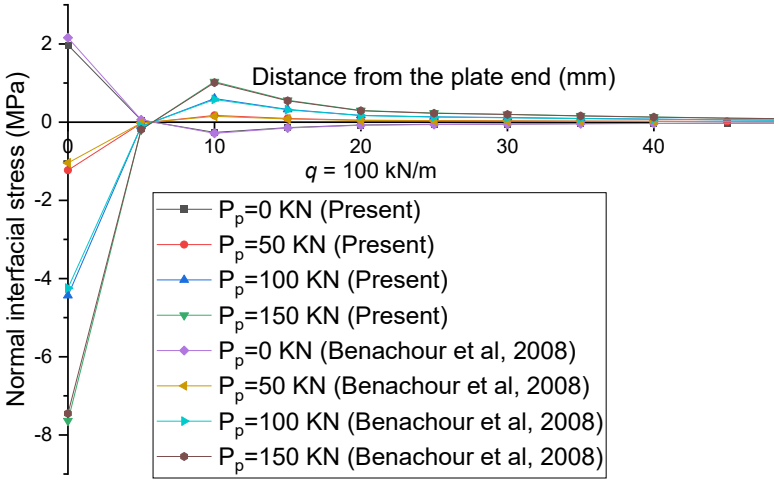

Figure 14 – Adhesive normal stress at the bond line for the FRP-strengthened beam under various prestressing forces Pp (the beam is under UDL)

Table 2 – Shear and normal interfacial stress at the plate end under UDL

Pp (KN)	$\tau(0)$ (Mpa)		$\sigma(0)$ (Mpa)	
	Concrete beam	*Prestressed concrete beam*	*Concrete beam*	*Prestressed concrete beam*
0	*5.965*	*5.456*	*2.158*	*1.971*
50	*-3.180*	*-3.689*	*-1.044*	*-1.231*
100	*-12.326*	*-12.835*	*-4.247*	*-4.435*
150	*-21.472*	*-21.981*	*-7.450*	*-7.638*

Shear and normal interfacial stresses for a single point load

The fluctuation of normal stress and interfacial shear for the prestressed concrete beam reinforced with a bonded prestressed FRP plate along its span for a single point load is depicted in Figs. 15 and 16. The edge values are reported in Table 5.

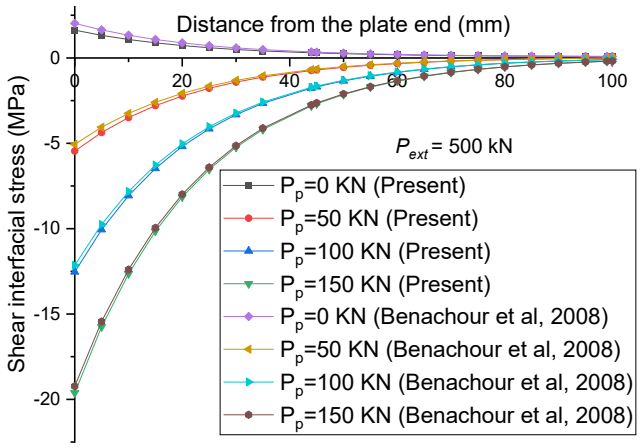

Figure 15 – Adhesive shear stress at the bond line for the FRP-strengthened beam under various prestressing forces Pp (the beam is under a single point load)

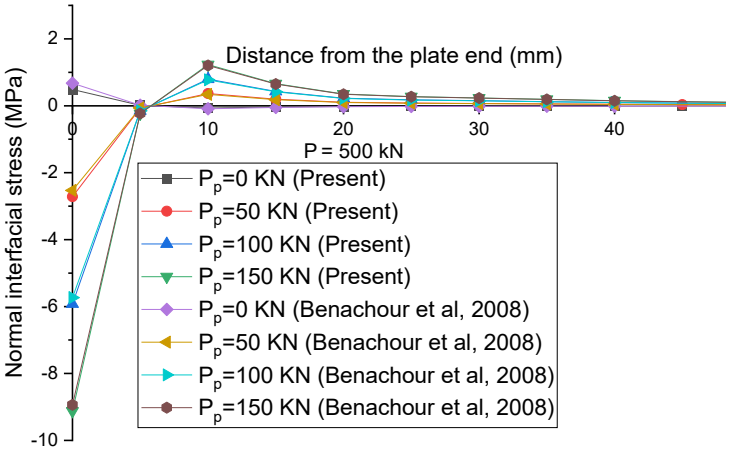

Figure 16 – Adhesive normal stress at the bond line for the FRP-strengthened beam under various prestressing forces Pp (the beam is under a single point load)

Table 3 – Shear and normal interfacial stress at the plate end under a single point load

Pp (KN)	$\tau(0)$ (Mpa)		$\sigma(0)$ (Mpa)	
	Concrete beam	*Prestressed concrete beam*	*Concrete beam*	*Prestressed concrete beam*
0	*2.024*	*1.630*	*0.674*	*0.486*
50	*-5.059*	*-5.453*	*-2.528*	*-2.716*
100	*-12.143*	*-12.538*	*-5.732*	*-5.919*
150	*-12.143*	*-19.622*	*-8.935*	*-9.122*

Shear and normal interfacial stresses for a two symmetric point load

The prestressed concrete beam reinforced with a bonded prestressed FRP plate exhibits variations in interfacial shear and normal stress along its span for a two point load, as shown in Figs. 17 and 18. The effect of the presstressing effort on the maximum interfacial stresses is shown in Table 6.

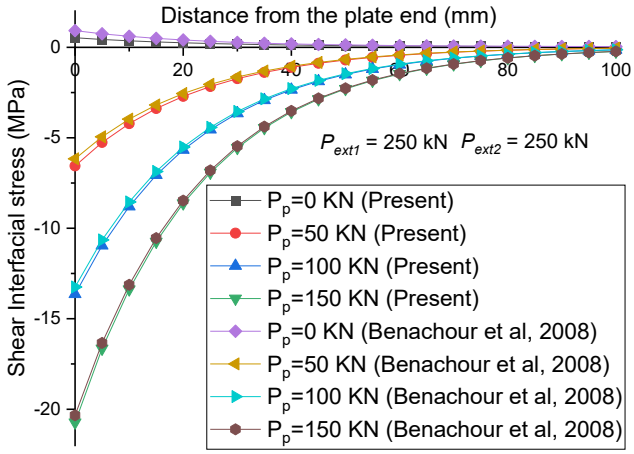

Figure 17 – Adhesive shear stress at the bond line for the FRP-strengthened beam under various prestressing forces Pp (the beam is under two symmetric point loads)

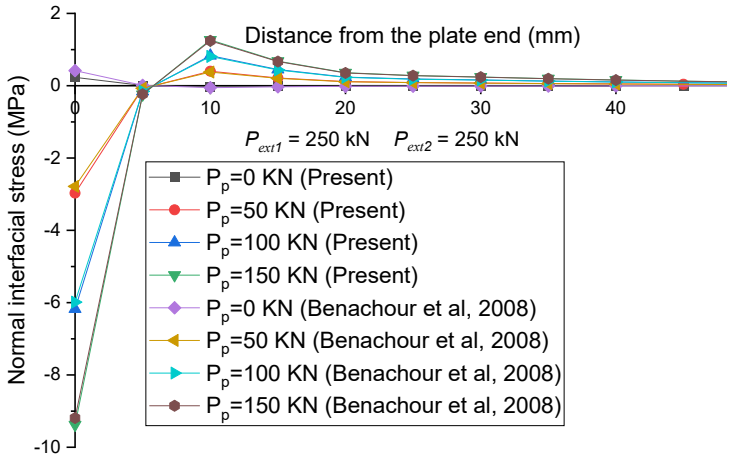

Figure 18 – Adhesive normal stress at the bond line for the FRP-strengthened beam under various prestressing forces Pp (the beam is under two symmetric point loads)

Table 4 – Shear and normal interfacial stress at the plate end under two symmetric point loads

Pp (KN)	$\tau(0)$ (Mpa)		$\sigma(0)$ (Mpa)	
	Concrete beam	Prestressed concrete beam	Concrete beam	Prestressed concrete beam
0	0.920	0.526	0.418	0.231
50	-6.164	-6.558	-2.784	-2.971
100	-13.248	-13.642	-5.987	-6.175
150	-20.332	-20.727	-9.190	-9.378

As it can be seen from the preceding figures, most interfacial stresses happen at the ends of adhesively attached plates and they start to decrease about 20 mm from the ends. Significant stress concentrations are also observed in the vicinity of the plate end when the prestressing force P_p value is increased. In contrast to a reinforced concrete beam, a small reduction in interfacial stresses is noted for the beams prestressed by a cable.

Effect of fiber orientation

Figures 19–24 illustrate how various fiber orientations affect adhesion stresses when viewed from the longitudinal direction of a beam. A 150 KN prestressing force is taken into account in the theoretical parametric analysis.

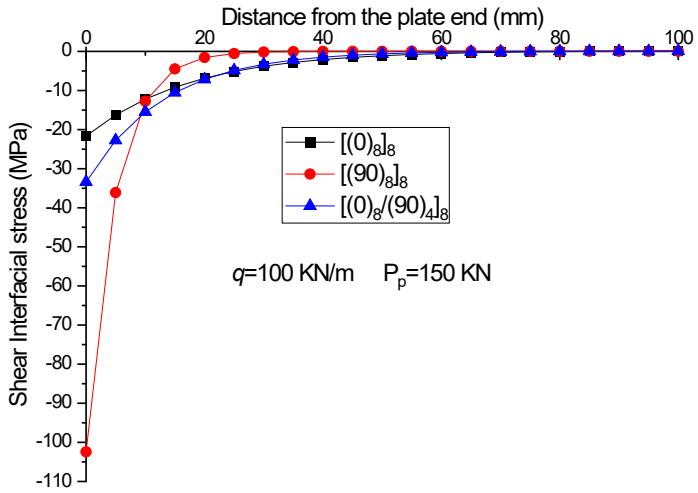

Figure 19 – Interfacial shear stress for a prestressed concrete beam with a bonded prestressed CFRP soffit plate having different fiber orientations (the beam is under UDL)

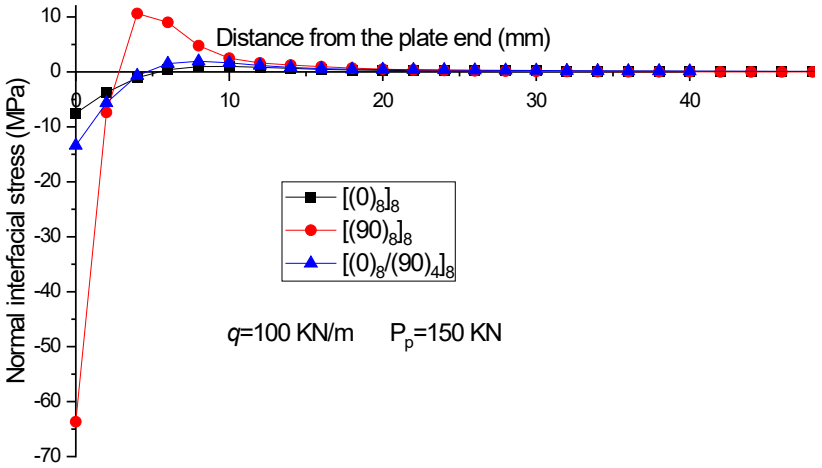

Figure 20 – Interfacial normal stress for a prestressed concrete beam with a bonded prestressed CFRP soffit plate having different fiber orientations (the beam is under UDL)

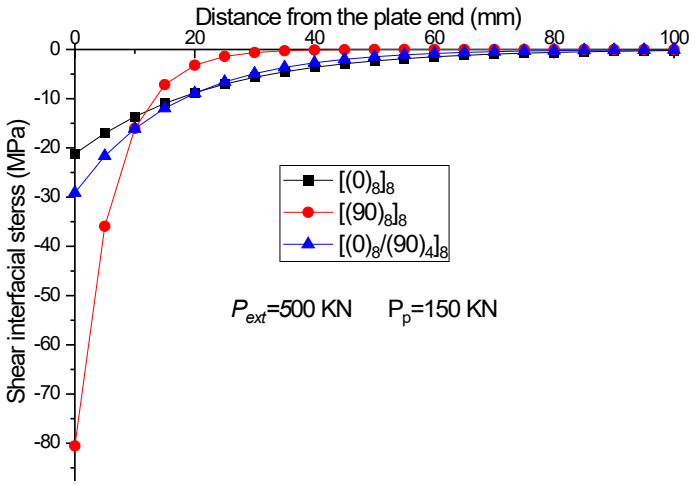

Figure 21 – Interfacial shear stress for a prestressed concrete beam with a bonded prestressed CFRP soffit plate having different fiber orientations (the beam is under a single point load)

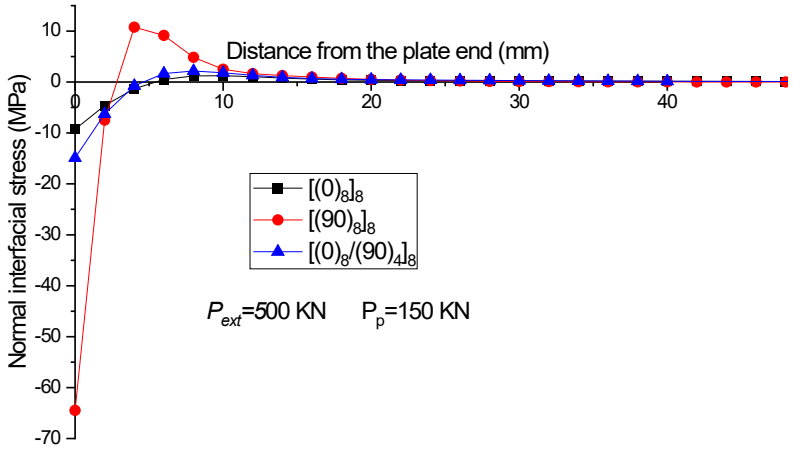

Figure 22 – Interfacial normal stress for a prestressed concrete beam with a bonded prestressed CFRP soffit plate having different fiber orientations (the beam is under a single point load)

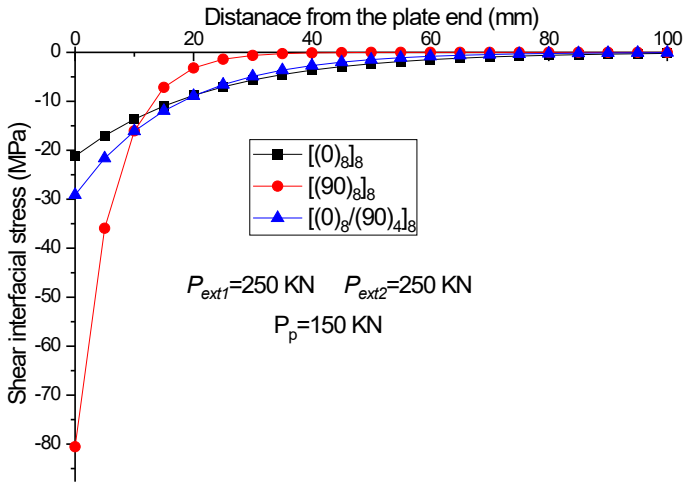

Figure 23 – Interfacial shear stress for a prestressed concrete beam with a bonded prestressed CFRP soffit plate having different fiber orientations (the beam is under two symmetric point loads)

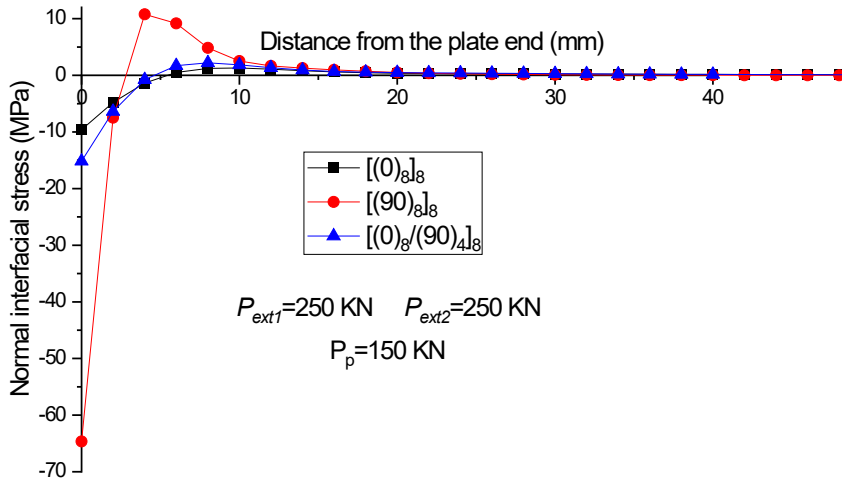

Figure 24 – Interfacial normal stress for a prestressed concrete beam with a bonded prestressed CFRP soffit plate having different fiber orientations (the beam is under two symmetric point loads)

The effective modulus of the composite plate varies when a fiber-reinforced polymer plate with various orientations is used. Fibers oriented towards the direction of the beam would increase the plate modulus, while fibers oriented perpendicular to the direction of the beam would significantly decrease the plate modulus. The effects of various fiber orientations on adhesion stresses as measured from the longitudinal direction of the beam are displayed in Figs. 10–15.

The FRP plate with fibers aligned perpendicular to the beam axis has the highest interfacial stresses, as shown in the above figures. This is in contrast to the findings of (Krour et al, 2013) who showed by a numerical study that the CFRP plate with fibers aligned perpendicular to the beam axis has the lowest interfacial stresses. It is also important to note that, with a prestressed CFRP plate, Bencahour et al. (2008) and Benali et al. (2023) arrived at the same conclusion as the current investigation.

Conclusion

This paper proposes a new analytical model to determine interfacial stresses for prestressed concrete beams reinforced by prestressed fiber-reinforced polymer (FRP) plates.

The model used takes into account the geometric shape of the cable along the span beam evolution as well as immediate and time-dependent losses expressed in terms of a polynomial function.

The model reveals the following main findings:

- A slight decrease in interfacial stresses is observed for prestressed concrete beams.
- Prestressing the FRP plate significantly raises the interfacial stresses, especially at the open edges of the plate.
- Prestressing the composite plate eliminates the effect of fiber orientation and maintains the lowest level of interface stress for fiber orientation in the longitudinal direction of the beam, enabling efficient use of the composite in the sense of its greater stiffness.
- The height level of interfacial stresses eventually results in the adoption of an anchoring mechanism that makes it possible to fix properly the composite plate.

In light of this, the investigation can be expanded to look at how time affects the general behavior of older prestressed buildings. Both the interface behavior and the cross-sectional behavior can be investigated in further detail.

References

Al-Emrani, M. & Kliger, R. 2006. Analysis of interfacial shear stresses in beams strengthened with bonded prestressed laminates. *Composites. Part B: Engineering*, 37(4-5), pp.265-272. Available at: https://doi.org/10.1016/j.compositesb.2006.01.004.

Aslam, M., Shafigh, P., Jumaat, M.Z. & Shah, S.N.R. 2015. Strengthening of RC beams using prestressed fiber reinforced polymers – A review. *Construction and Building Materials*, *82*, pp.235-256. Available at: https://doi.org/10.1016/j.conbuildmat.2015.02.051.

Bansal, P.P., Sharma, R. & Mehta, A. 2016. Retrofitting of RC girders using pre-stressed CFRP sheets. *Steel and Composite Structures*, 20(4), pp.833-849. Available at: https://doi.org/10.12989/scs.2016.20.4.833.

Benachour, A., Benyoucef, S., Tounsi, A. & Adda bedia, E.A. 2008. Interfacial stress analysis of steel beams reinforced with bonded prestressed FRP plate. *Engineering Structures*, 30(11), pp.3305-3315. Available at: https://doi.org/10.1016/j.engstruct.2008.05.007.

Benali, K., Krour, B., Atif Benatta, M., Hafid, K., Bachir Bouiadjra, M., Mechab, I. & Bernard, F. 2023. Investigation of dynamic behavior of prestressed FRP plate intended for strengthening prestressed RC beam. *Engineering structures*, 280, art.number:115690. Available at: https://doi.org/10.1016/j.engstruct.2023.115690.

Emdad, M.R. & Al-Mahaidi, R. 2015. Effect of prestressed CFRP patches on crack growth of centre-notched steel plates. *Composite Structures*, 123, pp.109-122. Available at: https://doi.org/10.1016/j.compstruct.2014.12.007.

Fahsi, B., Benrahou, K.-H., Krour, B., Tounsi, A., Benyoucef, S. & Bedia, E.A.A. 2011. Analytical analysis of interfacial stresses in FRP-RC hybrid beams with time-dependent deformations of RC beam. *Acta Mechanica Solida Sinica*, 24(6), pp.519-526. Available at: https://doi.org/10.1016/s0894-9166(11)60052-9.

-Fib-international. 1990. CEB-FIP Model Code 1990 - 1st Draft - Vol. 1, chapters 1-5. *FIB - International Federation for Structural Concrete* [online]. Available at: https://www.fib-international.org/publications/ceb-bulletins/ceb-fip-model-code-1990,-first-draft-vol-1-pdf-detail.html [Accessed: 15 October 2024].

Herakovich, C.T. 1997. *Mechanics of Fibrous Composites*. Wiley. ISBN: 978-0-471-10636-4.

Krour, B., Bernard, F. & Tounsi, A. 2013. Fibers orientation optimization for concrete beam strengthened with a CFRP bonded plate: A coupled analytical–numerical investigation. *Engineering Structures*, 56, pp.218-227. Available at: https://doi.org/10.1016/j.engstruct.2013.05.008.

Krour, B., Tounsi, A., Benyoucef, S. & Adda Bedia, E.A. 2010. An improved closed-form solution to interfacial stresses in rc beams strengthened with a composite plate. *Mechanics of Composite Materials*, 46(3), pp.331-340. Available at : https://doi.org/10.1007/s11029-010-9150-1.

Krour, B., Tounsi, A. & Meftah, S.A. 2011. A New Approach for Adhesive Stress Analysis of a Beam Bonded with Composite Plate Having Variable Fiber Spacing. *Composite Interfaces*, 18(2), pp.135-149. Available at https://doi.org/10.1163/092764411x567413.

Le Delliou, P. 2003. *Béton précontraint aux Eurocodes*. Presses Universitaires Lyon. ISBN: 978-2729707248.

Lou, T. & Karavasilis, T.L. 2018. Time-dependent assessment and deflection prediction of prestressed concrete beams with unbonded CFRP tendons. *Composite Structures*, 194, pp.365-376. Available at: https://doi.org/10.1016/j.compstruct.2018.04.013.

Mebsout, H., Krour, B. & Bachir Bouiadjra, M. 2018. Enhacing Pre-stressed Concrete Beam's Capacity Using Externally Bonded Pre-stressed Composite Plate. In: Abdelbaki, B., Safi, B. & Saidi, M. (Eds.) *Proceedings of the Third International Symposium on Materials and Sustainable Development. SMSD 2017.* Cham: Springer, pp.95-104. Available at: https://doi.org/10.1007/978-3-319-89707-3_12.

Mohamed, B.B., Abdelouahed, T., Samir, B. & El Abbas, A.B. 2009. Approximate analysis of adhesive stresses in the adhesive layer of plated RC beams. *Computational Materials Science*, 46(1), pp.15-20. Available at: https://doi.org/10.1016/j.commatsci.2009.01.020.

Mostakhdemin Hosseini, M.R., Dias, S.J.E. & Barros, J.A.O. 2016. Flexural strengthening of reinforced low strength concrete slabs using prestressed NSM CFRP laminates. *Composites Part B: Engineering*, 90, pp.14-29. Available at: https://doi.org/10.1016/j.compositesb.2015.11.028.

Páez, P.M. 2023. A simplified approach to determine the prestress loss and time-dependent deflection in cracked prestressed concrete members, prestressed

with fiber reinforced polymers or steel tendons. *Engineering Structures*, 279, art.number:115523. Available at: https://doi.org/10.1016/j.engstruct.2022.115523.

Páez, P.M. & Sensale-Cozzano, B. 2021. Time-dependent analysis of simply supported and continuous unbonded prestressed concrete beams. *Engineering Structures*, 240, art.number:112376. Available at: https://doi.org/10.1016/j.engstruct.2021.112376.

Rezazadeh, M., Barros, J. & Costa, I. 2015. Analytical approach for the flexural analysis of RC beams strengthened with prestressed CFRP. *Composites Part B: Engineering*, 73, pp.16-34. Available at: https://doi.org/10.1016/j.compositesb.2014.12.016.

Smith, S.T. & Teng, J.G. 2001. Interfacial stresses in plated beams. *Engineering Structures*, 23(7), pp.857-871. Available at: https://doi.org/10.1016/s0141-0296(00)00090-0.

Tounsi, A. & Benyoucef, S. 2007. Interfacial stresses in externally FRP-plated concrete beams. *International Journal of Adhesion and Adhesives*, 27(3), pp.207-215. Available at: https://doi.org/10.1016/j.ijadhadh.2006.01.009.

Tounsi, A., Hassaine Daouadji, T., Benyoucef, S. & Adda bedia, E.A. 2009. Interfacial stresses in FRP-plated RC beams: Effect of adherend shear deformations. *International Journal of Adhesion and Adhesives*, 29(4), pp.343-351. Available at: https://doi.org/10.1016/j.ijadhadh.2008.06.008.

Zhang, H., Guo, Q.-Q. & Xu, L.-Y. 2023. Prediction of long-term prestress loss for prestressed concrete cylinder structures using machine learning. *Engineering Structures*, 279, art.number:115577. Available at: https://doi.org/10.1016/j.engstruct.2022.115577.

Investigación analítica del comportamiento interfacial de una viga de hormigón pretensada reforzada con una placa pretensada unida con FRP

Hanane Mebsout[a], *Mohamed Atif* Benatta[b], *Baghdad* Krour[b], **autor de correspondencia**, *Oussama* Benachour[b], *Mohamed* Bachir Bouiadjra[bc], *Nacer* Rahal[ad]

[a] Universidad Mustapha Stambouli, Mascara, República Argelina Democrática y Popular

[b] Universidad de Djillali Liabes, Laboratorio de Estructuras y Materiales Avanzados en Ingeniería Civil y Obras Públicas (LSMAGCTP), Sidi Bel Abbes, República Argelina Democrática y Popular

[c] Agencia Temática de Investigación en Ciencia y Tecnología, Argel, República Argelina Democrática y Popular

[d] Universidad de Ciencias y Tecnología, Laboratorio de Estructura Mecánica y Estabilidad de la Construcción, Orán, República Argelina Democrática y Popular

CAMPO: ingeniería civil, materiales
TIPO DE ARTÍCULO: artículo científico original

Resumen:

Introducción/objetivo: El uso de materiales compuestos para reforzar estructuras de hormigón armado es una práctica muy común en la ingeniería civil. Sin embargo, la construcción con hormigón pretensado no suele utilizar este método. El objetivo principal del presente estudio es ampliar el uso de materiales compuestos para reforzar vigas de hormigón pretensado, considerando el efecto de la concentración de tensiones interfaciales en el comportamiento global de dichas estructuras.

Métodos: Se propone un nuevo modelo analítico que considera cómo los cambios en el pretensado de la viga de hormigón armado afectan las tensiones de interfaz. Se considera una función polinómica que expresa la variación de la forma geométrica del cable, así como las pérdidas instantáneas y no instantáneas de la viga de hormigón pretensado, para abordar el problema de la concentración de tensiones en la interfaz entre la placa adhesiva y el hormigón.

Resultados: Los principales hallazgos de la presente investigación demuestran que, en presencia del cable pretensado, las tensiones de interfaz disminuyen de manera no significativa; pero, a medida que aumenta la fuerza de pretensado aplicada a la placa de FRP, se observa un aumento más sustancial de las tensiones de interfaz.

Conclusión: Debido a un alto grado de tensiones de contacto en el extremo de la placa, el riesgo de desprendimiento es mayor y se recomienda un mecanismo de anclaje en el borde de la placa.

Palabras claves: viga de hormigón pretensado, compuestos FRP, tensiones interfaciales, orientación de fibras, refuerzo.

Аналитическое исследование межфазного взаимодействия предварительно напряженной бетонной балки, усиленной преднапряженной композитной арматурой

Анан Мебсоут[а], *Мухаммед Атиф* Бинатта[б], *Багдад* Кроур[б], **корреспондент**, *Оссама* Беначур[б], *Мухамед* Башир Буяжера[бв], *Насер* Рахал[аг]

[а] Университет им. Мустафы Стамбули, г. Маскара, Алжирская Народная Демократическая Республика

[б] Университет Джиллали Лиабеса, Лаборатория конструкций и передовых материалов в гражданском строительстве и общественных работах (LSMAGCTP), г. Сиди-Бель-Аббес, Алжирская Народная Демократическая Республика

[в] Тематическое агентство научно-технических исследований, г. Алжир, Алжирская Народная Демократическая Республика

[г] Университет естественных наук и технологий, Лаборатория машиностроения и прочности конструкций, г. Оран, Алжирская Народная Демократическая Республика

РУБРИКА ГРНТИ: 67.11.00 Строительные конструкции, 67.09.33 Бетоны. Железобетон. Строительные растворы, смеси, составы
ВИД СТАТЬИ: оригинальная научная статья

Резюме:

Введение/цель: Использование композитных материалов для усиления железобетонных конструкций в настоящее время является весьма распространенной практикой в области гражданского строительства. Однако в конструкциях из предварительно напряженного бетона этот метод обычно не используется. Главной целью данного исследования является расширение использования композитных материалов для усиления предварительно напряженных бетонных балок с учетом влияния концентрации межфазных напряжений на общее поведение таких конструкций.

Методы: В статье представлена новая аналитическая модель, учитывающая, как изменения предварительного напряжения преднапряженных железобетонных балок влияют на граничные напряжения. Для решения проблемы концентрации напряжений на месте соединения клей-плита-бетон рассматривается полиномиальная функция, выражающая изменение геометрической формы кабеля, а также временные и не постоянные деформации на предварительно напряженной бетонной балке.

Результаты: Основные результаты настоящего исследования показывают, что при предварительном напряжении кабеля граничные напряжения незначительно уменьшаются, однако по мере увеличения усилия предварительного напряжения, приложенного к термопластику FRP, наблюдается существенное увеличение граничных напряжений.

Вывод: Вследствие высокой степени контактных напряжений на грани плиты возрастает риск расслоения, поэтому рекомендуется использовать анкерный крепеж по ее краям.

Ключевые слова: предварительно напряженная бетонная балка, композиты FRP, межфазные напряжения, ориентация волокон, упрочнение.

Аналитичко испитивање понашања на интерфејсу код преднапрегнуте бетонске греде ојачане преднапрегнутом плочом везаном композитним материјалима

Анан Мебсоут[а], *Мухамед Атиф* Бината[б], *Багдад* Кроур[б], **аутор за преписку**, *Осама* Беначур[б], *Мухамед* Башир Бујажера[бв], *Насер* Рахал[ar]

[а] Универзитет „Мустафа Стамболи”, Маскара, Народна Демократска Република Алжир

[б] Универзитет „Ђилали Лиабес”, Лабораторија за напредне конструкције и материјале у грађевинарству и јавним радовима (LSMAGCTP), Сиди Бел Абес, Народна Демократска Република Алжир

Mebsout, H. et al, Analytical investigation of the interfacial behavior of a prestressed concrete beam strengthened with a prestressed FRP-bonded plate, pp.633-668

[в] Тематска агенција за истраживање науке и технологије,
Алжир, Народна Демократска Република Алжир

[г] Универзитет природних наука и технологије,
Лабораторија за машинске структуре и стабилност конструкције,
Оран, Народна Демократска Република Алжир

ОБЛАСТ: грађевинарство, материјали
КАТЕГОРИЈА (ТИП) ЧЛАНКА: оригинални научни рад

Сажетак:

Увод/циљ: Употреба композитних материјала за армирање армиранобетонских конструкција данас је веома честа у области грађевинарства. Међутим, овај метод се обично не користи код преднапрегнутих бетонских конструкција. Основни циљ овог рада јесте да прошири употребу композитних материјала на армирање преднапрегнутих бетонских греда узимајући у обзир утицај концентрације напона на интерфејсу на укупно понашање ових конструкција.

Методе: Предлаже се нови аналитички модел који узима у обзир начин на који преднапрегнутост преднапрегнутих бетонских греда утиче на напоне на интерфејсу. Разматра се полиномска функција која изражава варијацију геометријског облика кабла, као и тренутне и нетренутне губитке преднапрегнуте бетонске греде ради решавања питања концентрације напона на интерфејсу везиво-плоча-бетон.

Резултати: Главни налази овог испитивања показују да се, у присуству преднапрегнутости кабла, напони на интерфејсу незнатно смањују. Међутим, са повећавањем силе преднапрезања примењене на ФРП плочу уочава се знатније повећање напона на интерфејсу.

Закључак: Услед високог степена контактних напона на крају плоче, ризик од одвајања постаје већи, па се препоручује механизам за анкерисање на ивици плоче.

Кључне речи: преднапрегнута бетонска греда, ФРП композити, напони на интерфејсу, оријентација влакана, ојачавање.

Paper received on: 18.10.2024.
Manuscript corrections submitted on: 26.03.2025.
Paper accepted for publishing on: 27.03.2025.

ПРЕГЛЕДНИ РАДОВИ
ОБЗОРНЫЕ СТАТЬИ
REVIEW PAPERS

Enhancing armored crew safety: a scientometric and scoping review of key trends, challenges, and innovations

Elias M. Radzi[a], *Zuraida* Hassan[b], *Mohd Azril* Ismail[c], *Khairul Hafezad* Abdullah[d], *Intan Suraya* N. Arzahan[e], *Aswalni* Ishak[f], *Ejiro* U. Osiobe[g], *Muhammad Hazim* A. Ghalib[h]

[a] University Utara Malaysia, UUM College of Business, School of Business Management, Occupational Safety and Health Management Program, Kedah, Malaysia, e-mail: eliasmdradzi9@gmail.com, **corresponding author**, ORCID iD: https://orcid.org/0009-0000-5580-2869

[b] University Utara Malaysia, UUM College of Business, School of Business Management, Kedah, Malaysia, e-mail: h.zuraida@uum.edu.my, ORCID iD: https://orcid.org/0000-0003-2636-7540

[c] University Utara Malaysia, UUM College of Business, School of Technologies Management and Logistics, Kedah, Malaysia, e-mail: azril@uum.edu.my, ORCID iD: https://orcid.org/0000-0003-0990-6653

[d] University Utara Malaysia, UUM College of Business, School of Business Management, Social Security Management Center of Excellence, Kedah, Malaysia, e-mail: ezadneo88@gmail.com, ORCID iD: https://orcid.org/0000-0003-3759-6541

[e] University Utara Malaysia, UUM College of Business, School of Business Management, Kedah, Malaysia, e-mail: intanarzahan@gmail.com ORCID iD: https://orcid.org/0000-0002-0966-057X

[f] University Utara Malaysia, UUM College of Business, School of Business Management, Occupational Safety and Health Management Program, Kedah, Malaysia, e-mail: sonydenko2001@gmail.com ORCID iD: https://orcid.org/0009-0009-5470-8008

[g] Westcliff University, College of Business, Economics Department, Irvine, CA, United States of America, e-mail: jiji.osiobe@bakeru.edu ORCID ID: https://orcid.org/0000-0002-1107-6620

[h] University Utara Malaysia, UUM College of Business, School of Business Management, Human Resource Management Program, Kedah, Malaysia, e-mail: mhazimagy@gmail.com ORCID iD: https://orcid.org/0009-0002-0942-4718

Radzi, E.M. et al, Enhancing armored crew safety: a scientometric and scoping review of key trends, challenges, and innovations, pp.669-697

https://doi.org/10.5937/vojtehg73-54715

FIELD: military sciences, mechanical engineering
ARTICLE TYPE: review paper

Abstract:

Introduction/purpose: This study presents a comprehensive analysis of the existing literature on armored vehicle crew safety through an integrated scientometric and scoping methodology.

Methods: Data sourced from Scopus and Web of Science were employed to analyze a total of 197 documents following preprocessing and the removal of duplicates. Scientometric analysis was conducted utilizing ScientoPy and VOSviewer software to identify publication trends, keyword co-occurrence, and influential academic contributions. Furthermore, a scoping review based on the SPIDER framework was undertaken to synthesize critical insights related to whole-body vibration (WBV), vehicle design, and safety technologies.

Results: The findings indicate that the installation of bulletproof armor significantly reduces WBV exposure levels, with reductions ranging from 10% to 20%. These reductions are attributed to modifications in vehicle mass distribution and stiffness. Advanced materials, such as aluminum alloys, were identified as essential for enhancing blast resistance and vibration mitigation. The results emphasize the importance of structural modifications and adaptive technologies, including enhanced suspension systems, in managing WBV and improving overall crew safety.

Conclusion: This study establishes a robust foundation for future research, underscoring the necessity for optimized vehicle designs and integrated safety strategies to address the physiological and psychological stressors encountered by armored vehicle crews.

Key words: armored vehicle crew, whole-body vibration, scientometric analysis, scoping review, bulletproof armor.

Introduction

Armored vehicles are crucial in modern military operations, with various types serving specific functions. Tanks, for instance, are heavily armored and armed vehicles designed for frontline combat. They engage enemy forces with powerful weaponry while providing substantial protection for their crews, making them essential for penetrating enemy lines and delivering direct fire support (Radovanović et al, 2023). Armored Personnel Carriers (APCs) are built to transport infantry safely to the battlefield, offering protection against small arms fire and shrapnel. While they are less heavily armed than tanks, APCs play a vital role in ensuring the mobility and safety of troops in combat zones (Kokhan, 2023). Infantry

Fighting Vehicles (IFVs) are similar to APCs but feature heavier armament, allowing them to support infantry through direct fire and engage enemy forces more effectively. They strike a balance between firepower, protection, and mobility, making them versatile in various combat scenarios (Zelenyukh et al, 2020). The development and enhancement of these vehicles focus on improving protection, mobility, and operational efficiency. Modern advancements include optimizing design layouts, enhancing mine resistance, and utilizing high-strength materials to bolster protective capabilities (Zelenyukh et al, 2020). The effectiveness of armored vehicles in specific roles, such as technical reconnaissance, is assessed using specialized indicators, including the technical intelligence efficiency factor which helps evaluate their performance in diverse operational contexts (Kovtun et al, 2020; Jasman et al, 2018). The selection of military vehicles, including armored types, is guided by quality indicators that consider tactical and technical characteristics, ensuring they meet the demands of armed forces in challenging environments (Kokhan, 2023; Radzi et al, 2025). In summary, the strategic deployment and continuous enhancement of armored vehicles are essential for achieving military objectives and ensuring the safety and effectiveness of military operations.

Safety in armored vehicle operations is crucial due to unique and multifaceted risks faced by crews, especially in combat zones where these vehicles often become prime targets for attacks involving mines and improvised explosive devices (IEDs) (Kaidalov et al, 2023). The design of vehicle hulls, particularly double-V hulls (DVH), plays a key role in mitigating blast impacts by optimizing load transfer paths and reducing injury risks for occupants. Additionally, advancements in materials, such as aluminum alloys, improve resistance to mines and enhance energy absorption, thus increasing crew survivability (Cong et al, 2021; Bisyk et al, 2023). However, the confined interiors of armored vehicles can worsen injury severity—such as burns, extremity injuries, and exposure to depleted uranium—by complicating evacuation and medical treatment. Conditions like traumatic brain injuries and bone fractures require advanced medical intervention and effective evacuation systems (Li et al, 2023; Khorram-Manesh et al, 2021; Sheng & Solah, 2022). Moreover, psychological challenges stemming from high-stress combat environments, coupled with prolonged operations in cramped spaces and extreme temperatures, further undermine operational effectiveness. This highlights the necessity of addressing both physical and mental health concerns (Ameen et al, 2022). Together, these challenges emphasize the urgent need for integrated safety systems, innovative vehicle designs, and

comprehensive crew training to enhance operational effectiveness and resilience in armored vehicle missions.

Effective safety protocols are essential for preventing injuries and fatalities among crews of armored or combat vehicles, directly impacting operational readiness and mission success. The development and implementation of advanced protection strategies for military equipment, such as armored combat vehicles, are crucial for safeguarding personnel against various threats (Gijsbertse et al, 2021; Jasman et al, 2018). Integrating individual armor protection into training methodologies enhances service members' survivability by adapting firing techniques and regulations to accommodate the additional protection, thereby improving their response speed and mobility in combat (Gijsbertse et al, 2021; Schram et al, 2019). Furthermore, the application of systematic safety management systems, such as the Injury and Illness Prevention Program (IIPP), which includes error reduction techniques, can significantly enhance the organization of safety committees and engagement in hazard analyses, fostering a safer operational environment (Koshy et al, 2019; Radzi et al, 2024b). The Hazard and Operability Study (HAZOPS) method is also vital for identifying and mitigating potential hazards, underscoring the importance of personal protective equipment (PPE) in minimizing the risk of accidents and occupational diseases (Noor Arzahan et al, 2022).

Additionally, the implementation of advanced accident detection and alert systems in vehicles can expedite emergency responses and provide critical location data, thereby reducing the time required to address incidents and enhancing crew safety (Alsayaydeh et al, 2023). Collectively, these safety measures not only protect the crew but also ensure that vehicles and personnel are consistently prepared for deployment, contributing to the overall success of military missions. By prioritizing safety, military operations can maintain high levels of readiness and effectiveness, ultimately leading to successful mission outcomes and the preservation of human life.

The increasing complexity of safety challenges in high-stress and hazardous environments calls for a structured evaluation of existing research to guide innovation and address knowledge gaps. Scientometric analysis has emerged as a powerful tool for systematically mapping research trends, identifying influential contributions, and assessing the application of statistical methodologies to advance the field (Donthu et al, 2021). Complementing this approach, scoping reviews provide a comprehensive method for exploring and synthesizing the current state of knowledge, offering a broader perspective on various methodologies and applications (Munn et al, 2018). In the safety domain, the use of statistical

tools and database analyses is crucial for predictive modeling of blast impacts (Nguyen et al, 2019), analyzing human factors under high-stress conditions (Xie & Guo, 2018), and optimizing protective system designs through database-driven methods (Karr et al, 2007). Techniques such as machine learning algorithms and bibliometric databases are widely utilized to enhance precision and effectiveness (Huo et al, 2024). Moreover, significant advancements in armored crew safety—including lightweight composite materials, ergonomic vehicle designs, and digital innovations like IoT-based monitoring and augmented reality training—highlight the potential for transformative progress (Wibneh et al, 2024). Despite these advancements, persistent gaps in material scalability, human-system integration, and the application of emerging technologies underscore the necessity of this review to establish a critical foundation for future research.

Method and analysis design

Scientometric analysis

Scientometric analysis is a widely used methodological framework for evaluating and interpreting large scientific data sets. This approach deepens our understanding of the development of specific academic fields (Donthu et al, 2021). The application of scientometric parameters to assess research quality has become increasingly prevalent. Researchers utilize scientometric analysis for various purposes, such as identifying emerging trends and evaluating journal performance (Struck et al, 2021). Additionally, it aids in investigating collaboration patterns, research components, and publication trends within specific research domains (Wachsmann et al, 2019; Abdullah, 2022b). Moreover, scientometric analysis elucidates the intellectual structure of particular areas of inquiry, as demonstrated in several published studies (Simao et al, 2021). This study applies scientometric analysis to examine research publication patterns related to armored vehicle crew safety in military environments. The objective is to identify countries actively publishing in this field and to analyze the themes and subthemes reflected in the authors' keywords.

Scoping analysis

The primary objective of scoping reviews is to identify and categorize the diverse types of evidence that exist within a particular field (Munn et al, 2018). This study aims to explore the critical elements associated with armored vehicle crew safety in military environments by synthesizing the existing literature in this domain. Through this scoping review, the objective is to identify knowledge gaps and emphasize areas necessitating

further investigation. To accomplish this, the five-step scoping review framework developed by Arksey & O'Malley (2005) is employed:

1) Establishing the research question,
2) Identifying relevant studies,
3) Selecting studies,
4) Data charting and
5) Reporting results.

Establishing research question

The SPIDER tool (Sample, Phenomenon of Interest, Design, Evaluation, Research Type) offers a systematic approach for synthesizing research findings, especially in complex fields like armored vehicle crew safety. By organizing data around essential components of study design and evaluation, this framework enables a thorough examination of trends, innovations, and gaps in the existing literature (Cooke et al, 2012). As a result, it enhances our understanding of both the advancements and the challenges related to improving crew protection.

Research question:

What are the key findings from previous studies on armored vehicle crew safety, analyzed through the SPIDER framework, concerning innovations, design approaches, and evaluation methodologies?

Identifying relevant studies

Database

Accessing scientific publications across journals, repositories, archives, and other collections necessitates the utilization of databases and search engines (Abdullah & Abd Aziz, 2020). For the purposes of this study, the Scopus and Web of Science (WoS) databases were selected to analyze scientometric and scoping indicators. These databases were chosen due to their emphasis on the impact of document citations in comparison to other databases (Vieira & Gomes, 2009). Furthermore, modifications were implemented to ensure the validity of the coverage analysis, encompassing enhancements in metadata accuracy, document category classification, and discipline assignment. Consequently, both Scopus and WoS prioritize these factors (Stahlschmidt & Stephen, 2022).

Search strategy

After identifying the relevant keywords, a search was conducted utilizing an encyclopedia to identify synonyms. Table 1 presents the search

criteria employed to compile lists of publications from the Scopus and WoS databases. This search was conducted in October 2024 and encompassed titles, abstracts, and keywords from both databases. It is important to note that no restrictions were applied to the retrieved data during this phase, including limitations related to date, publication type, or language.

Table 1 – Search strategy for extracting data from the Web of Science and Scopus databases

Database	Search strategy	Records
Web of Science	Topic: ("armoured vehicle" OR "Armored vehicle" OR "Armored car" OR "combat vehicle" OR "fighting vehicle" OR "Armored Personnel Carrier" OR "Battle Tank" OR "main battle Tank" OR "Infantry Fighting Vehicle" OR "Armored Fighting Vehicle" OR "Armored troop carrier" OR "Protected mobility vehicle" OR "military combat vehicle") AND ("safety" OR "Security" OR "protection") AND ("soldier" OR "Driver" OR "crew" OR "operator" OR "gunner" OR "commander" OR "operators")	28
Scopus	Article Title, Abstract, Keywords: ("armoured vehicle" OR "Armored vehicle" OR "Armored car" OR "combat vehicle" OR "fighting vehicle" OR "Armored Personnel Carrier" OR "Battle Tank" OR "main battle Tank" OR "Infantry Fighting Vehicle" OR "Armored Fighting Vehicle" OR "Armored troop carrier" OR "Protected mobility vehicle" OR "military combat vehicle") AND ("safety" OR "Security" OR "protection") AND ("soldier" OR "Driver" OR "crew" OR "operator" OR "gunner" OR "commander" OR "operators")	222

Software

ScientoPy and VOSviewer are two widely utilized research tools within academic contexts. ScientoPy, a Python script, is specifically designed to extract valuable information from research articles, including primary subjects, authors, countries, and related documents. By employing keywords provided by authors, ScientoPy generates insights and aids in mitigating potential biases that may arise from independent investigations (Ruiz-Rosero et al, 2019). However, it is crucial to recognize that the analysis of studies based on author names may still introduce bias, particularly in instances of name similarities (Ruiz-Rosero et al, 2019).

VOSviewer, developed by Van Eck & Waltman (2010), is a software application that facilitates co-occurrence analyses of keywords, particularly in the context of armored vehicle crew safety challenges in military environments. It utilizes sophisticated mapping techniques to transform CSV data into visually informative diagrams or clusters (Abdullah, 2022a). These mapping strategies offer significant potential

benefits for researchers seeking to analyze specific data points, such as authors' keywords (Abd Aziz et al, 2021).

Selecting studies

Publications merge and removal of duplicates

The data from both databases were compiled and processed utilizing ScientoPy. During this stage, the data underwent standardization. This process involved substituting commas in the authors' names with semicolons, eliminating periods, commas, and distinctive formatting from the authors' names, and removing duplicate entries with identical titles and authors. Employing this methodology enhances the accuracy and reliability of the datasets. The results of the preprocessed data are presented in Diagram 1.

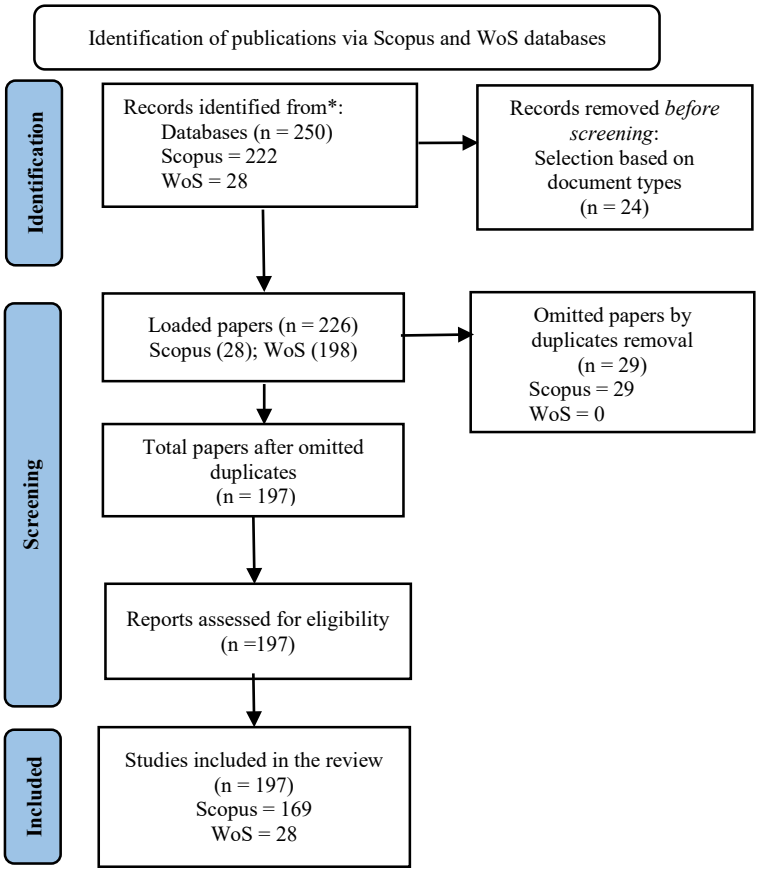

Diagram 1 – Flow diagram of the research of databases and registers

Figure 1 presents an overview of the preprocessing phase pertaining to research documents sourced from two databases: the Web of Science (WoS) and Scopus, within the framework of armored vehicle crew safety. The chart delineates the total number of documents processed and underscores the percentage of duplicate documents that were eliminated. Notably, no duplicates were removed from the WoS, indicating that all documents included were unique. In contrast, 15% of the documents from Scopus were classified as duplicates and subsequently discarded, leaving the remainder available for analysis. This preprocessing phase is essential for ensuring the accuracy and relevance of the data by removing redundant studies, thereby facilitating a more focused and efficient analysis of research trends and key findings related to crew safety. The elimination of duplicates refines the final dataset, thereby enhancing the quality of the subsequent scientometric and scoping review.

Diagram 1 offers additional insights by showing that the source dataset comprises 250 papers obtained from the WoS and Scopus databases. ScientoPy's automated categorization process eliminated 24 documents, which included books, letters, and errata, while classifying the remaining publications into various categories such as conference papers, articles, reviews, proceedings papers, and press articles. After the data reconciliation process, this study utilized a total of 197 entries from both databases: 28 papers from WoS and 169 from Scopus. Additionally, 29 duplicate entries from Scopus were removed.

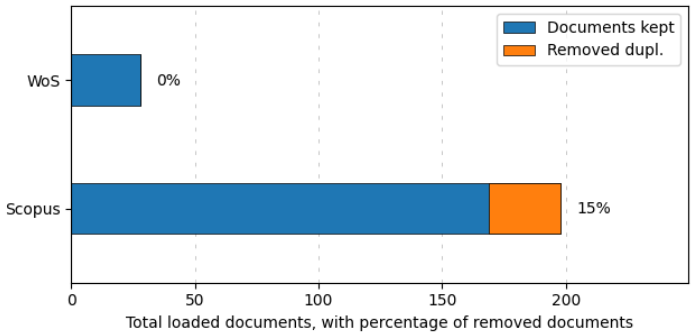

Figure 1 – Data combination and duplicates removal

Data charting

The publication growth graph exemplifies the evolution of publishing within the Scopus and WoS databases, offering significant insights into overarching publication trends. In order to attain a more comprehensive understanding of the articles selected in the preceding stage, we analyze the progression of the top 10 authors' keywords and investigate the co-occurrence of these keywords.

Reporting results

In alignment with the objectives of our study, we have prepared a succinct summary and report of our findings. We employed ScientoPy to analyze the growth of publications, identify countries actively engaged in research, and investigate relevant keywords. To assess the co-occurrence of authors' keywords, we utilized VOSviewer as a descriptive metric. It is noteworthy that a minimum of two keywords is required to generate co-occurrence results for authors' keywords using VOSviewer. Furthermore, we systematically reviewed and modified the thesaurus files to prevent duplication of authors' keywords, adhering to the recommendations of Abdullah (2022a).

The scoping review methodology aims to provide a comprehensive overview of the existing research within a specific field. A primary objective of conducting a scoping study is to identify gaps or deficiencies in the current literature. In this study, we sought to thoroughly examine and describe the current state of research on armored vehicle crew safety challenges in military environments, as well as to identify areas where the literature is lacking. To conduct this analysis, we utilized articles obtained from Scopus and WoS, which were preprocessed using ScientoPy. The specific inclusion criteria for this scoping review are detailed in Table 2.

1) Written in English,
2) Published since 2013,
3) Describe primary research, and
4) Use the keyword “whole-body vibration” in the authors’ keywords.

Results

Scientometric outcome

Publication growth

Figure 2 illustrates the temporal trends in publications related to armored vehicle crew safety, drawing on data from two prominent academic databases: Scopus and WoS, encompassing the years from 1996 to 2024, including some projected future data points. Notable findings indicate a substantial increase in publications around 2006 within Scopus, where over 25 documents were produced, representing a zenith of research activity during that period. Following this peak, the number of publications exhibited a gradual decline; however, a resurgence commenced around 2014, characterized by a consistent output of documents from 2015 to 2024. Conversely, WoS has consistently yielded

a lower volume of publications over the years, maintaining a stable rate of output with sporadic minor increases, particularly noted in 2008 and 2016. This trend implies that while Scopus has undergone phases of heightened research engagement, WoS has sustained a more subdued, yet stable, contribution to the literature concerning armored vehicle crew safety. The discrepancies in the publication volume between the two databases may reflect differing research emphases or coverage of the subject matter within these sources.

The increasing scholarly focus on the safety of armored vehicle crews reflects a broader recognition of the critical need to enhance survivability and operational safety for military personnel. This is evident in various research efforts aimed at addressing different aspects of military safety and health. For instance, the PREPARE study protocol underscores the importance of assessing and mitigating risks associated with musculoskeletal injuries among service members, which is crucial for maintaining operational readiness and ensuring safety in high-risk environments, such as those involving armored vehicles (Butowicz et al, 2022). Furthermore, the development of advanced protective clothing, including graphene-based intelligent personal protective equipment, highlights ongoing efforts to improve protection technologies against chemical threats relevant to armored vehicle crews who may encounter such hazards in combat situations (Giurgiu et al, 2023; Witte & Schwarz, 2023). In addition, research on the effects of load carriage on landing techniques provides insights into the physical demands placed on military personnel, including those operating armored vehicles, and the potential for injury, thereby informing safer operational practices (Witte & Schwarz, 2023). The implementation of mobile ultrasound vascular assessments in remote and conflict areas illustrates innovative approaches to healthcare delivery, ensuring that military personnel, including armored vehicle crews, have access to essential medical evaluations even in challenging environments (Jasman et al, 2018; Kaidalov et al, 2023; Radzi et al, 2025). Lastly, the long-term safety analysis of apremilast for conditions such as psoriasis and psoriatic arthritis, while not directly related to the safety of armored vehicle crews, exemplifies the broader commitment to ensuring the health and well-being of military personnel through safe and effective medical treatments (Prasanna et al, 2019). Collectively, these diverse research initiatives contribute to a comprehensive strategy aimed at enhancing the safety and effectiveness of armored vehicle crews, reflecting a growing recognition of the importance of this issue in military operations.

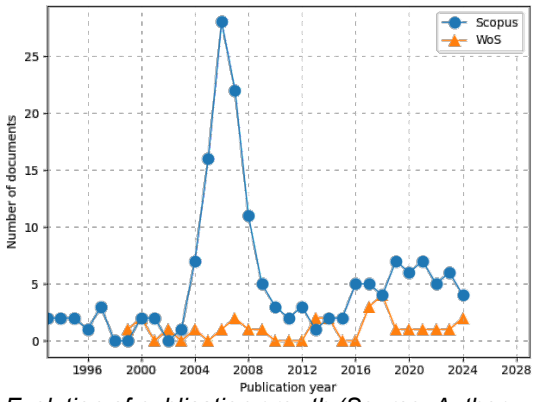

Figure 2 – Evolution of publication growth (Source: Author, using ScientoPy 2.1.3)

Most influential academic works

Figure 3 provides an overview of the most influential academic works on armored vehicle crew safety, highlighting institutional contributions based on the total number of documents published and the percentage of recent outputs (2022–2024). The Silesian Technical University in Poland stands out as the most influential institution, contributing the highest total number of publications, with 25% of its research outputs produced during the 2022–2024 period. In contrast, the China Agricultural University and the China North Vehicle Research Institute emerge as key contributors in the recent period, with 100% of their works published between 2022 and 2024, demonstrating their concentrated efforts and growing influence. While institutions from Germany, India, Malaysia, and Canada made significant earlier contributions, their lack of recent publications highlights a shift in research leadership, with Polish and Chinese institutions now driving the advancements in the field of armored vehicle crew safety.

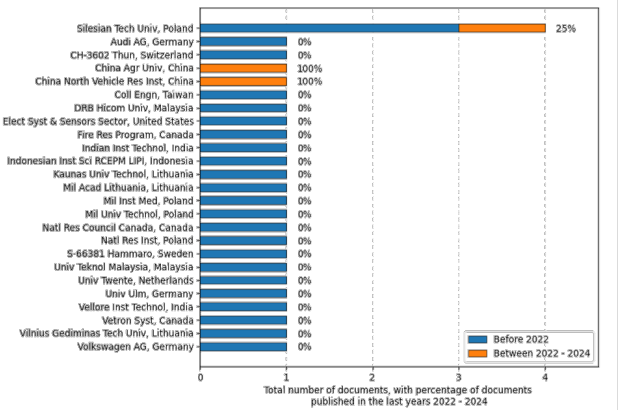

Figure 3 – Bar graph of institution trends

Authors' keywords

Figure 4 illustrates the distribution of authors' keywords pertinent to armored vehicle crew safety, comparing publications prior to 2022 with those published between 2022 and 2024. The keyword "armored vehicle" emerges as the most frequently utilized term, appearing in 75% of the related documents published during the latter period, which indicates a notable increase in scholarly focus on this subject. Additionally, the keywords such as "protection" and "whole-body vibration" demonstrate significant recent interest, accounting for 33% of the documents published between 2022 and 2024. This trend suggests that these domains are increasingly being investigated to enhance crew safety. In contrast, several other critical keywords, including "simulation," "uranium, depleted," "automated turret," "inhalation," "blast protection," "criterion of injuries," and "Madymo," have not been featured in recent publications (0% in 2022-2024), which may imply either a saturation of research in these areas or a pressing need for renewed inquiry. These findings underscore that while conventional safety aspects such as protection are attracting greater recent attention, other vital areas may necessitate further investigation to address the evolving challenges associated with armored vehicle crew safety.

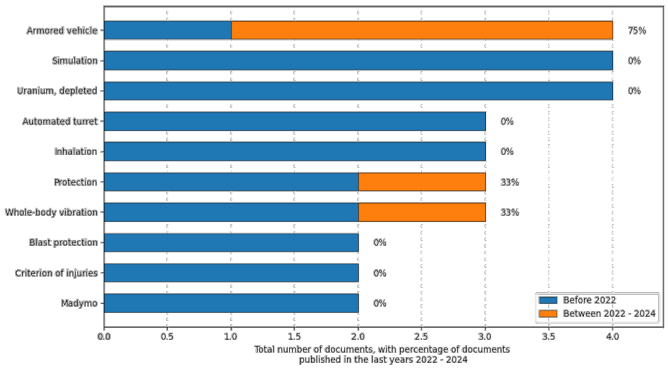

Figure 4 – Bar graph of the trend in research themes and emerging topics (Source: Author, using ScientoPy 2.1.3)

Figure 5 illustrates the overlay visualization generated by VOSviewer for armored vehicle crew safety, depicting the progression of research themes from 2017 to 2020. Initial research, represented by yellow and green nodes, concentrated on addressing critical threats and injury prevention, with terms such as "improvised explosive device," "criterion of injuries," "shock wave," and "blast protection." These keywords

underscore a significant emphasis on understanding and mitigating the impacts of explosive devices and associated injuries in earlier studies. As the timeline advances into 2018-2019 (blue and purple nodes), the focus transitions toward "protection" and "mobility," indicating an increased research interest in protective gear and ensuring crew mobility under armored conditions. More recently, in 2020 (red nodes), scholarly attention has expanded to encompass topics such as "suspension" and "vibration," reflecting a growing interest in vehicle dynamics and crew comfort. These latter keywords denote ongoing efforts to optimize vehicle design to minimize vibration and enhance safety and comfort for the crew. This timeline reveals an evolving research trajectory, transitioning from threat mitigation to improving overall vehicle and crew performance.

These findings indicate a clear evolution in the research focus on armored vehicle crew safety. Initially, efforts were primarily directed toward understanding and mitigating immediate threats such as improvised explosive devices and blast-related injuries. However, over time, the emphasis has shifted toward enhancing protective measures, improving crew mobility, and refining vehicle dynamics. The recent focus on suspension and vibration suggests that the field is now concerned not only with safeguarding the crew from external threats but also with optimizing vehicle design to improve comfort and reduce long-term health risks associated with vibrations and other mechanical stresses. This progression reflects a holistic approach to crew safety, integrating immediate protection with considerations for long-term well-being.

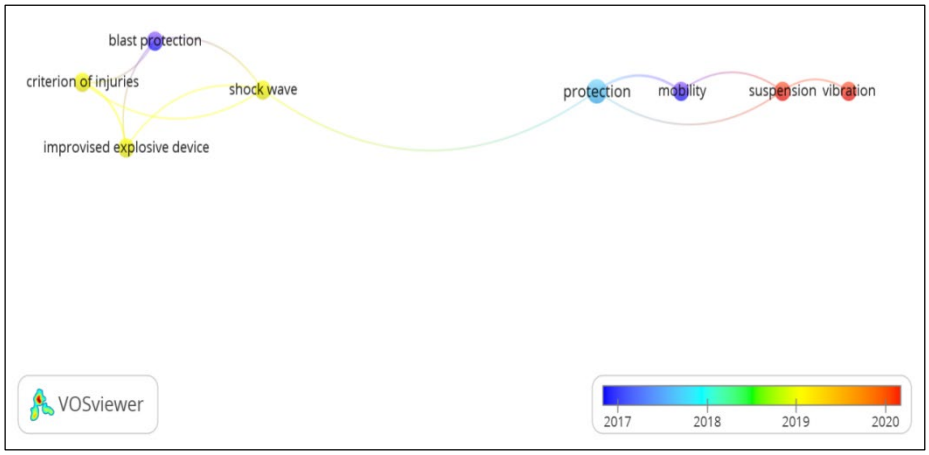

Figure 5 – Co-occurrence of authors' keywords

Scoping outcomes

This section provides a comprehensive examination of armored vehicle crew safety. Conducting this analysis represents a critical initial step in identifying knowledge gaps and guiding future research endeavors. Furthermore, it enhances the existing body of knowledge and establishes best practices within the field. To support this analysis, qualitative research questions were formulated, and the SPIDER tool was utilized as the search strategy. Table 2 presents a compilation of publications derived from the extended author keywords sourced from ScientoPy. Initially, the data in Table 2 were collected from a total of two documents. It is essential to note that this study focuses specifically on the scoping analysis of research articles; therefore, records that are not classified as research papers have been excluded at this stage.

Table 2 – List of inclusive publications

No	Sources	Sample	Phenomenon of interest	Design	Evaluation	Research type
1.	Alfaro Degan et al. (2017)	Compared whole-body vibration (WBV) exposure between a standard vehicle and an identical bulletproof armored vehicle, using the same driver for both to ensure consistent measurement conditions.	Focuses on how vehicle characteristics , especially bulletproof armor, influence WBV exposure in armored vehicle drivers and its potential impact on the risk of musculoskeletal injuries.	Measured WBV exposure in two phases: first in a standard vehicle, and then in the same vehicle model modified with bulletproof armor, both conducted on a curvilinear urban road under consistent conditions for reliable comparison	The installation of bulletproof armor altered the car's mass distribution and weight, leading to reduced WBV exposure, highlighting the significant impact of vehicle modifications on WBV levels according to ISO 2631-1(1997) standards	Quantitative

No	Sources	Sample	Phenomenon of interest	Design	Evaluation	Research type
2.	Alfaro Degan et al. (2016)	Involving 14 subjects driving urban vehicles, aimed to assess how vehicle armoring impacts whole-body vibration (WBV) exposure.	Investigates how the installation of bulletproof armor in armored vehicles impacts WBV exposure and the related health risks for professional drivers.	Utilized a case study approach with two sampling campaigns, comparing the performance of a standard vehicle and the same model modified with armor plating under controlled conditions for accurate comparison.	Indicates that vehicle characteristics, particularly the installation of bulletproof armor, significantly impact whole-body vibration (WBV) exposure, reducing the WBV dose by 10% to 20% depending on the driver's individual characteristic.	Quantitative

Discussion

The analysis of the keywords conducted in this study reveals a significant relationship between key methodologies—such as notational analysis, multivariate analysis, and kinetics—and their roles in evaluating and improving the safety of armored vehicle crews. Notational analysis, in particular, was identified as a crucial tool for systematically tracking and assessing crew actions, responses, and operational patterns. This approach facilitates the identification of performance gaps and opportunities to enhance safety in combat conditions. Additionally, this study examined the role of user state evaluations, underscoring the importance of understanding crew members' mental states and their interactions with human-machine interfaces. This comprehension is essential for developing tailored design solutions that support decision-making in high-stress environments (Witte & Schwarz, 2023). Furthermore, our analysis of factors influencing combat survivability—such as vehicle speed, acceleration, and detection distance—highlights the significance of accurate mobility predictions and logical operator actions in maintaining operational effectiveness and crew safety (Ostashevskiy & Piatkov, 2019).

The research provides evidence that advanced numerical simulations are vital for assessing the effects of explosive impacts and injury mechanisms, thereby contributing to the development of robust protection systems for armored vehicles.

The findings further demonstrate that the adverse effects of suspension and vibration on crew members are multifaceted, affecting both physiological and psychological aspects that compromise overall safety performance. Our analysis identifies whole-body vibration (WBV) as a significant risk factor for musculoskeletal pain, particularly low back pain (LBP), which is exacerbated by prolonged sitting and constrained postures during vehicle operation (Alfaro Degan et al, 2016; Bisyk et al, 2023). Moreover, cognitive performance significantly declines under vibration exposure, especially when compounded by occupational stressors typical in combat scenarios, such as elevated heart rate and respiratory frequency (Ismail et al, 2024; Aida et al, 2023). These findings underscore the necessity for strategies to mitigate both physical and psychological stressors, including enhanced ergonomic designs and technologies to reduce vibration exposure. This research identifies these areas as critical for improving safety outcomes and operational efficiency for armored vehicle crews.

Future directions emerging from this study emphasize the importance of integrating autonomous systems, hybrid vehicle designs, and advanced materials to bolster vehicle survivability and crew protection. The results suggest that incorporating technologies such as hybrid powertrains, blast-resistant materials, and IoT-based monitoring systems can provide more effective protective measures while enhancing vehicle performance (Piancastelli et al, 2023). Concurrently, our analysis stresses the necessity for standardized international safety protocols and collaborative efforts among stakeholders—including vehicle manufacturers, technology developers, and military organizations—to address the evolving challenges of military operations (Giurgiu et al, 2023; Hassan et al, 2020). Ultimately, this study underscores the critical need for comprehensive research into the long-term health impacts of WBV and blast exposure to inform future advancements in armored vehicle crew safety (Prasanna et al, 2019).

Based on a scoping analysis that examines the effects of bulletproof armor installation on WBV exposure among armored vehicle drivers, this study investigates how vehicle modifications impact vibration levels and associated health risks. The results indicate that the installation of bulletproof armor, primarily intended to enhance protection, can significantly reduce WBV exposure by 10% to 20%, depending on driver-

specific characteristics. This reduction is largely attributable to changes in vehicle mass and stiffness dynamics, as evidenced by our findings and supported by Alfaro Degan et al. (2017). The analysis reveals that the increased weight from armor installation lowers frequency-weighted root mean square (RMS) acceleration values, thereby attenuating WBV across various frequency spectra. Furthermore, advanced vehicle designs, such as anti-mine shields composed of aluminum alloy components, modify energy absorption and vibration response, leading to decreased WBV levels by influencing resonant frequencies (Bisyk et al, 2023). These findings underscore the significance of vehicle structure and weight distribution resulting from armor installation in mitigating WBV exposure and enhancing safety for armored vehicle drivers.

Additionally, this research highlights the necessity of optimizing vehicle design and implementing structural modifications to manage WBV. It demonstrates that careful adjustments to vehicle stiffness and mass properties can effectively reduce vibration amplitudes, similar to the results observed in vibration suppression technologies utilized in other transportation sectors (Aida et al, 2023). For instance, the baseline sensitivity method, which optimizes structural noise and vibration through strategic mass attachments, aligns with our findings that appropriate armor placement and material selection can minimize WBV levels across critical frequency peaks (Hong & Yoshimura, 2024). While not the primary focus of this study, it acknowledges advanced seat technologies and adaptive suspension systems as complementary solutions for further reducing vibration exposure. Overall, these findings suggest that the combined effects of bulletproof armor installation and structural modifications present a significant opportunity to mitigate WBV risks, thereby enhancing both driver safety and operational comfort. This study contributes to a deeper understanding of the engineering implications of armor installation, paving the way for future advancements in armored vehicle design and WBV management.

Armored vehicle crew safety is intricately linked to Sustainable Development Goal 3 (SDG 3), which emphasizes the need to mitigate the physiological and psychological impacts associated with operating in high-stress environments. Acute stress reactions (ASRs) are prevalent among military personnel, with 17.2% of soldiers reporting such experiences during combat, underscoring the necessity for effective prevention and management strategies to ensure the safety and well-being of the crew (Nordstrand et al, 2024; Radzi et al, 2024a).

The PREPARE study highlights the importance of addressing non-battle-related musculoskeletal injuries (MSKIs), which represent

significant medical issues affecting service member readiness. By identifying the physical and psychosocial factors that contribute to MSKI risks, the study seeks to enhance rehabilitation and risk mitigation strategies, thereby supporting the health and safety of military personnel (Butowicz et al, 2022; Radzi, 2024). Proactive psychological programs, as examined in the systematic analysis, demonstrate modest effectiveness in reducing posttraumatic stress injuries (PTSIs) and promoting psychological wellness through resilience and stress management strategies, which are critical for maintaining the mental health of individuals exposed to potentially traumatic events (Di Nota et al, 2021; Radzi et al, 2024a). The PRISMO study further underscores the long-term mental health impacts of military deployment, identifying biological and psychological factors that contribute to stress-related conditions, thereby informing strategies to support mental health post-deployment (Van Der Wal et al, 2020). Moreover, resilience has been shown to serve as a protective factor against psychiatric and physical health issues in combat-exposed veterans, suggesting that fostering resilience can mitigate the adverse effects of combat exposure, ultimately enhancing overall well-being (Di Nota et al, 2021; Radzi, 2024). Collectively, these studies highlight the multifaceted approach required to improve armored vehicle crew safety by addressing both physical and psychological health in alignment with the objectives of SDG 3.

Conclusion

The analysis presented in this study demonstrates that the installation of bulletproof armor in armored vehicles significantly influences WBV exposure levels, offering critical insights into the interaction between vehicle modifications and vibration mitigation. The results indicate that the addition of armor leads to a reduction in WBV exposure by approximately 10% to 20%, with variations attributed to vehicle mass distribution and specific driver characteristics. This reduction is primarily a consequence of alterations in the vehicle's stiffness and mass properties, which effectively decrease RMS acceleration values within critical frequency ranges, in accordance with ISO 2631-1 standards for vibration exposure.

Furthermore, the findings underscore the necessity for optimized vehicle designs that incorporate advanced structural modifications to manage WBV effectively. The study emphasizes the importance of integrating vibration-suppression technologies, such as enhanced suspension systems and structural improvements, to further mitigate WBV exposure. By addressing both protective and ergonomic dimensions of vehicle design, this research establishes a framework for enhancing the

safety and comfort of armored vehicle crews. These conclusions highlight that vehicle modifications aimed at improving survivability must also account for their impact on long-term crew health and operational efficiency.

Limitation of the current study

The inclusion of the publication list represents a significant limitation of this study. Although the analysis of scientometrics and scoping is founded on the Scopus and Web of Science (WoS) databases, future researchers could enhance the findings by also integrating data from Google Scholar, PubMed, and the Education Resources Information Center (ERIC).

Contribution to the body of knowledge and practices

This research contributes to the existing body of knowledge by systematically applying scientometric and scoping methods to evaluate publication trends, key research themes, and knowledge gaps related to armored vehicle crew safety. Through these methodologies, the study identified critical areas necessitating further exploration, such as the effects of WBV on crew health and the role of vehicle modifications in mitigating vibration exposure. The scientometric analysis elucidated publication growth patterns and the contributions of the leading institutions, thereby providing a clearer understanding of global research activity in this domain. Concurrently, the scoping review categorized evidence pertaining to technological advancements, including vehicle design modifications and material innovations, thereby emphasizing their potential impact on reducing WBV and enhancing blast protection. Collectively, these methodological approaches establish a robust foundation for advancing research priorities, guiding future inquiries, and informing the development of targeted safety strategies for military personnel operating armored vehicles.

References

Abd Aziz, F.S., Abdullah, K.H. & Samsudin, S. 2021. Bibliometric analysis of behavior-based safety (BBS): three decades publication trends. *Webology*, 18(Special Issue on Information Retrieval and Web Search), pp.278-293. Available at: https://doi.org/10.14704/WEB/V18SI02/WEB18072.

Abdullah, K.H. 2022a. Mapping of literature on risk assessment research using ScientoPy and VOSviewer. *Journal of Metrics Studies and Social Science*, 1(1), pp.36-49. Available at: https://doi.org/10.56916/jmsss.v1i1.75

Abdullah, K.H. 2022b. Publication trends in biology education: A bibliometric review of 63 years. *Journal of Turkish Science Education*, 19(2), pp.465-480. Available at: https://doi.org/10.36681/tused.2022.131.

Abdullah, K.H. & Abd Aziz, F.S. 2020. Safety Behaviour in the Laboratory among University Students. *The Journal of Behavioral Science*, 15(3), pp.51-65 [online]. Available at: https://so06.tci-thaijo.org/index.php/IJBS/article/view/241208 [Accessed: 10 November 2024].

Aida, K.-i., Takigami, T., Akiyama, Y. & Makita, Y. 2023. Development of Longitudinal Excitation Suppression Devices for Reducing Car-body Elastic Vibrations in Bullet Trains. *Quarterly Report of RTRI*, 64(3), pp.166-172. Available at: https://doi.org/10.2219/rtriqr.64.3_166.

Alfaro Degan, G., Antonucci, A., Coltrinari, G. & Lippiello, D. 2019. Safety-oriented multi-task approach to manage whole-body vibration exposure among quarry operators. *WIT Transactions on the Built Environment*, 189, pp.43-53. Available at: https://doi.org/10.2495/SAFE190051.

Alfaro Degan, G., Coltrinari, G., Lippiello, D. & Pinzari, M. 2016. Risk assessment of the whole-body vibration exposure for drivers of armored vehicles: A case study. *International Journal of Safety and Security Engineering*, 6(1), pp.53-62. Available at: https://doi.org/10.2495/SAFE-V6-N1-53-62.

Alfaro Degan, G., Coltrinari, G.I., Lipiello, D. & Pinzari, M. 2017. Effects of ground conditions on whole-body vibration exposure on cars: A case study of drivers of armored vehicles. *WIT Transactions on the Built Environment*, 176, pp.431-438. Available at: https://doi.org/10.2495/UT170371.

Alsayaydeh, J.A.J, Yusof, M.F.b, Abdillah, M.A.A., Al-Gburi, A.J.A., Herawan, S.G. & Oliinyk, A. 2023. Enhancing Vehicle Safety: A Comprehensive Accident Detection and Alert System. *International Journal of Advanced Computer Science and Applications (IJACSA),* 14(11), pp.28-41. Available at: https://doi.org/10.14569/ijacsa.2023.0141104.

Ameen, H.A., Shamman, A.H. & Ali, H. 2022. Vehicular Safety System: Driving Behaviour Identification Based on V2V Data Exchange System. *Evolution of Information, Communication and Computing System*, 3(1), pp.14-32 [online]. Available at: https://publisher.uthm.edu.my/bookseries/index.php/eiccs/article/view/31 [Accessed: 10 November 2024].

Arksey, H. & O'Malley, L. 2005. Scoping studies: towards a methodological framework. *International Journal of Social Research Methodology*, 8(1), pp.19-32. Available at: https://doi.org/10.1080/1364557032000119616.

Bisyk, S.P., Sanin, A.F., Poshyvalov, V.P., Aristarkhov, O.M., Prykhodko, M.V., Kuzmytska, A.I. & Lednianskyi, A.F. 2023. Combined shock and mine protection based on aluminum alloy parts. *Technical mechanics*, 2023(1), pp.76-89. Available at: https://doi.org/10.15407/itm2023.01.076.

Butowicz, C.M., Hendershot, B.D., Watson, N.L., Brooks, D.I., Goss, D.L., Whitehurst, R.A., Harvey, A.D., Helton, M.S., Kardouni, J.R., Garber, M.B. & Mauntel, T.C. 2022. Pre-neuromusculoskeletal injury Risk factor Evaluation and Post-neuromusculoskeletal injury Assessment for Return-to-duty/activity

Enhancement (PREPARE) in military service members: a prospective, observational study protocol. *Journal of Translational Medicine*, 20, art.number:619. Available at: https://doi.org/10.1186/s12967-022-03832-7.

Cong, M., Zhou, Y.-b., Zhang, M., Sun, X.-w., Chen, C. & Ji, C. 2021. Design and optimization of multi-V hulls of light armoured vehicles under blast loads. *Thin-Walled Structures*, 168, art.number:108311. Available at: https://doi.org/10.1016/j.tws.2021.108311.

Cooke, A., Smith, D. & Booth, A. 2012. Beyond PICO: The SPIDER Tool for Qualitative Evidence Synthesis. *Qualitative Health Research*, 22(10), pp.1435-1443. Available at: https://doi.org/10.1177/1049732312452938.

Di Nota, P.M., Bahji, A., Groll, D., Carleton, R.N. & Anderson, G.S. 2021. Proactive psychological programs designed to mitigate posttraumatic stress injuries among at-risk workers: a systematic review and meta-analysis. *Systematic Reviews*, 10, art.number:126. Available at: https://doi.org/10.1186/s13643-021-01677-7.

Donthu, N., Kumar, S., Mukherjee, D., Pandey, N. & Lim, W.M. 2021. How to conduct a bibliometric analysis: An overview and guidelines. *Journal of Business Research*, 133, pp.285-296. Available at: https://doi.org/10.1016/j.jbusres.2021.04.070.

Gijsbertse, K., Linssen, L., Woering, A. & Catoire, M. 2021. The effects of mass, bulk and stiffness of personal protective equipment and clothing on physical performance when performing a military mobility obstacle course. *Applied Ergonomics*, 95, art.number:103448. Available at: https://doi.org/10.1016/j.apergo.2021.103448.

Giurgiu, T., Virca, I., Grigoraş, C. & Năstăsescu, V. 2023. Trends in Development of Military Vehicles Capabilities Based on Advanced Technologies. In: *International Conference Knowledge-Based Organization*, 29(3), pp.15-22. Available at: https://doi.org/10.2478/kbo-2023-0070.

Hassan, Z., Subramaniam, C., Zain, M.L.M., Ramalu, S.S. & Shamsudin, F.M. 2020. Management commitment and safety training as antecedent of workers safety behavior. *International Journal of Supply Chain, Operation Management and Logistics (IJSCOL)*, 1(2), pp.12-20. Available at: https://doi.org/10.35631/IJSCOL.12002.

Hong, J. & Yoshimura, T. 2024. Baseline method for structural vibration and noise optimization, part I: baseline sensitivity method. *Mechanical Engineering Journal,* 11(3), art.number:23-00007. Available at: https://doi.org/10.1299/mej.23-00007.

Huo, Q., Luo, X., Xu, Z., & Yang, X., 2024. Machine learning applied to epilepsy: bibliometric and visual analysis from 2004 to 2023. Frontiers in Neurology, 15. Available at: https://doi.org/10.3389/fneur.2024.1374443

Ismail, M.A., Waris, A.M., Kamal, N.U.K.M., Zaini, N.S., Sharif, K.I.M. & Hassan, M.G., 2024. Optimising Safety: Investigating the Nexus of Safety Management, Safety Climate and Safety Performance in Malaysian Logistics Companies. *Journal of Maritime Logistics*, 4(1), pp.27-38. Available at: https://doi.org/10.46754/jml.2024.08.002.

Jasman, M.R., Jamaludin, S.N.S. & Yusof, K.M. 2018. Near Field Radio Frequency Radiation Hazard on Military Armoured Vehicle - Approach to a Dose Assessment. *International Journal of Automotive and Mechanical Engineering (IJAME)*, 15(4), pp.6052-6063. Available at: https://doi.org/10.15282/ijame.15.4.2018.24.0461.

Kaidalov, R., Bilenko, O. & Kudimov, S. 2023. Methods of ensuring the defined level of combat survival of armored wheeled vehicles. *The collection of scientific works of the National Academy of the National Guard of Ukraine*, 1(41), pp.65-72. Available at: https://doi.org/10.33405/2409-7470/2023/1/41/280883.

Karr, A., Fulp, W., Vera, F., Young, S., Lin, X., & Reiter, J., 2007. Secure, Privacy-Preserving Analysis of Distributed Databases. *Technometrics*, 49, pp.335-345. Available at: https://doi.org/10.1198/004017007000000209.

Khorram-Manesh, A., Goniewicz, K., Burkle, F.M. & Robinson, Y. 2021. Review of Military Casualties in Modern Conflicts—The Re-emergence of Casualties From Armored Warfare. *Military Medicine*, 187(3-4), pp.e313–e321. Available at: https://doi.org/10.1093/milmed/usab108.

Kokhan, V. 2023. Methodology for selection of military automotive equipment by quality indicators. *Scientific works of State Scientific Research Institute of Armament and Military Equipment Testing and Certification*, 18(4), pp.35-40. https://doi.org/10.37701/dndivsovt.18.2023.05.

Koshy, K., Preustti, M. & Rosen, M.A. 2019. Applying an Error Reduction Model to an Injury and Illness Prevention Program- Steps to Improve an Occupational Safety and Health Management System (OSHMS). *Journal of Management and Research*, 11(4), pp.1-11. Available at: https://doi.org/10.5296/jmr.v11i4.10775.

Kovtun, A., Kudimov, S., Savchenko, V. & Stepanov, P. 2020. Evaluation of the efficiency of using armored vehicles for technical intelligence. *Honor and Law*, 2(73), pp.33-41. Available at: https://doi.org/10.33405/2078-7480/2020/2/73/207157.

Li, Y., Yang, G.-M., Zhao, Y.-B. & Li, B.-C. 2023. Wounding characteristics and treatment principles of ground anti-armored vehicle ammunition against armored crew. *Chinese Journal of Traumatology*, 26(3), pp.125-130. Available at: https://doi.org/10.1016/j.cjtee.2023.03.002.

Munn, Z., Peters, M.D.J., Stern, C., Tufanaru, C., McArthur, A. & Aromataris, E. 2018. Systematic review or scoping review? Guidance for authors when choosing between a systematic or scoping review approach. *BMC Medical Research Methodology*, 18, art.number:143. Available at: https://doi.org/10.1186/s12874-018-0611-x.

Nguyen, H., Drebenstedt, C., Bui, X.-N., & Bui, D.T. 2019. Prediction of Blast-Induced Ground Vibration in an Open-Pit Mine by a Novel Hybrid Model Based on Clustering and Artificial Neural Network. *Natural Resources Research*, 29, pp.691-709. Available at: https://doi.org/10.1007/s11053-019-09470-z.

Noor Arzahan, I.S.N., Ismail, Z. & Yasin, S.M. 2022. Safety culture, safety climate, and safety performance in healthcare facilities: A systematic review.

Safety science, 147, art.number:105624. Available at: https://doi.org/10.1016/j.ssci.2021.105624.

Nordstrand, A.E., Barger, S.D., Tvedt, M.A., Gjerstad, C.L., Engen, H.G. & Adler, A. 2024. A novel intervention for acute stress reaction: exploring the feasibility of ReSTART among Norwegian soldiers. *European Journal of Psychotraumatology*, 15(1), art.number:2400011. Available at: https://doi.org/10.1080/20008066.2024.2400011.

Ostashevskiy, S. & Piatkov, M. 2019. Mathematical model of the logical actions of the armored automobile vehicles operator in motion speed choosing, consider the road spectrum of resistance. *Scientific Reports of the National University of Life and Environmental Sciences of Ukraine*, 15(6). Available at: https://doi.org/10.31548/DOPOVIDI2019.06.025.

Piancastelli, L., Toccaceli, M., Sali, M., Leon-Cardenas, C. & Pezzuti, E., 2023. Electric Hybrid Powertrain for Armored Vehicles. *Energies*, 16(6), art.number:2605. Available at: https://doi.org/10.3390/en16062605.

Prasanna, A., Sangasuri, S., Yaranal, S., Kannan, G.K. & Singh, U.K. 2019. Occupant injury simulation using human surrogate during vehicle underbody mine blast loading. In: *Proceedings of 31st International Symposium on Ballistics,* Hyderabad, India, November 4-8. Available at: https://doi.org/10.12783/ballistics2019/33292.

Radovanović, M., Petrovski, A., Smileski, S. & Jokić, Ž. 2023. Analysis of the development of five generation of anti-armor missile systems. *Scientific Technical Review*, 73(1), pp.26-37. Available at: https://doi.org/10.5937/str2301026r.

Radzi, E.M. 2024. Examining the impact of social security programs on military personnel and veterans: A scientometric and scoping review. *Social Security Management Journal*, 2(October), pp.1-18. Available at: https://doi.org/10.32890/ssmj2024.1.2.1.

Radzi, E.M., Abd Aziz, F.S. & Abdullah, K.H. 2024a. The interrelation between happiness and workplace safety: A bibliometric review. *Multidisciplinary Reviews*, 7(7), art.number:2024145. Available at: https://doi.org/10.31893/multirev.2024145.

Radzi, E.M., Abdullah, K.H. & Abd Aziz, F.S. 2024b. Exploring cutting-edge research trends in safety knowledge within military environments. *Vojnotehnički glasnik/Military Technical Courier*, 72(2), pp.869-895. Available at: https://doi.org/10.5937/vojtehg72-49554.

Radzi, E.M., Hassan, Z., Abdullah, K.H., Osiobe, E.U. & Ghalib, M.H.A. 2025. Assessing the Impact of Ergonomic Interventions in Military Settings: A Scientometric and Scoping Approach. *Spectrum*, 2(2) pp.97-108. Available at: https://doi.org/10.61552/SJSS.2025.02.005.

Ruiz-Rosero, J., Ramírez-González, G. & Viveros-Delgado, J. 2019. Software survey: ScientoPy, a scientometric tool for topics trend analysis in scientific publications. *Scientometrics*, 121(2), pp.1165-1188. Available at: https://doi.org/10.1007/s11192-019-03213-w.

Schram, B., Orr, R., Hinton, B., Pope, R. & Norris, G. 2019. The effects of body armour on the power development and agility of police officers. *Ergonomics*,

62(10), pp.1349-1356. Available at: https://doi.org/10.1080/00140139.2019.1648878.

Sheng, T.K. & Solah, M.S. 2022. Head Injuries in Rollover of Military Armoured Vehicle. *RSF Conference Series: Engineering and Technology*, 2(2), pp.183-189. Available at: https://doi.org/10.31098/cset.v2i2.571.

Simao, L.B., Carvalho, L.C. & Madeira, M.J. 2021. Intellectual structure of management innovation: bibliometric analysis. *Management Review Quarterly*, 71(3), pp.651-677. Available at: https://doi.org/10.1007/s11301-020-00196-4.

Stahlschmidt, S. & Stephen, D. 2022. From indexation policies through citation networks to normalised citation impacts: Web of Science, Scopus, and Dimensions as varying resonance chambers. *Scientometrics*, 127(5), pp.2413-2431. Available at: https://doi.org/10.1007/s11192-022-04309-6.

Struck, S., Stewart-Tufescu, A., Asmundson, A.J.N., Asmundson, G.G.J. & Afifi, T.O. 2021. Adverse childhood experiences (ACEs) research: A bibliometric analysis of publication trends over the first 20 years. *Child Abuse & Neglect*, 112, art.number:104895. Available at: https://doi.org/10.1016/j.chiabu.2020.104895.

Van Der Wal, S., Vermetten, E. & Elbert, G. 2020. Long-term development of post-traumatic stress symptoms and associated risk factors in military service members deployed to Afghanistan: Results from the PRISMO 10-year follow-up. *European Psychiatry*, 64(1), e10. Available at: https://doi.org/10.1192/j.eurpsy.2020.113.

Van Eck, N. & Waltman, L. 2010. Software survey: VOSviewer, a computer program for bibliometric mapping. *Scientometrics*, 84(2), pp.523-538. Available at: https://doi.org/10.1007/s11192-009-0146-3.

Vieira, E.S. & Gomes, J.A.N.F 2009. A comparison of Scopus and Web of Science for a typical university. *Scientometrics*, 81(2), pp.587-600. Available at: https://doi.org/10.1007/s11192-009-2178-0.

Wachsmann, M.S., Onwuegbuzie, A.J., Hoisington, S., Gonzales, V., Wilcox, R., Valle, R. & Aleisa, M. 2019. Collaboration Patterns as a Function of Research Experience Among Mixed Researchers: A Mixed Methods Bibliometric Study. *The Qualitative Report*, 24(12), pp.2954-2979. Available at: https://doi.org/10.46743/2160-3715/2019.3852.

Wibneh, A., Singh, A.K. & Karmakar, S. 2024. A comprehensive ergonomic validation of workspaces design employing digital and physical mock-ups in the case of light armored vehicle. *The Journal of Defense Modeling and Simulation: Applications, Methodology, Technology*. Available at: https://doi.org/10.1177/15485129241283092.

Witte, T.E.F. & Schwarz, J. 2023. A Concept of User State Analysis for Evaluations of Interaction Design in Armored Vehicles. In: Biehl, J., Carter, S. & Lucero, A. (Eds.) *ISS Companion '23: Companion Proceedings of the 2023 Conference on Interactive Surfaces and Spaces*, Pittsburgh, PA, USA, pp.32-34, November 5 - 8. Available at: https://doi.org/10.1145/3626485.3626536.

Xie, X. & Guo, D. 2018. Human factors risk assessment and management: Process safety in engineering. *Process Safety and Environmental Protection*, 113, pp.467-482. Available at: https://doi.org/10.1016/J.PSEP.2017.11.018.

Zelenyukh, O., Tymko, A. & Pynchuk, M. 2020. Justification of directions of improvement of technical characteristics of battle armed machines. *Control, Navigation and Communication Systems. Academic Journal*, 1(59), pp.50-53. Available at: https://doi.org/10.26906/SUNZ.2020.1.050.

Mejora de la seguridad de la tripulación blindada: una revisión cienciométrica y de alcance de tendencias, desafíos e innovaciones clave

Elias M. Radzi[ac], **autor de correspondencia**, *Zuraida* Hassan[ac], *Mohd Azril* Ismail[ad], *Khairul Hafezad* Abdullah[ac], *Intan Suraya* N. Arzahan[ac], *Aswalni* Ishak[ac], *Ejiro* U. Osiobe[b], *Muhammad Hazim* A. Ghalib[ac]

[a] Universiti Utara Malaysia, Facultad de Negocios UUM, Kedah, Malasia

[b] Universidad de Westcliff, Facultad de Negocios, Departamento de Economía, Irvine, CA, Estados Unidos de América

[c] Escuela de Gestión Empresarial

[d] Escuela de Gestión de Tecnologías y Logística

CAMPO: ciencias militares, ingeniería mecánica
TIPO DE ARTÍCULO: artículo de revisión

Resumen:

Introducción/objetivo: Este estudio presenta un análisis integral de la bibliografía existente sobre la seguridad de la tripulación de vehículos blindados a través de una metodología cienciométrica y de alcance integrada.

Métodos: Se utilizaron datos procedentes de Scopus y Web of Science para analizar un total de 197 documentos tras el preprocesamiento y la eliminación de duplicados. El análisis cienciométrico se realizó utilizando el software ScientPy y VOSviewer para identificar tendencias de publicación, coexistencia de palabras clave y contribuciones académicas influyentes. Además, se llevó a cabo una revisión de alcance basada en la estructura SPIDER para sintetizar conocimientos críticos relacionados con la vibración de todo el cuerpo (WBV), el diseño de vehículos y las tecnologías de seguridad.

Resultados: Los hallazgos indican que la instalación de armaduras antibalas reduce significativamente los niveles de exposición al WBV, con reducciones que oscilan entre el 10% y el 20%. Estas reducciones se atribuyen a modificaciones en la distribución de masa y la rigidez del vehículo. Se identificaron materiales avanzados, como las aleaciones de aluminio, como esenciales para mejorar la resistencia a las explosiones y mitigar las vibraciones. Los resultados enfatizan la importancia de las modificaciones estructurales y las tecnologías adaptativas, incluidos los sistemas de suspensión mejorados, para gestionar el WBV y mejorar la seguridad general de la tripulación.

Conclusión: Este estudio establece una base sólida para futuras investigaciones, subrayando la necesidad de diseños de vehículos optimizados y estrategias de seguridad integradas para abordar los factores estresantes fisiológicos y psicológicos que enfrentan las tripulaciones de vehículos blindados.

Palabras claves: tripulación de vehículos blindados, vibración de cuerpo entero, análisis cienciométrico, revisión de alcance, blindaje antibalas.

Повышение безопасности экипажей бронированных машин: наукометрический и аналитический обзор ключевых тенденций, проблем и инноваций

Элиас М. Раджи[ав], **корреспондент**, *Зураида* Хасан[ав], *Мохд Азрил* Исмаил[аг], *Хайрул Хафизад* Абдулах[ав], *Интан Сурая* Н. Арзахан[ав], *Асвални* Ишак[ав], *Еджиро* У. Осиобе[б], *Мухаммед Хазим* А. Галиб[ав]

[а] Университет Утара, Малайзия, Колледж бизнеса UUM, г. Кедах, Малайзия

[б] Вестклиффский университет, Колледж бизнеса, экономический факультет, г. Ирвин, Калифорния, Соединенные Штаты Америки

[в] Школа бизнеса и менеджмента

[г] Школа технологий менеджмента и логистики

РУБРИКА ГРНТИ: 78.25.10 Бронетанковая техника,
78.01.81 Измерения, контроль и управление качеством. Испытание образцов вооружения и военной техники

ВИД СТАТЬИ: обзорная статья

Резюме:

Введение/цель: В данном исследовании представлен всесторонний анализ существующей литературы по безопасности экипажа бронированной машины с применением интегрированной наукометрической и аналитической методологии.

Методы: Данные, полученные из Scopus и Web of Science, были использованы для анализа 197 документов после предварительной обработки и удаления дубликатов. Наукометрический анализ был проведен с помощью программного обеспечения Scientopia и VOSviewer для определения тенденций публикаций, совпадения ключевых слов и значимых научных вкладов. Помимо того, был проведен аналитический обзор, основанный на концепции SPIDER, с целью обобщения критических данных, касающихся вибрации всего

тела (WBV), проектирования транспортного средства и технологий обеспечения безопасности.

Результаты: Результаты исследования показали, что установка пуленепробиваемой брони значительно снижает уровень воздействия WBV, причем снижение составляет от 10% до 20%. Это снижение объясняется изменениями в распределении массы и жесткости транспортного средства. Современные материалы, такие как алюминиевые сплавы, являются необходимым фактором в повышении ударопрочности и снижения вибрации. Результаты подчеркивают значимость конструктивных изменений и адаптивных технологий, включая усовершенствованные системы подвески для управления ударопрочностью и повышения общей безопасности экипажа.

Вывод: Данная статья закладывает прочный фундамент для будущих исследований, подчеркивая необходимость оптимизации проектирования транспортных средств и внедрения стратегий по обеспечению безопасности для устранения физиологических и психологических стрессоров, с которыми сталкиваются экипажи бронированных машин.

Ключевые слова: экипаж бронированной транспортно-боевой машины, вибрация всего тела, наукометрический анализ, обзорный анализ, пуленепробиваемая броня.

Побољшање безбедности посаде оклопних возила: сциентометријска анализа и преглед заступљености кључних трендова, изазова и иновација

Елиас М. Раџи[ав], **аутор за преписку**, *Зураида* Хасан[ав], *Мохд Азрил* Исмаил[аг], *Хајрул Хафизад* Абдулах[ав], *Интан Сураја* Н. Арзахан[ав], *Асвални* Ишак[ав], *Еџиро* У. Осиобе[б], *Мухамед Хазим* А. Галиб[ав]

[а] Универзитет Утара Малезија, Колеџ бизниса УУМ, Кедах, Малезија

[б] Универзитет Вестклиф, Пословни колеџ, Одсек екеономије, Ервајн, Калифорнија, Сједињене Америчке Државе

[в] Школа за пословни менаџмент

[г] Школа технологије менаџмента и логистике

ОБЛАСТ: војне науке, машинство
КАТЕГОРИЈА (ТИП) ЧЛАНКА: прегледни рад

Сажетак:

Увод/циљ: Овај рад представља свеобухватну анализу постојеће литературе о безбедности посаде оклопних возила путем обједињавања сциентометрије и методологије заступљености.

Методе: Подаци из Scopus-а и Web of Science коришћени су у анализи укупно 197 докумената након претходне обраде и уклањања дупликата. У сциентометријској анализи коришћен је алат ScientoPy и софтвер VOSviewer за идентификовање трендова при објављивању, кључних речи, као и утицајних академских доприноса. Литература је анализирана по заступљености у окружењу SPIDER како би се синтетизовала најважнија знања из области вибрација целог тела (WBV), пројектовања возила и безбедносних технологија.

Резултати: Налази истраживања показују да инсталирање панцирног оклопа у знатној мери (од 10% до 20%) смањује изложеност целог тела вибрацијама. Ово смањење приписује се модификацијама у распореду масе и крутости возила. Напредни материјали, као што су алуминијумске легуре, идентификовани су као суштински важни за повећавање отпорности на удар и смањење вибрација. Резултати истичу важност структурних модификација и адаптивних технологија, укључујући побољшане системе вешања у решавању проблема вибрација целог тела, као и у повећању безбедности посаде у целини.

Закључак: Ова студија поставља чврсте основе за будућа истраживања, истичући потребу за оптимизованим пројектовањем возила, као и за интегрисаним безбедносним стратегијама ради решавања физиолошких и психолошких стресора којима су изложене посаде оклопних возила.

Кључне речи: посада оклопног возила, вибрација целог тела, сциентометријска анализа, преглед заступљености, панцирни оклоп.

Paper received on: 12.11.2024.
Manuscript corrections submitted on: 26.03.2025.
Paper accepted for publishing on: 27.03.2025.

Кина распоређује нови авион *KJ-3000* за рано упозорење и контролу[1]

Кинеска летелица за рано упозорење и контролу (*AEW&C*) *KJ-3000* извршила је свој први лет 26. децембра 2024. године. Њен домет детекције открива стелт летелице на даљинама до 360 километара. Летелица је заснована на домаћем транспортном авиону Y-20B, а покреће је мотори WS-20. Ова платформа позиционира *KJ-3000* као велики *AEW&C* систем, упоредив са *KJ-2000,* али се разликује од система средње величине као што су *KJ-200* и *KJ-500*.

Платформа Y-20B нуди значајне предности носивости; KJ-3000 може да носи до 66 тона, 16 тона више од KJ-2000

Летелица KJ-3000 користи конформни антенски радарски систем, што представља помак од традиционалног дизајна радара. Конформни радар је интегрисан директно у структуру авиона, обезбеђује податке о ситуацији у

[1] Defense News Aerospace, 27 December 2024

опсегу од 360 степени и побољшава детекцију скривених циљева. Према извештајима, радар нуди домет детекције између 600 и 1.000 км за конвенционалне мете и више од 360 км за стелт авионе попут *F-22* и *F-35.* Дизајн радара минимизира аеродинамички отпор, повећавајући ефикасност лета и оперативну издржљивост. Поред тога, систем наводно може да прати до 100 циљева истовремено.

Мотори авиона Y-20B побољшавају ефикасност горива, обезбеђују већи потисак и омогућавају продужене операције лета. Ова домаћа платформа смањује ослањање на увезене системе, као што је руски *Il-76* који се користи за KJ-2000, омогућавајући потенцијалну производњу и прилагођавање великих размера. Дизајн платформе је напреднији у односу на дизајн претходних летелица, као што је *KJ-2000*, који је имао ротирајућу радарску куполу постављену на оквир авиона *Il-76.* Прелазак *KJ-3000* на конформни радар омогућава његов дизајн, јер побољшава аеродинамичке перформансе уз одржавање високе способности детекције.

Радарска технологија *KJ-3000* интегрише дигиталне фазне системе, додатно побољшавајући могућности детекције и праћења. Овакав дизајн смањује тежину авиона и потрошњу горива, повећава радну брзину и домет авиона. Ране процене сугеришу да радар може да открије, идентификује и прати напредне стелт авионе, као што су амерички бомбардери *F-22* и *B-21.*

Авион укључује системе C4ISR (командовање, контрола, комуникације, компјутери, обавештајни надзор и извиђање), што му омогућава да функционише као свеобухватни командни центар. Ови системи олакшавају координацију у ваздухопловним, копненим и морским доменима. Очекује се да ће *KJ-3000* деловати заједно са напредним борбеним авионима, као што су J-*20, J-16* и *J-10C*, оснажавајући кинеску мрежу противваздухопловне одбране.

Стратешки посматрано, летелица KJ-3000 се бори против напредних стелт технологија. Захваљујући својим способностима може да се супротстави новој генерацији стелт авиона, укључујући ловце шесте генерације који се очекују до 2030. године. Непроверени извештаји сугеришу да *KJ-3000* има активне могућности електромагнетног напада, потенцијално ометајући или онеспособљавајући противничке електронске системе на великим удаљеностима. Такође, указују на подршку за интеграцију ракета ваздух-ваздух *PL-17,* што побољшава његову улогу у одбрамбеним и офанзивним операцијама, решавајући једну од дуготрајних слабости *AWACS* платформи.

Летелица *KJ-3000* развија се упоредо са кинеским прототиповима ловаца шесте генерације и јуришног носача типа 076. Ова представљања, као и презентовање ловца *J-20,* одражава стратешки напор да се покаже напредак кинеске одбране. Тајминг првог лета летелице *KJ-3000* наглашава њену релевантност за кинеске стратешке циљеве, посебно у пацифичком региону. Очекује се да ће способности ове летелице ојачати

способност Кине да открије и супротстави се напредним претњама, укључујући стелт технологије које користе потенцијални противници.

Летелица *KJ-3000* има значајну улогу у кинеској *AEW&C* флоти, допуњујући системе великог домета, као што је *KJ-2000,* и платформе средње величине, као што су *KJ-200* и *KJ-500*. Њен конформни радар и технологија дигиталне фазне решетке побољшавају прикривено праћење циљева и оперативну ефикасност. Изграђена на домаћој платформи *Y-20B*, има повећан домет, већи капацитет носивости и већу издржљивост, смањујући ослањање на увезене системе као што је руски *Il-76*. Као део вишеслојне мреже противваздухопловне одбране, *KJ-3000* је намењен за решавање еволуирајућих претњи из ваздушног простора и јачање оперативних капацитета. Непроверени извори говоре да би *KJ-3000* могао да замени старије платформе, попут *KJ-2000*, која је у употреби скоро две деценије.

Заснован на платформи транспортног авиона *Y-20B*, очекује се да *KJ-3000* обезбеди Ваздухопловству Народне ослободилачке армије (*PLAAF*) већу способност раног упозорења и контроле у ваздушном простору. Уз конформну антенску радарску технологију, пружа покривеност од 360 степени и побољшава детекцију стелт авиона, укључујући америчке ловце, као што су *F-22* и *F-35*, пројектоване да пружају мали радарски одраз. Ова побољшања могу умањити оперативне предности америчких стелт авиона повећањем њихове видљивости у спорним ваздушним просторима. Поред тога, унапређени системи командовања и контроле *KJ-3000* вероватно ће побољшати координацију између кинеских војних средстава, потенцијално компликујући стратешке операције противника.

Драган М. Вучковић (*Dragan* M. Vučković),
e-mail: draganvuckovic64@gmail.com,
ORCID iD: https://orcid.org/0000-0003-1620-5601

Пројектил *Hellfire* са оштрицама мача [2]

На интернету се појавио видео-снимак на којем су приказани остаци три пројектила *AGM-114R9X* који су коришћени у недавном нападу на терористе повезане са Ал Каидом у Сирији. Види се да унутрашњост ове мистериозне верзије ракете *Hellfire* има шест избацивих оштрица налик мачевима уместо традиционалне експлозивне бојеве главе.

Видео-клип се први пут појавио на друштвеним мрежама 17. јуна 2020, три дана након удара ракете *AGM-114R9X* на СУВ у сиријској губернији Идлиб. Сиријска организација за људска права са седиштем у Великој Британији касније је саопштила да су две особе, једна јорданске националности, а друга из Јемена, погинуле у возилу у том нападу. Обојица су наводно били чланови Хуррас ал-Дин, терористичке групе

[2] www.twz.com, 17 June, 2020

повезане са Ал Каидом, коју америчка влада такође назива Ал Каидом у Сирији или АК-С.

Остаци пројектила AGM-114R9X

Стручњаци и посматрачи су раније утврдили да су најмање три, а вероватно и четири ракете AGM-114R9X погодиле СУВ у Идлибу, што указује на компоненте три различите ракете на снимку. У једном случају виде се остаци најмање три лопатице које су причвршћене за централну структуру главчине. Види се и друга главчина, повезана са нечим што изгледа да има још потпунију оштрицу.

На снимку се виде и црвене сфере. Дијаграми претходних варијанти *АГМ-114*, укључујући основну верзију *AGM-114R,* показују сличну компоненту која се налази према задњем делу пројектила, а представља „пнеуматски акумулатор" који није карактеристичан за ову ретку варијанту пројектила.

Иста структура главчине и оштрице такође се виде на фотографији након претходног циљаног удара у којем је једна од ових ракета испаљена на комби у Идлибу у децембру 2019. године. У том удару убијен је члан ХТС-а (Хаи'ат Тахрир ал-Схам) , од којег се Хурас ал-Дин раздвојио 2017. године. Преименован из Ал Нусра фронта раније те године, ХТС се званично одрекао својих веза са Ал Каидом.

Међутим, према доступним информацијама, изгледа да је AGM-114R9G била оригинална ознака за варијанту са оштрицама, али да је преименована у R9X ради чувања тајности о новој верзији ракете. То би одговарало чињеници да се, упркос својој језивој ефикасности и малом ризику за посматраче, оружје издаје само на врло ограниченој основи.

System Description	Production	Characteristics	Performance
AGM-114A, B, C, F, FA – HELLFIRE Weight = 45 kg Length = 163 cm	1982 – 1992	A, B, C have a Single Shaped-Charge Warhead; Analog Autopilot	• Not Capable Against Reactive Armor • Non-Programmable
		F has Tandem Warheads; Analog Autopilot	• Reactive Armor Capable • Non-Programmable
AGM-114K/K2/K2A – HELLFIRE II Weight = 45 kg Length = 163 cm	1993 – Until Complete	• Tandem Warheads • Electronic Safe & Arm Device • Digital Autopilot & Electronics • Improved Performance Software	• Capable Against 21st Century Armor • Hardened Against Countermeasures • K-2 adds Insensitive Munitions (IM) • K-2A adds Blast-Frag Sleeve
AGM-114L – HELLFIRE LONGBOW Weight = 49 kg Length = 180 cm	1995 – 2005	• Tandem Warheads • Digital Autopilot & Electronics • Milimeter-Wave (MMW) Seeker • IM Warheads	• Initiate on Contact • Hardened Against Countermeasures • Programmable Software • All-Weather
AGM-114M – HELLFIRE II (Blast Frag) Weight = 49 kg Length = 180 cm	1998 – 2010	• Blast-Frag Warhead • 4 Operating Modes • Digital Autopilot & Electronics • Delayed-Fuse Capability	• For Buildings, Soft-Skin Vehicles • Optimized for Low Cloud Ceilings • Hardened Against Countermeasures • WH Penetrates Target Before Detonation
AGM-114N – HELLFIRE II (MAC) Weight = 49 kg Length = 180 cm	2003 – Until Complete	• Metal-Augmented Charge – Sustained Pressure Wave • 4 Operating Modes • Delayed-Fuse Capability	• For Buildings, Soft-Skin Vehicles • Optimized for Low Cloud Ceilings • Hardened Against Countermeasures • WH Penetrates Target Before Detonation
AGM-114R – HELLFIRE II (Bridge to JAGM – RW/UAS) Weight = 49 kg Length = 180 cm	2010 – Until Complete	• Integratef Blast Frag Sleeve Warhead • Designed for all platforms • Health Monitoring	• For all Target Sets • Increased Lethality and Engagement Envelope

Званичан дијаграм који приказује пресеке различитих верзија ракете AGM-114 са видљивим црвеним сферама у пројектилима AGM-114K, M, N и R

По свему судећи, чини се да само беспилотне летелице које користе Заједничка команда за специјалне операције (JSOC) и Централна обавештајна агенција носе ову нову верзију ракете. Коалиција предвођена САД, која се бори против ИСИС-а у Ираку и Сирији, изјавила је за АФП да није била укључена у најновији напад, што је у складу са претходним изјавама америчке војске које сугеришу да су овај и други удари против група повезаних са Ал Каидом на северозападу Сирије део посебне операције. Јавно доступне информације такође говоре да је америчко ратно ваздухопловство службено одговорно за управљање овом варијантом од 2017. године. То је уједно и година када се појавио први познати случај употребе овог оружја, односно када је један од пројектила убио тадашњег вођу Ал Каиде Абу Хајра ал Масрија док се возио у Идлибу.

Америчка војска до сада није званично потврдила постојање верзије R9X, за разлику од *AGM-114R9H,* за коју је јавно признала да представља

ракету са „веома ниским степеном колатералне штете”, верзије *Hellfire* која можда у својој унутрашњости нема бојеву главу било које врсте.

Упркос великој тајности, пројектил оставља јасне трагове удара, ефекте оштећења и препознатљиве олупине због недостатка експлозивне бојеве главе која би прикрила његову употребу. Чињеница да је оружје јасно означено као и сваки други *Hellfire* још је један показатељ да је сазнање о његовом постојању неопходно.

Верзија ракете са оштрицама добила је назив „нинџа бомба”, а након поменутог случаја користи се и у североисточној Сирији.

Незванични извештаји наводе да је настављено са употребом ове верзије ракете и након свргавања режима председника Асада и то против кампова и оперативаца ИСИС-а у Сирији.Наводи се да је најмање три ракете испаљено на возило у сиријској области Идлиб, близу границе са Турском. Нема информација о томе ко се налазио у возилима која су гађана, али је потврђено да се ради о нападима „нинџа бомбом”.

Циљ пројектовања овакве врсте бојеве главе јесте елиминисање или бар минимизирање колатералне штете.

Драган М. Вучковић (*Dragan* M. Vučković),
e-mail: draganvuckovic64@gmail.com,
ORCID iD: https://orcid.org/0000-0003-1620-5601

Русија формира први пук опремљен новим ракетним системом противваздухопловне одбране *S-500 Prometheus*[3]

Начелник Генералштаба Руске Федерације генерал Валериј Герасимов најавио је, 18. децембра 2024. године, формирање првог руског пука опремљеног високонапредним ПВО ракетним системом *S-500 Prometheus.*То представља значајан искорак у способностима руске противваздухопловне одбране, при чему је *S-500* систем нове генерације који комбинује функције противваздухопловне одбране и противракетног система. Ракетни систем ПВО *S-500* испоручује се у две основне конфигурације: једна је пројектована за противваздухопловну одбрану великог домета, а друга за противракетну одбрану. Међутим, генерал Герасимов није изнео конкретне детаље о томе колико је јединица *S-500* до сада испоручено, као ни колики је обим његовог распоређивања.

Систем *S-500Prometheus* требало би да унапреди одбрамбену моћ Русије. Дизајниран је за шири спектар претњи за разлику од претходних ракетних система противваздухопловне одбране *S-300* и *S-400.* Једна од најзначајнијих карактеристика *S-500* јесте његова способност да пресреће интерконтиненталне балистичке ракете (*ICBM*), хиперсоничне ракете, па чак и сателите у ниској орбити, што је директан одговор на новонастале ракетне претње широм света.

[3] Defense News Army, 25 December, 2024

Лансирна јединица противваздухопловног ракетног система S-500 Prometheus,изложена на одбрамбеној изложби Армија-2020 у Русији, представила је своје напредне могућности за пресретање ваздухопловних и ракетних претњи великог домета

Сваки пук *S-500* састоји се од 12 лансера, способних да открију и ангажују до десет бојевих глава балистичких ракета које се крећу брзином до седам км/с. Систем има време одзива од 3 до 4 с, што је побољшање у односу на 9 до 10 које захтева *S-400*. Такође, користи ракете *77N6-N* и *77N6-N1,* које су посебно пројектоване за кинетичко пресретање велике брзине. Тестови спроведени у фебруару 2024. потврдили су способност система да пресретне ракету *R-29RMU2 Sineva,* чиме је демонстрирана његова способност да гађа хиперсоничне циљеве.

Мада су *S-300* и *S-400* застрашујући системи, *S-500* је ефикаснији у погледу домета и свестраности циљева, што га чини заиста врхунским решењем за противваздухопловну одбрану.

Систем *S-500* надмашује *S-300* и *S-400* у неколико критичних области. Пре свега, домет његовог дејства је знатно већи; способан је да гађа циљеве на удаљености до 600 км (375 миља), што је много више у поређењу са ракетним системом *S-400* чији је радијус дејства до 400 км (250 миља) и ракетног система *S-300* са још мањим дометом . Повећани домет омогућава систему *S-500* да постави много већи заштитни кишобран, што га чини моћним средством одвраћања од широког спектра ваздушних претњи. Штавише, док је *S-400* способан да гађа балистичке и аеродинамичке мете, систем *S-500* има посебан фокус на пресретање хиперсоничних пројектила, што је област у којој се систем *S-400* не сналази најбоље због екстремне брзине и маневрисања ових ракета. Још једна

важна предност система *S-500* су његове антисателитске могућности. Он је наводно у стању да гађа сателите у ниској Земљиној орбити (LEO), што додаје нову димензију његовом оперативном обиму. То га чини не само високо способним одбрамбеним ракетним системом, већ и моћним оруђем које противницима ускраћује приступ кључним космичким средствима, као што су комуникације, извиђање и временски сателити. С тим у вези, то повећава способност Русије да омета операције противника, укључујући НАТО и друге западне земље, који се у великој мери ослањају на сателите у војне и стратешке сврхе.

Интеграција *S-500* у руску одбрамбену мрежу представља значајну ескалацију у способности Русије да заштити свој ваздушни простор, док истовремено представља директан изазов за НАТО и америчке системе ваздухопловне и ракетне одбране. Већи домет система и побољшане могућности аквизиције циљева значе да би систем потенцијално могао да неутралише многа средства противракетне одбране Запада, укључујући и она распоређена у источној Европи. Дакле,*S-500* би могао пореметити операције и значајно ограничити слободу маневара за НАТО снаге, посебно у сценаријима који укључују средства високе вредности као што су извиђачки авиони, бомбардери или одбрамбене ракете.

Систем *S-500* представља велики изазов за глобалну стратешку равнотежу Сједињених Држава. Његове напредне карактеристике директно га супротстављају америчким противракетним одбрамбеним системима, као што су ракетни системи *Patriot* и систем одбране од балистичких ракета *Aegis.* Способност супротстављања хиперсоничним пројектилима је посебно забрињавајућа, јер су се САД више фокусирале на развој сопственог хиперсоничног оружја. Успех Русије у размештању *S-500* могао би да примора САД да преиспита западне стратегије противракетне одбране, посебно у регионима у којима би Русија могла да користи ову технологију за супротстављање операцијама НАТО-а и САД.

Систем *S-500* би могао имати значајне импликације у рату у Украјини. Русија је већ распоредила системе *S-300* и *S-400* у региону, користећи их за супротстављање ваздухопловним средствима Украјине и НАТО-а . Долазак система *S-500* додатно јача одбрамбене способности Русије, пружајући моћан штит од ваздухопловних удара и ракетних напада. Са својом способношћу да пресретне широк спектар претњи, укључујући напредне ракетне системе које је обезбедио Запад, систем *S-500* би могао додатно отежати Украјини извођење прецизних удара на руске положаје или критичну инфраструктуру. Систем дугог домета могао би такође да гађа циљеве далеко изван граница Украјине, што би отежало све ваздухопловне операције које изводе НАТО или украјинске снаге.

Увођење ракетног система *S-500* могло би да утиче и на ланац снабдевања Украјине напредним наоружањем. На пример, прецизна муниција дугог домета, као што је ракетни систем *ATACMS* који испоручује САД или нови ракетни системи НАТО-а, можда ће имати потешкоћа да избегну могућности пресретања ракета *S-500*. То би могло ефективно да

умањи неке од стратешких предности које су се западне силе надале да ће пружити Украјини у борби против руских снага.

Петог јануара 2025. било је најављено да ће први руски пук противваздухопловних ракетних система *S-500 Prometheus* имати задатак да брани Кримски мост. Да су елементи *S-500* већ били распоређени на Криму у експерименталном капацитету известила је украјинска обавештајна служба још средином 2024. године.

На међународном плану, Русија је Индији понудила заједничку производњу *S-500*. Током посете премијера Нарендре Модија Москви, 2024. године, Русија је обновила овај предлог као део шире сарадње у области одбране. Индија тек треба да донесе одлуку, вероватно одмеравајући потенцијалне санкције и геополитичке импликације у односу на способности система. Потенцијални значај *S-500* у конкуренцији противракетне одбране наглашен је поређењима са ракетним програмом *BrahMos*, који је био резултат претходне сарадње Русије и Индије.

Упркос својим напредним карактеристикама, систем *S-500* се суочава са оперативним изазовима. Украјинске снаге су изнеле стратегију за борбу против њега, укључујући коришћење координираних ракетних напада, електронског ратовања и беспилотних ваздухопловних система. Крстарећа ракета *Trembita,* коју је пројектовала Украјина, могла би да се користи у нападима засићења како би се надвладали пресретачи *S-500*. Комбиновање таквих ракетних удара са електронским ометањем и операцијама дронова може смањити ефикасност система.

Наравно да ће Русија увезати системе *S-500* са постојећим системима *S-300* и *S-400*, као да ће ракетне батерије бити брањене системима *Панцир* и *Тор*.

Украјинци су и до сада повремено успевали да пробију тако слојевито организовану одбрану засићењем места напада великим количинама беспилотних летелица у комбинацији са крстарећим и другим врстама ракета.

Драган М. Вучковић (*Dragan* M. Vučković),
e-mail: draganvuckovic64@gmail.com,
ORCID iD: https://orcid.org/0000-0003-1620-5601

Нови турски тенк *Altay* [4] – поређење са модерним западним тенковима

Нови основни борбени тенк *Altay* (MBT) требало би да има кључну улогу у јачању оклопних способности, како турских оружаних снага, тако и њених међународних партнера. Овај нови тенк, за који се очекује да ће ући у употребу 2025. године, могао би да понуди неколико предности у односу

[4] Defense News Army, 13 January 2025

на модерне НАТО тенкове као што су *M1A2 SEPv3 Abrams, Leopard 2A8, Leclerc XLR, K2, Challenger 2* и *Ariete*. Серијска производња почела је у мају 2024. године, а турске копнене снаге су примарни оператери, са планираним циљем производње од 1.000 тенкова, испоручених у четири серије од по 250 јединица.

Укључујући искуства из јужнокорејског пројекта *K2 Black Panther, Altay* је основни борбени тенк четврте генерације (MBT) наоружан топом са глатком цеви од 120 мм L/55 који производи компанија МКЕ према споразуму о трансферу технологије са компанијом *Hyundai Rotem*.

Altay је производ Турског националног пројекта за производњу тенкова (MİTÜP), покренут средином деведесетих година, означивши велики развој тенкова од 1943. године

Серијска производња започела је у мају 2024, са стопом производње од најмање осам јединица месечно, а очекује се да ће тенк ући у употребу у Оружаним снагама Турске 2025. године, по процењеној цени од 13,75 милиона долара

Vučković, D., SAVREMENO NAORUŽANJE I VOJNA OPREMA / MODERN WEAPONS AND MILITARY EQUIPMENT, pp.698-709

Altay је развијен како би се успоставиле домаће способности за развој и одржавање оклопних платформи за Оружане снаге Турске. Програм је званично покренут 2007. године. Компанија *Otokar* је изабрана за главног извођача, са пројектом који укључује трансфер технологије и помоћ по пројекту јужнокорејске компаније *Hyundai Rotem*, ослањајући се на програм тенкова *K2 Black Panther*.

Пројекат је напредовао кроз развој прототипа, са почетним моделима произведеним 2012. године и фазама тестирања завршеним до 2016. године. Компанија BMC је 2018. добила уговор за серијску производњу, која је одложена због ембарга на немачке MTU моторе и извоз RENK трансмисије/мењача. Да би се решили ови проблеми, усвојене су јужнокорејске компоненте, што је омогућило да серијска производња почне у мају 2024. године. То је означило први потпуни развој турског основног борбеног тенка у односу на претходни покушај из 1943. године, који није напредовао даље од фазе прототипа.

Тенк *Altay* би могао да покаже значајан извозни потенцијал, с обзиром на то да је Катар наводно поручио 100 јединица, од којих се првих 40 очекује у року од две године. Заинтересовани су и Азербејџан, Пакистан, Саудијска Арабија и Оман, али и Мароко, Индонезија, Бангладеш и друге земље. Пројектована производња од 1.000 јединица до 2035. подржава капацитете за међународне испоруке, у складу са широм иницијативом Турске за успостављање капацитета домаће производње за извоз.

Altay је сада спреман за фазну производњу од 1.000 јединица у четири серије, са постепеним ажурирањем планираним за сваку фазу. Серијска производња започела је у мају 2024.године, са стопом производње од најмање осам јединица месечно, а очекује се да ће тенк ући у употребу у Оружаним снагама Турске 2025. године, по процењеној цени од 13,75 милиона долара. Варијанте укључују основну линију T1, побољшани модел T2 и T3 са куполом без посаде, заједно са конфигурацијама за градске операције (AXT), чишћење мина, полагање мостова и задатке опоравка. Док ће почетне серије користити јужнокорејске компоненте за погон, наредне јединице ће укључивати моторе развијене у домаћој индустрији.

У поређењу са тенком *M1A2 SEPv3 Abrams,* дизел мотор тенка *Altay* захтева већу потрошњу горива али је једноставнији за одржавање. У односу на тенк *Leopard 2A8, Altay* је опремљен системом активне заштите *AKKOR (APS*), пружајући додатне одбрамбене могућности против противтенковских вођених пројектила. У односу на тенк *Leclerc XLR*, модуларни дизајн оклопа тенка *Altay* омогућава прилагођавање и надоградњу његових нивоа заштите, нудећи флексибилност која није доступна у односу на фиксну конфигурацију оклопа француског тенка.

У поређењу са тенком *K2 Black Panther, Altay* укључује адаптације за различите оперативне терене, што може побољшати његове перформансе у различитим окружењима. У односу на тенк *Challenger 2,* глатка цев топа од 120 мм тенка *Altay* и напредни систем за контролу ватре компатибилни су са ширим спектром стандардне муниције НАТО-а, док олучена цев тенка

Challenger 2 ограничава употребу специфичне муниције (то је исправљено на следећем тенку *Challenger 3* који се вратио на систем глатке топовске цеви са НАТО калибром од 120 мм). Коначно, у поређењу са тенком *Ariete*, *Altay* има напредни оклоп и системе активне заштите, којих нема у старијем дизајну италијанског тенка. Ови упоредни аспекти карактеришу позицију тенка *Altay* међу тенковима НАТО-а на основу његовог дизајна и системске интеграције.

Укључујући лекције научене из јужнокорејског пројекта *K2 Black Panther, Altay* је основни борбени тенк четврте генерације (MBT) опремљен глатким топом од 120мм L/55 који производи компанија МКЕ према споразуму о трансферу технологије са компанијом *Hyundai Rotem.* Ово главно наоружање може да испаљује низ НАТО компатибилне муниције, са дометом од приближно 3 км, а допуњено је пакетом секундарног наоружања, укључујући даљински управљану оружну станицу од 12,7 мм (RCWS) и бацач граната од 40 мм. Систем за управљање ватром, систем командовања и управљања и систем електричног погона куполе испоручује компанија *Aselsan,* док модуларни композитни оклоп тенка производи компанија *Roketsan* уз пројектантску помоћ јужнокорејских фирми како би се обезбедила већа балистичка заштита.

Погонски склоп за прве производне серије биће турбодизел мотор *Hyundai Doosan DV27K V12* од 1.500 КС, повезан са мењачем *SNT Dynamics EST15K*. Будуће серије могу укључити домаћи мотор *BMC Power Batu V12. Altay* има максималну брзину на путу од 65 км/ч, брзину ван пута од 45 км/ч и радни домет од 450 км. Његов хидропнеуматски систем ослањања дизајниран је тако да оптимизује мобилност на различитим теренима и укључује аутоматски систем затезања гусеница. Такође, тенк је опремљен изолованим одељком за муницију, системима за сузбијање пожара и експлозија и сензорима за откривање хемијских, биолошких, радиолошких и нуклеарних (CBRN) претњи.

Драган М. Вучковић (*Dragan* M. Vučković),
e-mail: draganvuckovic64@gmail.com,
ORCID iD: https://orcid.org/0000-0003-1620-5601

.

ПОЗИВ И УПУТСТВО АУТОРИМА
ПРИГЛАШЕНИЕ И ИНСТРУКЦИЯ ДЛЯ АВТОРОВ РАБОТ
CALL FOR PAPERS AND INSTRUCTIONS FOR AUTHORS

ПОЗИВ И УПУТСТВО АУТОРИМА О НАЧИНУ ПРИПРЕМЕ ЧЛАНКА

Упутство ауторима о начину припреме чланка за објављивање у *Војнотехничком гласнику* урађено је на основу Правилника о категоризацији и рангирању научних часописа Министарства просвете, науке и технолошког развоја Републике Србије ("Службени гласник РС", број 159/20). Примена овог Правилника првенствено служи унапређењу квалитета домаћих часописа и њиховог потпунијег укључивања у међународни систем размене научних информација.

Војнотехнички гласник / Vojnotehnički glasnik / Military Technical Courier (втг.мо.упр.срб, www.vtg.mod.gov.rs, ISSN 0042-8469 – штампано издање, e-ISSN 2217-4753 – online, UDC 623+355/359, DOI: 10.5937/VojnotehnickiGlasnik; https://doi.org/10.5937/VojnotehnickiGlasnik), јесте рецензирани научни часопис.

Власници часописа су Министарство одбране Републике Србије и Војска Србије. Издавач и финансијер часописа је Универзитет одбране у Београду (Војна академија).

Програмска оријентација часописа заснива се на годишњој категоризацији часописа, коју врши надлежно државно министарство у одређеним областима, као и на његовом индексирању у међународним индексним базама.

Часопис обухвата научне, односно стручне области у оквиру образовно-научног поља **природно-математичких наука**, као и у оквиру образовно-научног поља **техничко-технолошких наука**, а нарочито области **одбрамбених наука и технологија**. Објављује теоријска и практична достигнућа која доприносе усавршавању свих припадника српске, регионалне и међународне академске заједнице, а посебно припадника војски и министарстава одбране. Публикује радове са уравнотеженим извештавањем о аналитичким, експерименталним и примењеним истраживањима, као и нумеричким симулацијама, обухватајући различите дисциплине. Објављени материјали су високог квалитета и релевантности, написани на начин који их чини доступним широкој читалачкој публици. Сви радови који извештавају о оригиналним теоријским и/или практично оријентисаним истраживањима или проширеним верзијама већ објављених радова са конференција су добродошли. Радови за објављивање одабиру се двоструко слепим поступком рецензије како би се осигурала оригиналност, релевантност и читљивост. Притом циљ није само да се квалитет објављених радова одржи високим већ и да се обезбеди правовремени, темељни и уравнотежени поступак рецензије.

Уређивачка политика *Војнотехничког гласника* заснива се на препорукама Одбора за етичност у издаваштву (COPE Core Practices) и заједничким принципима транспарентности и најбоље праксе у издаваштву COPE, DOAJ, OASPA и WAME, као и на најбољим прихваћеним праксама у научном издаваштву. *Војнотехнички гласник* је члан COPE (Committee on Publication Ethics) од 2. маја 2018. године и члан OASPA (Open Access Scholarly Publishers Association) од од 27. новембра 2015. године.

Министарство науке, технолошког развоја и иновација Републике Србије утврдило је дана 13. 12. 2024. године категоризацију *Војнотехничког гласника*, за 2024. годину:

– на листи часописа за рачунарске науке:
категорија врхунски часопис националног значаја **(M51)**,

– **на листи часописа за електронику, телекомуникације и информационе технологије:**
категорија врхунски часопис националног значаја **(М51)**,

– **на листи часописа за машинство:**
категорија врхунски часопис националног значаја **(М51)**,

– **на листи часописа за материјале и хемијске технологије:**
категорија национални часопис међународног значаја **(М24)**.

Усвојене листе домаћих часописа за 2024. годину могу се видети на сајту *Војнотехничког гласника*, страница *Категоризација часописа*.

Детаљније информације могу се пронаћи и на сајту Министарства просвете, науке и технолошког развоја Републике Србије.

Подаци о категоризацији могу се пратити и на сајту КОБСОН-а (Конзорцијум библиотека Србије за обједињену набавку).

Категоризација часописа извршена је према Правилнику о категоризацији и рангирању научних часописа Министарства просвете, науке и технолошког развоја Републике Србије ("Службени гласник РС", број 159/20).

Часопис се прати у контексту Српског цитатног индекса – СЦиндекс (база података домаћих научних часописа), Научно-информационог система Redalyc и Руског индекса научног цитирања (РИНЦ). Подвргнут је сталном вредновању (мониторингу) у зависности од утицајности (импакта) у самим базама. Детаљи о индексирању могу се видети на сајту *Војнотехничког гласника*, страница *Индексирање часописа*.

Војнотехнички гласник, у погледу свог садржаја, пружа могућност отвореног приступа (DIAMOND OPEN ACCESS) и примењује Creative Commons (CC BY) одредбе о ауторским правима. Детаљи о ауторским правима могу се видети на сајту часописа, страница *Ауторска права и политика самоархивирања*.

Радови се предају путем онлајн система за електронско уређивање АСИСТЕНТ, који је развио Центар за евалуацију у образовању и науци (ЦЕОН).

Приступ и регистрација за сервис врше се на сајту www.vtg.mod.gov.rs, преко странице *АСИСТЕНТ* или *СЦИНДЕКС*, односно директно на линку aseestant.ceon.rs/index.php/vtg.

Детаљно упутство о регистрацији и пријави за сервис налази се на сајту www.vtg.mod.gov.rs, страница *Упутство за АСИСТЕНТ*.

Потребно је да се сви аутори који подносе рукопис за објављивање у *Војнотехничком гласнику* региструју у регистар ORCID (Open Researcher and Contributor ID), према упутству на страници сајта *Регистрација за добијање ORCID идентификационе шифре*.

Војнотехнички гласник објављује чланке на енглеском језику (arial, величина слова 11 pt, проред Single).

Поступак припреме, писања и уређивања чланка треба да буде у сагласности са *Изјавом о етичком поступању* (http://www.vtg.mod.gov.rs/izjava-o-etickom-postupanju.html).

Чланак треба да садржи сажетак са кључним речима, увод (мотивацију за рад), разраду (адекватан преглед репрезентативности рада у његовој области, јасну изјаву о новини у представљеном истраживању, одговарајућу теоријску позадину, један или више примера за демонстрирање и дискусију о представљеним идејама), закључак и литературу (без нумерације наслова и поднаслова). Обим чланка треба да буде до

једног ауторског табака (16 страница формата А4 са проредом Single), а највише 24 странице.

Чланак треба да буде написан на обрасцу за писање чланка, који се у електронској форми може преузети са сајта на страници *Образац за писање чланка*.

Наслов

Наслов треба да одражава тему чланка. У интересу је часописа и аутора да се користе речи прикладне за индексирање и претраживање. Ако таквих речи нема у наслову, пожељно је да се придода и поднаслов.

Текући наслов

Текући наслов се исписује са стране сваке странице чланка ради лакше идентификације, посебно копија чланака у електронском облику. Садржи презиме и иницијал имена аутора (ако аутора има више, преостали се означавају са „et al.“ или „и др.“), наслове рада и часописа и колацију (година, волумен, свеска, почетна и завршна страница). Наслови часописа и чланка могу се дати у скраћеном облику.

Име аутора

Наводи се пуно име и презиме (свих) аутора. Веома је пожељно да се наведу и средња слова аутора. Имена и презимена домаћих аутора увек се исписују у оригиналном облику (са српским дијакритичким знаковима), независно од језика на којем је написан рад.

Назив установе аутора (афилијација)

Наводи се пун (званични) назив и седиште установе у којој је аутор запослен, а евентуално и назив установе у којој је аутор обавио истраживање. У сложеним организацијама наводи се укупна хијерархија (нпр. Универзитет одбране у Београду, Војна академија, Катедра природно-математичких наука). Бар једна организација у хијерархији мора бити правно лице. Ако аутора има више, а неки потичу из исте установе, мора се, посебним ознакама или на други начин, назначити из које од наведених установа потиче сваки од наведених аутора. Афилијација се исписује непосредно након имена аутора. Функција и звање аутора се не наводе.

Контакт подаци

Адреса или е-адреса свих аутора даје се поред имена и презимена аутора.

Категорија (тип) чланка

Категоризација чланака обавеза је уредништва и од посебне је важности. Категорију чланка могу предлагати рецензенти и чланови уредништва, односно уредници рубрика, али одговорност за категоризацију сноси искључиво главни уредник.

Војнотехнички гласник објављује научне чланке.

Научни чланак је:

– оригиналан научни рад (рад у којем се износе претходно необјављени резултати сопствених истраживања научним методом);

– прегледни рад (рад који садржи оригиналан, детаљан и критички приказ истраживачког проблема или подручја у којем је аутор остварио одређени допринос, видљив на основу аутоцитата);

– кратко или претходно саопштење (оригинални научни рад пуног формата, али мањег обима или прелиминарног карактера);

– научна критика, односно полемика (расправа на одређену научну тему, заснована искључиво на научној аргументацији) и осврти.

Изузетно, у неким областима, научни рад у часопису може имати облик монографске студије, као и критичког издања научне грађе (историјско-архивске, лексикографске, библиографске, прегледа података и сл.), дотад непознате или недовољно приступачне за научна истраживања.

Радови класификовани као научни морају имати бар две позитивне рецензије.

Ако се у часопису објављују и прилози ваннаучног карактера, научни чланци треба да буду груписани и јасно издвојени у првом делу свеске.

Пожељно је да обим кратких саопштења буде 4 до 7 страница, научних чланака и студија случаја 10 до 14 страница, док прегледни радови могу бити и дужи. Број страница није строго ограничен и, уз одговарајуће образложење, пријављени чланци такође могу бити дужи или краћи.

Ако су радови који су претходно објављени на конференцији проширени, уредници ће проверити да ли је додато довољно новог материјала који испуњава стандарде часописа и квалификује поднесак за поступак рецензије. Додати материјал не сме бити претходно објављен. Нови резултати нису нужно потребни, али су пожељни. Међутим, поднесак треба да садржи проширене кључне идеје, примере, разраде, итд., који су претходно били садржани у поднеску са конференције.

Језик рада

Језик рада треба да буде енглески.

Текст мора бити језички и стилски дотеран, систематизован, без скраћеница (осим стандардних). Све физичке величине морају бити изражене у Међународном систему мерних јединица – SI. Редослед образаца (формула) означава се редним бројевима, са десне стране у округлим заградама.

Сажетак

Сажетак јесте кратак информативан приказ садржаја чланка који читаоцу омогућава да брзо и тачно оцени његову релевантност. У интересу је уредништава и аутора да сажетак садржи термине који се често користе за индексирање и претрагу чланака. Саставни делови сажетка су увод/циљ истраживања, методи, резултати и закључак. Сажетак треба да има од 100 до 250 речи и треба да се налази између заглавља (наслов, имена аутора и др.) и кључних речи, након којих следи текст чланка.

Кључне речи

Кључне речи су термини или фразе које адекватно представљају садржај чланка за потребе индексирања и претраживања. Треба их додељивати ослањајући се на неки међународни извор (попис, речник или тезаурус) који је најшире прихваћен или унутар дате научне области. За нпр. науку уопште, то је листа кључних речи Web of Science. Број кључних речи не може бити већи од 10, а у интересу је уредништва и аутора да учесталост њихове употребе буде што већа. У чланку се пишу непосредно након сажетка.

Систем АСИСТЕНТ у ту сврху користи специјалну алатку KWASS: аутоматско екстраховање кључних речи из дисциплинарних тезауруса/речника по избору и рутине за њихов одабир, тј. прихватање односно одбацивање од стране аутора и/или уредника.

Датум прихватања чланка

Датум када је уредништво примило чланак, датум када је уредништво коначно прихватило чланак за објављивање, као и датуми када су у међувремену достављене евентуалне исправке рукописа наводе се хронолошким редоследом, на сталном месту, по правилу на крају чланка.

Захвалница

Назив и број пројекта, односно назив програма у оквиру којег је чланак настао, као и назив институције која је финансирала пројекат или програм, наводи се у посебној напомени на сталном месту, по правилу при дну прве стране чланка.

Претходне верзије рада

Ако је чланак у претходној верзији био изложен на скупу у виду усменог саопштења (под истим или сличним насловом), податак о томе треба да буде наведен у посебној напомени, по правилу при дну прве стране чланка. Рад који је већ објављен у неком часопису не може се објавити у *Војнотехничком гласнику* (прештампати), ни под сличним насловом и измењеном облику.

Табеларни и графички прикази

Пожељно је да наслови свих приказа, а по могућству и текстуални садржај, буду дати двојезично, на језику рада и на енглеском језику.

Табеле се пишу на исти начин као и текст, а означавају се редним бројевима са горње стране. Фотографије и цртежи треба да буду јасни, прегледни и погодни за репродукцију. Цртеже треба радити у програму word или corel. Фотографије и цртеже треба поставити на жељено место у тексту.

За слике и графиконе не сме се користити снимак са екрана рачунара програма за прикупљање података. У самом тексту чланка препоручује се употреба слика и графикона непосредно из програма за анализу података (као што су Excel, Matlab, Origin, SigmaPlot и други).

Навођење (цитирање) у тексту

Начин позивања на изворе у оквиру чланка мора бити једнообразан.

Војнотехнички гласник за референцирање (цитирање и навођење литературе) примењује Харвардски систем референци, односно Харвардски приручник за стил (Harvard Referencing System, Harvard Style Manual). У самом тексту, у обичним заградама, на месту на којем се врши позивање, односно цитирање литературе набројане на крају чланка, обавезно у обичној загради написати презиме цитираног аутора, годину издања публикације из које цитирате и, евентуално, број страница. Нпр. (Petrović, 2012, pp.10–12).

Детаљно упутство о начину цитирања, са примерима, дато је на страници сајта *Упутство за Харвардски приручник за стил*. Потребно је да се позивање на литературу у тексту уради у складу са поменутим упутством.

Систем АСИСТЕНТ у сврху контроле навођења (цитирања) у тексту користи специјалну алатку CiteMatcher: откривање изостављених цитата у тексту рада и у попису референци.

Напомене (фусноте)

Напомене се дају при дну стране на којој се налази текст на који се односе. Могу садржати мање важне детаље, допунска објашњења, назнаке о коришћеним

изворима (на пример, научној грађи, приручницима), али не могу бити замена за цитирану литературу.

Листа референци (литература)

Цитирана литература обухвата, по правилу, библиографске изворе (чланке, монографије и сл.) и даје се искључиво у засебном одељку чланка, у виду листе референци. Референце се не преводе на језик рада и набрајају се у посебном одељку на крају чланка.

Војнотехнички гласник, као начин исписа литературе, примењује Харвардски систем референци, односно Харвардски приручник за стил (Harvard Referencing System, Harvard Style Manual).

Литература се обавезно пише на латиничном писму и набраја по абецедном редоследу, наводећи најпре презимена аутора, без нумерације.

Детаљно упутство о начину пописа референци, са примерима, дато је на страници сајта *Упутство за Харвардски приручник за стил*. Потребно је да се попис литературе на крају чланка уради у складу са поменутим упутством.

Нестандардно, непотпуно или недоследно навођење литературе у системима вредновања часописа сматра се довољним разлогом за оспоравање научног статуса часописа.

Систем АСИСТЕНТ у сврху контроле правилног исписа листе референци користи специјалну алатку RefFormatter: контрола обликовања референци у складу са Харвардским приручником за стил.

Изјава о ауторству

Поред чланка доставља се *Изјава о ауторству* у којој аутори наводе свој појединачни допринос у изради чланка. Такође, у тој изјави потврђују да су чланак урадили у складу са *Позивом и упутством ауторима* и *Изјавом о етичком поступању часописа*.

Сви радови подлежу стручној рецензији.

Списак рецензената *Војнотехничког гласника* може се видети на страници сајта *Списак рецензената*. Процес рецензирања објашњен је на страници сајта *Рецензентски поступак*.

Уредништво

Адреса редакције:
Војнотехнички гласник
Вељка Лукића Курјака 33
11042 Београд
e-mail: vojnotehnicki.glasnik@mod.gov.rs.
тел: војни 40-260 (011/3603-260), 066/8700-123

ПРИГЛАШЕНИЕ И ИНСТРУКЦИЯ ДЛЯ АВТОРОВ О ПОРЯДКЕ ПОДГОТОВКИ СТАТЬИ

Инструкция для авторов о порядке подготовки статьи к опубликованию в журнале *«Военно-технический вестник»* разработана согласно Регламенту о категоризации и ранжировании научных журналов Министерства образования, науки и технологического развития Республики Сербия («Службени гласник РС», № 159/20). Применение этого Регламента способствует повышению качества отечественных журналов и их более полному вовлечению в международную систему обмена научной информацией.

Военно-технический вестник (**Vojnotehnički glasnik / Military Technical Courier**), втг.мо.упр.срб, www.vtg.mod.gov.rs/index-ru.html, ISSN 0042-8469 – печатное издание, e-ISSN 2217-4753 – online, UDK 623+355/359, DOI: 10.5937/VojnotehnickiGlasnik; https://doi.org/10.5937/VojnotehnickiGlasnik, является рецензируемым научным журналом.

Собственники журнала: Министерство обороны и Вооруженые силы Республики Србия.

Издатель журнала: Университет обороны в г. Белград (Военная академия).

Программная ориентация журнала основана на ежегодной категоризации журнала, которая производится соответствующим отраслевым министерством, в зависимости от области исследований, а также на его индексировании в международных наукометрических базах данных.

Журнал охватывает научные и профессиональные сферы в рамках учебно-научной области **естественно-математических наук**, а также в рамках учебно-научной области **технико-технологических наук**, особенно в области **оборонных наук и технологии**. В журнале публикуются теоретические и практические достижения, которые способствуют повышению квалификации представителей сербского, регионального и международного академического сообщества, особенно служащих Министерств Обороны и Вооружённых сил. В журнале публикуются статьи со соответствующими обзорами об аналитических, экспериментальных и прикладных исследованиях, а также о численном моделировании, охватывая различные дисциплины. Публикуемые материалы отличаются высоким качеством и актуальностью. Они написаны научным, но понятным и доступным для широкого круга читателей языком. Приветствуются все статьи, сообщающие об оригинальных теоретических и/или практических исследованиях и/или расширенные версии ранее опубликованных статей, представленных на конференциях. Статьи для публикации отбираются путем двойного слепого рецензирования, которое гарантирует оригинальность, актуальность и удобочитаемость. Цель состоит не только в поддержании высокого качества публикуемых статей, но и в обеспечении своевременного, тщательного и соответствующего процесса рецензирования.

Редакционная политика журнала *«Военно-технический вестник»* основана на рекомендациях Комитета по этике научных публикаций (COPE Core Practices), общих принципах прозрачности и лучшей практике издательской деятельности COPE, DOAJ, OASPA и WAME, а также на лучшей практике научно-издательской деятельности. Журнал *«Военно-технический вестник»* является членом COPE (Комитет по этике научных публикаций) со 2 мая 2018 года и членом OASPA (Ассоциация научных издателей открытого доступа) с 27 ноября 2015 года.

Министерством науки, технологического развития и инноваций Республики Сербия утверждена 13 декабря 2024 г. категоризация журнала *«Военно-технический вестник»* за 2024 год:

- **Область компьютерные науки:**
  ведущий журнал государственного значения **(M51)**,
- **Область электроники, телекоммуникаций и информационных технологий:**
  ведущий журнал государственного значения **(M51)**,
- **Область машиностроения:**
  ведущий журнал государственного значения **(M51)**,
- **Область материалов и химической технологии:**
  национальный журнал международного значения **(M24)**.

С информацией относительно категоризации за 2024 год можно ознакомиться на странице сайта *«Военно-технического вестника» Категоризация Вестника*.

Более подробную информацию можно найти на сайте Министерства образования, науки и технологического развития Республики Сербия.

С информацией о категоризации можно ознакомиться и на сайте КОБСОН (Консорциум библиотек Республики Сербия по вопросам объединения закупок).

Категоризация Вестника проведена согласно Регламенту о категоризации и ранжировании научных журналов Министерства образования, науки и технологического развития Республики Сербия («Службени гласник РС», № 159/20)

Журнал соответствует стандартам Сербского индекса научного цитирования (СЦИндекс/SCIndeks) - наукометрической базы данных научных журналов Республики Сербия, Научно-информационного система Redalyc, а также Российского индекса научного цитирования (РИНЦ). Журнал постоянно подвергается мониторингу и оценивается количественными наукометрическими показателями отражающими его научную ценность.

С информацией об индексировании можно ознакомиться на странице сайта журнала *Индексирование Вестника*.

«Военно-технический вестник» относительно своего содержания предоставляет пользователям возможность открытого доступа (DIAMOND OPEN ACCESS) и положениями об авторских правах, утвержденными Creative Commons (CC BY). С инструкцией об авторских правах можно ознакомиться на странице сайта журнала *Авторские права и политика самоархивирования*.

Рукописи статей направляются в редакцию журнала с использованием online системы ASSISTANT, запущенной Центром поддержи развития образования и науки (ЦПРОН). Регистрация в системе и оформление прав доступа выполняется по адресу http://www.vtg.mod.gov.rs/index-ru.html, через страницу *ASSISTANT* или *СЦИНДЕКС* (aseestant.ceon.rs/index.php/vtg). С инструкцией по регистрации и правам доступа можно ознакомиться по адресу http://www.vtg.mod.gov.rs/index-ru.html, на странице *Инструкция по ASSISTANT*.

Все авторы, предоставляющие свои рукописи для публикации в редакцию журнала *«Военно-технический вестник»* должны пройти предварительную регистрацию в реестре ORCID (Open Researcher and Contributor ID). Эта процедура осуществляется в соответствии с инструкцией, размещенной на странице сайта *Регистрация в реестре ORCID для присвоения идентификационного кода*.

«Военно-технический вестник» публикует статьи на английском языке (Arial, шрифт 11 pt, пробел Single). Процесс подготовки, написания и редактирования статьи должен осуществляться в соответствии с принципами *Этического кодекса*

(http://www.vtg.mod.gov.rs/etichyeskiy-kodyeks.html). Статья должна содержать резюме с ключевыми словами, введение (цель исследования), основную часть (соответствующий обзор представительного исследования в данной области, четкое изложение научной новизны в представленном исследовании, соответствующую теоретическую основу, один или несколько примеров для демонстрирования и обсуждения представленных тезисов), заключение и список литературы (без нумерации заголовков и подзаголовков). Объем статьи не должен превышать один авторский лист (16 страниц формата А4 с одинарным интервалом, максимум до 24 страниц, включая ссылки и приложения). Статья должна быть набрана на компьютере с использованием специально подготовленного редакцией макета, который можно скачать на странице сайта *Правила и образец составления статьи*.

Заголовок

Заголовок должен отражать тему статьи. В интересах журнала и автора необходимо использовать слова и словосочетания, удобные для индексации и поиска. Если такие слова не содержатся в заголовке, то желательно их добавить в подзаголовок.

Текущий заголовок

Текущий заголовок пишется в титуле каждой страницы статьи с целью упрощения процесса идентификации, в первую очередь копий статьей в электронном виде. Заголовок содержит в себе фамилию и инициал имени автора (в случае если авторов несколько, остальные обозначаются с «et al.» или «и др.»), название работы и журнала (год, том, выпуск, начальная и заключительная страница). Заголовок статьи и название журнала могут быть приведены в сокращенном виде.

ФИО автора

Приводятся полная фамилия и полное имя (всех) авторов. Желательно, чтобы были указаны инициалы отчеств авторов. Фамилия и имя авторов из Республики Сербия всегда пишутся в оригинальном виде (с сербскими диакритическими знаками), независимо от языка, на котором написана работа.

Наименование учреждения автора (аффилиация)

Приводится полное (официальное) наименование и местонахождение учреждения, в котором работает автор, а также наименование учреждения, в котором автор провёл исследование. В случае организаций со сложной структурой приводится их иерархическая соподчинённость (напр. Военная академия, кафедра военных электронных систем, г. Белград). По крайней мере, одна из организаций в иерархии должна иметь статус юридического лица. В случае если указано несколько авторов, и если некоторые из них работают в одном учреждении, нужно отдельными обозначениями или каким-либо другим способом указать в каком из приведённых учреждений работает каждый из авторов. Аффилиация пишется непосредственно после ФИО автора. Должность и специальность по диплому не указываются.

Контактные данные

Электронный адрес автора указываются рядом с его именем на первой страницы статьи.

Категория (тип) статьи

Категоризация статьей является обязанностью редакции и имеет особое значение. Категорию статьи могут предлагать рецензенты и члены редакции, т.е. редакторы рубрик, но ответственность за категоризацию несет исключительно главный редактор.

Журнал *«Военно-технический вестник»* публикует научные статьи.

Научные статьи:

– оригинальная научная статья (работа, в которой приводятся ранее неопубликованные результаты собственных исследований, полученных научным методом);

– обзорная статья (работа, содержащая оригинальный, детальный и критический обзор исследуемой проблемы или области, в который автор внёс определённый вклад, видимый на основе автоцитат);

– краткое сообщение (оригинальная научная работа полного формата, но меньшего объёма или имеющая предварительный характер);

– научная критическая статья (дискуссия-полемика на определённую научную тему, основанная исключительно на научной аргументации) и научный комментарий.

Однако, в некоторых областях знаний научная работа в журнале может иметь форму монографического исследования, а также критического обсуждения научного материала (историко-архивного, лексикографического, библиографического, обзора данных и т.п.) – до сих пор неизвестного или недостаточно доступного для научных исследований. Работы, классифицированные в качестве научных, должны иметь, по меньшей мере, две положительные рецензии. В случае если в журнале объявляются и приложения, не имеющие научный характер, научные статьи должны быть сгруппированы и четко выделены в первой части номера.

Объем кратких сообщений составляет 4-7 страниц, исследовательские статьи и тематические исследования с проблемно-ситуационным анализом − 10-14 страниц, однако объем обзорных статей может быть больше. Ограничения по количеству страниц не являются строгими, следовательно при соответствующем обосновании предоставленные работы могут быть длиннее или короче. В случае подачи расширенных версий ранее опубликованных докладов, представленных на конференции, редакция проверит было ли добавлено достаточно новых материалов для того, чтобы статья соответствовала стандартам журнала и условиям рецензирования. Добавленный материал должен быть новым, неопубликованным ранее. Новые результаты приветствуются, но не являются обязательным условием; однако ключевые тезисы, примеры, разработки и пр. должны быть более подробно представлены в статье по сравнению с первичным докладом на конфереции.

Язык работы

Статья должна быть написана на английском языке. Текст должен быть в лингвистическом и стилистическом смысле упорядочен, систематизирован, без сокращений (за исключением стандартных). Все физические величины должны соответствовать Международной системе единиц измерения – СИ. Очередность формул обозначается порядковыми номерами, проставляемыми с правой стороны в круглых скобках.

Резюме

Резюме является кратким информативным обзором содержания статьи, обеспечивающим читателю быстроту и точность оценки её релевантности. В интересах редакции и авторов, чтобы резюме содержало термины, часто используемые для индексирования и поиска статьей. Составными частями резюме являются введение/цель исследования, методы, результаты и выводы. В резюме должно быть от 100 до 250 слов, и оно должно находится между титулами (заголовок, ФИО авторов и др.) и ключевыми словами, за которыми следует текст статьи.

Ключевые слова

Ключевыми словами являются термины или фразы, адекватно представляющие содержание статьи, необходимые для индексирования и поиска. Ключевые слова необходимо выбирать, опираясь при этом на какой-либо международный источник (регистр, словарь, тезаурус), наиболее используемый внутри данной научной области. Число ключевых слов не может превышать 10. В интересах редакции и авторов, чтобы частота их встречи в статье была как можно большей. В статье они пишутся непосредственно после резюме.

Программа ASSISTANT предоставляет возможность использования сервиса KWASS, автоматически фиксирующего ключевые слова из источников/словарей по выбору автора/редактора.

Дата получения статьи

Дата, когда редакция получила статью; дата, когда редакция окончательно приняла статью к публикации; а также дата, когда были предоставлены необходимые исправления рукописи, приводятся в хронологическом порядке, как правило, в конце статьи.

Выражение благодарности

Наименование и номер проекта, т.е. название программы благодаря которой статья возникла, совместно с наименованием учреждения, которое финансировало проект или программу, приводятся в отдельном примечании, как правило, внизу первой страницы статьи.

Предыдущие версии работы

В случае если статья в предыдущей версии была изложена устно (под одинаковым или похожим названием, например, в виде доклада на научной конференции), сведения об этом должны быть указаны в отдельном примечании, как правило, внизу первой страницы статьи. Работа, которая уже была опубликована в каком-либо из журналов, не может быть напечатана в *«Военно-техническом вестнике»* ни под похожим названием, ни в изменённом виде.

Нумерация и название таблиц и графиков

Желательно, чтобы нумерация и название таблиц и графиков были исполнены на двух языках (на языке оригинала и на английском). Таблицы подписываются таким же способом как и текст и обозначаются порядковым номером с верхней стороны. Фотографии и рисунки должны быть понятны, наглядны и удобны для репродукции. Рисунки необходимо делать в программах Word или Corel. Фотографии и рисунки надо поставить на желаемое место в тексте. Для создания изображений и графиков использование функции снимка с экрана (скриншота) не допускается. В самом тексте статьи рекомендуется применение изображений и графиков, обработанных такими компьютерными программами, как: Excel, Matlab, Origin, SigmaPlot и др.

Ссылки (цитирование) в тексте

Оформление ссылок на источники в рамках статьи должно быть однообразным. *«Военно-технический вестник»* для оформления ссылок, цитат и списка использованной литературы применяет Гарвардскую систему (Harvard Referencing System, Harvard Style Manual). В тексте в скобках приводится фамилия цитируемого автора (или фамилия первого автора, если авторов несколько), год издания и по необходимости номер страницы. Например: (Petrović, 2010, pp.10-20). Рекомендации о способе цитирования размещены на странице сайта *Инструкция по использованию Гарвардского стиля*. При оформлении ссылок, цитат и списка использованной литературы необходимо придерживаться установленных норм. Программа

ASSISTANT предоставляет при цитировании возможность использования сервиса CiteMatcher, фиксирующего пропущенные цитаты в работе и в списке литературы.

Примечания (сноски)

Примечания (сноски) к тексту указываются внизу страницы, к которой они относятся. Примечания могут содержать менее важные детали, дополнительные объяснения, указания об использованных источниках (напр. научном материале, справочниках), но не могут быть заменой процедуры цитирования литературы.

Литература (референции)

Цитированной литературой охватываются, как правило, такие библиографические источники как статьи, монографии и т.п. Вся используемая литература в виде референций размещается в отдельном разделе статьи. Названия литературных источников не переводятся на язык работы. *«Военно-технический вестник»* для оформления списка использованной литературы применяет Гарвардскую систему (Harvard Style Manual). В списке литературы источники указываются в алфавитном порядке фамилий авторов или редакторов. Рекомендации о способе цитирования размещены на странице сайта *Инструкция по использованию Гарвардского стиля*. При оформлении списка использованной литературы необходимо придерживаться установленных норм. При оформлении списка литературы программа ASSISTANT предоставляет возможность использования сервиса RefFormatter, осуществляющего контроль оформления списка литературы в соответствии со стандартами Гарвардского стиля. Нестандартное, неполное и непоследовательное приведение литературы в системах оценки журнала считается достаточной причиной для оспаривания научного статуса журнала.

Авторское заявление

Авторское заявление предоставляется вместе со статьей, в нем авторы заявляют о своем личном вкладе в написание статьи. В заявлении авторы подтверждают, что статья написана в соответствии с *Приглашением и инструкциями для авторов*, а также с *Кодексом профессиональной этики журнала*.

Все рукописи статей подлежат профессиональному рецензированию.

Список рецензентов журнала *«Военно-технический вестник»* размещён на странице сайта *Список рецензентов*. Процесс рецензирования описан в разделе *Правила рецензирования*.

Редакция

Почтовый адрес редакции:

«Војнотехнички гласник»
ул. Велька Лукича Куряка 33, 11042 Белград, Республика Сербия
e-mail: vojnotehnicki.glasnik@mod.gov.rs,
тел: +381 11 3603 260, +381 66 8700 123

CALL FOR PAPERS AND ARTICLE FORMATTING INSTRUCTIONS

The instructions to authors about the article preparation for publication in the *Military Technical Courier* are based on the Regulations on categorization and ranking of scientific journals of the Ministry of Education, Science and Technological Development of the Republic of Serbia (Official Gazette of the Republic of Serbia, No 159/20). This Regulations aims at improving the quality of national journals and raising the level of their compliance with the international system of scientific information exchange.

The Military Technical Courier / Vojnotehnički glasnik (www.vtg.mod.gov.rs/index-e.html, втг.мо.упр.срб, ISSN 0042-8469 – print issue, e-ISSN 2217-4753 – online, UDC 623+355/359, DOI: 10.5937/VojnotehnickiGlasnik; https://doi.org/10.5937/VojnotehnickiGlasnik), is an peer-reviewed scientific journal.

The owners of the journal are the Ministry of Defence of the Republic of Serbia and the Serbian Armed Forces. The publisher and financier of the *Military Technical Courier* is the University of Defence in Belgrade (Military Academy).

The program of the journal is based on the annual classification of journals performed by a relevant Ministry as well as on its indexing in international indexing databases.

The journal covers scientific and professional fields within the educational-scientific field of **Natural-Mathematical Sciences**, as well as within the educational-scientific field of **Technical-Technological Sciences**, and especially the field of **defense sciences and technologies**. It publishes theoretical and practical achievements leading to professional development of all members of Serbian, regional and international academic communities as well as members of the military and ministries of defence in particular. It publishes papers with balanced coverage of analytical, experimental, and applied research as well as numerical simulations from various disciplines. The material published is of high quality and relevance, written in a manner that makes it accessible to a wider readership. The journal welcomes papers reporting original theoretical and/or practice-oriented research as well as extended versions of already published conference papers. Manuscripts for publication are selected through a double-blind peer-review process to validate their originality, relevance, and readability. This being so, the objective is not only to keep the quality of published papers high but also to provide a timely, thorough, and balanced review process.

The editorial policy of the *Military Technical Courier* is based on the COPE Core Practices, common COPE, DOAJ, OASPA and WAME Principles of Transparency and Best Practice in Scholarly Publishing as well as on the best accepted practices in scientific publishing. The Military Technical Courier has been a COPE (Committee on Publication Ethics) member since 2nd May 2018 and a member of OASPA (Open Access Scholarly Publishers Association) since 27th November 2015.

The Ministry of Science, Technological Development and Innovation of the Republic of Serbia classified the *Military Technical Courier* for the year 2024, on December 13, 2024

- **on the list of periodicals for computer sciences,**
  category: reputed national journal **(M51)**,
- **on the list of periodicals for electronics, telecommunications and IT,**
  category: reputed national journal **(M51)**,
- **on the list of periodicals for mechanical engineering,**
  category: reputed national journal **(M51)**,
- **on the list of periodicals for materials and chemical technology,**
  category: national journal of international importance **(M24)**.

The approved lists of national periodicals for the year 2024 can be viewed on the website of the *Military Technical Courier*, page *Journal categorization*.

More detailed information can be found on the website of the Ministry of Education, Science and Technological Development of the Republic of Serbia.

The information on the categorization can be also found on the website of KOBSON (Consortium of Libraries of Serbia for Unified Acquisition).

The periodical is categorized in compliance with the Regulations on categorization and ranking of scientific journals of the Ministry of Education, Science and Technological Development of the Republic of Serbia (Official Gazette of the Republic of Serbia, No 159/20). More detailed information can be found on the website of the Ministry of Education, Science and Technological Development.

The journal is in the Serbian Citation Index – SCIndex (data base of national scientific journals), in the Scientific Information System Redalyc, and in the Russian Index of Science Citation/Российский индекс научного цитирования (RINC/РИНЦ) and is constantly monitored depending on the impact within the bases themselves. More detailed information can be viewed on the website of the *Military Technical Courier*, page *Journal indexing*.

The *Military Technical Courier*, in terms of its content, offers the possibility of open access (DIAMOND OPEN ACCESS) and applies the Creative Commons Attribution (CC BY) licence on copyright. The copyright details can be found on the *Copyright notice and Self-archiving policy* page of the journal's website.

Manuscripts are submitted online, through the electronic editing system ASSISTANT, developed by the Center for Evaluation in Education and Science – CEON.

The access and the registration are through the *Military Technical Courier* site http://www.vtg.mod.gov.rs/index-e.html, on the page *ASSISTANT* or the page *SCINDEKS* or directly through the link (aseestant.ceon.rs/index.php/vtg).

The detailed instructions about the registration for the service are on the website http://www.vtg.mod.gov.rs/index-e.html, on the page *Instructions for ASSISTANT*.

All authors submitting a manuscript for publishing in the *Military Technical Courier* should register for an ORCID ID following the instructions on the web page *Registration for an ORCID identifier*.

The *Military Technical Courier* publishes articles in English, using Arial and a font size of 11pt with Single Spacing.

The procedures of article preparation, writing and editing should be in accordance with the *Publication ethics statement* (http://www.vtg.mod.gov.rs/publication-ethics-statement.html).

The article should contain an abstract with keywords, introduction (motivation for the work), body (adequate overview of the representative work in the field, a clear statement of the novelty in the presented research, suitable theoretical background, one or more examples to demonstrate and discuss the presented ideas), conclusion, and references (without heading and subheading enumeration). The article length should not normally exceed 16 pages of the A4 paper format with single spacing, up to a maximum of 24 pages with references and supplementary material included.

The article should be formatted following the instructions in the Article Form which can be downloaded from website page *Article form*.

Title

The title should be informative. It is in both Journal's and author's best interest to use terms suitable for indexing and word search. If there are no such terms in the title, the author is strongly advised to add a subtitle.

Letterhead title

The letterhead title is given at a top of each page for easier identification of article copies in an electronic form in particular. It contains the author's surname and first name initial (for multiple authors add "et al"), article title, journal title and collation (year, volume, issue, first and last page). The journal and article titles can be given in a shortened form.

Author's name

Full name(s) of author(s) should be used. It is advisable to give the middle initial. Names are given in their original form (with diacritic signs if in Serbian).

Author's affiliation

The full official name and seat of the author's affiliation is given, possibly with the name of the institution where the research was carried out. For organizations with complex structures, give the whole hierarchy (for example, University of Defence in Belgrade, Military Academy, Department for Military Electronic Systems). At least one organization in the hierarchy must be a legal entity. When some of multiple authors have the same affiliation, it must be clearly stated, by special signs or in other way, which department exactly they are affiliated with. The affiliation follows the author's name. The function and title are not given.

Contact details

The postal addresses or the e-mail addresses of the authors are given in the first page.

Type of articles

Classification of articles is a duty of the editorial staff and is of special importance. Referees and the members of the editorial staff, or section editors, can propose a category, but the editor-in-chief has the sole responsibility for their classification.

The *Military Technical Courier* publishes scientific articles.

Scientific articles:

– Original scientific papers (giving the previously unpublished results of the author's own research based on scientific methods);

– Review papers (giving an original, detailed and critical view of a research problem or an area to which the author has made a contribution demonstrated by self-citation);

– Short communications or Preliminary communications (original scientific full papers but shorter or of a preliminary character);

– Scientific commentaries or discussions (discussions on a particular scientific topic, based exclusively on scientific argumentation) and opinion pieces.

Exceptionally, in particular areas, a scientific paper in the Journal can be in a form of a monograph or a critical edition of scientific data (historical, archival, lexicographic, bibliographic, data survey, etc.) which were unknown or hardly accessible for scientific research.

Papers classified as scientific must have at least two positive reviews.

If the journal contains non-scientific contributions as well, the section with scientific papers should be clearly denoted in the first part of the Journal.

Short communications are usually 4-7 pages long, research articles and case studies 10-14 pages, while reviews can be longer. Page number limits are not strict and, with

appropriate reasoning, submitted manuscripts can also be longer or shorter. If extended versions of previously published conference papers are submitted, Editors will check if sufficient new material has been added to meet the journal standards and to qualify such manuscripts for the review process. The added material must not have been previously published. New results are desired but not necessarily required; however, submissions should contain expansions of key ideas, examples, elaborations, etc. of conference papers.

Language

The language of the article should be in English. The grammar and style of the article should be of good quality. The systematized text should be without abbreviations (except standard ones). All measurements must be in SI units. The sequence of formulae is denoted in Arabic numerals in parentheses on the right-hand side.

Abstract and summary

An abstract is a concise informative presentation of the article content for fast and accurate evaluation of its relevance. It contains the terms often used for indexing and article search. A 100- to 250-word abstract has the following parts: introduction/purpose of the research, methods, results and conclusion.

Keywords

Keywords are terms or phrases showing adequately the article content for indexing and search purposes. They should be allocated heaving in mind widely accepted international sources (index, dictionary or thesaurus), such as the Web of Science keyword list for science in general. The higher their usage frequency is, the better. Up to 10 keywords immediately follow the abstract and the summary, in respective languages. For this purpose, the ASSISTANT system uses a special tool KWASS for the automatic extraction of key words from disciplinary thesauruses/dictionaries by choice and the routine for their selection, i.e. acceptance or rejection by author and/or editor.

Article acceptance date

The date of the reception of the article, the dates of submitted corrections in the manuscript (optional) and the date when the Editorial Board accepted the article for publication are all given in a chronological order at the end of the article.

Acknowledgements

The name and the number of the project or programme within which the article was realised is given in a separate note at the bottom of the first page together with the name of the institution which financially supported the project or programme.

Article preliminary version

If an article preliminary version has appeared previously at a meeting in a form of an oral presentation (under the same or similar title), this should be stated in a separate note at the bottom of the first page. An article published previously cannot be published in the *Military Technical Courier* even under a similar title or in a changed form.

Tables and illustrations

All the captions should be in the original language as well as in English, together with the texts in illustrations if possible. Tables are typed in the same style as the text and are denoted by Arabic numerals at the top. Photographs and drawings, placed appropriately in the text, should be clear, precise and suitable for reproduction. Drawings should be created in Word or Corel.

For figures and graphs, proper data plot is recommended i.e. using a data analysis program such as Excel, Matlab, Origin, SigmaPlot, etc. It is not recommended to use a screen capture of a data acquisition program as a figure or a graph.

Citation in the text

Citation in the text must be uniform. The *Military Technical Courier* applies the Harvard Referencing System given in the Harvard Style Manual. When citing sources within your paper, i.e. for in-text references of the works listed at the end of the paper, place the year of publication of the work in parentheses and optionally the number of the page(s) after the author's name, e.g. (Petrovic, 2012, pp.10-12). A detailed guide on citing, with examples, can be found on *Military Technical Courier* website on the page *Instructions for Harvard Style Manual*. In-text citations should follow its guidelines. For checking in-text citations, the ASSISTANT system uses a special tool CiteMatcher to find out quotes left out within papers and in reference lists.

Footnotes

Footnotes are given at the bottom of the page with the text they refer to. They can contain less relevant details, additional explanations or used sources (e.g. scientific material, manuals). They cannot replace the cited literature.

Reference list (Literature)

The cited literature encompasses bibliographic sources such as articles and monographs and is given in a separate section in a form of a reference list. References are not translated to the language of the article.

In compiling the reference list and bibliography, the *Military Technical Courier* applies the Harvard System – Harvard Style Manual. All bibliography items should be listed alphabetically by author's name, without numeration. A detailed guide for listing references, with examples, can be found on *Military Technical Courier* website on the page *Instructions for Harvard Style Manual*. Reference lists at the end of papers should follow its guidelines. In journal evaluation systems, non-standard, insufficient or inconsequent citation is considered to be a sufficient cause for denying the scientific status to a journal.

Authorship Statement

The Authorship statement, submitted together with the paper, states authors' individual contributions to the creation of the paper. In this statement, the authors also confirm that they followed the guidelines given in *the Call for papers* and the *Publication ethics and malpractice statement of the journal*.

All articles are peer reviewed.

The list of referees of the *Military Technical Courier* can be viewed at website page *List of referees*. The article review process is described on the *Peer Review Process* page of the website.

Editorial Team

Address of the Editorial Office:
Vojnotehnički glasnik / Military Technical Courier
Veljka Lukića Kurjaka 33
11042 Belgrade, Republic of Serbia
e-mail: vojnotehnicki.glasnik@mod.gov.rs, tel.: +381 11 3603 260, +381 66 8700 123

Ликовно-графички уредник
Марија Марић, e-mail: marija.maric@mod.gov.rs

Лектор
Добрила Милетић, e-mail: miletic.dobrila@gmail.com

Превод на енглески
Јасна Вишњић, e-mail: jasnavisnjic@yahoo.com

Превод на шпански
Јована Јовановић, e-mail: jovana.jov92@gmail.com

Превод на руски
Др *Карина* Авагјан, e-mail: karinka2576@mail.ru

CIP – Каталогизација у публикацији
Народна библиотека Србије, Београд

623+355/359

ВОЈНОТЕХНИЧКИ гласник : научни часопис Министарства одбране и Војске Србије = Военно-технический вестник : научный журнал Министерства обороны и Вооружённых сил Республики Сербия = Military Technical Courier : scientific Journal of the Ministry of Defence and the Serbian Armed Forces / главни и одговорни уредник Драган Памучар. - Год. 1, бр. 1 (1. јан. 1953)- . - Београд : Универзитет одбране у Београду, Војна академија, 1953- (Београд : Војна штампарија). - 23 cm

Тромесечно. - Текст на срп., рус. и енгл. језику. - Друго издање на другом медијуму: Vojnotehnički glasnik (Online) = ISSN 2217-4753
ISSN 0042-8469 = Војнотехнички гласник
COBISS.SR-ID 4423938

Цена: 600,00 динара

Тираж: 100 примерака

На основу мишљења Министарства за науку, технологију и развој Републике Србије, број 413-00-1201/2001-01 од 12. 9. 2001. године, часопис „Војнотехнички гласник“ је публикација од посебног интереса за науку.

УДК: Народна библиотека Србије, Београд

Адреса редакције: Војнотехнички гласник,
Вељка Лукића Курјака 33, 11042 Београд

https://www.scopus.com/sourceid/21101207440
http://www.vtg.mod.gov.rs
http://aseestant.ceon.rs/index.php/vtg/issue/current
http://scindeks.nb.rs/journaldetails.aspx?issn=0042-8469
https://www.redalyc.org/revista.oa?id=6617
http://elibrary.ru/title_about.asp?id=53280
https://doaj.org/toc/2217-4753

Војнотехнички гласник је лиценциран код EBSCO Publishing-a.
Комплетан текст *Војнотехничког гласника* доступан је у базама података EBSCO Publishing-a.

e-mail: vojnotehnicki.glasnik@mod.gov.rs; X: @MilTechCourier

Претплата на штампано издање: e-mail: vojnotehnicki.glasnik@mod.gov.rs; тел. 066/87-00-123.

Часопис излази тромесечно.

Први штампани број *Војнотехничког гласника* објављен је 1. 1. 1953. године.

Прво електронско издање *Војнотехничког гласника* на Интернету објављено је 1. 1. 2011. г.

Штампа: Војна штампарија – Београд, Ресавска 40б, e-mail: vojna.stamparija@mod.gov.rs

Художественный редактор
Мария Марич, e-mail: marija.maric@mod.gov.rs

Корректор
Добрила Милетич, e-mail: miletic.dobrila@gmail.com

Перевод на английский язык
Ясна Вишнич, e-mail: jasnavisnjic@yahoo.com

Перевод на испанский язык
Йована Йованович, e-mail: jovana.jov92@gmail.com

Перевод на русский язык
Д.филол.н. *Карина* Кареновна Авагян, e-mail: karinka2576@mail.ru

CIP – Каталогизация в публикации
Национальная библиотека Сербии, г. Белград

623+355/359

ВОЈНОТЕХНИЧКИ гласник : научни часопис Министарства одбране и Војске Србије = Военно-технический вестник : научный журнал Министерства обороны и Вооружённых сил Республики Сербия = Military Technical Courier : scientific Journal of the Ministry of Defence and the Serbian Armed Forces / главни и одговорни уредник Драган Памучар. - Год. 1, бр. 1 (1. јан. 1953)- . - Београд : Универзитет одбране у Београду, Војна академија, 1953- (Београд : Војна штампарија). - 23 cm

Тромесечно. - Текст на срп., рус. и енгл. језику. - Друго издање на другом медијуму: Vojnotehnički glasnik (Online) = ISSN 2217-4753
ISSN 0042-8469 = Војнотехнички гласник
COBISS.SR-ID 4423938

Цена: 600,00 динаров

Тираж: 100 экземпляров

На основании решения Министерства науки и технологий Республики Сербия, № 413-00-1201/2001-01 от 12. 9. 2001 года, журнал «Военно-технический вестник» объявлен изданием, имеющим особое значение для науки.

УДК: Национальная библиотека Сербии, г. Белград

Адрес редакции: Војнотехнички гласник,
Ул. Велька Лукича Куряка 33, 11042 Белград, Республика Сербия

https://www.scopus.com/sourceid/21101207440
http://www.vtg.mod.gov.rs
http://aseestant.ceon.rs/index.php/vtg/issue/current
http://scindeks.nb.rs/journaldetails.aspx?issn=0042-8469
https://www.redalyc.org/revista.oa?id=6617
http://elibrary.ru/title_about.asp?id=53280
https://doaj.org/toc/2217-4753

«Военно-технический вестник» включен в систему EBSCO. Полный текст журнала «Военно-технический вестник» можно найти в базах данных EBSCO Publishing.

e-mail: vojnotehnicki.glasnik@mod.gov.rs, X: @MilTechCourier
Подписка на печатную версию журнала: e-mail: vojnotehnicki.glasnik@mod.gov.rs; тел. +381 66 87 00 123.

Журнал выпускается ежеквартально.

Первый номер журнала «Военно-технический вестник» выпущен 1.1.1953 года.

Первая электронная версия журнала размещена на интернет странице 1.1.2011 года.

Типография: Војна штампарија – Белград, Ресавска 40б, e-mail: vojna.stamparija@mod.gov.rs

Graphic design editor
Marija Marić, e-mail: marija.maric@mod.gov.rs

Proofreader
Dobrila Miletić, e-mail: miletic.dobrila@gmail.com

English translation and polishing
Jasna Višnjić, e-mail: jasnavisnjic@yahoo.com

Spanish translation and polishing
Jovana Jovanović, e-mail: jovana.jov92@gmail.com

Russian translation and polishing
Dr. *Karina* Avagyan, e-mail: karinka2576@mail.ru

CIP – Catalogisation in the publication
National Library of Serbia, Belgrade

623+355/359

ВОЈНОТЕХНИЧКИ гласник : научни часопис Министарства одбране и Војске Србије = Военно-технический вестник : научный журнал Министерства обороны и Вооружённых сил Республики Сербия = Military Technical Courier : scientific Journal of the Ministry of Defence and the Serbian Armed Forces / главни и одговорни уредник Драган Памучар. - Год. 1, бр. 1 (1. јан. 1953)- . - Београд : Универзитет одбране у Београду, Војна академија, 1953- (Београд : Војна штампарија). - 23 cm

Тромесечно. - Текст на срп., рус. и енгл. језику. - Друго издање на другом медијуму: Vojnotehnički glasnik (Online) = ISSN 2217-4753
ISSN 0042-8469 = Војнотехнички гласник
COBISS.SR-ID 4423938

Price: 600.00 RSD

Printed in 100 copies

According to the Opinion of the Ministry of Science and Technological Development No 413-00-1201/2001-01 of 12th September 2001, the *Military Technical Courier* is a publication of special interest for science.

UDC: National Library of Serbia, Belgrade

Address: Vojnotehnički glasnik/Military Technical Courier,
Veljka Lukića Kurjaka 33, 11042 Belgrade, Republic of Serbia

https://www.scopus.com/sourceid/21101207440
http://www.vtg.mod.gov.rs/index-e.html
http://aseestant.ceon.rs/index.php/vtg/issue/current
http://scindeks.nb.rs/journaldetails.aspx?issn=0042-8469
https://www.redalyc.org/revista.oa?id=6617
http://elibrary.ru/title_about.asp?id=53280
https://doaj.org/toc/2217-4753

Military Technical Courier has entered into an electronic licensing relationship with EBSCO Publishing. The full text of *Military Technical Courier* can be found on EBSCO Publishing's databases.

e-mail: vojnotehnicki.glasnik@mod.gov.rs, X: @MilTechCourier
Subscription to print edition: e-mail: vojnotehnicki.glasnik@mod.gov.rs; Tel. +381 66 87 00 123.

The journal is published quarterly.

The first printed issue of the *Military Technical Courier* appeared on 1st January 1953.
The first electronic edition of the *Military Technical Courier* on the Internet appeared on 1st January 2011.

Printed by Vojna štamparija – Belgrade, Resavska 40b, e-mail: vojna.stamparija@mod.gov.rs


ОД 1953.
70
ГОДИНА
ВТГ

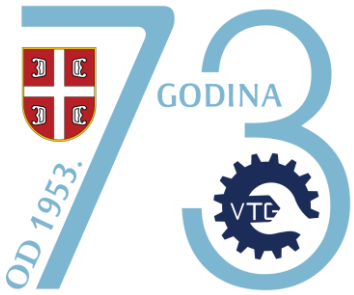
OD 1953.
70
GODINA
VTG


С 1953 г.
70
ЛЕТ
ВТБ


SINCE 1953
70
YEARS
MTG